

The Application of Vibration Characteristics to Damage Modelling and Identification in Plate Structures



Thesis submitted in fulfilment of the requirement for the degree of

Doctor of Philosophy

By

Yulin LUO

September 2019

School of Engineering

Cardiff University

Acknowledgements

In the journey towards submitting this thesis, I am indebted to many intelligent, patient and encouraging people who have helped me through the course of my PhD study. I would like to take this opportunity to appreciate their supports.

I would like to express my deepest appreciation and gratitude to my supervisors Prof. David Kennedy and Prof. Carol Featherston for their tremendous guidance, patience, encouragement and wisdom, and for being the friendliest supervisors during the past four years. Their valuable feedbacks and constructive comments helped me in all my time of research and writing of this thesis.

I would like to thank China Scholarship Council and Cardiff University who fund my PhD project. I am also quite thankful to my colleagues and friend whom I have worked with in the office S 2.35, in Queen's Building over the years for their kind suggestions and accompany. Special thanks to my friend Dr Chi Zhang, who kindly gave me valuable advice and offered me warm support during my life in the UK. Besides, during the difficulty I met in the past four years, I also need to thank to Jiawen Li, Kun Wang, Wei Xi, Huan Cai, Qiuju Wu and other cronies to comfort and help me.

I wish to thank my partner, Kaiyue Jiang, for her immense and endless emotional supports throughout my thesis writing stage. Without her love and care, it would have been much more stressful during difficult times. Finally, I would like to dedicate this thesis to my parents, Hong Lin and Wancheng Luo, for their consistent encouragement and unconditional support. It was their great love and sacrifice that made the completion of the thesis possible.

Abstract

Damage modelling is essential in the preliminary design of structures. Moreover, the identification of damage using numerical methods can make maintenance more efficient and economical. Also, applying damage detection procedures at an early stage can prevent catastrophic structure failures. For this project, vibration parameters (natural frequencies and mode shapes) are used to identify the location and severity of damage in classical thin plates.

A delaminated composite plate is introduced in a comparative study, for which natural frequencies are obtained using an exact strip model to verify the proposed detection method. Next, the direct problem of calculating the relative change in natural frequencies of an isotropic simple supported plate due to a predefined single arbitrary crack with random direction, location, depth and length is mainly addressed, giving a comprehensive understanding of the relationship between the location and severity of the crack and the free vibration natural frequencies and mode shapes. This study is highly pertinent, and a hybrid model is proposed which couples exact strip analysis for the undamaged part and finite element analysis for the damaged part. In the finite element part, a crack is modelled as a rotational spring stiffness giving additional degrees of freedom to the stiffness matrix. The finite element and exact strip dynamic stiffness matrices are assembled into a global dynamic stiffness matrix, coupled using Lagrangian Multipliers to equate the displacements at the boundaries of the two parts. Applying an efficient bandwidth method for Gaussian elimination, the resulting transcendental eigenvalue problem is solved by a simplified form of the Wittrick-Williams algorithm for the first six natural frequencies.

For the inverse problem, chosen natural frequencies are calculated accurately for both undamaged and damaged cases. The changes in natural frequencies are normalised to isolate the effect of damage location and severity individually. The same normalisation procedure is applied to measured natural frequencies. Point estimates of the damage location are obtained for noise free measurements, while an interval estimate is given by noisy measurements. A relevant severity range is then estimated. Mode shapes are monitored by an automatic sign method for correctly tracking the propagation of damage.

Contents

Acknowledgements.....	I
Abstract.....	II
Contents.....	III
List of Figures.....	IX
List of Tables	XIII
Abbreviation	XVIII
Nomenclature.....	XXI
Chapter 1--- Introduction.....	1
1.1 Motivation and Background.....	1
1.1.1 Aerospace Industry.....	1
1.1.2 Plate Structures.....	2
1.1.3 Types of Defect.....	3
1.1.4 Effects of Damage.....	6
1.2 Damage Detection.....	8
1.2.1 Non-destructive Testing.....	8
1.2.2 Different types of NDT.....	9
1.2.3 Global NDT.....	10
1.2.4 Vibration Characteristics.....	12
1.2.5 Natural Frequency.....	13
1.2.6 Importance and Improvement.....	14
1.3 Thesis Aims and Objectives.....	16
1.4 Thesis Overview.....	18
1.5 Publication List.....	21

Chapter 2---	Literature Review.....	22
2.1	Introduction.....	22
2.2	Modelling the Effects of Damage.....	23
2.2.1	Delamination.....	23
2.2.2	Cracks.....	25
2.2.3	Beam Structures.....	26
2.2.3.1	Stiffness Reduction.....	26
2.2.3.2	Spring Models.....	27
2.2.3.3	Multiple Cracks Problem with Advanced Approaches.....	27
2.2.4	Plate Structures.....	28
2.2.4.1	Numerical Analysis.....	28
2.2.4.2	Analytical Analysis.....	30
2.2.4.3	Experimental Analysis.....	31
2.2.4.4	Line Spring Model.....	32
2.2.5	Further Remarks.....	33
2.3	Inverse Problem.....	35
2.3.1	Beam-like Structures.....	35
2.3.1.1	Spring Model.....	35
2.3.1.2	Finite Element Method.....	36
2.3.1.3	Other Detection Methods.....	37
2.3.2	Plate-like Structures.....	38
2.3.2.1	General Detection Method.....	39
2.3.2.2	Optimality Criteria.....	40
2.3.3	Further Remarks.....	41
Chapter 3---	Exact Strip Plate Analysis.....	47
3.1	Introduction.....	47
3.2	Exact Strip Method.....	50

3.2.1 FSM and DSM	50
3.2.2 Dynamic Stiffness Formulation	51
3.2.3 DSM Application and ESM Development.....	52
3.2.4 ESM	54
3.2.5 Comparison of Different Methods	54
3.3 The Wittrick-Williams Algorithm.....	56
3.3.1 Finite system	57
3.3.2 Infinite System	58
3.3.3 Sign count of matrix.....	58
3.3.4 The basic algorithm.....	60
3.4 Lagrangian Multipliers.....	61
3.5 VICONOPT	64
3.5.1 VIPASA	64
3.5.2 VICON analysis	67
3.5.3 VICONOPT	69
3.6 Conclusions.....	71
Chapter 4--- Data Analysis and Processing.....	72
4.1 Introduction	72
4.2 Methodology	73
4.2.1 Modified Wittrick-Williams algorithm utilisation.....	73
4.2.2 Bandwidth method in W-W algorithm.....	76
4.2.2.1 Bandwidth methodology	77
4.2.3 Automatic mode shape sign method	79
4.2.3.1 Automatic mode shape sign methodology	81
4.3 Final Remarks	84

Chapter 5--- Free Vibration Modelling of Plates	85
5.1 Introduction.....	85
5.2 Damaged Plate Modelling Using Different Techniques	86
5.2.1 Damaged Plate Modelling in VICONOPT	86
5.2.1.1 Delamination Simulation	86
5.2.1.2 Crack Simulation.....	87
5.2.1.3 Further Remarks.....	90
5.2.2 Cracked Plate Modelling in Advanced Finite Element Method (MATLAB).....	90
5.2.2.1 Stiffness and Mass Properties of Plate Elements	91
5.2.2.2 Modified Stiffness Matrix with Arbitrary Crack	100
5.2.2.3 Rotational Spring Crack Simulation	101
5.2.3 Cracked Plate Modelling in ABAQUS	105
5.2.3.1 ABAQUS cracked plate modelling.....	105
5.2.3.2 Further Remarks.....	108
5.2.4 Cracked Plate Modelling in Hybrid Approach	108
5.2.4.1 Essential Derivation and Explicit Expressions of the Dynamic Stiffness Matrix of ESM	109
5.2.4.2 VICON Analysis with FEM---Global Stiffness Matrix	113
5.2.4.3 Further Remarks.....	114
5.3 Mode Shapes of Cracked Plates.....	115
5.4 Conclusions.....	117
Chapter 6--- Single predefined damage analysis in plates	118
6.1 Introduction.....	118
6.2 All through-the-length delamination.....	120
6.2.1 Model	120
6.2.2 Three different deformation statuses.....	121
6.2.3 Size effect and location effect.....	122

6.3 Parallel all through-the-length crack.....	126
6.3.1 Model	126
6.3.2 Results.....	127
6.4 Parallel partial through-the-length crack.....	139
6.4.1 Modelling Preparation.....	139
6.4.2 Results.....	140
6.4.2.1 ATDC Located at the Middle of Plate ($x_c, y_c = 0.05m, 0.05m$)	140
6.4.2.2 ATDC Locates at the Middle Edge of Plate ($x_e, y_e = 0.05m, 0.1m$)...	153
6.4.2.3 ATDC Locates at an Arbitrary Point of Plate ($x_e, y_e = 0.075m, 0.1m$)	159
6.4.2.4 PTDC with Fixed Length Ratio starting at Different Point	164
6.4.2.5 PTDC with Fixed Depth Ratio starting at an Arbitrary Point.....	172
6.4.3 Discussion	175
6.5 Arbitrary direction crack.....	176
6.6 Summary of results and discussion.....	186
6.7 Conclusion	190
Chapter 7--- Damage Detection in Plate Structures	192
7.1 Introduction.....	192
7.2 Severity and location effects	194
7.3 Single damage detection in plate-like structures using noise-free simulation	197
7.3.1 All through-the-length delamination.....	197
7.3.1.1 Normalisation procedure.....	197
7.3.1.2 Linear interpolation.....	199
7.3.2 All through-the-length crack.....	202
7.4 Single damage detection in plate-like structure with noisy simulated measurement	208
7.4.1 All through-the-length delamination.....	208
7.4.2 All through-the-length crack.....	215

7.5 Discussion	223
7.6 Conclusion	225
Chapter 8--- Conclusions and Further Work	226
8.1 Conclusions.....	226
8.2 Scope for future work	230
Appendix	233
Appendix A	233
Appendix B	234
Appendix C	238
Appendix D	246
Appendix E	247
Appendix F.....	249
Appendix G.....	250
Appendix H.....	252
Appendix I.....	253
References	255

List of Figures

<i>Figure 1-1 The simplified structural layout of a MiG-27 (Marcos 2013).</i>	1
<i>Figure 1-2 Different types of defect in plate-type structures (Shams and Elhajjar 2013).</i>	4
<i>Figure 1-3 Basic delamination forms (Ding 2000).</i>	4
<i>Figure 1-4 Crack representation in reality</i>	5
<i>Figure 1-5 Magnetic Fields (ASNT 2011).</i>	9
<i>Figure 1-6 Two frequent sound waves (ASNT 2011).</i>	9
<i>Figure 2-1 Embedded rectangular delamination model in VICONOPT (Damghani et al. 2014).</i>	24
<i>Figure 2-2 Hybrid delamination plate model reproduced from Suliman (2018).</i>	25
<i>Figure 3-1 Different discretisation in (a) FEM (b) FSM (Zhang 2018).</i>	49
<i>Figure 3-2 Banded matrix for Gauss elimination (Suliman 2018).</i>	59
<i>Figure 3-3 Comparison of mode shapes when Lagrangian Multipliers are included and not included in an analysis.</i>	62
<i>Figure 3-4 Plate assemblies in VICONOPT analysis (Williams et al. 1991).</i>	65
<i>Figure 3-5 A component plate showing the edge forces, displacements, and nodal lines (Wittrick and Williams 1974).</i>	66
<i>Figure 3-6 VICONOPT optimisation process (Butler and Williams 1992).</i>	70
<i>Figure 4-1 Hybrid cracked plate model (SSSS), coupling exact strip model and FE model.</i>	73
<i>Figure 4-2 Time taken to run a simply support isotropic plate in MATLAB.</i>	75
<i>Figure 4-3 Hybrid model used in bandwidth method illustration.</i>	78
<i>Figure 4-4 Mode shape for an isotropic simply supported cracked plate with different crack location and different crack severity, crack.</i>	80
<i>Figure 4-5 Variation of mode shapes with crack location α, for $\beta = 0.4$ (Luo et al. 2019), crack.</i>	83

Figure 5-1 Cross-section of an all through-the-length delamination in a composite plate.
..... 86

Figure 5-2 Different crack simulation methods...... 88

Figure 5-3 Nodes and related degrees of freedom in a single element. 92

Figure 5-4 Detail of a portion of the FE cracked plate model. 100

Figure 5-5 Rotational degrees of freedom at node 5 of the cracked portion...... 101

Figure 5-6 Arbitrary cracked plate and relative cracked element. 102

Figure 5-7 Different crack simulation techniques in ABAQUS...... 106

Figure 6-1 Simply supported isotropic square plate with corresponding notations. ... 118

Figure 6-2 Different damaged cases studied by various approaches in the study. 119

Figure 6-3 All through-the-length delamination plate model...... 120

Figure 6-4 Three different transformation statuses which exist during the propagation of delamination...... 121

Figure 6-5 The propagation of delamination with different starting points...... 121

Figure 6-6 All through-the-length delamination with fixed damaged width at a different locations along the y-axis...... 125

Figure 6-7 ATLC model simulated by different techniques at various location. 127

Figure 6-8 Mode shapes reproduced from VICONOPT...... 131

Figure 6-9 Mode shapes reproduced from AFE. 132

Figure 6-10 Comparison of RCNF for centrally located ATLC for VICONOPT and AFE.
..... 133

Figure 6-11 Comparison of RCNF for an arbitrary located ($y=0.075m$, quarter located) ATLC based on VICONOPT and AFE. 136

Figure 6-12 The dimensions ($a = 100mm$, $b = 100mm$) of the plate and the location of ATDC ($x_c, y_c = 0.05m, 0.05m$) when crack locates at the middle of plate. 139

Figure 6-13 The dimension ($a = 100mm, b = 100mm$) of plate and the location of ATDC ($x_e, y_e = 0.05m, 0.1m$) when crack develop from the middle edge of plate with various length ratio. 140


<i>Figure 6-14 Comparative figures of centrally located ATDC with various length ratio between AFE and previous studies.....</i>	<i>149</i>
<i>Figure 6-15 Comparison of AT, ATCS and approaches from the literature predicted values of RCNF for centrally located ATDC with various length ratio.....</i>	<i>151</i>
<i>Figure 6-16 Relative change in fundamental natural frequency, ATDC centrally located from AFE model with various mesh sizes.....</i>	<i>152</i>
<i>Figure 6-17 Comparison of the values of RCNF for different techniques for modelling an ATDC starting from the middle edge with various length ratio from various approaches.</i>	<i>157</i>
<i>Figure 6-18 Mode shape comparison between AFE and Huang and Leissa (2009). ...</i>	<i>158</i>
<i>Figure 6-19 The dimensions ($a = 100\text{mm}$, $b = 100\text{mm}$) of the plate and the location of ATDC ($x_e, y_e = 0.075\text{m}$, 0.1m) when crack locates an arbitrary point of plate... </i>	<i>159</i>
<i>Figure 6-20 Comparison of the values of RCNF for different techniques for modelling an ATDC starting from an arbitrary point with various length ratio from different approaches, </i>	<i>163</i>
<i>Figure 6-21 Comparison of mode shapes for different modes when the crack length ratio is 0.2 and 0.5; crack angle is 90°; crack start point $(x, y) = (0.075, 0.1)$.</i>	<i>164</i>
<i>Figure 6-22 The plate dimensions ($a = 100\text{mm}$, $b = 100\text{mm}$) and the location of a PTDC with fixed length ratio 0.5.</i>	<i>165</i>
<i>Figure 6-23 Different modes of comparative figures, PTDC starts from arbitrary point with various depth ratio from different approaches.....</i>	<i>168</i>
<i>Figure 6-24 Different modes of comparative figures, PTDC starts from arbitrary point with various depth ratio from different approaches.....</i>	<i>171</i>
<i>Figure 6-25 The plate dimensions ($a = 100\text{mm}$, $b = 100\text{mm}$) and the location of PTDC with a fixed depth ratio 0.5.....</i>	<i>172</i>
<i>Figure 6-26 Different modes of comparative figures, PTDC starting from an arbitrary point with various length ratio from different approaches.</i>	<i>174</i>
<i>Figure 6-27 The dimension of the plate and the location of ADC with through crack depth at orientation $\theta = 15^\circ$ or 30° with various crack lengths, which ADC arbitrarily locates starting at $(x, y) = (0.075, 0.1)$.....</i>	<i>176</i>

Figure 6-28 Comparison of RCNF for different modes for an ADC starting from an arbitrary point with various length ratios from different approaches. 182

Figure 6-29 Comparison of mode shapes for different modes when the crack length ratio is 0.2 and 0.5; crack angle is 15°; crack start point (x, y) = (0.075,0.1). 183

Figure 6-30 Comparison of RCNF for different modes for an ADC starting from an arbitrary point with various length ratios from different approaches. 184

Figure 6-31 The influence of a small increment in crack length on the change natural frequencies for different modes, ADC starts from the arbitrary point with various length ratios..... 185

*Figure 6-32 Time consumption for AFE 40*40 model. 191*

Figure 7-1 Degradation of natural frequencies with crack location and length (Luo et al. 2019)..... 195

Figure 7-2 ATLD case geometry..... 197

Figure 7-3 Normalised reference frequency and simulated frequency, from three chosen modes..... 198

Figure 7-4 ATLC case geometry..... 202

Figure 7-5 The normalised change natural frequencies of three chosen modes from the referred set for discrete points along the y-axis and simulated cases..... 210

List of Tables

<i>Table 2-1 Review of damage detection by different vibration-based parameters.</i>	<i>44</i>
<i>Table 3-1 ESM VS FEM.....</i>	<i>55</i>
<i>Table 3-2 Comparison between VIPASA, SMITH'S program and BUCLASP2 (Wittrick and Williams 1974).</i>	<i>67</i>
<i>Table 4-1 Normalised nodal displacements for two hypothetical crack cases.</i>	<i>82</i>
<i>Table 5-1 Comparison of change in natural frequencies of different modes for different techniques, d = 0.5mm</i>	<i>89</i>
<i>Table 5-2 Submatrix $\mathbf{k}_{I,I}$ of stiffness matrix for a rectangular plate in bending, all coefficients multiplied by $Et^3/(12(1-\nu^2)ab)$, where a and b are the plate dimensions (Przemieniecki 1985).....</i>	<i>96</i>
<i>Table 5-3 Submatrix $\mathbf{k}_{II,I}$ of stiffness matrix for a rectangular plate in bending, all coefficients multiplied by $Et^3/(12(1-\nu^2)ab)$, where a and b are the plate dimensions (Przemieniecki 1985).....</i>	<i>97</i>
<i>Table 5-4 Submatrix $\mathbf{k}_{II,II}$ of stiffness matrix for a rectangular plate in bending, all coefficients multiplied by $Et^3/(12(1-\nu^2)ab)$, where a and b are the plate dimensions (Przemieniecki 1985).....</i>	<i>98</i>
<i>Table 5-5 Mass matrix \mathbf{m} for a rectangular plate in bending, all coefficients multiplied by $\rho a b t/176400$, where a and b are the plate dimension (Przemieniecki 1985). ..</i>	<i>99</i>
<i>Table 5-6 Comparison of the dimensionless natural frequencies of undamaged SSSS plate from ABAQUS with previous studies.....</i>	<i>107</i>
<i>Table 6-1 All through-the-length delamination starting at different original locations with varying width, delamination depth d=0.5mm</i>	<i>123</i>
<i>Table 6-2 All through-the-length delamination with fixed width ($\beta = 10\text{mm}$) at varying locations (depth d=0.5mm).</i>	<i>125</i>
<i>Table 6-3 Non-dimensional natural frequencies---comparison for intact plate.....</i>	<i>129</i>
<i>Table 6-4 The ONF of an ATLC located at the middle of the plate using the VICONOPT model.</i>	<i>129</i>
<i>Table 6-5 The ONF of an ATLC located at the middle of the plate by AFE model.</i>	<i>129</i>

Table 6-6 The RCNF of an ATLC located at the middle of the plate by VICONOPT model.
..... 130

Table 6-7 The RCNF of an ATLC located at the middle of the plate by AFE model.... 130

Table 6-8 The ONF of an ATLC located at an arbitrary point of the plate using the VICONOPT model..... 134

Table 6-9 The ONF of an ATLC located at an arbitrary point of the plate using the AFE model. 134

Table 6-10 The RCNF of an ATLC located at an arbitrary point of the plate using the VICONOPT model..... 135

Table 6-11 The RCNF of an ATLC located at an arbitrary point of the plate using the AFE model..... 135

Table 6-12 The ONF of an ATLC located at the mid-point of the plate using different approaches, depth ratio 1..... 137

Table 6-13 The RCNF of an ATLC located at the mid-point of the plate using different approaches, depth ratio 1..... 137

Table 6-14 The ONF of intact plate obtained from different studies..... 141

Table 6-15 The ONF and RCNF of an ATDC located at the plate’s midpoint reproduced from different studies, length ratio 0.2. 142

Table 6-16 The ONF and RCNF of an ATDC located at the plate’s midpoint reproduced from different studies, length ratio 0.4. 143

Table 6-17 The ONF and RCNF of an ATDC located at the plate’s midpoint reproduced from different studies, length ratio 0.5. 144

Table 6-18 The ONF and RCNF of an ATDC located at the plate’s midpoint reproduced from different studies, length ratio 0.6. 145

Table 6-19 The ONF and RCNF of an ATDC located at the plate’s midpoint reproduced from different studies, length ratio 0.8. 146

Table 6-20 The ONF and RCNF of an ATDC located at the plate’s mid-point reproduced from different studies, length ratio 1. 147

Table 6-21 The ONF of the intact plate obtained from different studies..... 153

<i>Table 6-22 The ONF and RCNF of an ATDC starting at the middle of one edge of the plate, data reproduced from different studies. Crack case: Length ratio=0.1; Crack angle=90°; Depth ratio=1.</i>	<i>153</i>
<i>Table 6-23 The ONF and RCNF of an ATDC starting at the middle of one edge of the plate, data reproduced from different studies. Crack case: Length ratio=0.2; Crack angle=90°; Depth ratio=1.</i>	<i>154</i>
<i>Table 6-24 The ONF and RCNF of an ATDC starting at the middle of one edge of the plate, data reproduced from different studies. Crack case: Length ratio=0.3; Crack angle=90°; Depth ratio=1.</i>	<i>154</i>
<i>Table 6-25 The ONF and RCNF of an ATDC starting at the middle of one edge of the plate, data reproduced from different studies. Crack case: Length ratio=0.4; Crack angle=90°; Depth ratio=1.</i>	<i>155</i>
<i>Table 6-26 The ONF and RCNF of an ATDC starting at the middle of one edge of the plate, data reproduced from different studies. Crack case: Length ratio=0.5; Crack angle=90°; Depth ratio=1.</i>	<i>155</i>
<i>Table 6-27 The ONF and RCNF of an ATDC starting at the middle of one edge of the plate, data reproduced from different studies. Crack case: Length ratio=0.6; Crack angle=90°; Depth ratio=1.</i>	<i>156</i>
<i>Table 6-28 The ONF and RCNF of ATDC starting at an arbitrary point of the plate, data reproduced from Huang and Leissa (2009).</i>	<i>159</i>
<i>Table 6-29 The ONF and RCNF of ATDC starting at an arbitrary point, data reproduced from AT 20*20 model.</i>	<i>160</i>
<i>Table 6-30 The ONF and RCNF of ATDC starting at an arbitrary point, data reproduced from the ATCS 20*20 model.</i>	<i>160</i>
<i>Table 6-31 The ONF and RCNF of ATDC starting at an arbitrary point of the plate, data reproduced from the AFE 40*40 model.</i>	<i>161</i>
<i>Table 6-32 The ONF and RCNF of the PTDC shown in Figure 6-22 (a), data reproduced from AFE 40*40.</i>	<i>166</i>
<i>Table 6-33 The ONF and RCNF of the PTDC shown in Figure 6-22 (a), data reproduced from ATCS 20*20.</i>	<i>167</i>

<i>Table 6-34 The ONF and RCNF of PTDC shown in Figure 6-22 (b), data reproduced from AFM 40*40.</i>	169
<i>Table 6-35 The ONF and RCNF of PTDC shown in Figure 6-22 (b), data reproduced from ATCS 20*20.</i>	170
<i>Table 6-36 The ONF and RCNF of PTDC shown in Figure 6-25, data reproduced from AFE 40*40.</i>	173
<i>Table 6-37 The ONF and RCNF of PTDC shown in Figure 6-25, data reproduced from ATCS 20*20.</i>	173
<i>Table 6-38 The ONF and RCNF of ADC shown in Figure 6-27, data reproduced from Huang and Leissa (2009).</i>	177
<i>Table 6-39 The ONF and RCNF of ADC shown in Figure 6-27, data reproduced from ABAQUS AT 24*20 model.</i>	178
<i>Table 6-40 The ONF and RCNF of ADC shown in Figure 6-27, data reproduced from ABAQUS ATCS 24*20 model.</i>	178
<i>Table 6-41 The ONF of ADC shown in Figure 6-27, data reproduced from the AFE 48*20 model.</i>	179
<i>Table 6-42 The RCNF of ADC shown in Figure 6-27, data reproduced from the AFE 48*20 model.</i>	180
<i>Table 6-43 The ONF and RCNF of ADC shown in Figure 6-27, data reproduced from Huang and Leissa (2009).</i>	181
<i>Table 6-44 The ONF and RCNF of ADC shown in Figure 6-27, data reproduced from the AFE 48*20 model.</i>	181
<i>Table 7-1 Changes in natural frequencies for a fixed width delamination ($\beta = 10\text{mm}$).</i>	198
<i>Table 7-2 Changes in natural frequencies with varying width delaminations at arbitrary locations.</i>	200
<i>Table 7-3 Location based on calculated data from the inverse problem compared with actual data.</i>	201
<i>Table 7-4 Natural frequencies of through-the-length cracks with depth 0.5mm.</i>	203
<i>Table 7-5 Changes in natural frequencies for ATLC from the reference set.</i>	204

Table 7-6 Changes in natural frequencies for ATLC from simulated cracked cases. ...204

Table 7-7 The damage detection procedure for four different cases.206

Table 7-8 Normalised changes in natural frequencies for simulated cases within noise effect.211

Table 7-9 The delamination location interval and severity of the simulated ATLD cases with noise effect.212

Table 7-10 Maximum/minimum normalised changes in natural frequencies of the first six modes with noise factor $\varepsilon = 0.001$216

Table 7-11 Crack location region and severity for ATLC at $y=26\text{mm}$, $d=0.15\text{mm}$ with noise factor $\varepsilon = 0.001$218

Table 7-12 The selection of crack location region.220

Table 7-13 Crack location region and severity for simulated ATLC at $y=26\text{mm}$, $d=0.15\text{mm}$, noise factor $\varepsilon = 0.001$, chosen interval of the reference set is $[15, 20]$ and $[25, 30]$221

Table 7-14 Converged natural frequencies with a selected combination of different modes.222

Abbreviation

ADC	Arbitrary direction crack
AF	Autocorrelation Function
AFE	Advanced Finite Element method
ANNs	Artificial Neural Networks
AT	ABAQUS cracked plate model which uses only tie constraints to simulate the crack
ATCS	ABAQUS cracked plate model, which tie constraints are used to restrain displacements while a spring is used for the rotation along the crack direction and a coupling constraint is used to restrain the rotation for all other directions
ATDC	All through-the-depth crack
ATLC	All through-the-length crack
ATLD	All through-the-length delamination
BP	Back Propagation
BVID	barely visible impact damage
CA	Cepstrum Analysis
CNF	Change in natural frequency
CNF ²	the difference of square natural frequencies between the intact and damaged cases
CPT	Classical plate theory
DIM	the Damage Index based Method
DL	the distance to the mid- point of the delamination along the y-axis

DLF	the natural frequency
DQM	the Differential Quadrature Method
DS	the width of delamination region
DSM	Dynamic stiffness method
EAS	Enhanced assumed strain
ESM	Exact Strip method
ET	Electromagnetic Testing
FFT	Fast Fourier Transform
FRFs	Frequency Response Function Method
FSDT	First-order shear deformation theory
FSM	Finite Strip method
IR	Thermal/Infrared Testing
LSM	Line Spring Model
MCM	Modal Curvature based Method
MDM	Modal Damping based Method
MPC	Multiple point constraints
MSE-DI	Modal strain energy damage index
MSM	Mode Shape based Method
MT	Magnetic Particle Testing
NDT	Non-destructive testing
NFM	Natural Frequency based Method
NR	Neutron Radiographic Testing

OL	Original damage location
ONF	the original natural frequency
PTDC	Part through-the-depth cracks
PTLC	Part through-the-length crack
QEP	quadratic eigenproblems
RCNF	relative change in natural frequency
SEM	the Strain Energy Method
SHM	Structural Health Monitoring
SM	Smearing method
SSSS	square simple supported boundary condition
STARMA	Space-time autoregressive moving average process
UT	Ultrasonic Testing
VDI	Vibration-based Damage Identification
VFM	The hybrid model coupling both VICONOPT and FE method
VHM	Vibration Health Monitoring
VT	Visual Testing
WA	Wavelet Analysis
W-W	Wittrick-Williams algorithm

Nomenclature

a	the width of the plate along x-axis
a_e	the length of element along x direction
\mathbf{a}	a function of the position coordinates
b	the length of the plate along y-axis
b_e	the width of element along y direction
\mathbf{b}	the matrix of exact strain for a unit displacement
c	the ratio of the changes in natural frequencies from the expected value
C_x, C_y	rotational compliances along x-axis and y-axis
$C(d/h)$	a dimensionless function showing the relationship between the depth of crack and the compliance of crack
\mathbf{C}	constraint terms
$\mathbf{C}_1, \mathbf{C}_2$	constraint matrices
\mathbf{D}	the flexural rigidity of a long, thin, flat plate
\mathbf{D}_A	a complete complex Fourier series
\mathbf{D}_c	the amplitudes of the associated displacements
$\mathbf{D}_{j^*}, \mathbf{d}_q, \mathbf{D}_m$	displacement variables
\mathbf{e}	the strain vector
E	Young's modulus
$\mathbf{E}_j, \mathbf{E}_f$	the constraint matrices for VIPASA and the finite element part
$f_i(x/l)$	a dimensionless function of the crack location x/l
h	the cross-sectional thickness
i	the mode number
$J(\omega^*)$	the number of natural frequencies of the structure below any chosen frequency ω^*
$J_0(\omega^*)$	the number of fixed end natural frequencies below the chosen natural frequency ω^*
KS_b	the rotational stiffness of the beam

KS_p	a rotational spring stiffness to simulate the degraded stiffness of each cracked plate element.
\mathbf{K}	the global stiffness matrix
\mathbf{K}_a	condensed stiffness matrix
\mathbf{K}_c	the complete dynamic stiffness matrix dependent on the variable ω^2
\mathbf{K}_f	the finite element stiffness matrix
\mathbf{K}_j	the VIPASA stiffness matrix for different half-wavelengths λ_j ($j = 1, \dots, j^*$)
\mathbf{K}_m	the exact stiffness matrices
$\mathbf{K}(\omega)$	Dynamic stiffness matrix
L	differential operator
m	the mass per unit area of the plate
N_0, N_1	characteristic polynomials
N_L, N_T, N_S	in-plane longitudinal, transverse, shear load
\mathbf{P}, \mathbf{P}_A	the corresponding perturbation force
\mathbf{P}_c	the external vibrating force related frequency ω
$\mathbf{P}_{j^*}, \mathbf{p}_q$	force variables
$\mathbf{P}_L, \mathbf{P}_m$	a vector of Lagrangian Multipliers
q_x, q_y	the lateral shearing forces per unit length
r	mode number
r_w	the magnitude of the chosen modes
\mathbf{R}	an initial zero symmetric square matrix (82*82)
$s\{\mathbf{R}\}$	sign count of the matrix
\tilde{s}	a non-dimensional function of the crack severity that is independent of the mode number
T	the maximum values of kinetic energy
\mathbf{U}	a vector of the amplitudes of displacements
\mathbf{u}	the corresponding displacement vector
V	the maximum values of strain energy

w	the width of delamination region
X_{LL}, Y_{LL}	the lower limits of X and Y
X_{UL}, Y_{UL}	the upper limits of X and Y
y^L, y^U	the lowest and highest estimations for all the different modes
\dot{y}_l	an estimate of the damage location
y_{imin}, y_{imax}	the lower limit and the upper limit of the expected damage location according to the related normalised change natural frequencies $[\overline{\delta_{imin}}, \overline{\delta_{imax}}]$
$\alpha_{11}, \alpha_{12}, \alpha_{33}$	dimensionless ratios between the flexural rigidities
α, β	location and length parameter
β	width of delamination region
$\ddot{\beta}_l$	the recovered severity
δ	the displacement vector related to the nodal displacements
δ_{ij}	relative change natural frequencies
$\delta_{imin}, \delta_{imax}$	the lower limits and the upper limits of the change in natural frequency
$\overline{\delta_{imin}}, \overline{\delta_{imax}}$	the normalised of the lower limits and the upper limits of the change in natural frequency
$\overline{\delta}_l \left(\frac{x}{l} \right)$	the normalisation of change natural frequencies
$\dot{\delta}_l$	the change natural frequencies of the measured data
$\dot{\delta}_l$	the normalised measured natural frequency of the selected mode
$\dot{\delta}_l^L, \dot{\delta}_l^U$	the lowest and highest value of the measured changes in natural frequencies
$\ddot{\delta}_l$	the natural frequency based on the expectation from the reference points with a defined severity ratio (the width of the delamination)
$\ddot{\delta}_l^L, \ddot{\delta}_l^U$	expected lower and upper normalised changes in natural frequencies
Δ	severity factor
λ, λ_m	a typical half-wavelength
ν	Poisson's ratio
ξ	$\xi = 2n/M$ where n and M are integers

ρ	density
ψ	the rotation about the x -axis
ω	frequency (rad/s)
ω_{i0}, ω_{ic}	the natural frequencies in the undamaged and damaged cases
ω^{HP}, ω^{DP}	the natural frequencies of the undamaged and damaged plate
Ω_{mn}	non-dimensional natural frequencies

Chapter 1--- Introduction

1.1 Motivation and Background

1.1.1 Aerospace Industry

The UK aerospace industry is the third largest worldwide after the US and France and possesses key strengths in core components such as wings. The industry provides 230,000 jobs, and has an annual turnover of around £24 billion, of which over 70% is exported (Bourne et al. 2013). Opportunities are increasing at a tremendous rate. Air traffic doubled between 1992 and 2007 and is expected to double again by 2025 (CNBC 2007). As a result, 27,000 new large aircraft and 40,000 new civil helicopters will be required by 2030, worth almost \$4.165 trillion (Bourne et al. 2013). Similar growth has been experienced and predicted in the rest of the world. With this increasing number of aircraft, the establishment of efficient, effective damage detection techniques becomes increasingly important to ensure their safe operation.

Many aircraft structures can be idealised to an assembly of plates and beams, as shown in Figure 1-1. These are of general practical significance not only to aerospace engineering but also to many other application areas including the automotive, marine and civil sectors (Huang and Leissa 2009; Birman 2011). Beams, frames, plates and shells are therefore essential elements for structural analysis and design.

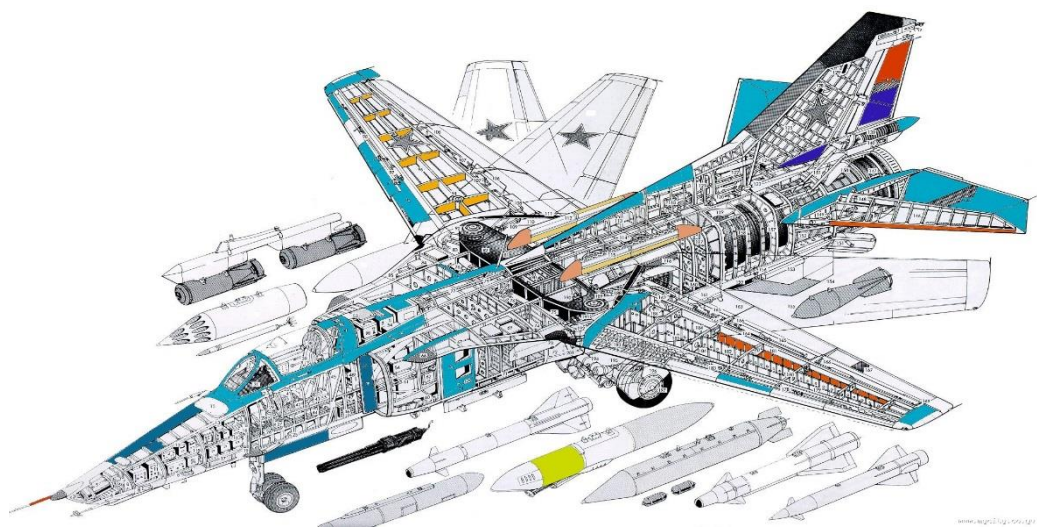


Figure 1-1 The simplified structural layout of a MiG-27 (Marcos 2013).

1.1.2 Plate Structures

In continuum mechanics, plate theories are mathematical descriptions of the mechanics of flat plates which are deduced as extensions of beam theories. Typically, plates can be grouped into three types (Ismail 2013): thin plates with small deflections, thin plates with large deflections, and thick plates. Different theories are generally accepted and utilised in engineering problems depending on the thickness of plates. Since the late 19th century, widely used theories are the Kirchhoff-Love plate theory (Classical plate theory (CPT)) and the Mindlin-Reissner plate theory (first-order shear deformation theory (FSDT)) (Carrera et al. 2017). For a thin plate with a typical thickness to width ratio less than 0.1, plates are defined as plane structural elements with a small thickness compared to their planar dimension (Timoshenko and Woinowsky-Krieger 1959). A comprehensive background to these theories has been presented by Timoshenko and Woinowsky-Krieger (1959) in which methods can take advantage of this disparity in length scale to reduce the three-dimensional mechanics problem to a two-dimensional plane problem (Love 1888). This study is focused on such thin-plate structures, developing advanced modelling techniques with high computational efficiency and accuracy to model their behaviour and in particular determine their vibration characteristics, so that these can be used to develop damage detection techniques.

The Kirchhoff-Love theory assumes that the mid-surface plane can be used to represent a three-dimensional plate in the two-dimensional form (Love 1888) while the following kinematic assumptions are made (Reddy 1999):

1. Straight lines normal to the mid-surface remain straight after deformation;
2. Straight lines normal to the mid-surface remain normal to the mid-surface after deformation;
3. The thickness of the plate does not change during deformation.

The Mindlin-Reissner theory of plates is an extended version of the Kirchhoff-Love theory for thick plates (Carrera et al. 2017). It assumes the normal to the mid-surface remains straight while not necessarily perpendicular to the mid-surface, and a linear displacement variation through the thickness during deformation. Moreover, the in-plane shear strains include and incorporate first-order shear effects.

1.1.3 Types of Defect

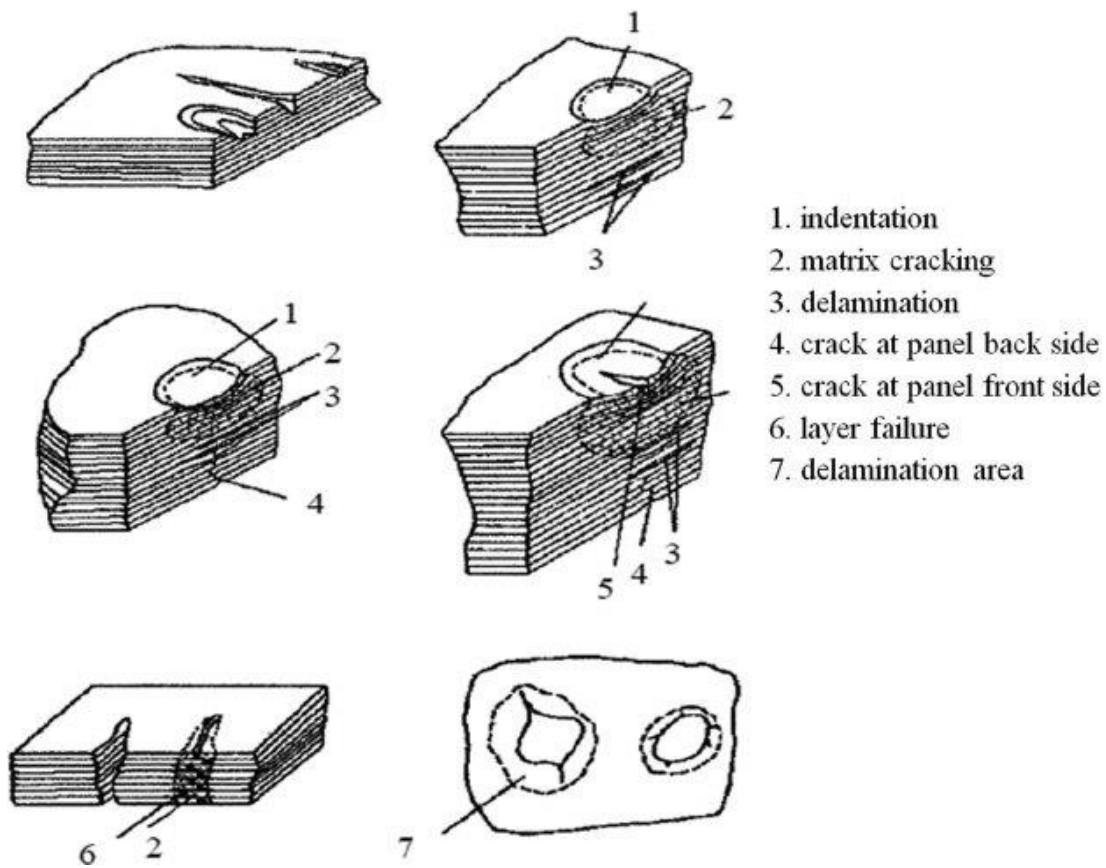
Both metal and composite plates and stiffened panels are used in aerospace and other applications (Zehnder and Viz 2005). Nowadays, engineers can design bespoke, enhanced composite materials with stiffer and lighter characteristics than any other structural materials (Vinson and Chou 1975). As well as these advantages, however, the use of composites introduces further possibilities for damage caused by impact and stress concentrations introduced during manufacture and operation, which can lead to sharp reductions in strength and stability (Israr 2008).

In metallic structures, previous research has shown that the strength of structural metals can be increased to very high levels by modifying the microstructure (Roylance 2001). However, this causes the material to become increasingly brittle resulting in the possibility that cracks can propagate catastrophically without warning.

In composites, during the manufacturing process, different types of defects introduced include (Figure 1-2): voids, foreign inclusions, fibre debonding, fibre misalignment, ply misalignment, wavy fibres, cracks and holes in the matrix materials, fibre breakage and delamination. During operation, mechanisms such as static overload, overheating, lightning strike, impact and fatigue load can lead to a variety of defects (Smith 2009) such as delaminations, bond failures, cracks, ingress of moisture, fracture or buckling of fibres and failure of the interface between the fibres and the matrix.

Delamination, caused in composites for example by tool drop or bird strike (Pipes 1970; O'Brien 1991; Bolotin 2001), is one of the most critical forms of damage in composite laminated structures due to its effect on the compressive strength (Noor et al. 1983; Gong et al. 2016). Delamination is also known as interface cracking which happens between the layers of lamination, and its presence can lead to significant reductions in the stiffness and strength of a plate.

Figure 1-3 shows three primary delamination modes (Ding 2000). Mode 1 is opening damage; Mode 2 is in-plane shear damage and Mode 3 is out of plane shear damage. During loading, a sudden structural failure could potentially be initiated by a rapidly growing delamination (Lee and Park 2007), which could also generate a significant reduction in the corresponding vibration characteristics or load-carrying ability.



- 1. indentation
- 2. matrix cracking
- 3. delamination
- 4. crack at panel back side
- 5. crack at panel front side
- 6. layer failure
- 7. delamination area

Figure 1-2 Different types of defect in plate-type structures (Shams and Elhajjar 2013).

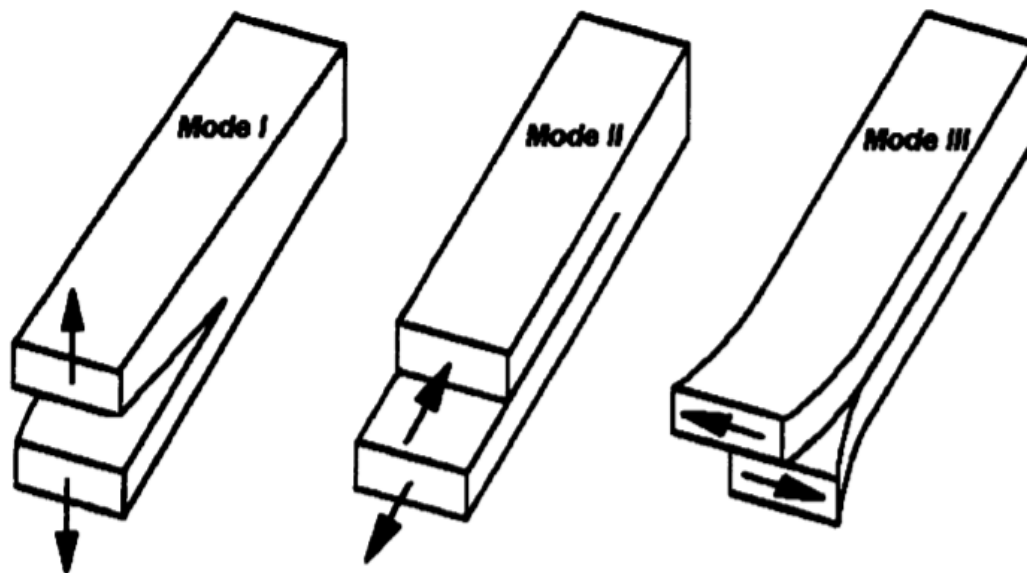


Figure 1-3 Basic delamination forms (Ding 2000).

A crack is a natural phenomenon that occurs in both composite and isotropic plate, a type of discontinuity caused by tensile stress. The two examples shown in Figure 1-4 (a) and (b) could make a significant difference to the vibration parameters of a plate compared

with its intact behaviour (Doebling et al. 1998; Huang et al. 2011). This type of failure occurs for many reasons, including uncertainties in loading or the environment, defects in the material, inadequacies in the design, and deficiencies in construction or maintenance (Roylance 2001; Hooton 2016). Fatigue cracks for example, are particularly common in aircraft (Rovik 1998) resulting from cyclic loading during take-offs and landings, cabin pressurisation and vibration. The characteristics of a fatigue crack will vary in different aircraft structures and for different materials. For example the floor of the galley area of a Boeing 777 is made from a relatively new aluminium lithium alloy (Rovik 1998), introduced to reduce corrosion. Although relatively insensitive to corrosion, this new material was found to develop cracks when drilled.



(a)



(b)

Figure 1-4 Crack representation in reality.

(a) Crack in aircraft fuselage (Schwaner 2012); (b) Stop drilled and crack with a patch behind (Schwaner 2012).

1.1.4 Effects of Damage

Structural performance is degraded by the presence of damage such as delaminations and cracks, which are often difficult to detect visually, depending on the level of damage particularly in built-up structures such as wing and fuselage panels (Escobar et al. 2005; Fang et al. 2005; Ge and Lui 2005; Caddemi and Greco 2006; Wang and Ong 2008; Chatzi et al. 2011).

It is well known that depending on the form, severity and nature of the damage, the dynamic behaviour of a damaged plate can be significantly different from that of the intact plate. The presence of delaminations or cracks causes changes in the physical properties of the structure which introduces flexibility, and thus reduces the stiffness and strength properties of the structure. This can be dangerous and result in disastrous structural failures particularly for composites where BVID (barely visible impact damage) is a big problem (Banerjee and Guo 2009; Huang et al. 2011; Labib et al. 2015; Moazzez et al. 2018). In 1983, the National Bureau of Standards (now the National Institute for Science and Technology) and Battelle Memorial Institute (Reed 1983) predicted the cost of general failure caused by fracture to be \$119 billion per year and increasing year on year. As well as the cost, failures threaten human life (Chang 1998). In 26th June 1997, a Eurocopter AS 332L1 Super Puma was operating over the Norwegian Sea. An accident was caused by a fatigue crack in the spline, which eventually caused the power transmission shaft to fail. The helicopter finally crashed into the sea (HSL 2001). Another accident happened in 1988, when an Aloha Airlines Boeing 737-200 decompressed due to the separation of a 5m section of the upper cabin fuselage (Werfelman 2011). Despite this, a failure resulting in a 1.5m gap in the fuselage of the same type of aircraft occurred in 2011 (Berger and Wilson 2011). Delaminations have also caused catastrophes in the aerospace industry, for example the American Airlines Flight 587 on the 12th November 2001. In this case an incident was caused by the separation of the vertical stabiliser following excessive rudder input (National Transportation Safety Board 2001).

These failures draw the attention of both the public and the regulatory bodies to the importance of testing, monitoring, and evaluation to ensure the safety of aircraft structures. The need to address these concerns and to develop advanced damage detection methods to locate and characterise this difficult to detect damage before it causes catastrophic failure therefore is increasingly important.

In order to detect damage or deterioration at an early stage to ensure safety and avoid catastrophic failure, it is necessary to understand the effect of that damage has on different mechanical properties during its propagation. Vibration characteristics are typical signals which reflect the nature of plates, and which are affected by the length, position, depth and orientation of damage. An understanding of the influence of damage on the free vibration of plates will enable the use of vibration parameters as the base of a damage model used to detect damage in a plate which will form the basis of the work in this thesis.

1.2 Damage Detection

The increasing interest in the capability to monitor structures and detect damage at the earliest stage is widespread in the civil, mechanical, and aerospace engineering areas (Doebbling et al. 1998). Related techniques have been improved and applied to deal with the problem of damaged structures in the past. The main concern and difficulty is the detection of damage, as repairing the structure is relatively simple. Damage detection techniques also form the basis of structural health monitoring, in which the condition of a machine or structures is assessed continuously, and which is of increasing interest in a number of sectors.

A regular assessment of structures and machinery is usually necessary while in service, hence a scheduled and repeatable method is required. In 1868 the first Non-destructive testing (NDT) was recorded, the magnetic characteristics of a compass being used to find cracks in gun barrels (TSPNDT 2014). NDT is comprehensively utilised in many engineering areas and can detect defects in structural elements while satisfying the ‘Non-destructive’ requirement.

Damage detection includes the determination of damage (locations and severities), which when combined with the estimation of the remaining serviceability of the structure is known as Structural Health Monitoring (SHM) (Rytter 1993; Wang and Ong 2008). A reliable SHM system should guarantee the practical assessment of the evaluated structure, in terms of time, economic considerations and accuracy. Then, maintenance can be performed without any loss of life or service (Wang and Ong 2008).

In this thesis, a hybrid model is therefore proposed which couples the analysis of the exact strip software VICONOPT (Williams et al. 1990) for the undamaged part and finite element analysis for the damaged part. The hybrid model, denoted as VFM (VICONOPT and Finite element Method) was previously developed for modelling delamination damage (Suliman 2018) will be extended to cover cracks based on a novel crack modelling technique. This will form the first stage in solving the inverse damage detection problem, detecting a single crack or delamination with and without experimental noise.

1.2.1 Non-destructive Testing

As mentioned above, Non-destructive Testing (NDT) is an essential part of damage detection. NDT is the process of inspecting, testing, or evaluating materials, components or assemblies for discontinuities, or differences in characteristics, without destroying the

serviceability of the part or system (ASNT 2011). Destructive tests which are generally used to determine the physical characteristics of materials are only performed on a small number of samples (ASNT 2011). NDT which retains materials, components or assemblies in service, can be used to detect discontinuities and differences in material parameters and is widely used in manufacturing, fabrication and in-service inspections.

1.2.2 Different types of NDT

There are a variety of types of NDT which can be employed to identify the presence of damage such as cracks. Typically, NDT technologies are grouped into local and global techniques. Local NDT includes experimental methods like Visual Testing (VT), Ultrasonic Testing (UT), Acoustic Emission Testing, Magnetic Particle Testing (MT), Electromagnetic Testing (ET), Thermal/Infrared Testing (IR), and Neutron Radiographic Testing (NR) (Doebbling et al. 1998; ASNT 2011).

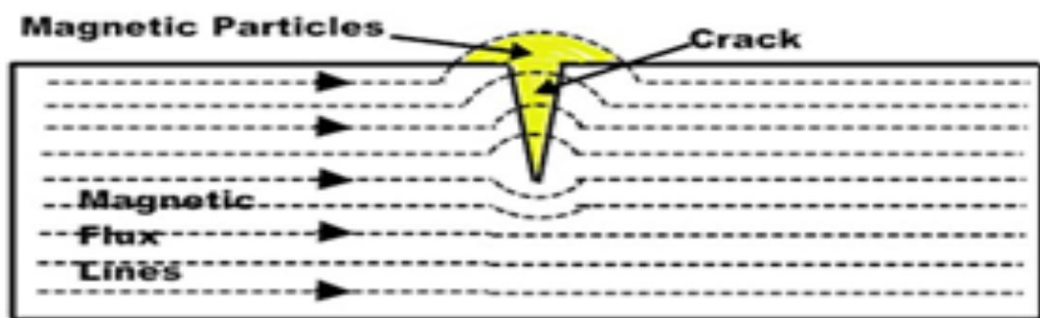


Figure 1-5 Magnetic Fields (ASNT 2011).

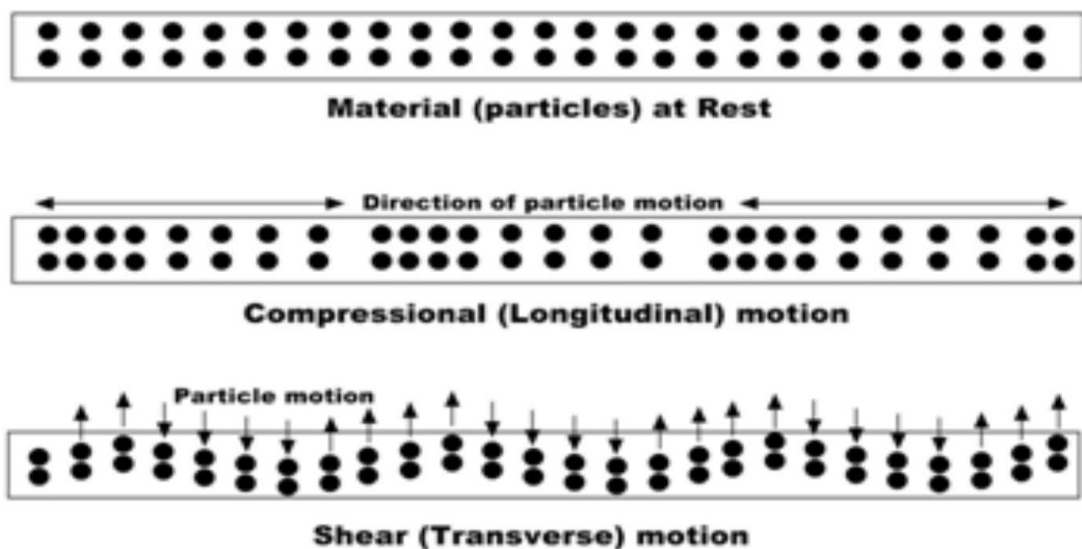


Figure 1-6 Two frequent sound waves (ASNT 2011).

MT is one of the oldest NDT methods in the world. It was first recorded in 1868, and used in an industrial application in 1929 by Alfred Victor de Forest and Foster Baird Doane (TSPNDT 2014). A permanent magnet or an electromagnet was used to generate magnetic fields that could locate the discontinuities on the surface or near-the surface of ferromagnetic materials through the application of magnetic particles which coalesce around the crack as shown in Figure 1-5 (ASNT 2011).

UT is another traditional NDT technique. The first ‘exciting’ ultrasound method was found by James Prescott Joule in 1847, and the first ‘industrial’ application was in 1929 (Sokolov) (TSPNDT 2014). UT uses a similar idea to naval SONAR and echosound. An ultra-high frequency sound wave is introduced into the part being inspected, and if this wave hits something with different acoustic impedance (density and acoustic velocity), such as a crack, some of the sound is reflected back to the sending receptor and visually presented (ASNT 2011). Sound frequencies generally applied in UT are between 1.0 and 10.0 MHz, and the two most common sound waves used are compression (longitudinal) waves and shear (transverse) waves as shown in Figure 1-6 (ASNT 2011).

1.2.3 Global NDT

Local NDT however, needs a preliminary prediction of the damage locations before performing the test and cannot be used on inaccessible members of a structure (Rytter 1993; Teughels et al. 2002; Caddemi and Greco 2006; Wang and Ong 2008; Chatzi et al. 2011; Danai et al. 2012; Ismail 2013). Local testing is based on such a preliminary estimation, and if this is not available or cannot be acquired, an inspection of the whole structure needs to be performed which is time consuming and expensive. Global NDT can overcome this limitation with no prior knowledge regarding location needed. For example vibration-based NDT methods, which are based on numerical analysis and experimental data, are used in complex structures by determining changes in vibration characteristics such as the natural frequencies and mode shapes of the structure (Cawley and Adams 1979; Hearn and Testa 1991; Nandwana 1997; Doebbling et al. 1998; Ip and Tse 2002; Kim et al. 2003).

Whilst plate or beam-like structures are used extensively in structures in civil, aerospace, and mechanical engineering. There are only a few pieces of literature regarding NDT for plate-like structures while there are many for beams. The most common global NDT methodologies for plates are the Damage Index based Method (DIM) and Vibration-based Damage Identification (VDI). DIM comprises the Frequency Response Function Method

(FRFs), Wavelet Analysis (WA), Artificial Neural Networks (ANNs), Fast Fourier Transform (FFT) Analysis, Autocorrelation Function (AF), and Cepstrum Analysis (CA) (Zubaydi et al. 2000; ZANG and IMREGUN 2001; Yan and Yam 2002; MAIA et al. 2003; Taghvaei et al. 2006; Trendafilova 2006a; Cusido et al. 2008; Trendafilova 2009) etc. VDI methodologies include the Strain Energy Method (SEM), Natural Frequency based Method (NFM), Modal Damping based Method (MDM), Mode Shape based Method (MSM), and Modal Curvature based Method (MCM) (Adam et al. 1978; Cawley and Adams 1979; Pandey et al. 1991; Cornwell et al. 1999; Kawiecki 2001; Colakoglu 2003) etc. The next section will introduce the methodology and history of the most representative global NDT techniques.

For the Damage Index Method, Wavelet Analysis which has been derived from the branch of applied mathematics since the 1980s is the most common technique used. It can be applied in variate signals especially for a nonstationary signal. WA uses Gaussian Wavelets to automatically decouple the structural system, and then uses an impulse response function to recognise the modal parameters. WA can detect small cracks in composite plates by the energy variation of structural vibration responses (Yan and Yam 2002). The relationships between Lamb Waves and damage in plates was examined using the amplitude changes of wavelet coefficients (Paget et al. 2003), while a general numerical approach for the development of wave and damage detection in cracked plates was presented by Krawczuk et al. (2004). A spectral plate element was considered as a tool to investigate wave propagation and showed it split into two signals when the wave ran through the crack location, which indicated the damaged part (Krawczuk et al. 2004). Chang and Chen (2004) proposed an approach based on spatial wavelets for damage detection of a rectangular plate. The distributions of the wavelet parameters could be used to recognise the damage position in a rectangular plate by identifying the peak position where the response is most sensitive to damage severity. However, similar indications of damage were found at the clamped edges, and therefore, it was inaccurate when the crack occurred at these edges. Rucka and Wilde (2006) used a two dimensional (2D) continuous wavelet transform to analyse a steel plate with four clamped supports. The spatial change of the deformed response was used to detect the location of the damage based on the fundamental mode shape. Artificial Neural Networks is another DIM technique. The neural networks mathematical model was presented by Mcculloch and Pitts (1943) and developed for structural damage detection later in the 1980s. ANN is an algorithmic mathematical model which processes distributed information analogous to the characteristics of an animal's neural networks. It simulates the function of the brain's

nervous system, which can deal with a signal moving through the model and connections between individual neurons. This system possesses intelligent information processing functions like learning, association, memory and pattern recognition. Back Propagation (BP) is an efficient training ANN method which is based on a gradient optimisation algorithm to represent the chain rule (Goodfellow et al. 2016). Stephens and VanLuchene (1994) used several quantitative indexes with a BP network on post-earthquake structures for damage detection, validating the ANN method compared to a traditional NDT method. Tsou and Shen (1994) identified the reduction of stiffness of single and multiple spring systems using ANN according to the change of eigenvalues, using residual stress as an input vector quantity to analyse in the ANN system. The significant advantages of ANNs are: Large-scale parallel processing and distributed information storage, adaptability and self-organization, favourable learning, association and fault tolerance.

1.2.4 Vibration Characteristics

VDI offers significant advantages to aircraft structures, including increased safety, extension of structural life, reduced inspections, minimisation of weight and hence operating costs and the detection of cracks, corrosion and fatigue damage in inaccessible areas (Trendafilova 2009). Generally, there are two measurements used for VDI. The first is the static deflections which reflect the magnitude of the strain energy of the structure. The more prominent the deflection the more energy work input into the system (Caddemi and Morassi 2007)(Caddemi and Morassi 2007)(Caddemi and Morassi 2007)(Caddemi and Morassi 2007), since deflection depends on the external load (Caddemi and Morassi 2007). The second is based on modal parameters, mainly the natural frequencies, mode shapes and modal damping, which reflect the nature of the structure (mass, damping and stiffness). VDI is attractive because it is a form of global NDT, with no prior information needed. Moreover, inaccessible or problematically located structures are still detectable under VDI. A thorough mathematical and physical understanding of the effects of damage on the properties and behaviours of the structure, is however critical. Comprehensive reviews of vibration-based methodologies have been performed in Doebling et al. 1998; Wang and Chan 2009 and Fan and Qiao 2011.

For Vibration-based Damage Identification, the Strain Energy Method is one of the most common NDT techniques. It is based on the change of strain energy and only mode shapes are required from the undamaged stage and damaged stage. An advanced algorithm was presented to effectively locate damage with relatively few modes and a low value of

stiffness reduction of around 10% (Cornwell et al. 1999). The Differential Quadrature Method (DQM) was then introduced to calculate the strain energy based on the mode shapes obtained using modal analysis. A damage index was subsequently acquired which could recognise the surface crack location by the peak value shown in the damage index (Hu et al. 2006). Because of irregularities in the mode shapes, some peak values occurred at some intact segments (Hu et al. 2006). A modal strain energy damage index (MSE-DI) algorithm was applied for identification and localisation of delamination of a composite stiffener of a type commonly used in aircraft components (Loendersloot et al. 2010). An advanced data-based damage detection which has aroused interest among researchers more recently is the time domain methodology. This method uses a measured dynamic response related to time series analysis for damage identification in vibrating structures (Ismail 2013). The time series includes a sequence of data points, measured typically at successive times, and spaced at time intervals (Ismail 2013). Trendafilova (2006b) considered pure time series analysis for damage detection in a reinforced concrete plate based on the state space methodology and the extraction of damage sensitive parameters from the state space representation. Latterly, two reliable methods have been presented for a thin vibrating plate using significant amplitude vibrations and nonlinear time series analysis. One method used the statistical distribution of state-space points on the attractor of a vibrating structure, and another method applied the Poincare map of the state space projected dynamic response (Trendafilova and Manoach 2008). A method was developed for damage identification in plates based on space-time series analysis. The plate was divided into several sub-regions and a space-time autoregressive moving average process (STARMA) was used to recognise the dynamic response of sub-region (Hu et al. 2011). NDT based on time series and space-time series shows an ability to identify and localise damage using these studies. But a unique feature of this methodology is that noise sensitivity affects the results and can even lead to failure of the detection algorithm.

1.2.5 Natural Frequency

The presence of a crack or loosening of a connection in a structural element will change its physical properties, e.g. by reduction its stiffness which can be recognised by modal properties. Discontinuities in the static deflections and mode shapes, as well as the degradations of natural frequencies have been observed by Teughels et al. (2002); Escobar et al. (2005); Fang et al. (2005); Ge and Lui (2005); Caddemi and Greco (2006); Caddemi and Morassi (2007); Wang and Ong (2008); Chatzi et al. (2011); Danai et al. (2012). Modal characteristics are widely used in VHM (Vibration Health Monitoring),

especially for lower natural frequencies, which are easy to detect experimentally (Doebbling et al. 1998; Verboven et al. 2002; Trendafilova 2009). Natural frequency is chosen as the main parameter of the damage identification method because it can be measured from a few accessible points on the structure and is less contaminated by experimental noise. Minimal testing is required if attention is constrained to natural frequencies rather than static deflections and mode shapes for inaccessible structural elements (Hassiotis and Jeong 1995; Salawu 1997).

Natural frequencies are the first applied parameters in VDI because they are easily acquired, and with high accuracy. Cawley and Adams (1979) first presented an NDT based on the change of natural frequencies. A square aluminium plate was tested and validated the method. It showed the possibility that without the measurement of the intact plate, a damaged plate can be used as a reference to monitor the propagation of damage for future tests. Salawu (1997) reviewed previous studies on the relationship between changes in the natural frequencies and damage in the structure. Natural frequency is a highly sensitive indicator for the integrity of the structure, and the test is inexpensive. However, other parameters like temperature, humidity, additional mass, and boundary conditions could cause a failure of the damage detection. Furthermore, the magnitude of the variation of natural frequencies is quite small. Trendafilova (2006a) used an aircraft wing scaled model to study the localisation of damage and distributed damage. The wing was divided into five parts, and the first ten natural frequencies were chosen to analyse the damaged structure. The change of natural frequencies was small when the length of the crack was less than half of the width of the wing, or the distributed damage was less than 30% in any of the individual parts. Matching results were also found for cracks at specific locations of the isotropic plate (Trendafilova 2006a). Trendafilova (2009) then discussed the sensitivity of the first few natural frequencies to certain types of damage in circular plates and found the limitation of the sensitivity of lower natural frequencies to damaged plates. Methods for crack identification such as the Bayesian approach will be introduced in detail in Chapter 2.2.

1.2.6 Importance and Improvement

Because of the importance of the safety and integrity of plates containing cracks and other types of damage, the static, dynamic, buckling and post-buckling behaviours of cracked plates is of primary concern in engineering. Local NDT methods need an expected damage location and access to the part of the structure to be inspected, in order to be

efficient. Hence, a quantitative global NDT method based on natural frequencies is particularly helpful when applied to complicated, large, plate-type structures.

In this thesis, a computationally efficient damage model, able to determine changes in natural frequencies, which couples the exact strip method with an advanced FE model using Lagrangian multipliers, is proposed. The hybrid damage model (VFM) is able to simulate the effect of part through-the-length cracks (PTLC) and part through-the-depth cracks (PTDC) which start and finish at any location and have any orientation, along with other damaged plate models. The models are first used to determine the natural frequencies and related mode shapes prior to and following the introduction of damage at a defined set of positions. The resulting data with regard to normalised natural frequency changes can then be applied to solve the inverse problem based on the measurement of these natural frequency changes. The VFM model can simulate a crack at any location with arbitrary depth, length and orientation. The Wittrick-Williams algorithm and bandwidth method are used to acquire an outstanding computational efficiency and accuracy. An automatic mode shape sign method is introduced to group the mode shapes and natural frequencies correctly.

1.3 Thesis Aims and Objectives

Many researchers have studied damage detection in structures based on vibration parameters from analytical, numerical and experimental aspects. For damage identification in plate-like structures, the literature reveals that a useful approach is to study the relative changes in natural frequencies when an arbitrary crack with random location, direction, depth and length occurs in the plate. This requires a comprehensive understanding of the relationship between the location and severity of the crack with these natural frequencies and mode shapes. Consequently, this research aims to narrow this research gap and present a computationally efficient method to achieve this by using a hybrid model which couples an exact strip method of the undamaged regions with a rectangular FE model of the longitudinal strips containing the damage region (Luo et al. 2019).

In this thesis, a composite plate is used as a comparative study of the relationship between related change natural frequency and delamination location, and this case is only chosen at the preliminary research stage to understand the use of the VFM model. For the main direct problem and related inverse problem, an isotropic square simply supported plate is easy to simulate and can be compared with previous studies for validation purpose. The isotropic square plate is then chosen as the research object to analyse. After validation, this study could be extended in the future to discuss the influence of aspect ratio or boundary conditions on the natural frequencies of a cracked plate or to model multiple cracks. Displacements and rotations at the boundaries are coupled using Lagrangian Multipliers, and natural frequencies are found using the Wittrick-Williams algorithm. Mode shapes are obtained by an automatic sign method as an assistant factor to analyse the degradation in stiffness. The results obtained from the hybrid model will be used to provide data as a datum for the solution of the inverse problem of damage detection in the second stage of this project. This study then addresses the damage detection procedure with/without a noise factor in plate-like structure. Therefore, the main objectives in this thesis are as follows.

1. Review the literature concerning damage modelling and relevant solutions of inverse problem.
2. Study the features of the exact strip method with the corresponding software VICONOPT, extract the equations and matrices to be prepared for the upcoming hybrid model.

3. Investigate data processing methods to improve the computational efficiency and avoid potential mistakes when recording results.
4. Propose a FE model containing a crack with arbitrary location, length, orientation and depth based on an isotropic square simply supported thin plate. The FE model will then be coupled with an ESM model to generate the hybrid model.
5. Verify the proposed FE model through a comparison with previous studies and ABAQUS models. The predefined damage cases chosen for study include all through-the-length delaminations, all through-the-length cracks, partial through-the-length cracks and arbitrary direction cracks.
6. Using the obtained results, carry out a preliminary study of the inverse problem of damage detection with/without an introduced noise factor.
7. Identify if any improvements or possible extended studies could be made in the damage modelling or inverse problem.

1.4 Thesis Overview

This thesis will be presented in eight chapters, including the introduction chapter. The first three chapters cover the motivation, background and literature review. The remaining chapters show innovative work.

Chapter 2 reviews the literature relating to the direct and inverse problems. Delamination in a composite plate will be firstly studied as a comparative analysis and briefly discussed in the literature review; Cracks in an isotropic plate will be mainly discussed and the direct problem is a simulated mathematical damage model which has been studied by various researchers in the past decades. The review of the cracked structure will begin with a damage model for beam-like structures and then proceed to plate-like structures. The inverse problem is then introduced, and various methods to solve the inverse problem are shown.

Chapter 3 presents the history and development of the software VICONOPT. The crucial part of VICONOPT is the exact strip method (ESM) and a comparison between the exact strip method, finite element method, and finite strip method will be tabled to show the differences. For the ESM, an accurate and fast methodology, the Wittrick-Williams algorithm (W-W), is described to solve the eigenvalue problem (Wittrick and Williams 1971). Then, Lagrange Multipliers are described and will be applied in a coupled model, which will constrain the deflections at the boundary.

Chapter 4 is about data analysis and processing. Several methods are devised for obtaining accurate and fast computational results for natural frequencies of plate-type structures. In the study, only the first six natural frequencies will be adopted for solving the inverse problem. It has been shown by Yang et al. (1985) and Labib et al. (2015) that this number of natural frequencies is sufficient for damage identification. A modified W-W algorithm is applied for the specific case which ignores the fixed-end condition. During processing of the W-W algorithm, Gauss elimination is needed to transform the global stiffness matrix into an upper triangular matrix to obtain the sign count. A massive iterative calculation exists in Gauss elimination because the global stiffness matrix can have a large order (always exceeding 1000*1000 elements in this work), but most of the elements are zero and make no contribution to the computation. Hence a bandwidth method is introduced in this part to reduce the computations. A visible improvement in computational efficiency occurs after the advanced bandwidth method is applied. In the last stage of the direct problem, the computed natural frequencies are displayed in an

ascending sort order related to their mode shape. Sometimes the natural frequency does not match with the corresponding model. The reason is that with the propagation of a crack in the plate, the natural characteristics of the structure are affected, especially the mode shape, changing the sequence of results. In some cases, it is hard for the researcher to group the mode shapes visually. An automatic mode shape sign method is therefore introduced to categorise the vibration parameters automatically.

Chapter 5 shows several methods for solving the direct problem using different software. Firstly, pure ESM is used to simulate a single all through-the-length damage in a prismatic plate. Two types of damage (delamination and crack) models are discussed in VICONOPT, and different damage simulation ideas are presented here in order to find the best way to establish an appropriate damaged plate-type model using ESM. Without solving a finite element or boundary value problem, ESM can obtain a faster and more accurate calculation. An advanced pure FE model is introduced for modelling a rectangular plate containing cracks of arbitrary length, depth, location and orientation. A rotational spring model allows the discontinuity in rotation and the W-W algorithm are applied to the FE model which is programmed in MATLAB. No omission of results is guaranteed while other root calculation algorithms may miss some natural frequencies. Such generality and comprehensiveness in terms of the form of the crack are mostly absent from the literature, where results are commonly restricted to cracks located at the centre or edge of the plate, running parallel to the edges of the plate, over the full length or width, or through the full thickness (Stahl and Keer 1972; Liew et al. 1994; Huang and Leissa 2009 and Bose and Mohanty 2013). Therefore, an alternative FE model using the commercial software ABAQUS is prepared for comparison of cracked isotropic plates. Finally, a hybrid model (VFM) is presented, where ESM is used for the uncracked parts of the structure, and coupled with FEM for the cracked regions with a suitable constraint matrix using Lagrangian multipliers to allow continuity of deflection (vertical displacement and bending rotation) on boundaries. VFM is a general technique that can solve either prismatic or non-prismatic structures with computational efficiency and accurate results (natural frequency and mode shape).

Chapter 6 presents comparative studies for delaminations in a composite all simply supported (SSSS) square plate firstly. Then, cracks occurring in a square SSSS isotropic plate with different damage conditions are shown. Numerical results are presented for each case. For the delamination case studies, the differences between the various ways to establish all through-the-length delaminations in a composite plate models obtained from

chapter 5 are presented, and the relationship between the change in natural frequency (CNF) and the width of the delamination is introduced. Then, a crack occurring in a square isotropic SSSS plate is studied. Several specific cases are modelled using a pure FE model and compared with those published in the literature. Once validated, the theoretical cracked FE model is used to couple with the ESM model for further comparison. Besides, the ABAQUS model will be used as a reference for each case in the verification study.

Chapter 7 presents the methodology for solving the inverse problem. A single all through-the-length delamination in a simply supported (SSSS) square composite plate is analysed to examine a one-dimensional damage detection procedure and then a simply supported square isotropic plate (SSSS) with a single crack is studied for further validation. The relationship between the crack location/severity and the changes in the variation parameters is discussed first. Preliminary data is then prepared to analyse the effect of severity and location. Based on the obtained relationship, damage detection for a single damage with noise-free and contaminated measurements will be discussed for different damage scenarios according to the model from Chapter 5. The one-dimensional damage detection problem will form a preliminary study for the two-dimensional problem and the multiple damage detection problem, relevant theories and procedures will be briefly discussed in the future work of Chapter 8.

Chapter 8 is the concluding chapter, which describes the outcomes of this research in terms of modelling, coding, analysing and processing. This study shows the feasibility and potential for the application of a plate-like structure damage modelling and detection technique. If applied in the aircraft industry this could save lives and reduce costs and emissions. Some suggestions and improvements for future work are presented and inspired by several conference presentations related to this thesis.

1.5 Publication List

Two journal papers have been prepared, the first is based on the proposed efficient hybrid method for modelling a crack with arbitrary length, orientation, depth and location described in Chapters 4, 5 and 6 of the thesis.

1. **Luo, Y.,** Kennedy, D., & Featherston, C., 2019. An efficient hybrid method of flat damaged plates modelling with cracks in arbitrary orientation, length, depth and location. In preparation. For submission to Composite Structures.

The second is based on the damage detection procedure for two-dimensional problems (transverse direction and longitudinal direction) such as plate-type structures. The related damage location and severity recovery problems are analysed preliminarily based on the one-dimensional problem in Chapter 7 and further discussion in Chapter 8.

2. **Luo, Y.,** Kennedy, D., Huang, Z., & Featherston, C., 2019. Two-dimensional crack localisation and severity recovery in plate-type structures using frequency-based method. In preparation. For submission to Journal of Sound and Vibration.

Moreover, five conference papers have been presented which have arisen from Chapters 4, 5 and 6.

1. **Luo, Y.,** Kennedy, D., & Featherston, C., 2019. Natural frequency Degradations in Cracked Plates. Corvara in Badia, 12th International Symposium on Vibrations of Continuous Systems.
2. **Luo, Y.,** Kennedy, D., Featherston, C & Labib, A., 2018. Modelling and vibration based detection of cracks in plate structures. Barcelona, 13th International Conference on Computational Structures Technology.
3. **Luo, Y.,** Kennedy, D & Featherston, C., 2018. An Efficient Hybrid Method for Determining the Vibration Response of Flat Plates. Cambridge, International Conference on Modern Practice in Stress and Vibration Analysis.
4. Kennedy, D., Featherston, C., Suliman, B & **Luo, Y.,** 2017. Exact Strip Modelling and Vibration Based Identification of Damage in Plate Assemblies. Snowdonia, 11th International Symposium on Vibrations of Continuous Systems.
5. **Luo, Y.,** Kennedy, D., Featherston, C. A. & Cheng, X., 2016. Modelling and Detection of Delamination in Composite Laminated Structures Based on the Dynamic Characteristics. Seoul, 12th World Congress on Computational Mechanics.

Chapter 2--- Literature Review

2.1 Introduction

Structural failures can be caused by many factors, such as unexpected loading or environmental conditions leading to defects in materials or damage to the structure, insufficiency in design, and inadequacies in construction or maintenance. Damaged structures can have significantly reduced structural properties leading to sudden failure with potentially catastrophic consequences including in the worst cases, loss of life. This is particularly true for thin walled structures, where potential instability is a significant factor. For this reason, being able to detect damage in terms of localisation and assessment of severity at the very early stages of propagation can enhance the performance and safety of these structures.

A range of techniques is available for the detection of damage. One such technique involves the study of the effect of this damage on the structure's vibration response. By studying changes in either natural frequencies or mode shapes it is possible to infer the location and severity of damage by comparison with the behaviour of an undamaged structure. This is achieved in two stages, the direct problem and the inverse problem. In the direct problem the effect of damage of a range of severities in different locations is determined. Using this information, the inverse problem is solved to locate and characterise the damage based on changes in vibration behaviour.

In this work, we study the effects of both delaminations and cracks on the natural frequencies of a series of flat plates. Moreover, in this thesis, delaminations are regarded as gaps existing at the interface between different layers in an anisotropic plate, while cracks are simulated as virtual lines in an isotropic plate. The delamination is studied as a comparative research for which a brief literature review is included in this chapter, to be followed by a more detailed review on crack cases. A novel cracked plate model coupling versatility, accuracy and efficiency is developed and used to predict the effect of damage on the plates' natural frequencies. These natural frequencies can then be used to solve the inverse problem, enabling a quantitative relation between the crack length, crack depth, crack orientation and crack location with the vibration characteristics to be derived.

2.2 Modelling the Effects of Damage

2.2.1 Delamination

Delamination, caused for example by tool drop or bird strike, is one of the most important forms of damage in composite laminated structures due to its effect on residual compressive strength and the difficulties in detection due to the lack of visibility from the surface of the structure (BVID). A range of techniques have been used to determine the effect of such damage on the performance of composite structures.

Cappello and Tumino (2006) discussed the effect of delamination location, severity and stacking sequence of layers on the buckling and post-buckling behaviour of plates by ANSYS. Enhanced assumed strain (EAS) was used to investigate the buckling behaviour of composites, with the relationship between the location and dimensions of damage and vibration parameter for through-the-width delamination studied (Lee and Park 2007). Karihaloo and Stang (2008) developed guidelines for assessing the threat posed by interlaminar matrix delamination, making a significant simplification to assess the analysis procedure for determining the pre-buckling and post-buckling behaviour of a composite plate. In terms of delamination growth, there are variety of techniques available to explore this effect including the virtual crack closure technique (Liu et al. 2011) and layerwise theory (Nikrad et al. 2016). The buckling and post-buckling behaviour of plates containing multiple delaminations was studied using first-order shear deformation theory by Yazdani et al. (2016).

Most of the previous research has used finite element analysis to model delaminations in plates. Use of the FE method allows a wider range of loading and boundary conditions for complicated damage cases to be explored. However, this often comes at a high computational cost particularly when repeated analysis is needed for example for iterative solutions of non-linear problems and optimum design. In the preliminary design stage, when engineers need to consider many alternative configurations and loading cases, a fast and reliable analysis is required. The software VICONOPT employs a quicker alternative delamination modelling method for investigating the change of buckling and vibration behaviour of plates based on the exact strip method, examining the effects of damage in terms of an equivalent prismatic model. For example, Damghani et al. (2011) presented a smearing method (SM) to enable an embedded delamination to be modelled as an equivalent through-the-length delamination at the same location as shown in Figure 2-1 for the critical buckling behaviour. His paper emphasises the simplicity of modelling and

competitive computational times of the exact strip method versus FE. Damghani et al. (2014) also explored the effect of a single rectangular delamination on the global buckling behaviour of a composite plate. To achieve a solution for this non-prismatic problem, the strip containing the delaminating was exchanged for three strips with the same length and at the same location, with two strips representing the top and bottom parts of delamination, and the third one representing the undamaged part. This configuration enabled the SM to be used to determine the global buckling behaviour of the delaminated composite plate, however due to the way in which the delamination was modelled, local behaviour was limited in some circumstances.

To avoid these limitations whilst continuing to benefit from the efficiency and accuracy of the exact strip method, Suliman (2018) combined the use of the exact strip method to simulate the intact part of a damaged plate with an appropriate FE method based on the FE theory of Przemieniecki (1985) to simulate delaminated part (Suliman 2018). This hybrid model was used to study the effects of damage in both isotropic and composite structures allowing complex structures to be handled by coupling the ability of FE (Figure 2-2).

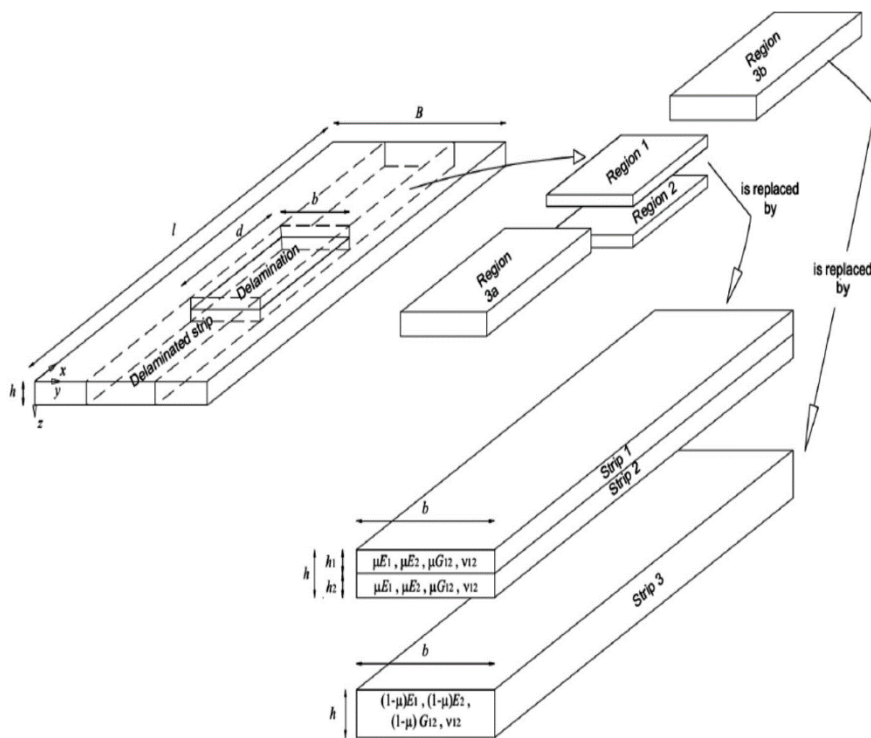


Figure 2-1 Embedded rectangular delamination model in VICONOPT (Damghani et al. 2014).

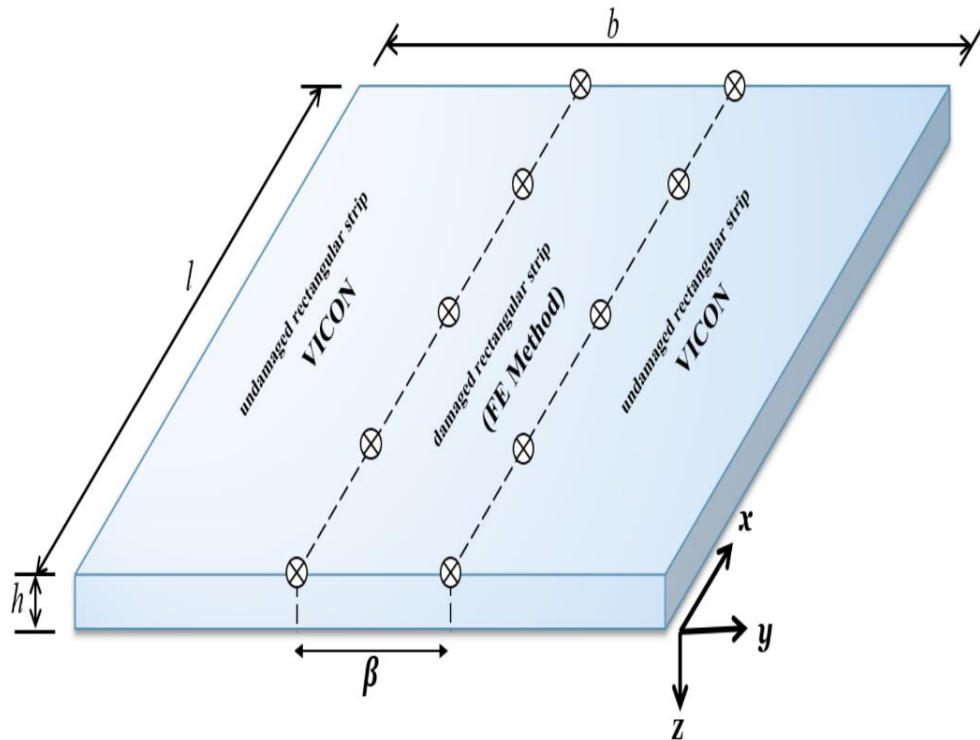


Figure 2-2 Hybrid delamination plate model reproduced from Suliman (2018).

This thesis will refer to the work of Suliman, using one stacking sequence of a laminated plate as an example for a preliminary study of the hybrid model (VFM), while the change of natural frequency is sensitive to different layup of laminated structure and more detail of the influence by different stacking sequences are shown in (Suliman 2018). Therefore, this thesis extends the damage types handled to incorporate the effects of cracks. (a more applicable and updated calculation method will then be shown in Chapter 4 of methodology part and Chapter 5 of hybrid cracked plate modelling part).

2.2.2 Cracks

Previous work has modelled cracks in two different ways: as a reduction in stiffness along the crack path; or by a series of springs (Liang et al. 1991; Cerri and Vestroni 2000; Vestroni and Capecchi 2000; Friswell 2007). In the first case, the reduction in stiffness can be represented by a decrease in either cross-sectional area or Young's modulus of the material (Labib et al. 2014). Alternatively, spring models simulate the behaviour surrounding a crack by introducing a compliance corresponding to the crack depth. Different relationships have been found experimentally using a strain energy density function based on the fracture mechanics method (Rizos et al. 1990; Ostachowicz and Krawczuk 1991; Dimarogonas 1996; Chondros et al. 1998; Caddemi and Calìò 2009).

Relevant reviewed literature about cracked simulation models will be introduced in the following sections by beam-like structures and plate-like structures, respectively. The crack model used in this thesis adopts the second approach, with rotational springs added to give additional freedoms to finite elements in the area of damage to represent the cracks and cracks are supposed to be always open. This is in an analogous manner to that previously applied to beam structures (Caddemi and Calì 2008; Labib et al. 2014), and the cracked problem could be then presented as a linear one. In the cracked elements, the construction of a nodal stiffness matrix which incorporates stiffness due to the crack and the ways in which the rotational spring is formulated are an essential part of the present study. The modified W-W algorithm is finally used to calculate the natural frequencies and mode shapes of the cracked plate structure.

2.2.3 Beam Structures

Beam-like structures are the fundamental element of many complex structures, and the mechanical theory of other types of structure can often be deduced or is analogous to beam-type structures. The presence of cracks will damage the continuity and reliability of the physical and geometrical properties of the beam and has been widely studied in the literature.

Changes in natural frequencies have been formulated to simulate single cracks in simply supported and cantilever beams by Liang et al. (1992). Morassi (1993) demonstrated that, for any boundary conditions, changes in natural frequencies are functions of the square of the mode shape curvature of an intact beam coupled with crack severity. A comprehensive review of the methods used to solve vibration problems in damaged structures, which particularly illustrates the differences between the behaviours of a notch and a crack is given by (Dimarogonas 1996).

2.2.3.1 Stiffness Reduction

Christides and Barr (1984) applied the Rayleigh-Ritz method to solve the boundary value problem for the natural frequencies of damaged Bernoulli-Euler beams with open cracks. In this work the stiffness reduction simulates the presence of a crack according to an exponential variation law which is not limited to a local influence. Shen and Pierre (1990) extended this theory by presenting a Galerkin solution. Papadopoulos and Dimarogonas (1987) described a full matrix in terms of an arbitrary loading for cracked beam calculated frequencies using a fracture mechanics method. Sinha et al. (2002) presented an alternative approach based on measured vibration data in which stiffness reduction was governed by the local effect through a triangular variation.

2.2.3.2 *Spring Models*

Okamura et al. (1969) introduced coupling terms to the flexibility parameters used to evaluate the effects of cracks in beam based on measured vibration data. Christides and Barr (1984) presented a one-dimensional cracked beam theory using experimental results for simply supported beams with single-edge or double-edge open cracks. Gounaris and Dimarogonas (1988) considered rotational, shear, axial and torsional springs, and coupled them together for their crack model. Chondros et al. (1998) used displacement fields to simulate the additional flexibility at a crack location based on a fracture mechanics method, and simulated the crack by a continuous flexibility, which is a summary and extension of the proposed cracked beam theory by Christides and Barr (1984). Banerjee and Guo (2009) simplified the spring crack model, with only rotational, shear and axial springs being considered. A further simplified model used to express the effect of a crack on flexural stiffness only involved an equivalent rotational spring connecting two adjacent parts of the beam (Gounaris and Dimarogonas 1988; Rizos et al. 1990; Ostachowicz and Krawczuk 1991; Caddemi and Calìò 2008; Freund and Herrmann 2010). This crack model displayed slope singularity at the cross-section where the cracks existed using fracture mechanics theory.

2.2.3.3 *Multiple Cracks Problem with Advanced Approaches*

For calculation of the natural frequencies of beams containing singularities, many previous studies have developed complex solutions relying on the integration of the governing equations between the singularities and the location of the continuity conditions where cracks occur. With increasing numbers of cracks, these solutions become more difficult incurring significant computational cost. Substantial effort has therefore been put into developing methods which provide accurate results with high computational efficiency and can therefore be incorporated into standard engineering practice. Dirac's delta distribution functions for example can be used to simplify the solution of problems involving multiple cracks (Shifrin and Ruotolo 1999). Yavari et al. (2000) applied the distribution theory of Schwarz to a beam bending problem, with an auxiliary beam method proposed to solve the governing differential equations of an equivalent boundary-value problem in the space of classical functions. A further simplified solution is proposed using transfer matrix methods (Khiem and Lien 2001; Lin et al. 2002) and Caddemi and Calìò (2009) utilised Heaviside and Dirac's delta functions to solve beam vibration problem with multiple open cracks, with reduced dynamic stiffness matrices used for cracked frames.

2.2.4 Plate Structures

2.2.4.1 Numerical Analysis

The vibration responses of rectangular plates with cracks or singularities under different loading and boundary conditions has been the subject of significant investigation and many methods have been presented to solve this problem. As for the plate, the length, position, depth and orientation of a crack will impact on vibrational characteristics and material properties. Irwin (1962) found cracks in plate elements could lead to local changes in plate stiffness, with the first investigation of the vibration behaviour of a cracked plate in which the Green's function approach is used to obtain the homogeneous Fredholm integral equation presented by Lynn and Kumbasar (1967). This was the first study of its kind to satisfy mixed boundary conditions along a virtual line simulating a crack and used changes in natural frequencies to analyse the vibration of thin simply supported rectangular plates in relation to different crack lengths and associated moment distributions along intact parts. Leissa (1969) presented a review of about 500 publications and 1500 papers written before 1966 regarding the free vibration of plates. Few publications exist dealing with the cracked rectangular plates explored in this thesis, with most of these considering cracks parallel to the plate edges based on extensive literature and existing methods for solving the problem of an intact plate.

Some previous research has been restricted to cracks running only along the axis of symmetry. Solecki (1980) used a finite Fourier transformation coupled with a generalised Green-Gauss theory to analyse the vibration characteristics of an isotropic simply supported rectangular plate with internal rigid supports. Good agreement with other studies was seen for cracks parallel to one edge of the plate as well as diagonal cracks. Hirano and Okazaki (1980) used a Fourier expansion and the weighted residual methods to form the mixed boundary conditions along the fictitious line of a crack. Subsequently, Solecki (1983) studied the vibration response of a simply supported rectangular plate within an arbitrarily located parallel crack using a finite Fourier transformation of discontinuous functions by representing the singularity at the crack tips.

Despite some success, insufficiently accurate results were obtained when the crack extended to the edges (the length of the crack is equal to the width of the plate). A finite Fourier transform to the differential equation was applied in these studies (Hirano and Okazaki 1980; Solecki 1980; Solecki 1983), and a system of integral equations represented the unknown singularity around the crack. The unknown quantities were expanded into a Fourier series, but this method was limited to the localisation of the crack or the boundary conditions of the plate.

Qian et al. (1991) established a finite element model to investigate the vibration response of a cracked plate. In this model the stiffness matrix of the plate is obtained by the addition of the strain energy of the crack which is related to the stress intensity factor. The stiffness matrix is then used to explore the behaviour of a finite plate with a through crack under bending, twisting and shearing. Good agreement and a higher level of efficiency are found compared with the model from Solecki (1983), since mesh subdivision next to the crack tip is unnecessary. Krawczuk (1993) presented a closed form solution formulating the stiffness matrix required to simulate a static through crack in a rectangular plate. Changes in natural frequencies were formulated as a function of the length and location of the crack, the boundary conditions, and the mode shape. A similar method was used to solve for an internal static crack based on transverse forced vibration, and a relationship between increasing vibration amplitudes and the parameters of the crack was proposed (Krawczuk and Ostachowicz 1994). An investigation of the effect of the plastic zone around a crack on the flexibility of the structure compared with pure elastic behaviour, demonstrated a rather small influence in contrast to elastic and elasto-plastic crack models (Krawczuk et al. 2001). Fujimoto et al. (2003) used a hybrid of the finite element method and the body force method to discuss the vibration response of a centrally cracked plate under uniaxial tension. Saito et al. (2009) used a finite element model to analyse the linear and nonlinear vibration response of a cantilever plate within a transverse crack. Bachene et al. (2009) proposed an extended finite element method to describe the vibration response of a cracked plate under different boundary conditions. Considering both shear deformation and rotational inertia based on Mindlin plate theory, their results showed that the extended finite element method was an efficient method for dynamic analysis of plates containing singularities.

2.2.4.2 *Analytical Analysis*

Solutions for cracked plates have been developed using a range of different analytical methods. Keer and Sve (1970) presented dual series equation solution methods to explore the stress singularity at the crack tips. Despite producing accurate results, the technique incurred significant computation cost compared with Lynn and Kumbasar (1967) while the limitation that crack could only run along the axis of symmetry. Stahl and Keer (1972) firstly used homogeneous Fredholm integral equations of the second kind to obtain the natural frequencies of a plate with different crack locations.

Lee (1992) used the Rayleigh-Ritz method with a simple sub-section technique to find the natural frequency of annular plates with internal cracks. This method could be applied for different boundary conditions but was restricted to the first natural frequency. Lee and Lim (1992) subsequently used the Rayleigh-Ritz principle with a domain decomposition technique to obtain natural frequencies based on the simplified Reissner theory. Liew et al. (1994) applied the domain decomposition method with the Rayleigh-Ritz method to find the upper bound of natural frequencies for cracked plates. The solutions obtained however lacked an important parameter of the Rayleigh-Ritz method because the displacement and slope continuities did not match at points along the interconnecting boundaries or the virtual springs assembled along the crack segment were not stiff enough. As a result, the singularity of the crack tip stress was not properly generated. Khadem and Rezaee (2000) presented modified comparison functions based on the Rayleigh-Ritz method to analyse the behaviour of cracked plates under external loading with different boundary conditions. Whilst the effect of the crack on the vibration response was expected to change depending on the depth and location of the crack, unacceptable levels of error were present in the results due to nonlinearity being ignored. Chen and Bicanic (2000) applied incomplete modal information to detect damage in a cantilever plate. Lee et al. (2003) then extended the equations of motion for a thin uniform plate with line crack-like local damage. The locations and severities of damage parameters could be functionalised by a damage distribution, and a small damaged region could be expressed as the effective orthotropic elastic stiffness which was derived in terms of the damage severity (orientation and size). This study showed that line crack-like damage may change the material behaviour which could be applied to detect the orientation of this type of damage.

A solution based on the Galerkin method was used in analysing beam-like structures by Shen and Pierre (1990). Wu and Shih (2005) extended this to use Von Kármán plate theory to analyse the dynamic instability and nonlinear response of simply supported cracked plates subject to a periodic in-plane load. The incremental harmonic balance method was then used to solve the cracked model and found that both stability behaviour and vibration response were affected by crack location, aspect ratio, amplitude of vibration and loading conditions. Xiao et al. (2008) used the Galerkin method and the harmonic balance method to solve nonlinear vibration equations based on Reissner plate theory and the Hamilton variational principle. Israr et al. (2009) applied Galerkin's solution to reformulate the governing equation for a cracked plate into time dependent modal coordinates based on Berger's method (Berger 1954). Huang et al. (2011) proposed new sets of admissible functions to represent the stress singularity along the crack tip and the discontinuities of transverse displacement and bending rotations. The admissible functions were developed from Rayleigh-Ritz method based on Mindlin plate theory.

2.2.4.3 *Experimental Analysis*

Literature relating to the study of cracked plate behaviour is mainly based on centrally located cracks or edge cracks located parallel or perpendicular to one side of the plate. Only a few studies have dealt with the effects of arbitrary cracks at different angles of inclination to the side of the plate. Maruyama and Ichinomiya (1989) carried out experimental real-time measurement of the vibration of a series of plates based on time-averaged holographic interferometry. The influence of the length, location, and orientation of all through-the-thickness crack on the natural frequencies and mode shapes of a series of panels was investigated. Wu and Law (2004a; 2004b; 2004c) presented a new effective stiffness model based on the theory proposed by Lee (1992) for an anisotropic thick cracked plate. Huang and Leissa (2009) used a set of corner functions to simulate the stress singularities and extract the natural frequencies of the plate using the Rayleigh-Ritz method. This method was extended to thick rectangular plates with arbitrary cracks based on Mindlin theory (Huang et al. 2011). A relationship was found between the crack orientation and the change in natural frequencies with different boundary conditions having different effects on the vibration response. However, this is one of only a few research studies which describe the effect of change of crack angle on vibration response, most of which studied through-the-depth cracks with no results on part through-the-depth cracks (Huang and Leissa 2009; Ismail and Cartmell 2012). Bose and Mohanty (2013) incorporated stress theory and strain gradient theory to study the

effect of microstructure on vibration response by a modified LSM, but the change in natural frequencies obtained from this study is significantly different from that of previous literature (Stahl and Keer 1972; Liew et al. 1994).

2.2.4.4 *Line Spring Model*

The Line Spring Model (LSM) mentioned earlier is a commonly used approximate analytical solution first proposed by Rice and Levy (1972). Continuous line springs represent partial through-the-thickness cracks with compliance coefficients matching the edge-cracked strip in plane strain. LSM reduces the complexity of the cracked structure problem and is especially valid for classical thin plates (assuming Kirchhoff's plate bending theory). Suitable compliance coefficients are determined under different loading conditions and different crack locations and used to reduce the three-dimensional crack problem to a similar two-dimensional problem. Stress intensity factors are determined by the force and moments around the cracked segment and the solution is formulated as an Airy stress function. Although providing a good approximation of the effect of a part through-the-thickness crack, this technique incurs significant computational cost, and newer methods based on the LSM have been developed to overcome the problem. Delale and Erdogan (1981) reformulated the LSM based on Reissner plate bending theory including transverse shear effects. The expression for the stress intensity factor of the plane strain problem of a cracked strip was updated with a valid crack depth to plate thickness ratio of up to 0.8. King (1983) then proposed a simplified LSM where the crack is represented by a virtual ligament spring enforced at the centre of the crack. Reasonable predictions of fracture characteristics like J-integral and crack opening displacement are included in the paper. Yang (1988) demonstrated an effective approximate solution applying the LSM to a complicated three-dimensional crack problem in plates and shells with an acceptable level of accuracy. Miyazaki (1989) described a transient analysis of the dynamic stress intensity factor through the coupling of finite element method with a static LSM.

Compared with full three-dimensional cracked plate models, the LSM is versatile and can be applied in conjunction with various boundary conditions and loading cases (mixed mode, elastic-plastic fracture problems, crack contact problems and arbitrary residual stress loading cases) (Cordes and Joseph 1994). Joseph and Erdogan (1991) pointed out that LSM could be applied to find the stress intensity factors along the cracked segment of different forced vibration systems under mixed mode conditions. Israr (2008) and Israr et al. (2009) presented a model for a horizontal part-through centrally located crack based

on the Duffing equation. The relationship between the nominal tensile and bending stresses at the crack location and far sides of the plate was obtained. Joshi et al. (2014) derived new crack terms to analyse the frequencies of an internally cracked plate by LSM, and Gupta et al. (2015) developed an analytical model for vibration analysis of isotropic and functionally graded cracked plates based on a modified coupled stress theory.

A simplified LSM has also been proposed in which the impact of a crack on the flexural stiffness of a structure is simulated by an equivalent rotational spring. This idea was first used in the beam-like structures mentioned above (Gounaris and Dimarogonas 1988; Rizos et al. 1990; Ostachowicz and Krawczuk 1991; Caddemi and Calì 2008; Freund and Herrmann 2010; Labib et al. 2014). An analogous simplified form of this LSM will be studied in this thesis for the direct problem. There are few sources in the literature describing solutions to the free vibration problem for plates and shells containing cracks based on the LSM, especially for arbitrary cracks of random length, depth, location and inclination angle. Hence, an efficient and accurate consideration of the modelling of free vibration of cracked plates is useful and will be presented in Chapter 5.

2.2.5 Further Remarks

When damage occurs in the structure, it will cause a significant effect on the performance of the structural properties and mechanics. Hence, damage detection needs to be applied and studied for locating and assessing its severity. Different types of damage with different locations and severity will have different influences on both buckling and vibration behaviours. The work in this thesis aims to study the effect of damage based on the natural frequency of the structure for both delaminated and cracked structures.

In practical engineering scenarios, structures are subject to a range of loading conditions including asymmetric out-of-plane loading, resulting in a combination of in-plane tension and out-of-plane shear leading to the cracking failures of plate structures (Potyondy et al. 1995; Harris et al. 1998). In this thesis, out-of-plane effects present the main concern, and out-of-plane degree of freedoms are used in developing a cracked plate model.

Dynamic stiffness analysis (the exact strip dynamic stiffness method) provides an efficient, accurate alternative to the finite element method utilising a transcendental stiffness matrix based on exact solutions to the governing differential equations. The exact strip method (ESM) will be elaborated in detail in chapter 3 accompanied by a discussion of the ESM based software VICONOPT. The exact strip method needs the

parameters of the plates and loading conditions to be invariant along the longitudinal direction, in terms of describing the vibration modes by sinusoidal terms in the longitudinal direction (Anderson. et al. 1983).

Delaminated plates (with all through-the-length delamination) will be shown first using ESM modelling and then a related inverse problem will be solved as a preparation for cracked plates. Because the assumption of longitudinal invariance is not valid for arbitrary cracks, the efficiency and accuracy of the LSM model and ESM also need to be considered. In this thesis, a simplified LSM based on an equivalent rotational spring model has been incorporated with a singularity integral formulation of an isotropic simply supported plate based on the classical thin plate theory. It has been added to a finite element model of the cracked segment and coupled with an exact strip model of the intact segment by Lagrangian multipliers at boundaries to solve arbitrary crack problems. A hybrid cracked model is shown in Figure 4-1, while results are tabulated and validated by previous published results and the commercial FE software ABAQUS with related mode shapes. It is then used to determine the natural frequencies of a simply supported rectangular plate with a crack of arbitrary location, length, depth and inclination angle. Such generality is largely absent from the literature, where results are commonly restricted to cracks located at the centre or at an edge of the plate, running parallel to the edges of the plate, over the full length or width, or through the full thickness (Stahl and Keer 1972; Liew et al. 1994; Bose and Mohanty 2013; Labib et al. 2015). An advanced and efficient cracked plate model will be the essential part of the study and one-dimensional cracked plate detection will be shown in Chapter 7.

2.3 Inverse Problem

As discussed in chapter 1.2, there are a wide range of techniques which can be used to detect damage in plates including DIM, VDI, FRFs, WA, ANNs, FFT, AF and CA. In this section, methods relating to the use of changes in vibration characteristics especially natural frequencies to detect damage in beams and plates based on models such as those reviewed in section 2.1 will be examined. Establishing a cracked beam/plate model and obtaining natural frequencies from it, the inverse problem is then applied to localise the crack and estimate its severity based on changes in natural frequencies or mode shapes.

2.3.1 Beam-like Structures

2.3.1.1 *Spring Model*

Cracks in beam structures have been successfully modelled as a set of rotational, axial and shear springs. Rizos et al. (1990) proposed a crack identification technique for one-dimensional structures based on measuring the amplitude of vibration at two different positions with one of its natural frequencies. A rotational spring was used to simulate the crack and the Newton-Raphson method was applied to solve the iterative boundary value problem based on measured vibration modes to obtain the location and magnitude of the crack. The technique was validated experimentally on a cantilever beam with a harmonic exciter. The method is restricted to small cracks, where the crack depth to beam thickness ratio is smaller than 0.1. It also suffers from a lack of sensitivity compared with ultrasonic or radiography methods and cannot recognise symmetrically localised cracks in a simply supported beam. Liang et al. (1991) developed this method based on two or three natural frequencies without the need for a mode shape, enabling a noniterative procedure to be used to locate the crack based on Euler-Bernoulli beam theory. They went on (Liang et al. 1992) to determine the frequency sensitivity using bending theory and presented the relationship between the first-order change in the eigen-frequencies and the crack parameters (location and severity). Morassi (1993) considered the simplicity of Liang's model, and proposed a general perturbation approach instead of the symbolic manipulators used.

Nikolakopoulos et al. (1997) used 3D contour plots to illustrate the relationship between changes in natural frequencies and the presence of a crack. Cerri and Vestroni (2000) presented two different damage identification techniques based on frequency measurement utilising Saint-Venant's principle and optimality criteria. The first method

used the characteristic equation error (the change in natural frequencies between the undamaged and intact status of beam); the second method was based on the comparison between the analytical and experimental frequency values. An experimental validation was then performed on cracked reinforced concrete beams (Cerri and Vestroni 2003). Caddemi and Morassi (2007) provided an exact closed-form expression to solve the inverse problem to determine the location and magnitude of the crack. The crack was formulated as a function of deflection measurements for different boundary conditions and could be extended to multiple cracks. The effects of errors caused by the presence of noise during measurement was discussed. Greco and Pau (2012) adopted the dynamic stiffness matrix with the rotational spring crack model. They used the least sum of squares of the differences between the theoretical and virtual experimental changes in natural frequencies as the optimality criteria. The W-W algorithm (Wittrick and Williams 1971) was used to calculate the theoretical natural frequencies in a cracked frame, while the effect of noise was considered by Monte Carlo simulations. Diaferio and Sepe (2016) developed this theory and modified the optimality criteria in multi-bay and multi-storey plane frames in vibration-based crack detection. The noise effect was simulated by calculating the average mean error and standard deviation in crack parameters (location and severity). Sharma et al. (2015) described a method of crack identification for a single crack with different boundary conditions. An unconventional frequency-based damage detection method was applied to multi-span beam structures based on the change in natural frequencies. Several studies have discussed the difference between vibration-based identification based on spring models and finite element models, with some authors combining the two (Vestroni and Capecechi 2000; Chinchalkar 2001). A small number of studies have used rotational spring models for multiple crack detection in beams, however, the total number of cracks need to be known a priori (Lee 2009; Maghsoodi et al. 2013). Caddemi and Caliò (2014) proposed explicit expressions to identify an arbitrary number of cracks and Labib et al. (2015) used natural frequency degradations to detect cracks in beam-like structures.

2.3.1.2 *Finite Element Method*

Many crack identification methods use the finite element method, discretising the structure into a set of elements represented by stiffness and mass matrices and modelling cracks as reductions in stiffness at the cracked element. Yang et al. (1985) experimented with a cracked cantilever beam validating his analytical results by using the first six natural frequencies. Kam and Lee (1992) examined vibration response based on this type

of model. Static deflection analyses were performed for both intact and damaged cases and a strain energy equilibrium was proposed to determine the severity of the crack. The first ten natural frequencies and mode shapes were obtained from experiments (Rizos et al. 1990) for various sizes and locations of crack, and then these natural frequencies were calculated to identify crack severity. Good agreement was shown with the potential for extension to multiple cracks. Hassiotis and Jeong (1995) applied a number of quadratic optimality criteria to detect single and multiple damages in beam-like structures. Lee and Chung (2000) presented a crack detection technique using the lowest four natural frequencies which were first calculated based on finite element analysis. They then applied Armon's rank-ordering method with the obtained frequencies to calculate the approximate crack location. By applying the result of the crack position range, they were able to adopt an appropriate FEM model and the crack size was determined by FEM. Finally, the actual crack location was identified by Gudmundson's equation using the determined crack size and the aforementioned natural frequencies.

2.3.1.3 Other Detection Methods

Besides the aforementioned methods, several different damage detection methods have also been used to solve the inverse problem (Salawu 1997; Doebling et al. 1998; Carden and Fanning 2004; Friswell 2007). For example: changes in curvature (Pandey et al. 1991), the finite element model updating method (Teughels et al. 2002) and wavelet analysis of mode shape differences (Solís et al. 2013). Stubbs et al. (1992) presented a method based on examining the curvature of the measured mode shapes to find the decrease in modal strain energy between two structural degrees of freedom. Ratcliffe (2000) utilised frequency response functions for damage detection covering a wide range of frequencies with numerous measurement points needed.

Several advanced numerical techniques have also been applied to solve the inverse problem. Examples include genetic algorithms (Friswell et al. 1998); neural networks (Fang et al. 2005) and the bees algorithm (Kang et al. 2009). For more complicated structures like frames, generally, each frame member is regarded as one finite element or two elements to avoid the symmetry effect (Hassiotis and Jeong 1995; Escobar et al. 2005; Ge and Lui 2005). Morassi and Rovere (1997) discretised the frame members into numerous elements to detect a single crack in a five-storey frame.

2.3.2 Plate-like Structures

Most of the damage detection techniques and optimality criteria developed for plate-like structures were extended from those for beam-like structures. However, damage detection in thin plate structures is a simplified 2D problem. Compared with the theories developed for beam structures, more parameters and more complicated geometrical conditions need to be considered for plate structures. In the past decades, many vibration-based damage detection methods have been proposed. Rytter (1993) classified these into four levels:

Level 1: Determination that damage is present in the structure;

Level 2: Level 1 plus determination of the geometric location of the damage;

Level 3: Level 2 plus quantification of the severity of the damage;

Level 4: Level 3 plus prediction of the remaining service life of the structure.

Furthermore, by considering the parameters which can be compared to determine the relationship between an intact structure and a damaged structure, damage detection methods can be grouped into (Pérez and Serra-López 2019):

1. modal domain methods (natural frequencies, modal damping, mode shapes, strain energy, curvatures);
2. spatial model domain methods (mass matrices, stiffness matrices, damping matrices);
3. response domain methods, encompassing spatio-temporal domain methods and spatio-spectral domain methods (frequency response functions).

Frequency-based methods have been widely used in the modal domain due to their inexpensive measurements and global nature. Using the frequencies obtained from an analytical model, numerical model or experimental data, changes in natural frequencies can be analysed from structures of different status (intact or damaged). Natural frequency degradations can then be used to solve the inverse problem of determining the location and severity of the damage. In general, the first few natural frequencies are used in inverse algorithms to find the damage indexes. Previous studies have proposed numerous methods and algorithms for use in the analysis and detection of damage in plate-like structures. There is no consensus on the optimal criteria for damage identification in such structures based on vibration data, and different representative approaches have been chosen which are explored in the following sections.

2.3.2.1 *General Detection Method*

Cawley and Adams (1979) found the ratio of the natural frequency changes in two modes could be formulated to deduce damage location in a two-dimensional structure. This technique was applied to an aluminium rectangular plate and a composite plate based on both experimental techniques and the finite element method. Damage locations were calculated based on the comparison of theoretical and measured natural frequencies. Cornwell et al. (1999) extended the theory to general plate-like structures characterised by two-dimensional curvature. Unlike the low accuracy achieved in practice using the curvature of the mode shape, Zhang et al. (2013) used the curvature of the frequency shift surface. Local damage was found only to cause a local change in the frequency shift surface.

Sampaio et al. (1999) proposed the frequency response function method which was based on measured data without any modal identification. Dems and Mróz (2001) introduced damage indices (frequency variation) to evaluate damage location and severity. For this method however, the computation cost needs to be considered and the indices need to be carefully chosen. Li et al. (2002) also used damage indices, with a strain mode technique based on the Rayleigh-Ritz method proposed to determine damage location by two damage sensitive parameters. Results coming from the modified method shown good agreement and significant capability in practice. Yam et al. (2002) systematically studied the sensitivities of static and dynamic parameters of damaged plate-like structures. Out-of-plane deflection and its slope, curvature and the frequency of the deformation response function were formulated as the damage indices in dynamic analyses. Also, low frequency modes were examined to narrow down the possible damage location region. Lee and Shin (2002) adopted statistical pattern recognition to verify the state of damage. Changes in the vibration modes and frequency spectra were used to determine the type and location of damage in plates. However, since the damage-induced changes could often be confused with the effects of other variables like temperature fluctuation, this method needed every possible damage state to be explored in order to permit pattern recognition. Lu et al. (2009) used artificial neural networks in cracked aluminium plates to solve the inverse problem. Khatir and Wahab (2019) solved the inverse problem in cracked plates based on proper orthogonal decomposition and radial basis functions.

Williams et al. (1997) proposed the damage location assurance criterion based on the modal assurance criterion in modal analysis. This could also be used in multiple damage location identification. Hosseini-Hashemi et al. (2011) proposed solutions based on exact

characteristic equations of natural frequencies for rectangular plates using Reissner-Mindlin theory. Yang et al. (2013) input natural frequencies measured in a thick plate into a database, and plotted contour lines for three of the obtained frequencies to identify the severity and location of damage. Jiang et al. (2017) used the wavelet finite element method to obtain the modal shapes and natural frequencies of aluminium plates. Numerical simulation and experimental validation for a free aluminium plate with multiple cracks were used to verify the method. Pan et al. (2019) proposed a novel theory of noise response rate that could evaluate the sensitivity of each mode of the frequency shift to noise. Their method showed that appropriate selection of vibration modes with low noise response rates could improve the behaviour of frequency-based damage identification techniques in composite curved plates.

2.3.2.2 *Optimality Criteria*

For different parameter-based techniques, various optimality criteria have been proposed for structural damage identification. Krawczuk et al. (2004) chose the given vibration response to predict the damage parameters with special spectral elements used to analyse waves in cracked plates. Friswell et al. (1998) used genetic algorithms based on vibration data. The target of their study was to identify multiple damage locations and assess the severity of the damage applying a genetic algorithm. The genetic algorithm was used to optimise the damage location variables. For a given damage location site or sites, an eigensensitivity method was used to optimise the extent of the damage. This two-level approach had the advantages of both the genetic algorithm and the eigensensitivity method. Horibe and Watanabe (2011) continually applied a genetic algorithm to determine crack location in plates but only for cracks running parallel to one edge of the plate.

Yin et al. (2010) explored a Bayesian probabilistic approach in classical thin plates, with only a few points measured to obtain the dynamic response. Moore et al. (2011) developed and applied a Bayesian approach for freely vibrating cracked plates using dynamic impulse response data based on the analytical model proposed by Solecki (1985). Simulated time series are used in the parameter estimation process. Li et al. (2019) used the Markov chain Monte Carlo algorithm to measure structural parameters which were compared with simulated scattered field data, a Bayesian approach was then used to determine the quality and quantity of damage data.

Singh et al. (2011) used the least squares method in relation to the reflection and transmission coefficients of a pure incident Lamb wave sent towards the defect to quantify two unknown parameters representing the geometry of the defect. A FE model is used to simulate this scattering for various values of the parameters, with postprocessing to predict the reflection and transmission coefficients. When the predicted reflection and transmission coefficients best fit those from the initial experiment of the process stops. Chatzi et al. (2011) applied the extended finite element formulation with genetic algorithms to accelerate the convergence of detection for any types of damage. However, this study was restricted to complicated damage shape like elliptical shape or multiple damage. Xiang and Liang (2012) presented a two-step method for multiple damage detection. Firstly, a 2-D wavelet transform to the mode shape was used for damage localisation, then the severity of damage at the detected location was calculated using particle swarm optimisation algorithm. Higher natural frequencies are recommended for damage severity calculations due to the increased levels of accuracy obtained. Mohan et al. (2013) used particle swarm optimisation with a frequency response function to detect the magnitude of the damage in beam-like and plate-like structures. Accuracy was found to improve based on the use of frequency response functions rather than the mode shape when examining the response of damaged structures.

Jiang et al. (2017) used a hybrid technique to detect multiple damage by coupling singular value decomposition for damage locations with an ant colony optimisation algorithm for damage severity. Dinh-Cong et al. (2017) provided a multi-stage optimisation approach for damage detection in plate-like structures. The objective function was minimised by flexibility changes of the structure after which a modified differential evolution algorithm was used through a series of stages of damage detection. At each stage the low damage variables were gradually eliminated to reduce the dimension of searching space and to increase the convergence rate of the problem. Other methods including the use of empirical probability distributions in interval arithmetic (Labib et al. 2015) to predict possible crack locations have also been considered for solving the inverse problem.

2.3.3 Further Remarks

Damage detection is a comprehensive and systematic discipline, different detection mentioned in this chapter are summarised in Table 2-1. Technological enhancements of the damage identification method have resulted from cost-effective computing memory and speed, advanced experimental measurements, developments of the finite element

method and the dynamic stiffness method, and enabled the development of increasingly advanced linear and nonlinear detection techniques (Chang 1998). In damage detection, many of the studies reviewed have used the mode shape as the basic feature in damage detection techniques like the fractal dimension method (Hadjileontiadis and Douka 2007) and modified comparison functions (Khadem and Rezaee 2000).

The main concept behind the mode shape-based method is that local information reflected by the mode shape leads to identification of singularities near the damage location. Moreover, the mode shape is less sensitive to environmental effects compared with natural frequencies (Fan and Qiao 2011; Jiang et al. 2017). The main drawbacks of the mode shape-based method are that more sensors are needed for measurement than those required to determine natural frequencies, and the mode shape is more sensitive to noise contamination.

Natural frequency methods have some restrictions when applied to practical situations. It will provide the same variation of natural frequencies when damage locates symmetrically of symmetric structure. Furthermore, the damage occurs at different place with variant severity may result in the same changes in natural frequencies which will mislead the damage detection procedure (Yan et al. 2007). Moreover, natural frequencies reflect the global response of the structure while mode shapes contain local information. Natural frequencies are cheaper to obtain which perfectly performed in the lab environment and generally can be used for simple structures. However, the frequency-based method is limited for real complex structures (Fan and Qiao 2011).

Previous research has demonstrated that lower natural frequencies can provide accurate results for small cracks and could be used as a starting modal parameter to explore in this work using the VFM model, to develop an efficient technique to detect damage in plate-like structures.

In this thesis therefore, natural frequencies will be used to assess the damage location and magnitude while mode shapes will be applied as a baseline reference. This will be achieved in two stages. Firstly, the forward problem, in which a vibration-based analytical model will be established to obtain the changes in natural frequencies and mode shapes corresponding to damage of varying severity at a series of chosen locations. The obtained data will be normalised to eliminate the effect of severity and location separately. Processed data will then be tabulated according to related mode shapes. The first few natural frequencies will be chosen and plotted as reference curves, and the measured data

or numerical simulated values normalised by the same data processing procedure. Secondly, the inverse problem will be examined, using the natural frequency degradation method used by Labib et al. (2015). Measured changes in natural frequency will be compared with the normalised reference curves to find the intersection points, combining results obtained from different modes to converge on the point/range of crack location (with a factor introduced to handle experimental noise).

Table 2-1 Review of damage detection by different vibration-based parameters.

Author	Structure	Studied damage	Parameter
(Rizos et al. 1990)	Beam	Crack	Amplitude
(Liang et al. 1991)	Beam	Crack	Natural frequency
(Liang et al. 1992)	Beam	Crack	Natural frequency
(Morassi 1993)	Beam	Crack	Natural frequency
(Nikolakopoulos et al. 1997)	Frame	Crack	Natural frequency
(Cerri and Vestroni 2000)	Beam	Crack	Natural frequency
(Cerri and Vestroni 2003)	Beam	Crack	Natural frequency
(Caddemi and Morassi 2007)	Beam	Crack	Static deflection
(Greco and Pau 2012)	Crack/Frame	Crack	Natural frequency
(Diaferio and Sepe 2016)	Frame	Crack	Natural frequency
(Sharma et al. 2015)	Beam	Crack	Natural frequency
(Vestroni and Capecchi 2000)	Beam	Stiffness reduction	Natural frequency
(Chinchalkar 2001)	Beam	Crack	Natural frequency
(Lee 2009)	Beam	Multiple cracks	Natural frequency
(Maghsoodi et al. 2013)	Beam	Multiple cracks	Natural frequency and mode shape
(Caddemi and Calio 2014)	Beam	Stiffness reduction	Natural frequency and mode shape
(Labib et al. 2015)	Beam/Frame	Multiple cracks	Natural frequency
(Kam and Lee 1992)	Beam	Crack	Natural frequency and mode shape
(Hassiotis and Jeong 1995)	Beam/Frame	Stiffness reduction	Natural frequency
(Yang et al. 1985)	Beam	Crack	Natural frequency
(Lee and Chung 2000)	Beam	Crack	Natural frequency

Table 2-1 (continued)

(Pandey et al. 1991)	Beam	Crack	Curvature mode shape
(Teughels et al. 2002)	Beam	Stiffness reduction	FRF
(Solís et al. 2013)	Beam	Crack	Mode shape
(Stubbs et al. 1992)	Jacket-type offshore structure	Stiffness reduction	Mode shape
(Ratcliffe 2000)	Beam	Crack (slot)	FRF
(Friswell et al. 1998)	Beam/Plate	Stiffness reduction	Genetic algorithm
(Fang et al. 2005)	Beam	Stiffness reduction	FRF
(Kang et al. 2009)	Dam-foundation system	Young modulus reduction	Artificial bee colony algorithm
(Escobar et al. 2005)	Frame	Stiffness reduction	Transformation matrix
(Ge and Lui 2005)	Beam/Frame/Plate	Stiffness/Mass reduction	Natural frequency and mode shape
(Morassi and Rovere 1997)	Frame	Crack (notch)	Natural frequency
(Pérez and Serra-López 2019)	Plate	Crack/Thickness reduction	FRF
(Cawley and Adams 1979)	Plate	Stiffness reduction	Natural frequency
(Cornwell et al. 1999)	Plate	Stiffness reduction	Mode shape
(Zhang et al. 2013)	Plate	Stiffness reduction	Mode shape
(Sampaio et al. 1999)	Concrete bridge	Stiffness reduction	FRF
(Dems and Mróz 2001)	Beam/plate		Natural frequency
(Li et al. 2002)	Plate	Thickness reduction	Mode shape
(Yam et al. 2002)	Plate	Local thickness reduction	Mode shape

Table 2-1 (continued)			
(Lee and Shin 2002)	Plate	Young modulus reduction	FRF
(Lu et al. 2009)	Plate	Crack	Artificial neural network
(Khatir and Wahab 2019)	Plate	Crack/Multiple cracks	Static strains
(Williams et al. 1997)	Planer frame	Stiffness reduction	Natural frequency
(Hosseini-Hashemi et al. 2011)	Plate		Natural frequency
(Yang et al. 2013)	Plate	Stiffness reduction	Natural frequency
(Jiang et al. 2017)	Plate	Multiple cracks	Natural frequency and mode shape
(Pan et al. 2019)	Plate		Natural frequency
(Krawczuk et al. 2004)	Plate	Crack	Wave propagation
(Horibe and Watanabe 2011)	Plate	Crack	Genetic algorithm
(Yin et al. 2010)	Plate	Crack	Mode shape
(Moore et al. 2011)	Plate	Crack	Natural frequency and mode shape
(Li et al. 2019)	Plate		Signal
(Singh et al. 2011)	Plate	Strip-like damage	Mode shape
(Chatzi et al. 2011)	Plate	Crack/Hole	Genetic algorithm
(Xiang and Liang 2012)	Plate	Stiffness reduction	Mode shape
(Mohan et al. 2013)	Beam/Plate	Stiffness reduction	FRF
(Dinh-Cong et al. 2017)	Plate	Stiffness reduction	Flexibility change
(Labib et al. 2015)	Frame	Crack	Natural frequency

Chapter 3--- Exact Strip Plate Analysis

3.1 Introduction

Structural design is generally characterised into conceptual design, preliminary design and detailed design (Kennedy and Featherston 2010). The conceptual design stage defines major structural components, establishes load paths through the structure and determines structural and material concepts. At this stage, many alternatives are considered in a qualitative analysis. A deeper understanding is gained from more detailed numerical analysis of the structure's integrity carried out during the preliminary design stage, which consists of analyses to examine the stability, dynamic loads and fatigue life. Finally, during detailed design, the most powerful techniques and design tools are needed to obtain detailed data for tooling and manufacture. In this stage, the computational cost requires a high level of resources. This thesis will focus on an alternative computationally efficient analysis method for the preliminary design stage.

For a simplified aircraft design, structures such as the wings and fuselage can be generalised as a series of individual stiffened panels and modelled as prismatic structures. A good design should consider the optimum structure, for example minimising the mass of the structure itself and analysing it to determine its behaviour under different combinations of loading conditions. During preliminary design, many configurations and load cases need to be considered causing the process to become computationally intensive. A faster and more accurate alternative is urgently needed and will be presented in this Chapter.

In Chapter 2, a general review of the research carried out in order to locate cracks in plates was performed. Particular attention was paid to the use of vibration behaviour with solutions based on a two stage process in which the effect on natural frequencies and mode shapes due to cracks (direct problem) was used to determine the location and severity of those cracks based on changes in the vibration behaviour (the inverse problem). In solving the direct problem, different forms of FEM provide the versatility to accurately simulate the behaviour of the damaged plate, some of which have been successfully used in practice. FEM is based on assumed interpolation polynomials to define the deformation of discrete elements (Figure 3-1 (a)). The large number of elements needed and approximate deformations incur a huge computational cost (particularly for iterative solutions of nonlinear problems and optimum design) and a potential for calculation

errors. Against FEM, alternative approaches like the finite strip method (FSM) which provides precise and efficient solutions based on an appropriate assumption along the longitudinal direction and a discretised solution of the governing differential equations in transverse direction. The dynamic stiffness method (DSM) also assumes sinusoidal variation in the longitudinal direction but solves the governing differential equation analytically in the transverse direction. Thus, DSM has the potential to reduce the computational cost significantly and also to improve the accuracy. However, only a few techniques are based on the FSM or DSM.

In this chapter, the exact strip method (ESM), an efficient and accurate method which incorporates the advantages of both FSM and DSM will be introduced. This method allows the modelling and computational costs of discretisation to be minimised by obtaining analytical solutions of the governing differential equations in transverse direction. The Wittrick-Williams algorithm (Wittrick and Williams 1971) then extracts the natural frequencies from the resulting transcendental eigenproblem. ESM has been proved much faster and more accurate than FEM in the analysis of prismatic structures, especially for parametric preliminary design studies for large and complex structures (Williams et al. 1991). To improve the versatility of the technique, Lagrangian Multipliers can be introduced to allow the analysis of anisotropic panels or those with different combinations of loading conditions. These methods have been combined in the advanced computational software (VICONOPT).

For many complex and large structures, however, FEM software is still needed for structural computation. As a result, ESM has been combined with FEM in structural analysis or optimisation software, for example in studies of embedded delaminations by Suliman (2018). Moreover, a hybrid model that considers the advantage of both ESM and FEM for arbitrary cracked plate will be described in section 5.2 of this thesis.

Aerospace designers still search for alternatives to achieve faster and more reliable analysis to save computational cost especially in preliminary design. The work in this thesis will contribute to this by developing an efficient method to predict the effect of delaminations and cracks on vibration response.

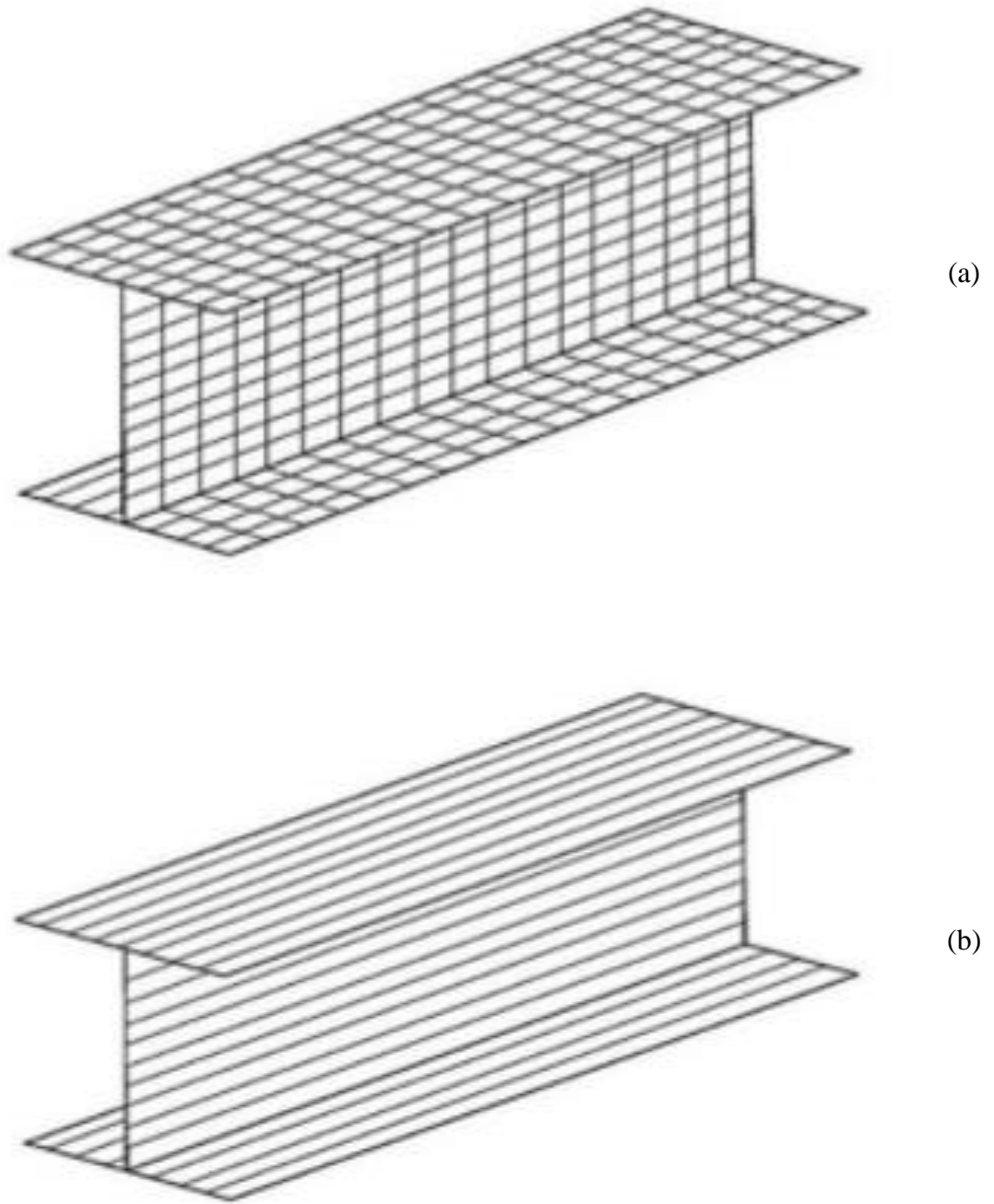


Figure 3-1 Different discretisation in (a) FEM (b) FSM (Zhang 2018).

3.2 Exact Strip Method

3.2.1 FSM and DSM

Plates are an important component in many engineering fields, for example an aircraft planform comprises a series of flat plates rigidly connected together (Dawe 2002). To simplify the problem, the basic plate structure can be assumed to be prismatic. FSM provides an efficient and accurate method for determining the vibration characteristics of such plates with discrete finite strips in the perpendicular direction (Figure 3-1 (b)) instead of discretising into elements. It can also analyse more complex structures such as skewed or curved panels which can be approximated as prismatic (Dawe 2002). FSM could be regarded as a special case of FEM based on multi-field forms of the traditional single-field combined with potential energy or virtual work principles (Dawe 2002). It was first presented by Cheung (1968) for a linear static analysis of single rectangular plates with two opposite edges simply supported. Guo et al. (1997) improved the classical FSM by replacing the static shape function of the strip model with dynamic functions in a stepped thickness plate structure. A more general approach to FSM has been described by Cheung (2013). With the development of approximate displacement fields-based FSM, an exact FSM (Wittrick 1968b) could be applied based on a direct solution of the governing differential equations of classical plate theory (CPT). To solve this ‘exact’ problem, the dynamic stiffness method (DSM) was proposed. DSM provides exact solutions in the same way as other classical methods, and can handle complicated structures comprising individual element stiffness matrices (Banerjee et al. 2015).

DSM is known as an exact method due to the exact shape functions solved, and the exact solution of the governing differential equations for free or forced vibration problems (Banerjee 1997). It provides a more accurate model compared to other approaches because the dynamic stiffness matrix is independent of the number of elements in the model (Banerjee 1997). DSM refers to the idea of forming a single stiffness matrix that includes the effects of load /or vibration (Banerjee 1997). This contrasts with finite element analysis, which use a separate static stiffness matrix, together with a mass matrix which is multiplied by frequency squared or a geometric stiffness matrix which is multiplied by the load factor. Several computer programs have been developed based on DSM, for application to beam-like structures including BUNVIS, BUNVIS-RG and CALFUN (Banerjee 1997).

3.2.2 Dynamic Stiffness Formulation

The formulation of DSM can be derived as follows (Banerjee 1997), Writing the governing differential equations of motion in free vibration symbolically:

$$L(\mathbf{u}) = 0 \quad \text{Eq. 3-1}$$

where L is a differential operator and \mathbf{u} is the corresponding displacement vector. Solving for the harmonic displacement \mathbf{u} :

$$\mathbf{u} = \mathbf{U} * e^{i\omega t} \quad \text{Eq. 3-2}$$

where \mathbf{U} is a vector of the amplitudes of displacements, ω is frequency (rad/s), t is time and $i = \sqrt{-1}$. Substituting Eq. 3-2 into Eq. 3-1 to eliminate the time dependent terms:

$$L_1(\mathbf{U}, \omega) = 0 \quad \text{Eq. 3-3}$$

Here L_1 is a differential operator. The general solution of Eq. 3-3 is:

$$\mathbf{U} = \mathbf{A} * \mathbf{C} \quad \text{Eq. 3-4}$$

where \mathbf{C} is a constant vector and \mathbf{A} is a frequency dependent square matrix. Applying the boundary conditions to eliminate the constant vector in Eq. 3-4 to obtain the force-displacement relationship:

$$\boldsymbol{\delta} = \mathbf{B} * \mathbf{C} \quad \text{Eq. 3-5}$$

where $\boldsymbol{\delta}$ is the displacement vector related to the nodal displacements and \mathbf{B} is a square matrix derived from \mathbf{A} by imposing the boundary conditions. Applying force to the nodes of each element:

$$\mathbf{F} = \mathbf{D} * \mathbf{C} \quad \text{Eq. 3-6}$$

where \mathbf{F} is the force vector related to the nodal force and \mathbf{D} is a frequency dependent square matrix. Eliminating the constant vector \mathbf{C} by combining Eq. 3-5 and Eq. 3-6:

$$\mathbf{F} = \mathbf{D} * \mathbf{B}^{-1} * \boldsymbol{\delta} = \mathbf{K} * \boldsymbol{\delta} \quad \text{Eq. 3-7}$$

where (Banerjee 1997)

$$\mathbf{K} = \mathbf{D} * \mathbf{B}^{-1} \quad \text{Eq. 3-8}$$

or (Wittrick and Williams 1971)

$$\mathbf{K} = \mathbf{A} - \omega^2 * \mathbf{B} \quad \text{Eq. 3-9}$$

Here \mathbf{K} is the equivalent stiffness matrix and is a nonlinear function of ω^2 for an infinite number of degrees of freedom system, \mathbf{K} has a transcendental dependence on ω^2 (Wittrick and Williams 1971). The calculation of \mathbf{K} can be performed either numerically or algebraically but the use of explicit analytical expressions of the elements of the dynamic stiffness matrix can save significant computational time (Banerjee and Williams 1994). It is notable that not all the stiffness coefficients are needed in DSM, and an equivalent formulation of the frequency dependent square matrix \mathbf{D} has been derived by (Przemieniecki 1985). Gupta (1976) proposed a more general plate element derivation from polynomial shape functions. The structural elements are assembled by integrating shape functions with two terms:

$$N = N_0 + \omega^2 * N_1 \quad \text{Eq. 3-10}$$

where N_0 and N_1 are characteristic polynomials in the plan dimensions x and y within satisfied boundary conditions among the nodes.

3.2.3 DSM Application and ESM Development

The idea behind applying DSM to the analysis of free vibration problems in structures is simple. The dynamic stiffness matrices of each of the individual elements are assembled as is usual in FEM and then the eigenvalue solution is applied to obtain the vibration characteristics. The elements of the dynamic stiffness matrix are normally highly transcendental functions of the frequency and lead to a nonlinear eigenvalue problem. The standard linear eigenvalue method cannot therefore extract the buckling load or frequency. Williams and Wittrick (1970, 1971) proposed an efficient and accurate algorithm that gives all required natural frequencies below a chosen trial frequency with any desired accuracy. Generally, the algorithm needs the whole dynamic stiffness matrix of the final structure and the clamped-clamped natural frequencies of the individual structural element that will be introduced in the section 3.3.

For beam-like structures, DSM is well established and as previously mentioned has been incorporated into a range of software (Banerjee 1997) for exact problems. For plate-like structures, Wittrick and Williams proposed solutions including an algorithm to solve the transcendental eigenvalue problem as mentioned above for exact free vibration analysis (Wittrick 1968a, 1968b; Williams and Wittrick 1969; Wittrick and Williams 1971, 1973, 1974; Williams 1972), which were continually developed over many decades. To determine the vibration parameters and buckling stress of prismatic structures without

considering shear and anisotropy, Wittrick (1968a, 1968b) first presented the Exact Strip Method based on solving explicit expressions of the governing differential equations. Plates are divided where necessary into a series of strips which are rigidly connected along their longitudinal edges. Sinusoidal variation of the mode is assumed in the longitudinal direction. The spatial phase differences between the forces and displacements are recorded by defining complex quantities and the sinusoidal variation terms are divided into two uncoupled systems: out-of-plane (mainly considered in the study) and in-plane displacements (Wittrick 1968b). Two stiffness matrices are defined for each strip according to these two systems and in general the out-of-plane stiffness matrix is formulated from complex terms. When these are assembled into a global stiffness matrix, the resulting buckling or vibration problem is an exact transcendental eigenproblem, rather than the discretised linear eigenproblem of FE analysis. When shear load is included, the mode shape becomes skewed and a spatial phase difference is introduced across the width of the plate. Wittrick and Curzon (1968) solved this problem approximately by assuming the structure is long compared with the half-wavelength of the buckling mode.

One of the most important outcomes of this work on the exact strip method was the corresponding software. First VIPASA (Wittrick and Williams 1974), which can be applied to classical thin plates with two opposite sides simply supported, and in which the deformation of the plate varies sinusoidally along the longitudinal direction, was developed. Then Williams and Anderson (1983) incorporated Lagrangian multipliers to couple responses from different assumed wavelengths of stiffness matrices in the program VICON to solve the skewed problem and satisfy typical simply supported end conditions. Continued development of the above programs including an optimum design feature (CONMIN) (Williams et al. (1990)). The resulting software called VICONOPT combined the features of VIPASA and VICON and could solve eigenvalue problems for prismatic components under any boundary conditions or loading combinations.

Extensions to DSM based on plate theory and including the influence of shear deformation and/or rotatory inertia cover both isotropic and anisotropic plates (Anderson and Kennedy 1993; Boscolo and Banerjee 2011, 2012a, 2012b, 2014; Fazzolari et al. 2013). In most of these studies however the shear problems considered are restricted to those with simply supported boundary conditions (Banerjee 1997; Banerjee et al. 2015).

3.2.4 ESM

The ESM supposes a continuous distribution of stiffness and mass over the structure rather than discretised values at nodal points (Kennedy et al. 2007; Kennedy and Featherston 2010). The assumption of sinusoidal variation enables a classical simply supported thin plate structure to be reduced from a two-dimensional to a one dimensional element through a characterised dynamic stiffness matrix (Wittrick 1968b). This section will introduce some general information about ESM. More detail, including algorithms and stiffness matrices, will be included in section 5.2.4 and will be used in solving the direct problem in this study. The analytical solution (Wittrick and Williams 1974), which is quite similar to DSM, involves the solution of partial differential equations governing the deformations of the strips according to exact stiffness matrices \mathbf{K}_m . The global stiffness matrix \mathbf{K} is assembled from \mathbf{K}_m and relates the displacement set \mathbf{D} at the nodes to the corresponding perturbation forces \mathbf{P} :

$$\mathbf{K} * \mathbf{D} = \mathbf{P} \quad \text{Eq. 3-11}$$

Critical buckling loads or natural frequencies are calculated by:

$$\mathbf{K} * \mathbf{D} = \mathbf{0} \quad \text{Eq. 3-12}$$

Because \mathbf{K} incorporates transcendental, nonlinear functions of the eigenparameter λ (Wittrick and Williams 1974), Eq. 3-12 cannot be solved by standard numerical methods. The Wittrick-Williams (W-W) algorithm performs an iterative search to obtain all eigenvalues under a given trial value with any required accuracy (Wittrick and Williams 1971, 1973). More detail on establishing a plate model will be given in section 5.2.4.

3.2.5 Comparison of Different Methods

In this section, FEM, FSM and DSM (ESM is a special case of DSM) are compared. FEM (Kennedy et al. 2007), is the most popular and mature method in structural analysis providing versatile analysis of complex structures. In a plate modelled using FEM, the structure is divided into many elements with connections at nodes. Stiffness and mass matrices relate forces to displacements at the nodes. Deformations are calculated by interpolation and lead to approximation errors. Buckling or vibration analysis is a large linear eigenvalue problem which can incur high computational cost.

FSM is one of few alternative approaches that provides a feasible, accurate and efficient analytical solution to one-dimensional problems. For plate-like structures, similar but different approximations to FEM are made in the transverse direction of FSM, but a sinusoidal variation is assumed in the longitudinal direction. For example, for a simply supported plate, the buckling or vibration mode is assumed to vary sinusoidally in the longitudinal direction with a certain number of half-wavelengths over the whole plate length.

DSM provides a more efficient and accurate alternative to FEM. For the ESM which is a special case of DSM, the modelling and computational cost of discretisation and inaccuracy of calculation can be avoided by explicit expression of the analytical solution of governing differential equations in the transverse direction (Williams 1972). ESM also assumes a sinusoidal variation in the longitudinal direction. The eigenvalue analysis results in a nonlinear transcendental eigenvalue problem. A highly efficient and reliable algorithm (Wittrick and Williams 1973) can find the number of eigenvalues under any trial value, and then the eigenvalue can be obtained to any desired accuracy. Modes can be found by applying a random force vector (Hopper and Williams 1977). ESM and the derived software VICONOPT have proved to be much faster than FEM for the analysis of prismatic plate structures (Butler and Williams 1992). Table 3-1 shows the main differences between ESM and FEM.

Table 3-1 ESM VS FEM.

ESM	FEM
No discretisation of plates	Discretised into many elements
Exact internal displacements	Internal displacements depend on shape functions
Small, nonlinear transcendental eigen-problem	Large, linear eigen-problem
W-W algorithm	Standard methods of solution
Prismatic geometry and loading limited	Complex loading and geometry problem
Fast solution time	Slower solution time

3.3 The Wittrick-Williams Algorithm

Extracting frequencies from an established plate model is the key part of the direct problem to be solved in this work. There are many methods to solve eigenvalue problems, such as Householder's method for linear eigenvalue problems, or the methods for quadratic eigenproblems (QEP) proposed by Gupta (1973, 1976). Gupta (1973) proposed systematic solutions of the QEP based on bisection, and applied Sturm counts to separate the roots following a higher order interpolation scheme for convergency. Of particular note is the advanced bandwidth method used in the Gauss elimination process with an array of size $(m + 1) * (2m + 1)$ where m is the half-bandwidth of the matrix. A similar idea has been applied in the present study. The computation time is determined by the m and the matrix order n , and assessed in the program QMES (Gupta 1973). A more efficient, accurate approach however is offered by the W-W algorithm which can solve nonlinear transcendental eigenproblems (Wittrick and Williams 1971). This study therefore will adopt the idea of the W-W algorithm and use it (in modified form) to obtain the lowest few natural frequencies for a simply supported plate.

The W-W algorithm determines the natural frequencies for any linear structure with known dynamic stiffness matrix $\mathbf{K}(\omega)$ corresponding to any finite set of displacements \mathbf{D} (Wittrick and Williams 1971). Generally, $\mathbf{K}(\omega)$ is a nonlinear function of ω^2 , and the W-W algorithm is a versatile approach for both finite and infinite degrees of freedom systems (Wittrick and Williams 1971). Without directly determining the values of the natural frequencies, the algorithm can obtain the number of natural frequencies below any given trial frequency and hence locate their values to any desired accuracy. The algorithm can also count coincident natural frequencies or singular values when $\mathbf{D} = \mathbf{0}$ rather than when $\det \mathbf{K}(\omega) = 0$. Moreover, it has the advantage in the analysis of large structures of being able to decompose them into identical sub-structures.

3.3.1 Finite system

In this section, using a finite model as an example, N is the total number of degrees of freedom corresponding to nodes. The vector \mathbf{P}_c represents the external vibrating force related frequency ω , the vector \mathbf{D}_c contains the amplitudes of the associated displacements (Wittrick and Williams 1971), the index c denotes that the two variables are complete. The maximum values of strain energy V and kinetic energy T of the system during vibration are (Wittrick and Williams 1971):

$$V = \frac{1}{2} * \mathbf{D}_c^t * \mathbf{A} * \mathbf{D}_c \quad \text{Eq. 3-13}$$

$$T = \frac{1}{2} * \omega^2 * \mathbf{D}_c^t * \mathbf{B} * \mathbf{D}_c \quad \text{Eq. 3-14}$$

\mathbf{A} and \mathbf{B} have the same symbolic meanings as in Eq. 3-9. They are the stiffness matrix and mass matrix respectively, and both are symmetrical $N * N$ matrices. In Eq. 3-13 and Eq. 3-14, t represents the transposition. Applying Lagrange's equations as (Wittrick and Williams 1971):

$$(\partial/\partial \mathbf{d}_j) * (V - T) = \mathbf{P}_j, j = 1, 2, \dots, N \quad \text{Eq. 3-15}$$

Here, \mathbf{P}_j and \mathbf{d}_j denote the j^{th} components of \mathbf{P}_c and \mathbf{D}_c and Eq. 3-11 can be deduced. For a free vibration system, the force vector \mathbf{P}_c is zero, and the eigenvalue problem changes into:

$$\mathbf{K}_c(\omega) * \mathbf{D}_c = (\mathbf{A} - \omega^2 * \mathbf{B}) * \mathbf{D}_c = 0 \quad \text{Eq. 3-16}$$

where the symmetric $N * N$ matrix \mathbf{K}_c is the complete dynamic stiffness matrix (Wittrick and Williams 1971), and every element of \mathbf{K}_c is linearly dependent on the variable ω^2 . \mathbf{D}_c contains all the degrees of freedom. Eq. 3-16 should satisfy the following condition:

$$\det \mathbf{K}_c(\omega) = 0 \quad \text{Eq. 3-17}$$

Since \mathbf{K}_c is a linear function of ω^2 , various algorithms can be used to compute the natural frequencies under any given frequency with the desired accuracy. Wittrick and Williams (1971) adopted Householder's method by means of a sequence of matrix operations. The transformed element possessed Sturm sequence properties and related roots could be obtained by a bisection method. Another possible solution occurs when clamping forces ($\mathbf{D} = \mathbf{0}$) are applied. $\mathbf{D} = \mathbf{0}$ modes will only occur at relatively high frequency, and these modes can be neglected in this study because it will only consider the lowest few natural frequencies.

3.3.2 Infinite System

One of the most distinctive features of the W-W algorithm compared to other algorithms is its ability with respect to infinite models. Any stiffness matrix of an infinite system should be considered as a condensed stiffness matrix \mathbf{K}_a , and any dynamic stiffness matrix $\mathbf{K}(\omega)$ of an infinite system will be a transcendental function of ω (Wittrick and Williams 1971). The difficulty is in the calculation of natural frequencies of an infinite system within a small variation of ω , searching the value for which the determinant of $\mathbf{K}(\omega)$ becomes zero. The calculation should not miss any of the eigenvalues, and the singularity of the determinant should be paid attention to. The W-W algorithm overcomes all the mentioned difficulties efficiently. The algorithm is valid for all types of eigenvalue problems based on Rayleigh's theorem (Wittrick and Williams 1971).

3.3.3 Sign count of matrix

Considering a general symmetrical $N * N$ stiffness matrix \mathbf{K} , define the characteristic values λ_j ($j = 1, 2, \dots, N$) as the N roots of $\det(\mathbf{K} - \lambda\mathbf{I})$, where \mathbf{I} is the unit matrix. The number of positive characteristic values is known as the index of \mathbf{K} , while the number of positive characteristic values minus the number of negative characteristic values is called the signature of the matrix (Wittrick and Williams 1971). In the algorithm, only the number of negative characteristic values is considered, and is known as the sign count of the matrix $s\{\mathbf{K}\}$. To calculate the sign count, \mathbf{K}_r , the leading principal minor of order r ($r = 1, 2, \dots, N$) of \mathbf{K} is introduced. The sign count $s\{\mathbf{K}\}$ of \mathbf{K} is equal to the number of changes of sign between consecutive members of the Sturm sequence $\{\mathbf{K}_0, \mathbf{K}_1, \mathbf{K}_2, \dots, \mathbf{K}_N\}$ (Wittrick and Williams 1971). The matrix \mathbf{K} is converted to its upper triangular form \mathbf{K}^Δ using a Gaussian elimination procedure, without row interchanges. The basic principles of this Gaussian elimination procedure are briefly introduced below, and the code is attached in Appendix A (Wittrick and Williams 1971):

1. Subtract a series of suitable multiples of the first row of \mathbf{K} from the subsequent rows to make all elements under the diagonal in the first column zero.
2. Subtract a series of suitable multiples of the second row of the modified \mathbf{K} from the subsequent rows to make all elements below the diagonal in the second column zero.
3. Repeat the process on each row in turn until all elements below the diagonal are zero.

Due to the large number of zero elements in the symmetric stiffness matrix, a bandwidth method can be applied to the iterative calculation for computational efficiency. Figure 3-2 shows the nonzero elements of a banded matrix used in Gauss elimination, where only the banded interval needs to be stored and only the active triangle shown in Figure 3-2 needs to be updated when a particular row is pivotal. This method will be introduced in section 4.2.3, with the code in Appendix A. The diagonal elements of \mathbf{K}^Δ are arranged in order and the sign count $s\{\mathbf{K}\}$ of the matrix \mathbf{K} is equal to the number of negative elements. To avoid missing values when one or more of diagonal elements is exactly zero, a slightly different value of frequency is chosen. The sign count of the characteristic values is used in the W-W algorithm.

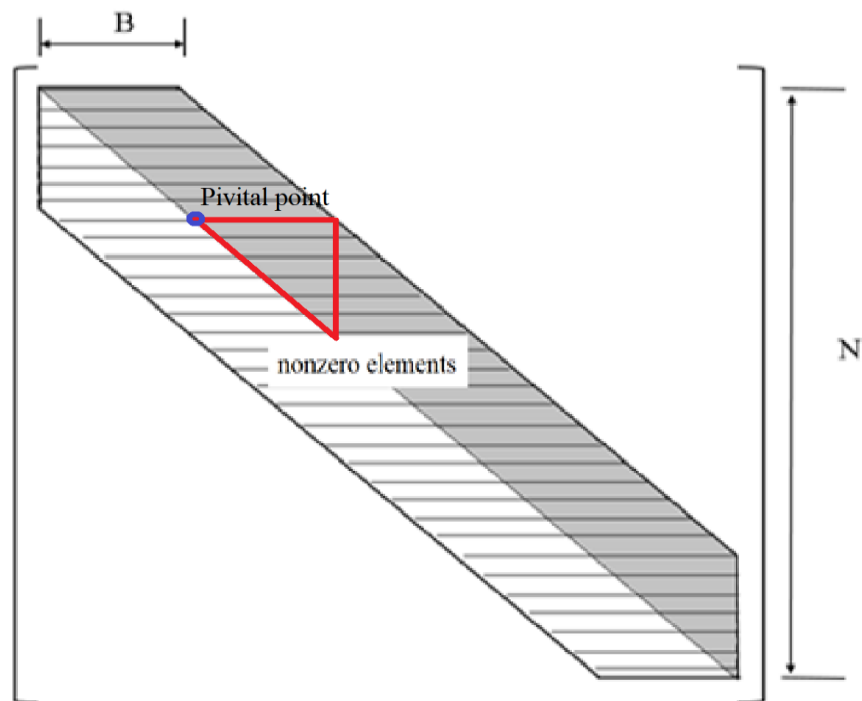


Figure 3-2 Banded matrix for Gauss elimination (Suliman 2018).

3.3.4 The basic algorithm

After the dynamic stiffness matrix is assembled and the sign count calculated, the core algorithm can be introduced. For a general case, $\mathbf{K}(\omega)$ is a $N * N$ dynamic stiffness matrix associating a set of N degrees of freedom to a displacement vector \mathbf{D} . A new variable $J(\omega^*)$ is then introduced which expresses the number of natural frequencies of the structure below any chosen frequency ω^* . If $J_0(\omega^*)$ represents the number of fixed end natural frequencies below the chosen natural frequency ω^* which make all displacements \mathbf{D} to zero (Wittrick and Williams 1971), then the basic algorithm can then be written as:

$$J(\omega^*) = J_0(\omega^*) + s\{\mathbf{K}(\omega^*)\} \quad \text{Eq. 3-18}$$

It should be noted that fundamental vibration modes are easier to compute. This study only considers the first six natural frequencies, for which $J_0(\omega^*)$ remains zero. Thus, the calculation of $J_0(\omega^*)$ will not be performed in this study. The modified W-W algorithm used when the clamped-clamped frequencies of individual modes are not exceeded by the trial frequency ω^* . Therefore, the modified algorithm is:

$$J(\omega^*) = s\{\mathbf{K}(\omega^*)\} \quad \text{Eq. 3-19}$$

Based on Eq. 3-19, Wittrick and Williams (1971) chose the same procedure as Gupta (1969) (re-calculating and triangulating $\mathbf{K}(\omega^*)$ for a sequence of trial values ω^*) to converge on the desired natural frequencies.

In this section, an efficient and versatile algorithm has been introduced for both finite and infinite system. The algorithm gives a fast and accurate solution for the transcendental eigenvalue problem without missing any natural frequencies even when the system contains a number of identical sub-structures (Wittrick and Williams 1971). Wittrick and Williams (1973) also extended the algorithm to be used in the calculation of buckling loads. The W-W algorithm can be applied to count the number of critical buckling loads below any chosen trial load to any desired accuracy. For this study, the eigenvalues (natural frequencies) and eigenvectors (mode shapes) need to be obtained for the direct problem. The natural frequencies will be found using the W-W algorithm and the mode shapes will be obtained by a subsequent solution of Eq. 3-11 with a random force vector (Hopper and Williams 1977). Detailed code is attached in Appendix C.

3.4 Lagrangian Multipliers

The W-W algorithm introduced in Section 3.3 has been developed extensively to obtain the natural frequencies or critical load parameters of an increasing range of geometries, load and boundary conditions. One of the most important developments introduced by Williams and Anderson (1983) extended the W-W algorithm using Lagrangian Multipliers. This extended algorithm enabled the coupling of component structures connected to each other which could then be calculated as a single structure. It also enabled the coupling of different wavelengths of sinusoidal response to satisfy the desired boundary conditions for anisotropic and shear loaded plate assemblies (Williams and Anderson 1983). Whilst retaining the generality and capability of the previous algorithm this extension can be applied to more complicated cases such as plates attached to beam-type transverse supports (Figure 3-3).

To introduce the basic concept of using Lagrangian Multipliers in the ESM and in the VICONOPT software, suppose j^* independent structures are connected at a number of discrete points. If the equation for the j^{*th} structure is denoted by the subscript j^* , Eq. 3-11 can be written as (Williams and Anderson 1983):

$$\mathbf{K}_{j^*} * \mathbf{D}_{j^*} = \mathbf{P}_{j^*}, \quad (j^* = 1, 2, \dots, j^{*'}) \quad \text{Eq. 3-20}$$

where \mathbf{P}_{j^*} is not null because of the connections between the independent structures. The constraint equation denoting the connections between the degrees of freedom of the structures can be represented by (Williams and Anderson 1983):

$$\sum_{j^*=1}^{j^{*'}} \mathbf{E}_{j^*} \mathbf{D}_{j^*} = 0 \quad \text{Eq. 3-21}$$

Eq. 3-21 is a general formulation that could denote any linear combination of any degrees of freedom of the whole system. Assume the total energy of the $j^{*'}$ components including the inertia effects of vibration problems is V .

$$V = \sum_{j^*=1}^{j^{*'}} \frac{1}{2} \mathbf{D}_{j^*}^t \mathbf{K}_{j^*} \mathbf{D}_{j^*} + \mathbf{P}_L^t \sum_{j^*=1}^{j^{*'}} \mathbf{E}_{j^*} \mathbf{D}_{j^*} \quad \text{Eq. 3-22}$$

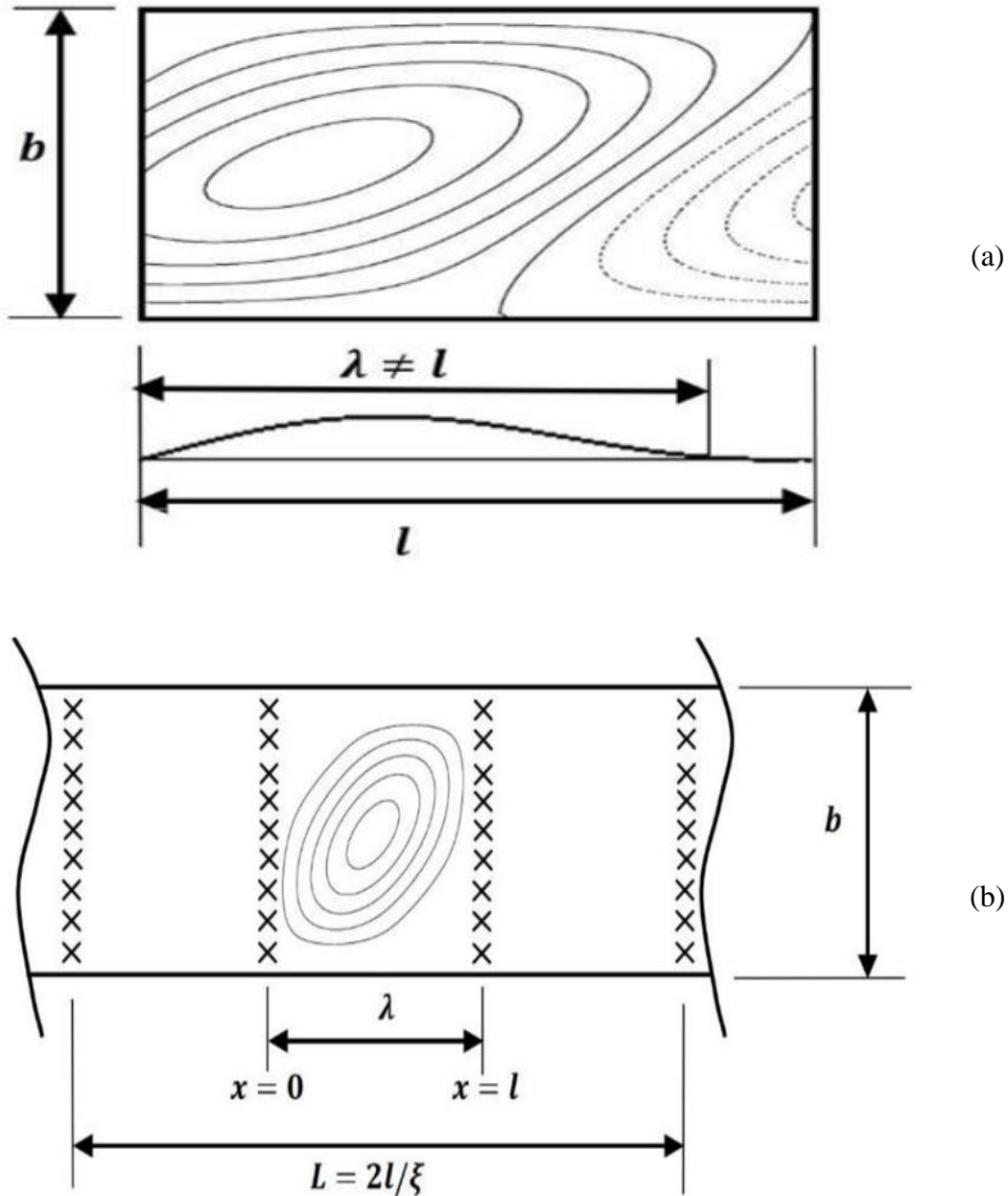


Figure 3-3 Comparison of mode shapes when Lagrangian Multipliers are included and not included in an analysis.

(a) without Lagrangian Multipliers; (b) including Lagrangian Multipliers for analysis of an infinitely long structure, where the λ is a typical half-wavelength, L is the length over which the mode shape repeats, l is the plate length, and ξ ($0 \leq \xi \leq 1$) is given as: $\xi = 2n/M$ where n and M are integers (Zhang 2018).

where \mathbf{P}_L is a vector of Lagrangian Multipliers and superscript t expresses the transpose of a matrix. To minimise V , the partial derivatives of V with respect to the elements of the displacement vector are set to zero (Williams and Anderson 1983), giving

$$\mathbf{K}_{j^*} \mathbf{D}_{j^*} + \mathbf{E}_{j^*}^H \mathbf{P}_L = \mathbf{0}, (j^* = 1, 2, \dots, j^{*'}) \quad \text{Eq. 3-23}$$

where H denotes the Hermitian transpose of a matrix. The values in Eq. 3-20 to Eq. 3-23 can be obtained from Eq. 3-18. Using a simply supported plate as an example, the eigenvalue problem of Eq. 3-23 and Eq. 3-21 can be written as:

$$\begin{bmatrix} l\mathbf{K}_1 & \mathbf{0} & \mathbf{0} & \cdots & \mathbf{0} & \mathbf{E}_1^H \\ \mathbf{0} & l\mathbf{K}_2 & \mathbf{0} & \cdots & \mathbf{0} & \mathbf{E}_2^H \\ \mathbf{0} & \mathbf{0} & l\mathbf{K}_3 & \cdots & \mathbf{0} & \mathbf{E}_3^H \\ \vdots & \vdots & \vdots & \ddots & \vdots & \vdots \\ \mathbf{0} & \mathbf{0} & \mathbf{0} & \mathbf{0} & l\mathbf{K}_{j^*} & \mathbf{E}_{j^*}^H \\ \mathbf{E}_1 & \mathbf{E}_2 & \mathbf{E}_3 & \cdots & \mathbf{E}_{j^*} & -\epsilon\mathbf{I} \end{bmatrix} \begin{bmatrix} \mathbf{D}_1 \\ \mathbf{D}_2 \\ \mathbf{D}_3 \\ \vdots \\ \mathbf{D}_{j^*} \\ \mathbf{P}_L \end{bmatrix} = \begin{bmatrix} \mathbf{0} \\ \mathbf{0} \\ \mathbf{0} \\ \vdots \\ \mathbf{0} \\ \mathbf{0} \end{bmatrix} \quad \text{Eq. 3-24}$$

where l is the length of the plate, and the displacement and force variables \mathbf{D}_{j^*} and \mathbf{P}_{j^*} will be introduced in section 3.5. From Eq. 3-24, a small modification $-\epsilon\mathbf{I}$ is introduced which leads to a zero for the initial rigid connections to obtain the original Lagrangian Multiplier form (Williams and Anderson 1983). To solve the complex transcendental eigenvalue problem, the extended W-W algorithm is introduced with Lagrangian Multipliers:

$$J = \sum_{j^*=1}^{j^*} (J_{0j^*} + s\{\mathbf{K}_{j^*}\}) + s\{\mathbf{R}\} - r \quad \text{Eq. 3-25}$$

In Eq. 3-25, the first two items count the number of eigenvalues exceeded for each half-wavelength. $s\{\mathbf{R}\}$ is the sign count of the matrix which replaces $-\epsilon\mathbf{I}$ after partial triangulation of the preceding rows in Eq. 3-24, and r denotes the number of constraints. Whilst Eq. 3-25 gives the general form of the extended W-W algorithm, here it is simplified by omitting the J_{0j^*} terms since only the lowest natural frequencies are required.

Lagrangian Multipliers have been introduced in the form of the extended W-W algorithm and successfully applied in the VICONOPT software over the last four decades. In this study, the method used to model damaged plates combines ESM to model the intact part of the structure with FEM to model the damaged part. Hence the intact part needs to couple the stiffness matrices for different assumed wavelengths of sinusoidal response, subject to constraint conditions to equate displacements at the boundaries with the damaged part. The application of Lagrangian Multipliers to this type of problem uses complex arithmetic and will be explained in section 5.1.3.

3.5 VICONOPT

For the solution of the direct problem of damage detection in plate structures, FEM, FSM and DSM have been studied extensively by other researchers in the last few decades. In this work the use of the exact strip software VICONOPT to determine the effect of delaminations and cracks on the vibration behaviour of plates will be explored. In this section the VICONOPT software will be discussed.

The ESM and the W-W algorithm have been applied in the software VICONOPT to solve critical buckling or free vibration problems in isotropic or anisotropic prismatic plate components for many years. They were first incorporated into the VIPASA analysis software developed by Wittrick and Williams (1974). Extension of this code with the introduction of Lagrangian Multipliers (Williams and Anderson 1983) led to the development of VICON (Anderson. et al. 1983; Williams and Anderson 1985). Building on this, Williams et al. (1990) released VICONOPT (VIpasa with CONstraints and OPTimisation), a 23,000 line Fortran 77 computer program combining the advantages of VIPASA and VICON (Williams et al. 1991). The program was developed by Cardiff University in collaboration with NASA and British Aerospace (Williams et al. 1990) in order to study the behaviour of structures with cross sections such as those shown in Figure 3-4. VICONOPT can be used to determine critical buckling load factors or undamped natural frequencies of any prismatic structure comprising isotropic (Figure 3-4 (a)) or anisotropic plates loaded by any combination of in-plane longitudinal (N_L), transverse (N_T) and shear (N_S) load, see Figure 3-4 (b).

3.5.1 VIPASA

VIPASA, proposed by Wittrick and Williams (1974) is a program based on exact flat plate theory. The program determines the critical buckling load factors or natural frequencies of assemblies of thin prismatic plates using the W-W algorithm. It significantly reduces the computational time, data preparation and memory usage required to solve this type of problem (Williams et al. 1991) compared to finite element analysis. The modes of buckling or vibration are assumed to vary sinusoidally along the longitudinal direction x , either with the far ends simply supported or with the half-wavelength λ of the mode being much smaller than the overall length l of the structure (Wittrick and Williams 1974).

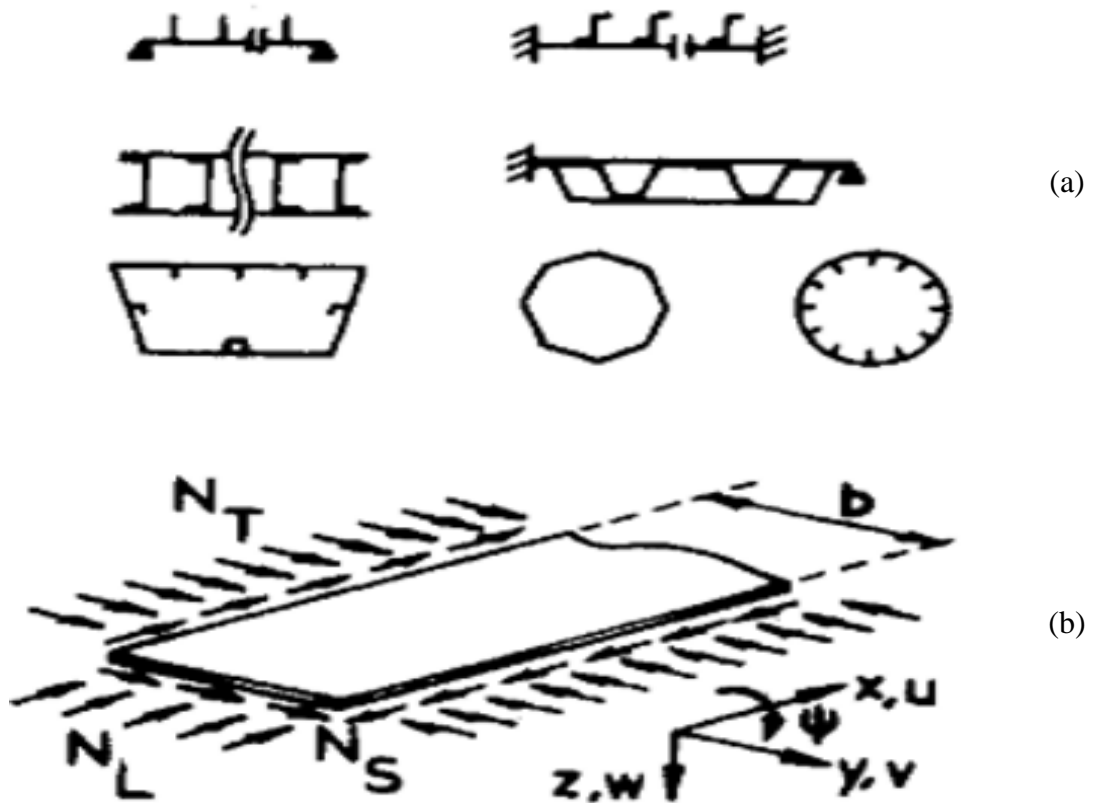


Figure 3-4 Plate assemblies in VICONOPT analysis (Williams et al. 1991).

(a) Cross-sections of typical plate assemblies and (b) loading conditions on an individual plate.

Figure 3-5 shows the perturbation edge forces and displacements, which vary according to $\exp(i\pi x/\lambda) * \cos(2\pi n t)$ where n is the frequency, $i = \sqrt{-1}$ and t is time (Wittrick and Williams 1974). If λ divides exactly into l , the sinusoidal variation enforce simply supported end conditions if the nodal lines run in the transverse direction y , but otherwise only approximate them (Figure 3-5). For isotropic and orthotropic plates the out-of-plane and in-plane behaviours are uncoupled (Wittrick and Williams 1974).

The force and displacement terms in general contain complex quantities, and there are phase differences between them (Wittrick and Williams 1974). As shown in Figure 3-5, each nodal line has four degrees of freedom, where u and v are the in-plane displacements in the x and y directions, respectively, W is the out-of-plane displacement and ψ is the rotation about the x -axis. The perturbation force vector \mathbf{p}_q and displacement vector \mathbf{d}_q are defined at edge q ($q = 1$ or 2) as:

$$\mathbf{p}_q = \{m_q \ p_{zq} \ p_{yq} \ p_{xq}\}$$

$$\mathbf{d}_q = \{\psi_q \ w_q \ v_q \ u_q\}$$

Eq. 3-26

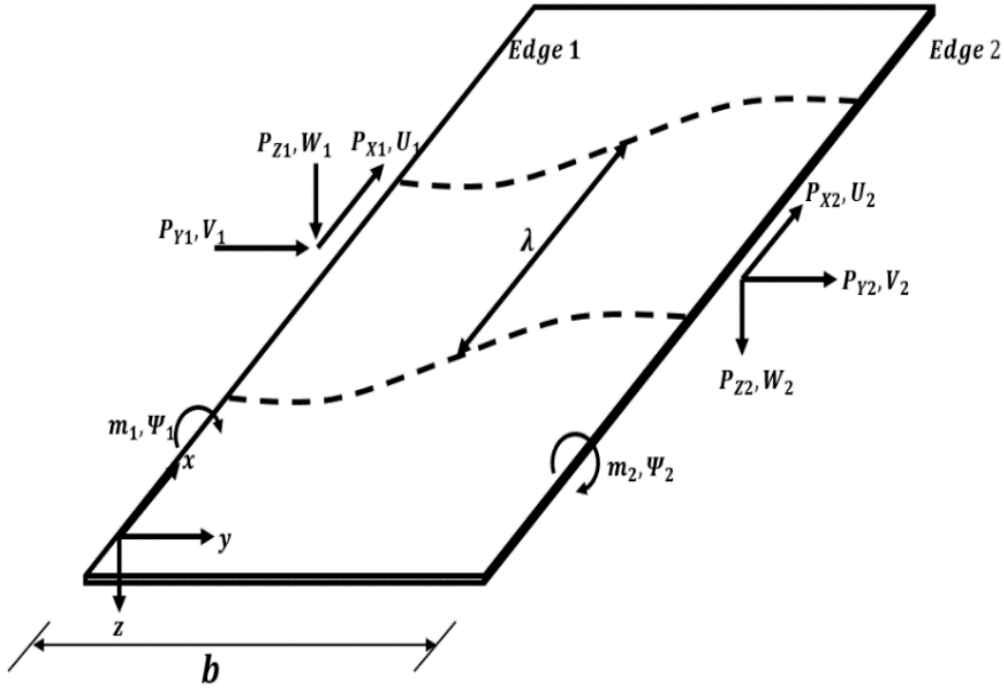


Figure 3-5 A component plate showing the edge forces, displacements, and nodal lines (Wittrick and Williams 1974).

These are related by stiffness matrices \mathbf{k}_{ij} as follows:

$$\begin{aligned} \mathbf{p}_1 &= \mathbf{k}_{11} \mathbf{d}_1 + \mathbf{k}_{12} \mathbf{d}_2 \\ \mathbf{p}_2 &= \mathbf{k}_{21} \mathbf{d}_1 + \mathbf{k}_{22} \mathbf{d}_2 \end{aligned} \quad \text{Eq. 3-27}$$

which can be simplified to:

$$\mathbf{p} = \mathbf{k} * \mathbf{d} \quad \text{Eq. 3-28}$$

For the uncoupled systems, the elastic properties are defined individually by the following two equations:

$$\text{Out-of-plane: } \begin{bmatrix} m_x \\ m_y \\ m_{xy} \end{bmatrix} = - \begin{bmatrix} D_{11} & D_{12} & D_{13} \\ D_{12} & D_{22} & D_{23} \\ D_{13} & D_{23} & D_{33} \end{bmatrix} \begin{bmatrix} \kappa_x \\ \kappa_y \\ 2\kappa_{xy} \end{bmatrix} \quad \text{Eq. 3-29}$$

$$\text{In-plane: } \begin{bmatrix} n_x \\ n_y \\ n_{xy} \end{bmatrix} = \begin{bmatrix} A_{11} & A_{12} & 0 \\ A_{12} & A_{22} & 0 \\ 0 & 0 & A_{33} \end{bmatrix} \begin{bmatrix} \epsilon_x \\ \epsilon_y \\ \gamma_{xy} \end{bmatrix} \quad \text{Eq. 3-30}$$

Eq. 3-29 and Eq. 3-30 define the elastic properties of these two systems, where m_x , m_y , m_{xy} are the bending and twisting moments per unit length; n_x , n_y , n_{xy} are the membrane forces per unit length; κ_x , κ_y , κ_{xy} are the curvatures and twist and ϵ_x , ϵ_y , γ_{xy} are the membrane strains (Wittrick and Williams 1974). \mathbf{D} and \mathbf{A} are the out-of-plane bending

and membrane stiffness matrices respectively. A comparison between VIPASA and two other codes (Smith's (1968) program and BUCLASP2 (Viswanathan et al. 1973)) is given in Table 3-2. The main advantage of VIPASA is its computational speed which is 1100 times faster than FEM with less than 1% error (Butler and Williams 1992).

3.5.2 VICON analysis

VIPASA provides faster solutions, efficient data preparation and less computer memory usage than other techniques in the preliminary design stage (Wittrick and Williams 1974). However, when considering shear loading or anisotropic materials it lacks accuracy. VICON (VIPASA with Constraints) is an extended version of VIPASA which uses Lagrangian Multipliers to solve problems with shear loading or anisotropy more accurately by coupling responses from sets of half-wavelengths λ as shown in Figure 3-3. It models an infinitely long plate assembly, applying constraints in the form of repetitive point supports at longitudinal intervals of the panel length l to create the desired boundary conditions. The eigenvalues of the transcendental stiffness matrix obtained by solving the governing differential equations are found using the modified W-W algorithm (Williams and Anderson 1983).

Table 3-2 Comparison between VIPASA and earlier programs, SMITH'S program and BUCLASP2 (Wittrick and Williams 1974).

VIPASA	Smith (1968)	BUCLASP2 (Viswanathan et al. 1973)
Includes only flat plate elements	Includes flat plate and longitudinal beam elements	Includes both flat and curved plates, and longitudinal beam elements
Includes full anisotropy in bending but ignores coupling between bending and middle surface deformation of component plates	Assume only orthotropic bending properties and ignores coupling between bending and middle surface deformations	Assumes only orthotropic bending properties, but includes effect of coupling between bending and middle surface deformations
Includes shear as well as longitudinal and transverse direct stress in the component plates with limitations	Does not include shear in the component plates	Does not include shear in the component plates
Calculates any number of natural frequencies or critical buckling stresses	Calculates any number of natural frequencies or critical buckling stresses	Calculates the lowest critical buckling stress only

The displacement vectors of the plate assemblies \mathbf{D}_A are written as a complete complex Fourier series (Anderson. et al. 1983):

$$\mathbf{D}_A = \sum_{m=-\infty}^{\infty} \mathbf{D}_m \exp(i\pi x/\lambda_m) \quad \text{Eq. 3-31}$$

where \mathbf{D}_m are complex displacement amplitude vectors of the plate assembly for half-wavelength λ_m and i is the imaginary number which was defined in section 3.5.1. Hence, the structural parameters of the component are described in the region $0 \leq x < l$. The required λ_m are defined by the series:

$$\lambda_m = \frac{l}{\xi + 2m}, \quad (0 \leq \xi \leq 1; m = 0, \pm 1, \pm 2, \dots, \pm q) \quad \text{Eq. 3-32}$$

When m takes a negative value, λ_m contributes the same as the positive value but the mode shape has a 180° phase difference. The structure is simulated as infinite with a mode shape repeating at intervals of L as shown in Figure 3-3. The perturbation forces \mathbf{P}_A can be expressed similarly as:

$$\mathbf{P}_A = \sum_{m=-\infty}^{\infty} \mathbf{K}_m \mathbf{D}_m \exp(i\pi x/\lambda_m) \quad \text{Eq. 3-33}$$

where \mathbf{K}_m is the VIPASA stiffness matrix corresponding to the half-wavelength λ_m . Further detail regarding \mathbf{K}_m will be given in section 5.2.4. Hence, by minimising the energy function in Eq. 3-22, the VICON stiffness matrix containing the \mathbf{K}_m of each half-wavelength with corresponding \mathbf{D}_m , \mathbf{P}_m and Lagrangian Multipliers \mathbf{P}_L are defined as in Eq. 3-24. Then, the stiffness matrix of Eq. 3-24 can be simplified as:

$$\mathbf{K}_{VICON} = \begin{bmatrix} \mathbf{K}_{GlobalVIPASA} & \mathbf{C}^H \\ \mathbf{C} & -\epsilon \mathbf{I} \end{bmatrix} \quad \text{Eq. 3-34}$$

where $\mathbf{K}_{GlobalVIPASA}$ contains stiffness terms and \mathbf{C} contains constraint terms. \mathbf{K}_{VICON} can then be transformed by Gauss elimination into an upper triangular complex transcendental matrix and the eigenvalue problem solved using the modified W-W algorithm. By introducing Lagrangian Multipliers VICON thus overcomes the insufficiency for complicated structure assemblies or loading conditions while retaining all the advantages of VIPASA. Further development and applications related to VICON have been proposed by Wittrick and Horsington (1984) with the combination of the Rayleigh-Ritz method to handle folded structures of finite length in coupled shear and compression conditions.

3.5.3 VICONOPT

VICONOPT (VIpasa with CONstraints and OPTimization) incorporates both VICON and VIPASA. This software is used in the analysis and optimum design of structures in the aerospace industry, calculating critical buckling load factors and undamped natural frequencies. As well as the limitation of the classical plate theory, Anderson and Kennedy (1993) demonstrated its application of first order shear deformation theory.

For optimum design, VICONOPT includes features from PASCO (Stroud and Anderson 1980), reducing the mass of a structure subject to initial buckling, strength, stiffness and geometric constraints (Kennedy and Featherston 2010). Butler and Williams (1992) introduced a sizing strategy based on the linear optimiser COMIN (Vanderplaats and Moses 1973). The optimisation process is shown in Figure 3-6, which promises a just feasible solution at each stage. As well as the sizing strategy mentioned above, other types of optimisation incorporated into VICONOPT over the last 20 years have included discrete optimisation (Kennedy et al. 1999), discontinuous cost function optimisation (Kennedy et al. 1999), vibration constraint optimisation (Kennedy et al. 1999) and multi-level optimisation in combination with MSC/NASTRAN (Fischer et al. 2002).

VICONOPT was evaluated by the team at Cardiff University and the Group for Aeronautical Research and Technology in Europe (Harris 2001). Subsequent developments include (Kennedy et al. 2007):

1. Postbuckling analysis in which non-linear stress distributions are simulated by strips with different stresses and each loading level converges simultaneously at consistent values;
2. The prediction of mode jumping;
3. The provision of discrete design capability;
4. Discontinuous cost functions;
5. Optimization with vibration constraints;
6. Response surface applications.

However, it is the efficiency of the VICONOPT software rather than its optimisation ability which is important to the work in this thesis. Williams et al. (1991) found for the analysis of a composite blade stiffened panel, compared with STAGS FEM program, VICONOPT could run 1000 times faster with 1% difference in results when $N_s = 0$. Further improvement in efficiency can be gained through exact multi-level substructuring (Wittrick and Williams 1974), whilst Williams and Anderson (1985) presented an efficient infinitely wide model of transversely repetitive components.

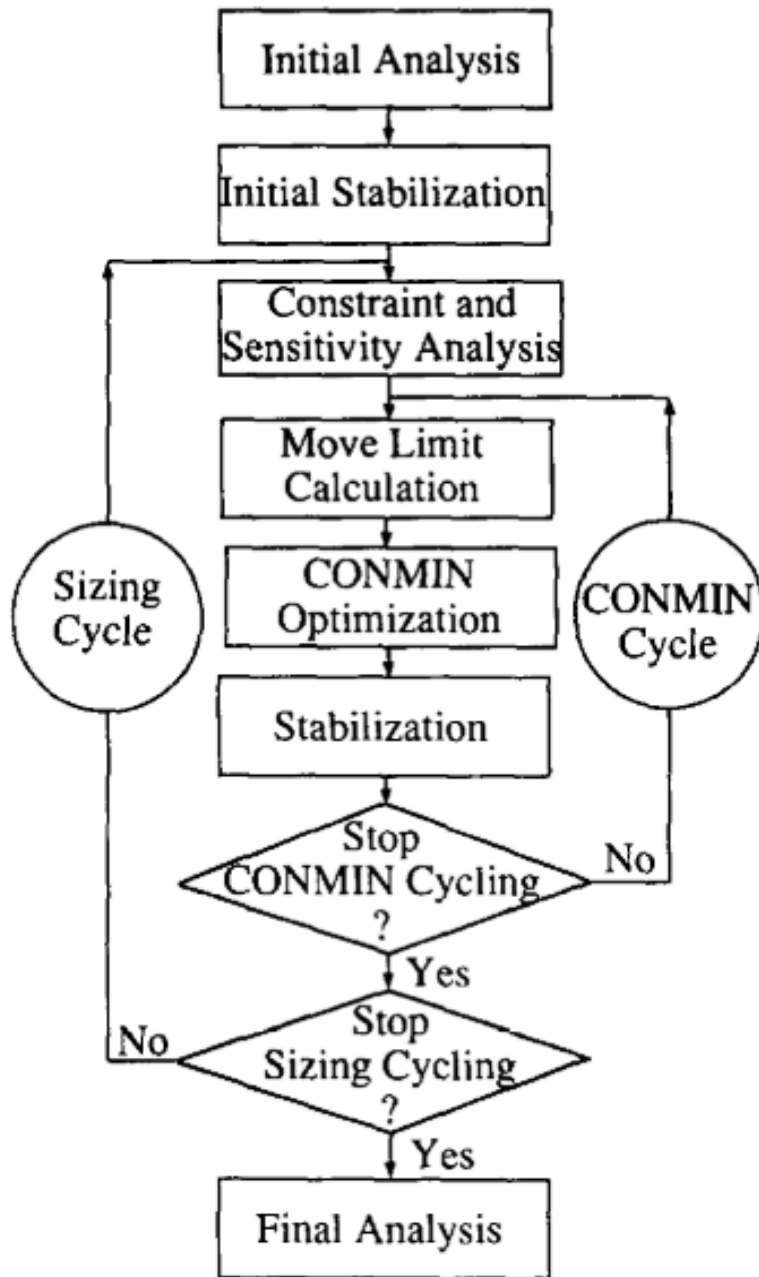


Figure 3-6 VICONOPT optimisation process (Butler and Williams 1992).

3.6 Conclusions

ESM and the related software VICONOPT provide efficient, accurate analysis and optimum design capability that has been developed for aerospace structures since the 1960s. The component plates can be isotropic or anisotropic. VICONOPT contains two main options: VIPASA analysis, in which the mode is assumed to vary sinusoidally in the longitudinal direction, can be used to derive solutions for simply supported isotropic or orthotropic components without shear loading (Kennedy et al. 2007); and VICON analysis, in which shear loading or anisotropic material, can be handled by coupling modes using Lagrangian Multipliers and implementing approximate end conditions (Kennedy et al. 2007). Whilst the software can analyse prismatic structural assemblies, it lacks some versatility for more complicated cases like three-dimensional structures with complex external loading or damage. Despite its limitations, VICONOPT is widely used in preliminary analysis and design in both industry and academia. Recently researchers have improved the versatility of VICONOPT, by coupling with FEM to model the damaged part of a structure, with ESM using Lagrangian Multipliers to take advantage of the benefits of both techniques whilst overcoming their limitations. It is this work which will be explored in this thesis.

Chapter 4--- Data Analysis and Processing

4.1 Introduction

Previous chapters have introduced the motivation and background for the study. Before illustrating the modelling process (Chapters 5 and 6) and the analysis of the inverse problem (Chapter 7), Chapter 4 describes several methodologies which will be used.

In addition to the introduction of a hybrid model (Chapter 5) which balances accuracy, efficiency and versatility by combining ESM with the finite element method to model more complex structures such as those incorporating damage. A number of other data analysis and processing methods are used to significantly improve computational efficiency whilst ensuring accurate results.

The W-W algorithm which is critical to the ESM and can be applied in more general cases when incorporated with another methods like FEM, can determine all the natural undamped frequencies of vibration of any linearly elastic structure to any desired accuracy (Wittrick and Williams 1974). However, since in this study only the first few natural frequencies are needed, and a modified W-W algorithm is adopted which is sufficient to calculate the required natural frequencies of a simply supported isotropic square plate.

When combining ESM with FEM in the new hybrid method, the computational time is hugely increased, especially the iteration procedure in the W-W algorithm. To counter this, a bandwidth method has been introduced in the data processing. Based on this, instead of carrying out calculations on the whole stiffness matrix, a partial banded matrix is used in the Gauss elimination.

When data obtained from the solution of the direct problem is prepared for the inverse problem. It is important that modes are correctly identified such that reductions in natural frequencies due to damage can be verified. To prevent mode sequencing problems during processing, an automatic mode shape sign method is presented to solve the problem.

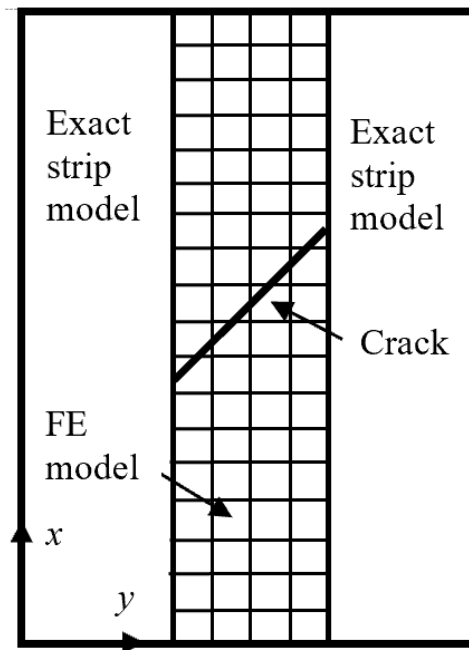


Figure 4-1 Hybrid cracked plate model (SSSS), coupling exact strip model and FE model.

4.2 Methodology

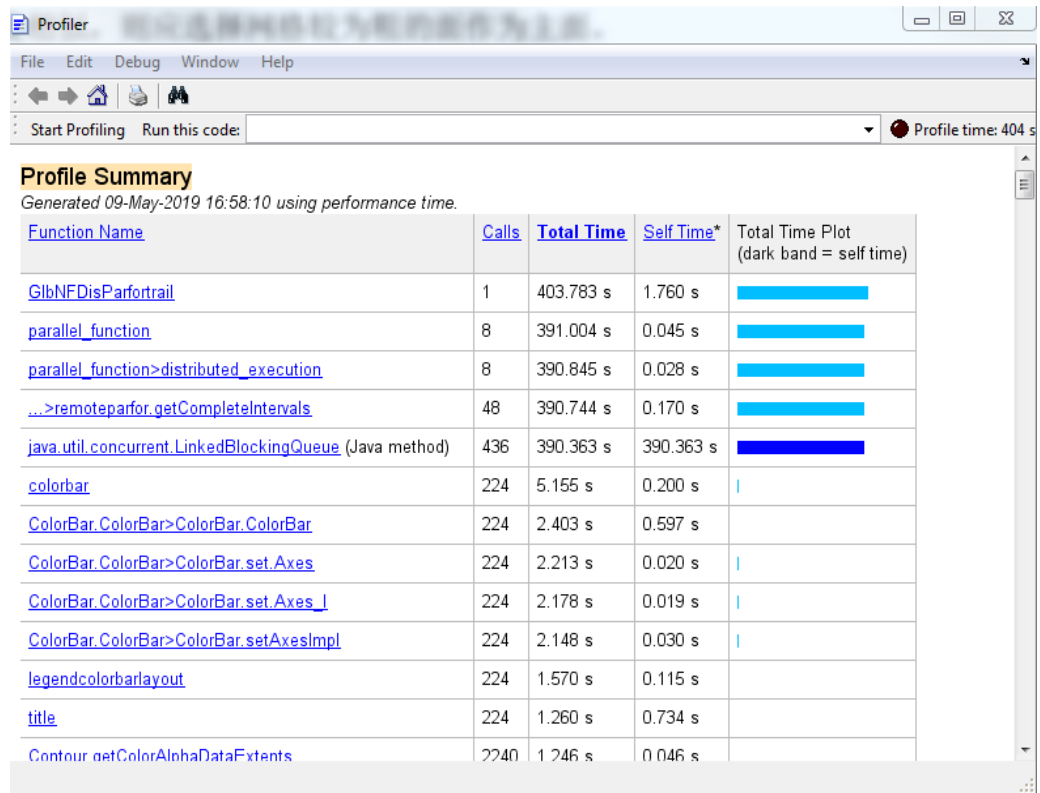
4.2.1 Modified Wittrick-Williams algorithm utilisation

The W-W algorithm is crucial to this study. The algorithm provides a methodology to obtain the natural frequencies of a structure under any trial value to any required accuracy. It can be used for any loading or boundary conditions for both isotropic and anisotropic plates and plate assemblies. In Chapter 3.3, the algorithm was introduced for both finite and infinite cases. In this research, the simplest case is studied, namely a simply supported isotropic square plate (SSSS). The results obtained from the direct problem are used for the inverse problem and only the first few natural frequencies are needed (Labib et al. 2014; Labib et al. 2015). In this study, the first six natural frequencies (Yang et al. 1985) are needed so the clamped end term J_0 does not come into play. Hence, the infinite system is simplified to a finite problem (Eq. 3-17 and Eq. 3-19). A method for performing a numerical vibration analysis using a modified W-W algorithm to obtain the related natural frequencies is illustrated later in this section.

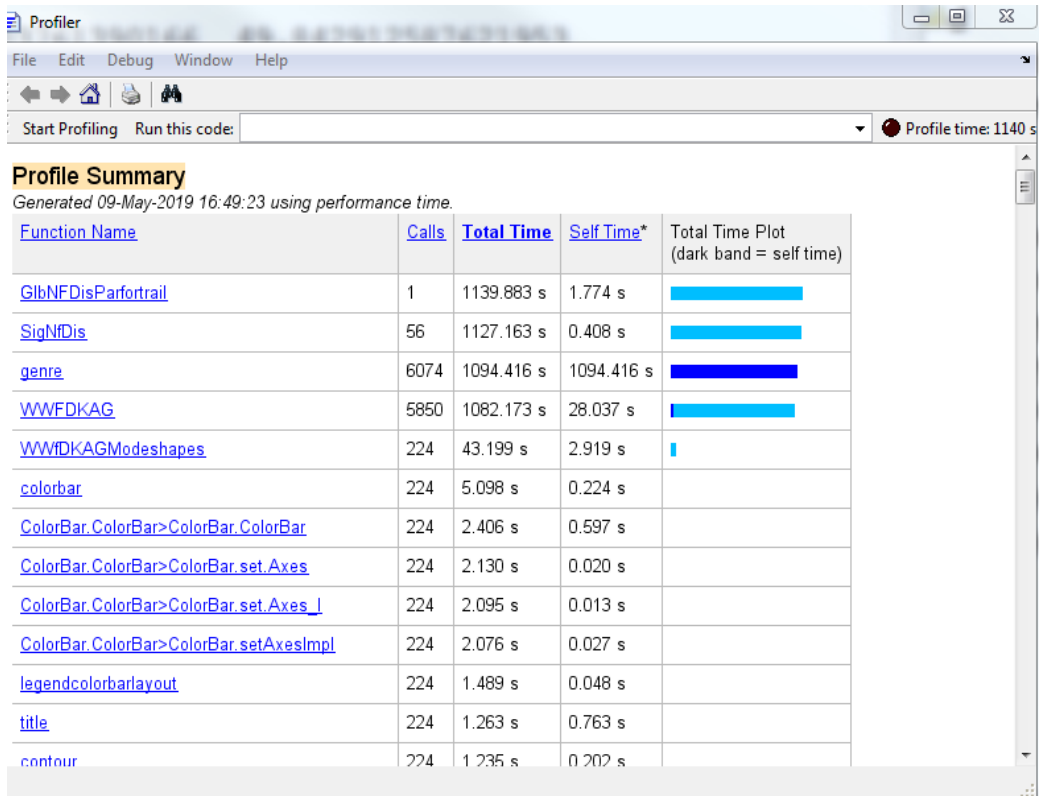
Use the arbitrary cracked plate in Figure 4-1 as an example to show the modified Wittrick-Williams algorithm calculation procedure. A brief diagram of the hybrid model cracked plate model is shown here, and details of the model will be explained thoroughly in section 5.2.4. The calculation of the required natural frequencies starts with assembling them in ascending order of modes. For the lowest mode r , a trial value ω is given. To

calculate the sign count J , the stiffness matrix for the ESM (Eq. 3-24) and FE (section 5.2.2) parts are obtained. Apply the banded Gauss elimination (section 4.2.3) procedure on the global stiffness matrix of hybrid VFM, an upper triangular matrix is obtained, and the sign count J is obtained by counting the number of negative elements on its leading diagonal. If $J \geq r$, an upper bound on mode r has been found. Otherwise, a lower bound has been found. In this case, the trial value ω is doubled and the process repeated until $J \geq r$. Once lower and upper bounds have been found, the bisection method is introduced to achieve the desired convergence. At each iteration, the mid-point between the closest lower and upper bounds is selected as the new trial value ω , and then the new sign count is calculated. The new interval is dependent on the comparison of J and r . The calculation is repeated until the difference between the limits reduces to the required tolerance; the final bisected value is chosen as the desired natural frequency for the mode r . For higher modes, the procedure is the same, using the previously obtained natural frequency as the first lower bound. Besides the bisection method, Williams and Kennedy (1988) proposed a multiple determinant parabolic interpolation method. This improves the efficiency for solving large transcendental eigenproblems. For a required relative accuracy of 10^{-4} for non-coincident eigenvalues, this approach can reduce the time by 31% over the bisection method. For higher levels of accuracy, more time could be saved. However, considering the simplicity of the examples in the present study and the speed of today's computers, the bisection method remains competitive.

The bisection iteration procedure is coded into MATLAB as shown in Appendix C. For a tolerance of 10^{-3} rad s⁻¹, based on the solution of 56 different crack cases (with different locations and lengths of crack) for a simply supported plate (Figure 4-1) while only using a pure finite element model with a 20*20 mesh, the total time (Figure 4-2 (a)) for calculating the first 4 natural frequencies was 403.783s run on a computer with an i7-4790K CPU @ 4.00GHz with 32GB RAM and 64-bit operating system. These results were obtained by running the problem within the Parfor function in MATLAB which can run different cracked plate cases simultaneously. This improves the calculation efficiency significantly when compared with the original case running without the function (Figure 4-2 (b)) which took 1139.883s. The parallel function (referred to in the Appendix D) in this case saves nearly 75% of the total time.



(a)



(b)

Figure 4-2 Time taken to run a simply support isotropic plate in MATLAB.
(a) FE model including the parfor code; (b) FE model with the original code.

4.2.2 Bandwidth method in W-W algorithm

Computational efficiency is one of the most important considerations in damage detection and the related forward problem due to the large number of iterations which need to be performed. ESM can significantly enhance the efficiency of modelling the effect of damage on the vibration characteristics of a structure by avoiding discretisation into elements, with the W-W algorithm providing exact solutions for the transcendental eigenvalue problem. However, related techniques such as those implemented in VICONOPT are only suitable for prismatic structures. For more complicated structures, it is still necessary to consider both efficiency and accuracy. For a cracked plate, the crack will break the prismatic status of the plate. Hence a hybrid method is introduced, and the computational time significantly increases even using a powerful computer. The Gauss elimination requires the greatest part of that computing time.

As mentioned in Chapter 3.3, the necessary Gauss elimination procedure can be regarded as a matrix transformation without row interchanges. As an example (Figure 4-3), consider an isotropic simply supported plate which contains a single arbitrary crack. In modelling the crack, the plate has been divided into three parts, two intact parts and one damaged part. Before introducing the crack, assume the intact parts of the model have 6 (line) nodes and 12 different half-wavelengths are used, and the damaged part has 400 elements in total (20*20). For the intact part, using ESM to establish the stiffness matrix, each node has 2 degrees of freedom for each half-wavelength. A 12*12 stiffness matrix is thus obtained for a single half-wavelength and the total size of ESM part is 144*144 for 12 different half-wavelengths. For the damaged part, FEM is used to set up the stiffness and mass matrix while each point has 3 degrees of freedom, where the size of stiffness matrix for FE is 1323*1323 (21 nodes in each direction, and $1323=3*21*21$). For the constraint, the matrix will be an $82*(1323+144)$ matrix (21 nodes per direction, two degrees of freedom for each node, and two of the edges of the FE part are taken into the calculation while ignoring the displacement degree of freedom of far end nodes. Hence, $82=21*2*2-2$). The complete stiffness matrix is thus 1549*1549 ($1549=1323+144+82$, which is the summation of all the degrees of freedom produced from the ESM, FEM and the constraint matrix) and includes many zero elements. As shown in Eq. 4-1, the majority of the complete global stiffness matrix elements are zero. Using the cracked plate as an example, if only the non-zero elements are considered when transforming the matrix using Gauss elimination, the computational cost will be around 1% compared with the calculation of the whole stiffness matrix 1549*1549 using the

formula given by Suliman (2018). Moreover, according to Suliman et al. (2019), the pure FEA analysis is about 4.25 times longer than hybrid VFM approach. This is a massive improvement in computational efficiency for the arbitrary damage case, and hence to achieve it an advanced bandwidth method is introduced as explained below.

4.2.2.1 Bandwidth methodology

For the complete stiffness matrix shown in Eq. 4-1, to use the W-W algorithm, a Gauss elimination needs to be performed to transform the matrix into an upper triangular matrix without row interchanges to count the negative sign count. Eq. 4-1 is deduced from Eq. 3-24 shown below:

$$\begin{bmatrix} l\mathbf{K}_1 & 0 & 0 & \cdots & 0 & 0 & \mathbf{E}_1^T \\ 0 & l\mathbf{K}_2 & 0 & \cdots & 0 & 0 & \mathbf{E}_2^T \\ 0 & 0 & l\mathbf{K}_3 & \cdots & 0 & 0 & \mathbf{E}_3^T \\ \vdots & \vdots & \vdots & \ddots & \vdots & \vdots & \vdots \\ 0 & 0 & 0 & 0 & l\mathbf{K}_{j^*} & 0 & \mathbf{E}_{j^*}^T \\ 0 & 0 & 0 & 0 & 0 & \mathbf{K}_f & \mathbf{E}_f^T \\ \mathbf{E}_1 & \mathbf{E}_2 & \mathbf{E}_3 & \cdots & \mathbf{E}_{j^*} & \mathbf{E}_f & \mathbf{R} \end{bmatrix} \begin{bmatrix} \mathbf{D}_1 \\ \mathbf{D}_2 \\ \mathbf{D}_3 \\ \vdots \\ \mathbf{D}_{j^*} \\ \mathbf{D}_f \\ \mathbf{P}_L \end{bmatrix} = \begin{bmatrix} \mathbf{P}_1 \\ \mathbf{P}_2 \\ \mathbf{P}_3 \\ \vdots \\ \mathbf{P}_{j^*} \\ \mathbf{P}_f \\ \mathbf{0} \end{bmatrix} \quad \text{Eq. 4-1}$$

where \mathbf{K}_j is the VIPASA stiffness matrix for different half-wavelengths λ_j ($j = 1, \dots, j^*$); \mathbf{K}_f is the finite element stiffness matrix ($\mathbf{K}_f = \mathbf{K} - \mathbf{M}(\omega^2)$); \mathbf{E}_j and \mathbf{E}_f are the constraint matrices for VIPASA and the finite element part; \mathbf{R} is initially a zero matrix but will change to have non-zero terms after Gauss elimination; T denotes the transpose; \mathbf{D}_j and \mathbf{D}_f which are the vectors of displacement for VIPASA and the finite element part; \mathbf{P}_L is the vector of Lagrangian Multipliers; \mathbf{P}_j and \mathbf{P}_f are the random force vectors.

VFM uses the W-W algorithm to count the number of negative leading diagonal elements of the upper triangular matrix obtained from the complete stiffness matrix. Only terms on and above the leading diagonal need to be stored and processed. During the Gauss elimination, consider the way to process the leading diagonal.

Assuming the global stiffness matrix is a $(n + r) * (n + r)$ matrix and choosing one of the main stiffness elements as an example. Here, triangulating $l\mathbf{K}_1$, the transformation has been described in Chapter 3.3. Each pivotal element of $l\mathbf{K}_1$ will be used to modify other elements in $l\mathbf{K}_1$; the pivotal element and related elements of $l\mathbf{K}_1$ and \mathbf{E}_1^T will be used to alter \mathbf{E}_1^T ; elements of \mathbf{E}_1^T will then used to modify \mathbf{R} . During the transformation of $l\mathbf{K}_1$ and \mathbf{E}_1^T , there are no changes to the rest of the stiffness matrices and constraint matrices. The same procedure is repeated for the remaining $l\mathbf{K}_j$ and \mathbf{E}_j^T , \mathbf{K}_f and \mathbf{E}_f^T . The

final process is the triangulation of \mathbf{R} that the pivotal elements of \mathbf{R} will be used to modify other elements in \mathbf{R} .

For the advanced bandwidth method used in the global stiffness matrix, related program codes have been attached in the Appendix A. It is helpful to store different components of the complete stiffness matrix separately as expressed in Eq. 4-1, and some information are shown below (Figure 4-3):

1. $l\mathbf{K}_j$ are small, symmetric, banded VIPASA matrices with different half-wavelengths from the VICONOPT part of the model (all of them have the same size 12×12);
2. \mathbf{K}_f is a larger, symmetric, banded matrix from the FEM part (1323×1323);
3. \mathbf{E}_j^T are rectangular matrices from the constraint part (all have the same size 1×82) with initially only a few non-zero elements, but further non-zero terms will appear during Gauss elimination. During the transformation of \mathbf{E}_j^T , one may allow for the bandwidth method, but this is tricky to deal with;
4. \mathbf{E}_f^T is a larger rectangular constraint matrix (1323×82), with the same number of columns as \mathbf{E}_j^T but with more rows;
5. \mathbf{R} is a symmetric square matrix (82×82). Its terms are initially all zero but non-zero terms will appear during the Gauss elimination. It becomes dense and cannot be allowed for the bandwidth method, so this part of the assessment of Gauss elimination could cost a long time if many constraints exist in the structure.

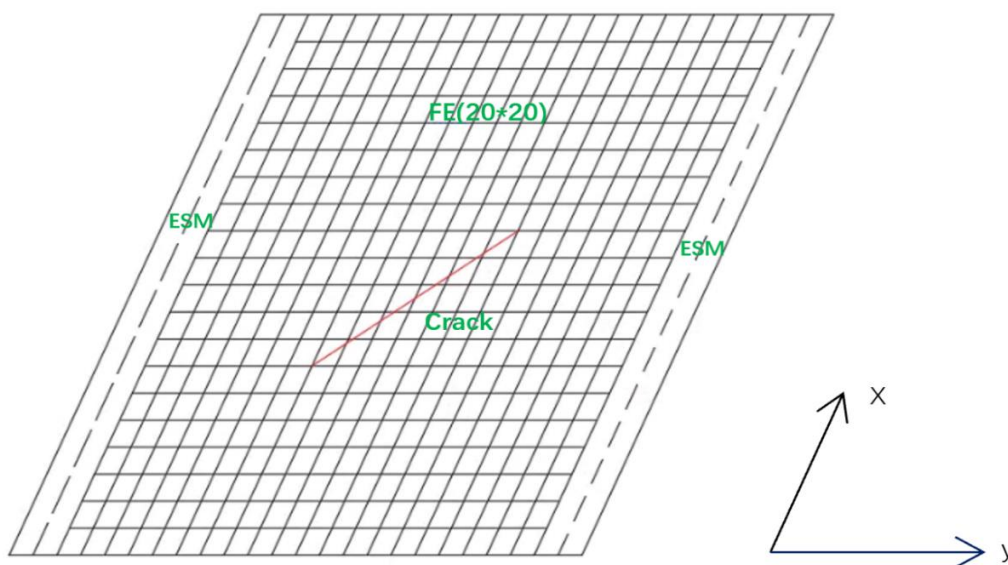


Figure 4-3 Hybrid model used in bandwidth method illustration.

The advanced bandwidth method is the primary technique which can improve computational efficiency significantly. Besides the method, because the forward problem needs to prepare data for cracks with different locations and severity, a parallel computation method could be considered in the study mentioned in section 4.2.1.

4.2.3 Automatic mode shape sign method

As described in the introduction, it is important, in determining the effect of damage, which is characterised by changes in natural frequencies and mode shape, to ensure frequency comparison and mode normalisation are performed using data corresponding to the same mode shape.

For example (Figure 4-4) for a ‘parallel crack’ (a crack arbitrarily located in the plate and parallel to one side), as the crack is moved parallel to one of the axes, and the length/depth are changed, the vibration characteristics (natural frequencies and mode shapes) will change, and the data obtained will contain many results obtained from different cases. A mode sequencing problem can occur when changing the location of the crack or increasing the severity of the crack, the natural frequencies of a higher-order mode swap over with those of a low-order mode. This plate problem is illustrated in Chapter 6 which shown in Figure 6-20 and Figure 6-21 including the characteristics including natural frequencies and mode shapes are shown for a plate having cracks located in different positions and having differing severity (length). The mode sequence is based on the intact plate. For Figure 4-4 (a) and (b), crack location $x=0.01$, the zero-contour line divides the plate into two parts in two directions. When moving the crack to location $x=0.04$ (Figure 4-4 (c) and (d)), zero-contour lines separate the plots into two parts in the opposite direction compared to $x=0.01$. However, at the same crack location $x=0.04$, when the crack length is increased from $l=0.01$ to $l=0.08$ (Figure 4-4 (e) and (f)), the zero-contour line changes to a third direction. If using the mode plot of the intact plate as a reference datum, for adjacent modes like mode 2 and mode 3, it is hard to recognise the sequence of modes from the natural frequency results or the contour plots of the mode shapes. However, in the damage detection problem, researchers need to use corresponding modes prior to and following the onset of damage to normalise data and find the crack location (section 7.3). It is important therefore to be able to sort the modes into the correct order. The development of a method to solve the sequencing problem is therefore essential for successful damage detection.

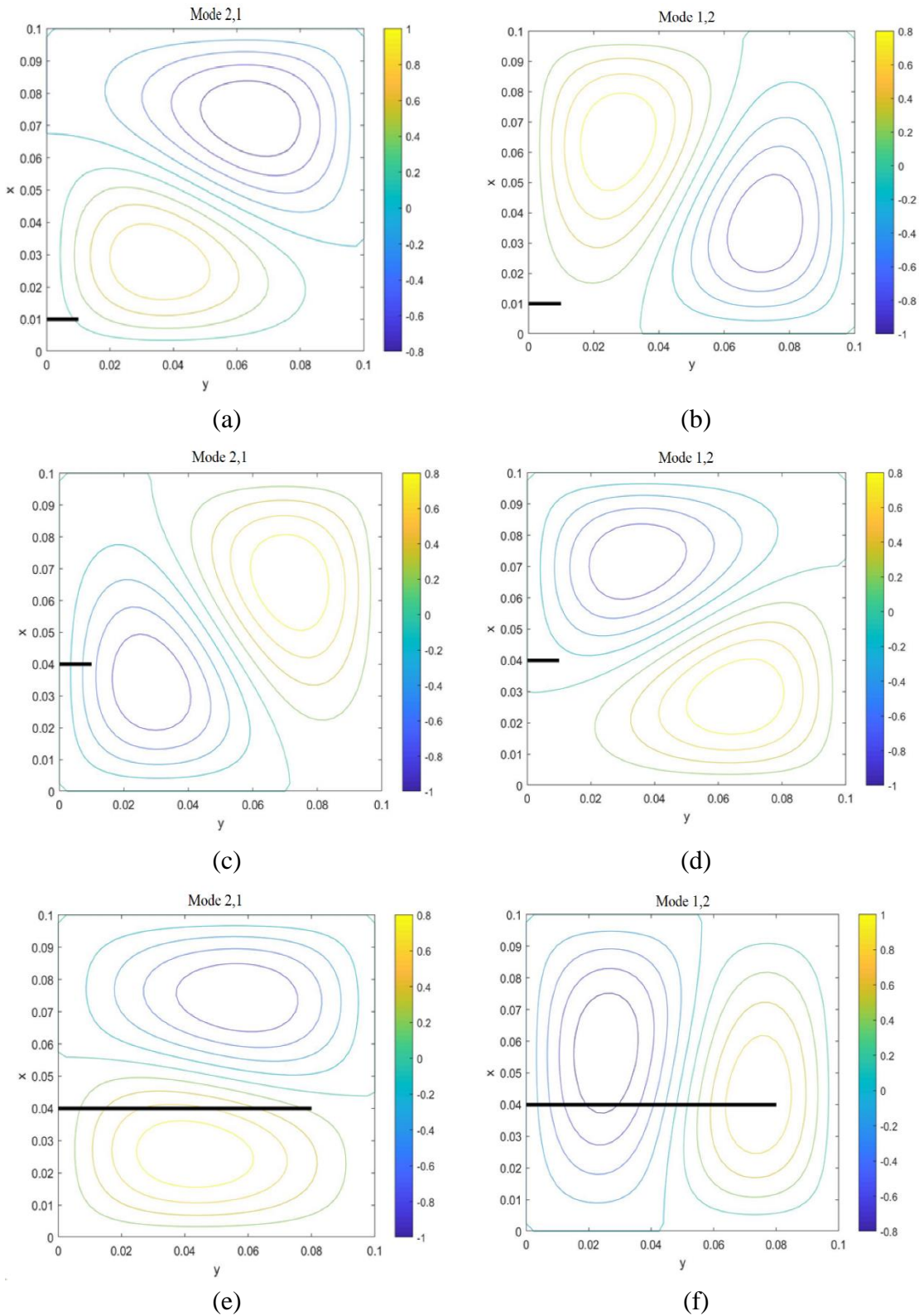


Figure 4-4 Mode shape for an isotropic simply supported cracked plate with different crack location and different crack severity, **—** crack.

(a) crack location $x=0.01$, crack length $l=0.01$, mode number $r=2$; (b) crack location $x=0.01$, crack length $l=0.01$, mode number $r=3$; (c) crack location $x=0.04$, crack length $l=0.01$, mode number $r=2$; (d) crack location $x=0.04$, crack length $l=0.01$, mode number $r=3$; (e) crack location $x=0.04$, crack length $l=0.08$, mode number $r=2$; (f) crack location $x=0.04$, crack length $l=0.08$, mode number $r=3$.

4.2.3.1 Automatic mode shape sign methodology

To ensure the correct mode is assigned to a particular natural frequency, a damaged plate model is first established. The W-W algorithm is then used to obtain the related natural frequencies, by default in ascending order. Then the obtained natural frequencies are substituted into the complete stiffness matrix and the modal displacements are found by solving the stiffness equations with a random force vector (Hopper and Williams 1977) on the right-hand side. A set of displacements is obtained with the default order. It is notable that, for a single cracked plate for example, when slightly moving the crack or increasing its severity (e.g. its depth or length), the mode shape will be similar for the cross-reference. The difference in the vertical displacements is then used as a reference variable to sort modes. Before sequencing the mode, a reference standard needs to be confirmed. In this example using a crack location as the standard, means that the next mode sequence of the longer crack length is based on the previous model with a smaller crack length at the same crack location.

As an illustration, for the crack starting point of Figure 4-4, the mode shape of the intact plate is used as the first reference standard. For case 1: $x = 0.01, l = 0.01, r = 1$, the vertical displacements of example 1 are subtracted from those of the intact plate from the same default order of modes and add the absolute value of the differences. Extracting the minimum value from the above two data sets in terms of d_1 , repeat the same procedure for the next default order $r = 2$ with the intact plate mode $r = 1$ and the obtained minimum value d_2 . Comparing the minimum values from the two calculation, if $d_1 < d_2$, the order of natural frequency and mode shape keeps the same sequence as default. Otherwise, the order is changed.

The actual value of displacement now settles down for case 1 and becomes the standard for case 2: $x = 0.01, l = 0.01, r = 2$. Iteration 1 is stopped when the mode number meets the requirement. For the next iteration 2, case 3: $x = 0.01, l = 0.02$ and $r = 1$, case 1 will be chosen as the first reference standard and the same procedure repeated as for the previous iteration until the crack length reaches its final value. Hence, a group of data where $x = 0.01, l = (0.01 \text{ to required value}), r = (1 \text{ to required modes})$ are obtained and are in the right order. Using the vertical displacement of $x = 0.01, l = 0.01$ and $r = (1 \text{ to required modes})$ as the first reference for case 4: $x = 0.02, l = 0.01$ and $r = (1 \text{ to required modes})$, the same calculation procedure is repeated as for iteration 1 and iteration 2. The iterations will stop when all parameters meet the desired values.

Table 4-1 Normalised nodal displacements for two hypothetical crack cases.

Crack cases	Node	Mode 1	Mode 2
Case 1	Node 1	1	0.7
	Node 2	0.8	0.9
	Node 3	0.6	1
Case 2	Node 1	0.65	1
	Node 2	0.85	0.85
	Node 3	1	0.65

This iteration procedure has been programmed into MATLAB and is attached in the Appendix B. Table 4-1 will use two hypothetical crack cases with assumed normalised displacement data to show the basic procedure described above which is called the mode shape sign method.

Case 1 and Case 2 in Table 4-1 represent a crack occurring in the same plate structure with different locations or lengths, based on the normalised displacement results obtained by the mode shape calculation (section 5.3) at different nodes. The sequence of modes defined in case 1 is used as the reference, the recorded sequence of modes for case 2 needs to be determined by the mentioned method. Using $(case2, mode1)$ with $(case1, mode1/mode2)$ to determine the first mode sequence of case 2. The summation of the difference in nodal displacements for those cases are:

1. Compare $(case2, mode1)$ with $(case1, mode1)$

$$|0.65 - 1| + |0.85 - 0.8| + |1 - 0.6| = 0.8$$

2. Compare $(case2, mode1)$ with $(case1, mode2)$

$$|0.65 - 0.7| + |0.85 - 0.9| + |1 - 1| = 0.1$$

The summation for these two comparisons, comparing the obtained summation: $0.1 < 0.8$. Hence, the assumed $(case2, mode1)$ should be recorded as $(case2, mode2)$. Again, for the assumed $(case2, mode2)$, a similar procedure is followed:

3. Compare $(case2, mode2)$ with $(case1, mode1)$

$$|1 - 1| + |0.85 - 0.8| + |0.65 - 0.6| = 0.1$$

4. Compare $(case2, mode2)$ with $(case1, mode2)$

$$|1 - 0.7| + |0.85 - 0.9| + |0.65 - 1| = 0.7$$

According to the above procedure, $(case2, mode2)$ matches $(case 1, mode1)$, which should be corrected to $(case2, mode1)$. Through the above iterations, all modes will comply with the right order, and corresponding vibration characteristics will be recorded correctly. It should be noted that a few modes still need to have their sequence adjusted manually. For example, when a crack runs from $(x, y) = (\alpha l, 0)$ to $(\alpha l, \beta l)$ where α is a location parameter in the range $0.1 \leq \alpha \leq 0.9$ and β is a length parameter in the range $0.2 \leq \beta \leq 0.8$. For the cracked plated cases shown in Figure 4-5, $\beta = 0.4$ and α is a location parameter in the range $0.1 \leq \alpha \leq 0.5$. The contour plots show a singularity when cracks occur at the middle of a square plate compared with other cases due to the way the crack is simulated, the geometry conditions and the crack location.

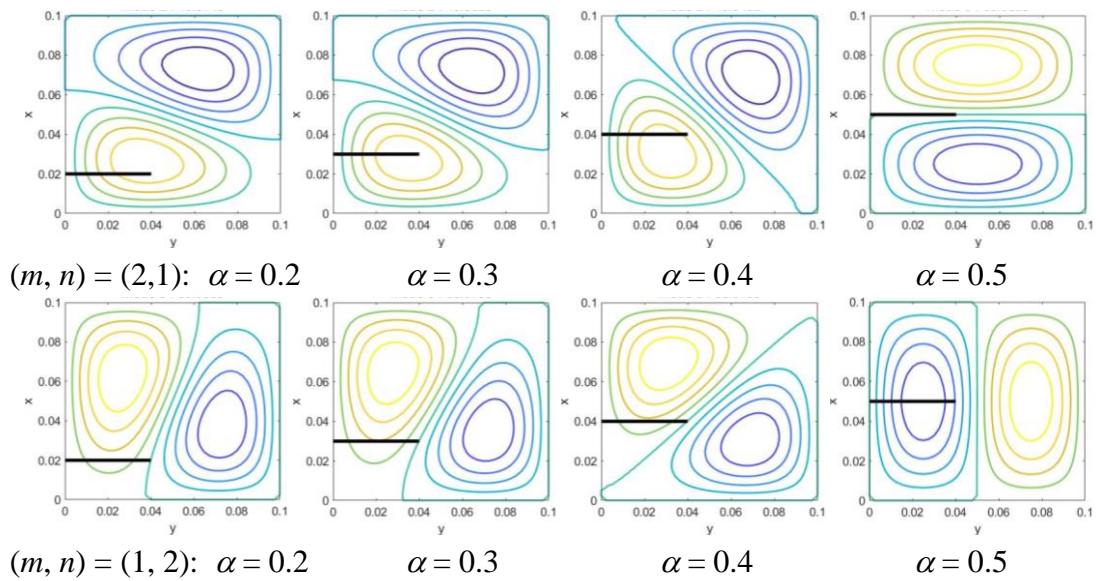


Figure 4-5 Variation of mode shapes with crack location α , for $\beta = 0.4$ (Luo et al. 2019), **—** crack.

4.3 Final Remarks

In this chapter, the W-W algorithm provides accurate solutions of the transcendental eigenvalue problem; an automatic mode shape sign method sorts modes to the right order; the bandwidth method significantly improves the computation behaviour in the iteration process. Besides those methodologies, other potential methods also could increase the speed of data processing, for example mentioned in section 4.2.1, parallel computation in MATLAB. In this study, MATLAB R2017A (MathWorks 2019) is used to program the hybrid cracked plate model. In the forward problem, a group of single cracked plate cases need to be analysed, and each case is independent. A parfor-loop in MATLAB processes a series of statements in the iteration calculation in parallel. A parfor-loop can provide significantly better behaviour than a for-loop because several MATLAB workers can calculate simultaneously on the same iteration. MATLAB works independently to compute iterations with no particular order, and if the number of workers is equal to the number of loop iterations, each worker can deal with one loop iteration simultaneously. For eight workers, the maximum performance could be 8 times faster than its analogous for-loop in MATLAB. For further efficiency improvements, a reasonable eigenvalue accuracy should be considered in the study which is generally no less than 0.0001.

Chapter 5--- Free Vibration Modelling of Plates

5.1 Introduction

The presence of cracks or delaminations in a plate element will change the nature of its structural mechanics and vibration characteristics as well as those of the structure in which it is assembled (Teughels et al. 2002; Escobar et al. 2005; Fang et al. 2005; Caddemi and Greco 2006; Danai et al. 2012 and Suliman 2018). A database of the effects of damage on natural frequencies and mode shapes needs to be prepared in order to solve the inverse problem of the damage detection based on the change of vibration characteristics. To this end, the forward problem of calculating the natural frequencies and mode shapes of an isotropic simply supported square plate with pre-existing cracks or delaminations is studied in this chapter.

As introduced in Chapter 2, a crack can be modelled as a rotational spring and is assumed to be always open. Any loss of mass at the crack is ignored. Hence, the problem is simplified to a linear problem. In this study, the crack will be arbitrarily located in the plate and have random severity; with the shear and axial stiffness remaining intact and the effects of structural damping ignored.

The crack will be utilized in a modified hybrid damaged model (VFM). For the theoretical derivation of the stiffness matrix, the FEM part is based on Przemieniecki (1985), while the ESM part is from Wittrick and Williams (1974). The W-W algorithm (Wittrick and Williams 1971) is applied to calculate the natural frequencies numerically using a MATLAB code (Appendix C).

An isotropic simply supported plate example is used to study the effect of changing the location and severity of the crack on vibration parameters like the natural frequencies and mode shapes. All the displacements at the plate boundaries are assumed to be zero. Only the first six out-of-plane natural frequencies are needed in the study. These are decoupled from the in-plane natural frequencies which are much higher. Thus, it is possible to consider only the out-of-plane behaviour and ignore the dynamic effects.

Results obtained using different techniques (VICONOPT, FEM (MATLAB, ABAQUS) and VFM) are compared with previous studies by Stahl and Keer (1972), Liew et al. (1994), and Huang and Leissa (2009). As a result, an insight is given to the inverse problem of damage identification.

5.2 Damaged Plate Modelling Using Different Techniques

5.2.1 Damaged Plate Modelling in VICONOPT

VICONOPT is a powerful software which can model plates having different properties and different thickness along the transverse direction by representing them as different components. VICONOPT is based on the ESM, and the dynamic stiffness matrix derivation is taken from Wittrick and Williams (1974). ESM is also one of the fundamental theories of VFM; the dynamic stiffness matrices and their derivation will be given later in this section and applied in VFM. All through-the-length damage does not change the prismatic status of the plate, and hence VICONOPT can simulate such damage directly. The critical challenge is the simulation of more general forms of damage. The following sections describe the different methods which can be used to model delaminations and cracks separately.

5.2.1.1 Delamination Simulation

As mentioned above, VICONOPT can quickly simulate any prismatic structure. For a plate, if the properties and mechanical characteristics are invariant along the longitudinal direction, it remains prismatic even though it varies in the transverse direction. Hence, the software can model through-the-length damage. For the through-the-length delamination case, the delamination was initially simulated by removing the upper part of the damaged region. After calculation, it was found that this did not reflect the real behaviour of the delaminated plate case, the change in natural frequencies predicted being greater than the actual decrease.

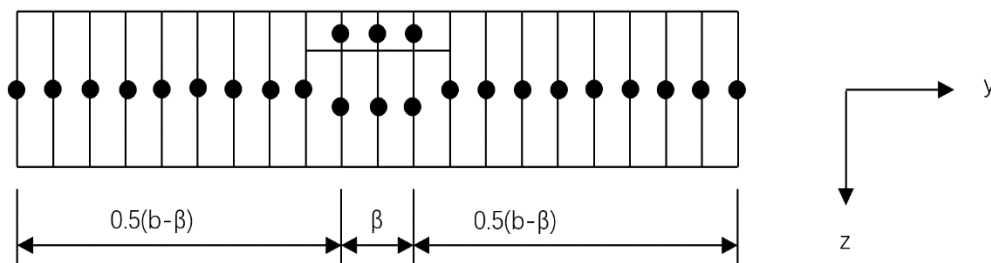


Figure 5-1 Cross-section of an all through-the-length delamination in a composite plate.

Black dots represent point supports.

Next, as shown in Figure 5-1, it was assumed that the plate is divided into strips, with point supports located at nodes at the strip edges to represent the simply supported ends. The damaged region is then separated into two parts caused by the delamination, which deflect independently within the damaged region but equally at its edges. The axial stiffness remains the same and this model ignores damping, contact and penetration between the two parts, as well as environmental effects. Here, b is the width of plate along the transverse direction, and β is the width of the delaminated region. For all through-the-length delaminations in composite plates, a brief illustration of the application of this method will be included in Chapter 6.2, and more detail about the modelling and related inverse problem examples are given in Luo (2015).

5.2.1.2 Crack Simulation

An all through-the-length crack can be defined as a damaged region of finite width and modelled by a reduction in stiffness throughout this region as shown in Figure 5-2 (b) and (c). In Figure 5-2 (b), the damaged region is divided into two parts according to the depth of the crack; the bottom part retains its full stiffness while in the upper part there is a separation of the material on either side of the crack. The strip distribution and relevant node connections of this crack modelling idea are shown in Figure 5-2 (b). For the simulation case shown in Figure 5-2 (c), the reduction in stiffness is achieved by removal of the corresponding material in the upper part. The amount of material removed depends on the depth of crack, and the material remains in the bottom part.

For the crack simulation shown in Figure 5-2 (a), the crack is simulated by a rotational spring of stiffness k^* about the longitudinal direction which is analogous to beam theory (Caddemi and Calìò 2008; Morassi *et al.* 2008 and Labib *et al.* 2014). The spring stiffness is assumed to be related to the crack depth d , which is analogous to that of a beam structure (Labib *et al.* 2014):

$$k^* = \frac{D}{b} * \frac{1}{\lambda^*} \quad \text{Eq. 5-1}$$

where D is the flexural rigidity of a long, thin, flat plate (Wittrick 1968b). Assuming the width of the plate is b , the cross-sectional thickness h , Young's modulus E , Poisson's ratio ν and density ρ , D is given by:

$$D = \frac{Eh^3}{12 * (1 - \nu^2)} \quad \text{Eq. 5-2}$$

And λ^* is the dimensionless local compliance given by:

$$\lambda^* = \frac{h}{b} * C(d/h) \quad \text{Eq. 5-3}$$

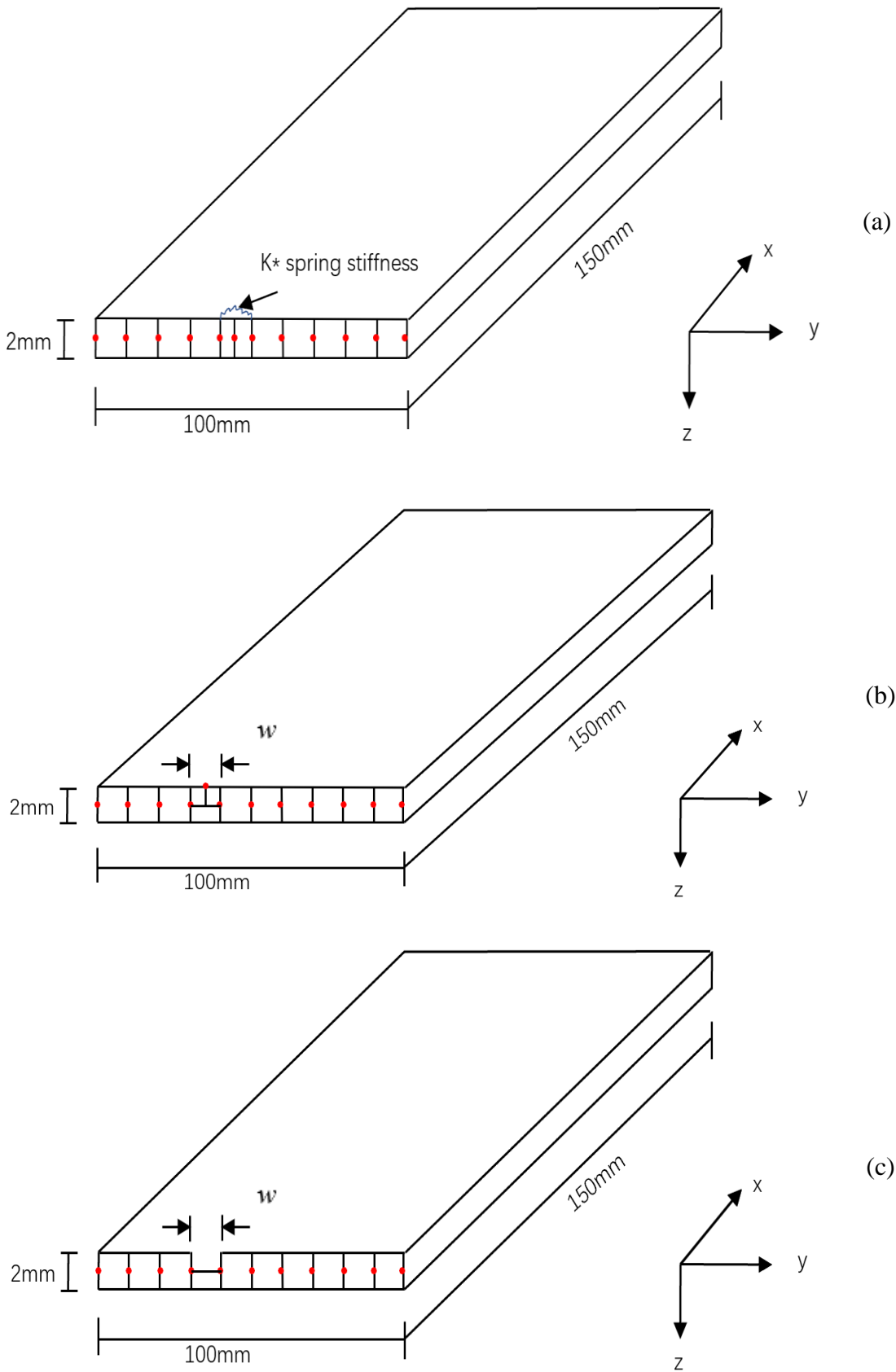


Figure 5-2 Different crack simulation methods.

(a) rotational spring model; (b) reduction of stiffness by defining a relatively small damage region; (c) reduction of stiffness by removing the upper part of the material.

In which, $C(d/h)$ is a dimensionless function that can be generalised as (Labib 2015):

$$C(d/h) = a_0 \sum_{n=1}^{10} a_n (d/h)^n \quad \text{Eq. 5-4}$$

Previous literature has given different formulas for a_0 and a_n , but this study adopts the formulation by Caddemi and Calio (2013):

$$C(d/h) = \frac{(d/h)[2 - (d/h)]}{0.9[(d/h) - 1]^2} \quad \text{Eq. 5-5}$$

The crack simulation presented in this Chapter will also extend to element level, and the modified simulation of rotational spring stiffness will be used in FEM to represent a crack. Table 5-1 shows a comparison of the changes in natural frequencies of various vibration modes predicted by different crack models of an isotropic plate. The plate is shown in Figure 5-2, and is a rectangular simply supported plate. It has been divided into 10 strips with added point supports at the edge along the transverse direction. Related eigenfrequencies obtained of intact plate from this model need to verify the convergence, the results match well with previous studies shown in Table 5-6. The width b and length a of the plate are 100mm and 150mm, respectively; the thickness h is 2mm. The material properties are $E = 110\text{kN mm}^{-2}$, $\rho = 4480\text{kg/m}^3$ $\nu = 0.3$. The crack is all through-the-length and is located at $y = 45\text{mm}$ with the partial depth $d = 0.5\text{mm}$. The damping factor and the loss of mass are ignored.

Table 5-1 Comparison of change in natural frequencies of different modes for different techniques, $d = 0.5\text{mm}$

CNF (Hz)	Model (a)	Model (b)			Model (c)		
		$w=5$	$w=1$	$w=0.1$	$w=5$	$w=1$	$w=0.1$
$\xi = 1, n=3$	6.15E-4	9.29E-3	1.74E-3	1.84E-4	1.21E-2	2.33E-3	2.37E-4
$\xi = 1, n=2$	3.48E-4	1.14E-2	2.36E-3	2.40E-4	1.02E-2	2.14E-3	2.19E-4
$\xi = 1, n=1$	1.85E-3	2.26E-2	5.18E-3	5.40E-4	1.61E-2	3.92E-3	4.14E-4
$\xi = 0, n=3$	7.78E-4	1.08E-2	2.34E-3	2.46E-4	1.09E-2	2.40E-3	2.50E-4
$\xi = 0, n=2$	3.62E-4	9.78E-3	2.06E-3	2.11E-4	9.48E-3	1.98E-3	2.03E-4
$\xi = 0, n=1$	1.02E-3	1.31E-2	2.87E-3	2.93E-4	1.34E-2	2.91E-3	2.97E-4

In Table 5-1, ξ is the VICON wavelength parameter, n is termed the number of half-wavelengths along the y -direction and w (mm) is the width of damage region that is defined in the crack simulation models (b) and (c). For models (b) and (c), the change in natural frequencies (CNF) is related to the assumed width of the damaged region; the CNF reduces with the reduction of damaged region w . The magnitude of CNF for models (b) and (c) approaches that of model (a) only when w is small enough. There may exist a reasonable assumption on which to base the width of the damaged region which will simulate the reduction of stiffness caused by a crack. However, it is difficult to find such a relationship for different types of plates, and this approach will not therefore be discussed further in this study. This thesis will adopt the rotational spring to represent a crack, and this assumption is more precise for a small crack (Morassi et al. 2008). The inverse problem of crack detection for all through-the-length cracks will be illustrated in Chapter 7 with and without the effects of experimental noise.

5.2.1.3 Further Remarks

VICONOPT is an efficient software that can model any prismatic structure, even if the material or mechanical properties change along the transverse direction. For all through-the-length damage, the difficulty is to simulate the damage in an appropriate way which has been discussed above, and other related calculations can be handled by the software. However, for part through-the-length damage or any arbitrary damage which may breach the prismatic status, the hybrid method (VFM) will be introduced and is discussed later in section 5.2.4. This study will start with an isotropic simply supported plate and only out-of-plane deformations will be considered. The derivation of the corresponding stiffness matrices of ESM (Wittrick and Williams 1974) and the combined constraint matrices for use with Lagrangian multipliers (Williams and Anderson 1983) as a part of VFM will be shown in section 5.2.4.

5.2.2 Cracked Plate Modelling in Advanced Finite Element Method (MATLAB)

VICONOPT can provide accurate, quick solutions to eigenvalue problems involving prismatic structures. However, for more complicated structures or arbitrary damage cases, it cannot establish an appropriate model to obtain the vibration characteristics or critical buckling load factors. To balance computational efficiency and universality, this study takes advantage of the versatility of FEM, coupling ESM for the intact part of the structure and FEM to model the damaged part with appropriate coupling through Lagrangian

Multipliers. The new hybrid method is named VFM; the FEM part is discussed first in this chapter. The critical part of the FEM in the study is to find the right technique to simulate arbitrary damage in plates. In this thesis, cracked plates will be studied and examined with reference to previous results in the literature.

5.2.2.1 Stiffness and Mass Properties of Plate Elements

FE analysis is a general method which is widely used in various engineering areas. It assumes an idealised discrete-element model for the stiffness matrix method. The actual plate is represented by a mathematical model with known characteristic elements whose stiffness is given in matrix form. For the free vibrations studied in the thesis, the hypothesis of rectangular plate bending theory is chosen for the relevant static stiffness matrix and equivalent mass matrix (Przemieniecki 1985). The characteristics of stiffness and mass are obtained for the individual elements and then assembled into a global stiffness matrix and mass matrix for solving relevant eigenvalue problems of plates.

The compatibility of deflection and rotation between adjacent elements is ensured by displacement functions (Bogner et al. 1965) for the global stiffness matrix. The stiffness matrix for a typical element (Eq. 5-6) is related to the degrees of freedoms at each node shown in Figure 5-3. Note that the sequence of the degrees of freedom is slightly different from that in the reference (Przemieniecki 1985).

$$\mathbf{k} = \begin{matrix} 1 \\ \vdots \\ 6 \\ 7 \\ \vdots \\ 12 \end{matrix} \begin{bmatrix} \mathbf{k}_{I,I} & \text{Symmetric} \\ & \\ & \\ & \\ & \\ \mathbf{k}_{II,I} & \mathbf{k}_{II,II} \end{bmatrix} \quad \text{Eq. 5-6}$$

The following (Przemieniecki 1985) derives the stiffness matrix given in equilibrium Eq. 5-6. Symbols used in the derivations from this literature are listed as follows: b is the plate length along the y-axis; a is the plate width along the x-axis; h is the plate thickness in the vertical direction; E is the Young's modulus; ρ is the density and ν is the Poisson's ratio.

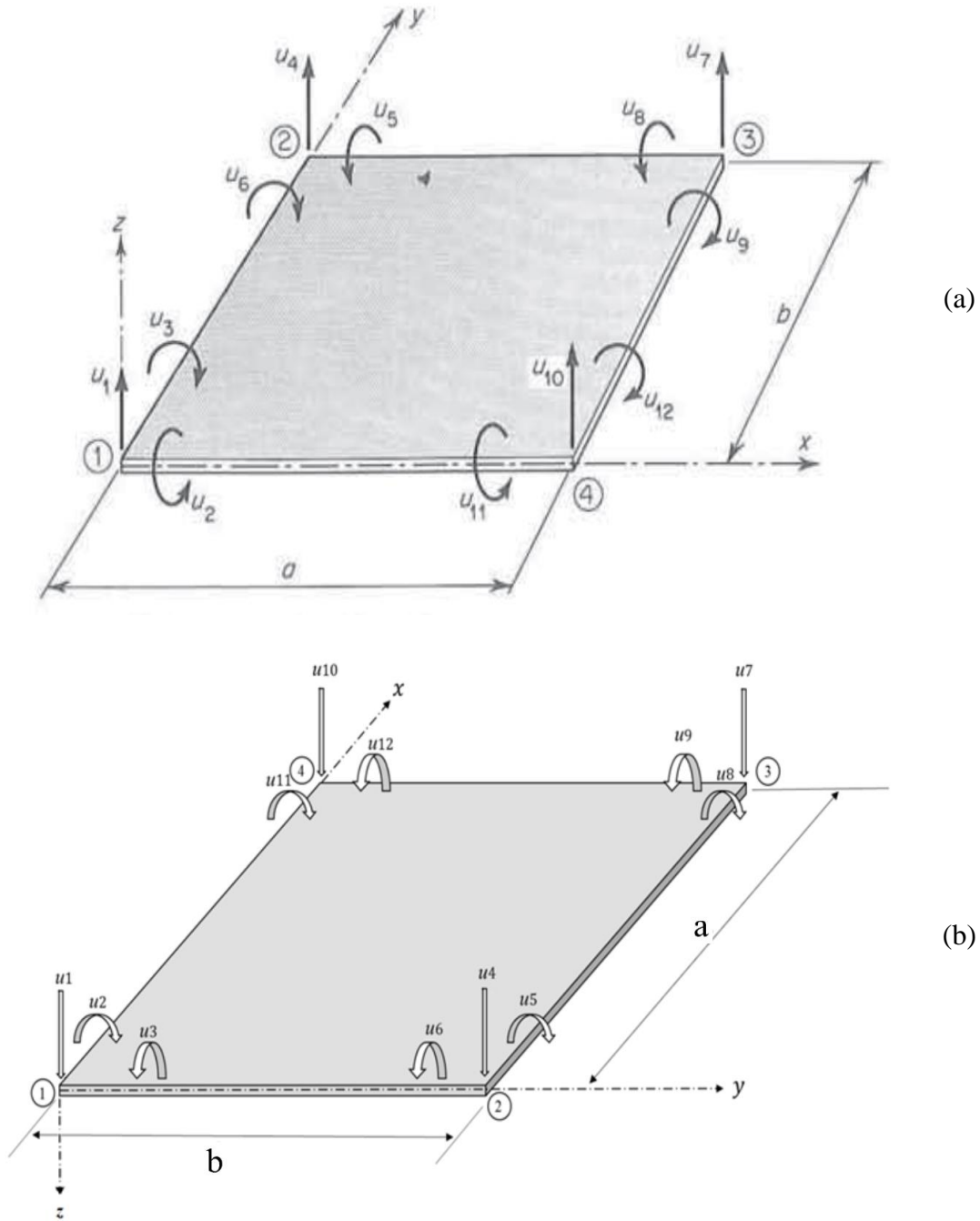


Figure 5-3 Nodes and related degrees of freedom in a single element.

(a) An unassembled rectangular element with the corresponding degree of freedoms (Przemieniecki 1985); (b) the actual sequence and symbolic parameters used in the study.

The deflection function (Clough 1965) of the z -axis is utilised in the calculation of the stiffness properties of bending rectangular plates:

$$u_z = \mathbf{a} * \mathbf{u} \quad \text{Eq. 5-7}$$

where the matrix \mathbf{a} is a function of the local coordinates and \mathbf{u} is a displacement vector with positive directions as in Figure 5-3(a):

$$\mathbf{u} = \{u_1 \ u_2 \ \dots \ u_{12}\} \quad \text{Eq. 5-8}$$

while matrix \mathbf{a} is given as:

$$\mathbf{a}^T = \begin{matrix} 1 \\ 2 \\ 3 \\ 4 \\ 5 \\ 6 \\ 7 \\ 8 \\ 9 \\ 10 \\ 11 \\ 12 \end{matrix} \begin{bmatrix} (1 + 2\xi) (1 + 2\xi)^2 (1 + 2\eta) (1 - \eta)^2 \\ (1 + 2\xi) (1 - 2\xi)^2 \eta (1 - \eta)^2 a \\ -\xi (1 - \xi)^2 (1 + 2\eta) (1 - \eta)^2 b \\ -(1 + 2\xi) (1 - \xi)^2 (3 - 2\eta) \eta^2 \\ -(1 + 2\xi) (1 - \xi)^2 (1 - \eta) \eta^2 a \\ -\xi (1 - \xi)^2 (3 - 2\eta) \eta^2 b \\ (3 - 2\xi) \xi^2 (3 - 2\eta) \eta^2 \\ -(3 - 2\xi) \xi^2 (1 - \eta) \eta^2 a \\ (1 - \xi) \xi^2 (3 - 2\eta) \eta^2 b \\ (3 - 2\xi) \xi^2 (1 + 2\eta) (1 - \eta)^2 \\ (3 - 2\xi) \xi^2 \eta (1 - \eta)^2 a \\ (1 - \xi) \xi^2 (1 + 2\eta) (1 - \eta)^2 b \end{bmatrix} \quad \text{Eq. 5-9}$$

in which

$$\eta = x/a \text{ and } \xi = y/b \quad \text{Eq. 5-10}$$

Using the assumed deflection function given by Eq. 5-9 guarantees the compatibility of the boundary deflections and slope for adjacent elements. Using the flat-plate theory to calculate the strain vector \mathbf{e} in Eq. 5-12 (Przemieniecki 1985):

$$\begin{aligned} e_{xx} &= -z \frac{\partial^2 u_z}{\partial x^2} \\ e_{yy} &= -z \frac{\partial^2 u_z}{\partial y^2} \\ e_{xy} &= -2z \frac{\partial^2 u_z}{\partial x \partial y} \end{aligned} \quad \text{Eq. 5-11}$$

Combine the Eq. 5-9 and Eq. 5-12, we then have:

$$\mathbf{e} = \mathbf{b} * \mathbf{u} \quad \text{Eq. 5-12}$$

where \mathbf{e} is the strain vector and \mathbf{b} is the matrix of exact strain for a unit displacement. Substitute Eq. 5-9 and Eq. 5-12 into Eq. 5-11 to generate the matrix \mathbf{b} , expressing the total strains by unit displacement as Eq. 5-14. Substituting Eq. 5-14 into Eq. 5-12 with essential operations, the stiffness matrix is then obtained as Eq. 5-6, with the submatrices $\mathbf{k}_{I,I}$, $\mathbf{k}_{II,I}$ and $\mathbf{k}_{II,II}$ given in Table 5-2, Table 5-3 and Table 5-4.

Two different displacement distributions (Przemieniecki 1985) are introduced to determine the stiffness properties of bending rectangular plates. The compatible displacement distribution is adopted in this study and is used in the derivation of mass matrices to ensure the continuity of deflection and translation between adjacent elements. As shown in Figure 5-3, the mass matrix will be determined by the nodal displacements, and the equivalent mass matrix (Przemieniecki 1985) is calculated as:

$$\mathbf{m} = \int_V \rho \mathbf{a}^T \mathbf{a} dV \quad \text{Eq. 5-13}$$

Here ρ is the density and \mathbf{a} is the function of local coordinates from Eq. 5-9. Substituting Eq. 5-9 into Eq. 5-13 to express the integration over the whole volume of the rectangular element, the mass matrix is obtained as in Table 5-5.

$$\mathbf{b}^T = \begin{matrix} 1 \\ 2 \\ 3 \\ 4 \\ 5 \\ 6 \\ 7 \\ 8 \\ 9 \\ 10 \\ 11 \\ 12 \end{matrix} \left[\begin{array}{ccc} (1 - 2\xi)(1 + 2\eta)(1 - \eta)^2 \frac{6z}{b^2} & (1 + 2\xi)(1 - \xi)^2(1 - 2\eta) \frac{6z}{a^2} & -\xi(1 - \xi)\eta(1 - \eta) \frac{72z}{ba} \\ (1 - 2\xi)\eta(1 - \eta)^2 \frac{6az}{b^2} & (1 + 2\xi)(1 - \xi)^2(2 - 3\eta) \frac{2z}{a} & \xi(1 - \xi)(1 - \eta)(1 - 3\eta) \frac{12z}{b} \\ -(2 - 3\xi)(1 + 2\eta)(1 - \eta)^2 \frac{2z}{b} & -\xi(1 - \xi)^2(1 - 2\eta) \frac{6bz}{a^2} & -(1 - \xi)(1 + 3\xi)\eta(1 - \eta) \frac{12z}{a} \\ (1 - 2\xi)(3 - 2\eta)\eta^2 \frac{6z}{b^2} & -(1 + 2\xi)(1 - \xi)^2(1 - 2\eta) \frac{6z}{a^2} & \xi(1 - \xi)\eta(1 - \eta) \frac{72z}{ba} \\ -(1 - 2\xi)(1 - \eta)\eta^2 \frac{6az}{b^2} & (1 + 2\xi)(1 - \xi)^2(1 - 3\eta) \frac{2z}{a} & -\xi(1 - \xi)\eta(2 - 3\eta) \frac{12z}{b} \\ -(2 - 3\xi)(3 - 2\eta)\eta^2 \frac{2z}{b} & \xi(1 - \xi)^2(1 - 2\eta) \frac{6bz}{a^2} & (1 - \xi)(1 + 3\xi)\eta(1 - \eta) \frac{12z}{a} \\ -(1 - 2\xi)(3 - 2\eta)\eta^2 \frac{6z}{b^2} & -(3 - 2\xi)\xi^2(1 - 2\eta) \frac{6z}{a^2} & -\xi(1 - \xi)\eta(1 - \eta) \frac{72z}{ba} \\ (1 - 2\xi)(1 - \eta)\eta^2 \frac{6az}{b^2} & (3 - 2\xi)\xi^2(1 - 3\eta) \frac{2z}{a} & \xi(1 - \xi)\eta(2 - 3\eta) \frac{12z}{b} \\ -(1 - 3\xi)(3 - 2\eta)\eta^2 \frac{2z}{a} & -(1 - \xi)\xi^2(1 - 2\eta) \frac{6bz}{a^2} & -\xi(2 - 3\xi)\eta(1 - \eta) \frac{12z}{b} \\ -(1 - 2\xi)(1 + 2\eta)(1 - \eta)^2 \frac{6z}{b^2} & (3 - 2\xi)\xi^2(1 - 2\eta) \frac{6z}{a^2} & \xi(1 - \xi)\eta(1 - \eta) \frac{72z}{ba} \\ -(1 - 2\xi)(1 + 2\eta)(1 - \eta)^2 \frac{6az}{b^2} & (3 - 2\xi)\xi^2(2 - 3\eta) \frac{2z}{a} & -(1 - \xi)(1 - \xi)\eta(1 - 3\eta) \frac{12z}{b} \\ -(1 - 3\xi)(1 + 2\eta)(1 - \eta)^2 \frac{2z}{b} & (1 - \xi)\xi^2(1 - 2\eta) \frac{6bz}{a^2} & \xi(1 - \xi)\eta(1 - \eta) \frac{12z}{a} \end{array} \right] \quad \text{Eq. 5-14}$$

Table 5-2 Submatrix $\mathbf{K}_{I,I}$ of stiffness matrix for a rectangular plate in bending, all coefficients multiplied by $Et^3/(12(1 - \nu^2)ab)$, where a and b are the plate dimensions (Przemieniecki 1985).

$\frac{156}{35}(\beta^2 + \beta^{-2}) + \frac{72}{25}$					
$\left[\frac{22}{35}\beta^2 + \frac{78}{35}\beta^{-2} + \frac{6}{25}(1 + 5\nu) \right] b$	$\left(\frac{4}{35}\beta^2 + \frac{52}{35}\beta^{-2} + \frac{8}{25} \right) b^2$				
$-\left[\frac{78}{35}\beta^2 + \frac{22}{35}\beta^{-2} + \frac{6}{25}(1 + 5\nu) \right] a$	$-\left[\frac{11}{35}(\beta^2 + \beta^{-2}) + \frac{1}{50}(1 + 60\nu) \right] ab$	$\left(\frac{52}{35}\beta^2 + \frac{4}{35}\beta^{-2} + \frac{8}{25} \right) a^2$	Symmetric		
$\frac{54}{35}\beta^2 - \frac{156}{35}\beta^{-2} - \frac{72}{25}$	$\left(\frac{13}{35}\beta^2 - \frac{78}{35}\beta^{-2} - \frac{6}{25} \right) b$	$\left[-\frac{27}{35}\beta^2 + \frac{22}{35}\beta^{-2} + \frac{6}{25}(1 + 5\nu) \right] a$	$\frac{156}{35}(\beta^2 + \beta^{-2}) + \frac{72}{25}$		
$\left(-\frac{13}{35}\beta^2 + \frac{78}{35}\beta^{-2} + \frac{6}{25} \right) b$	$\left(-\frac{3}{35}\beta^2 + \frac{26}{35}\beta^{-2} - \frac{2}{25} \right) b^2$	$\left[\frac{13}{70}\beta^2 - \frac{11}{35}\beta^{-2} - \frac{1}{50}(1 + 5\nu) \right] ab$	$-\left[\frac{22}{35}\beta^2 + \frac{78}{35}\beta^{-2} + \frac{6}{25}(1 + 5\nu) \right] b$	$\left(\frac{4}{35}\beta^2 + \frac{52}{35}\beta^{-2} + \frac{8}{25} \right) b^2$	
$\left[-\frac{27}{35}\beta^2 + \frac{22}{35}\beta^{-2} + \frac{6}{25}(1 + 5\nu) \right] a$	$\left[-\frac{13}{70}\beta^2 + \frac{11}{35}\beta^{-2} + \frac{1}{50}(1 + 5\nu) \right] ab$	$\left(\frac{18}{35}\beta^2 - \frac{4}{35}\beta^{-2} - \frac{8}{25} \right) a^2$	$-\left[\frac{78}{35}\beta^2 + \frac{22}{35}\beta^{-2} + \frac{6}{25}(1 + 5\nu) \right] a$	$\frac{11}{35}(\beta^2 + \beta^{-2}) + \frac{1}{50}(1 + 60\nu) ab$	$\left(\frac{52}{35}\beta^2 + \frac{4}{35}\beta^{-2} + \frac{8}{25} \right) a^2$

Table 5-3 Submatrix $\mathbf{k}_{II,I}$ of stiffness matrix for a rectangular plate in bending, all coefficients multiplied by $Et^3/(12(1-\nu^2)ab)$, where a and b are the plate dimensions (Przemieniecki 1985).

$-\frac{54}{35}(\beta^2 + \beta^{-2}) + \frac{72}{25}$	$(-\frac{13}{35}\beta^2 - \frac{27}{35}\beta^{-2} + \frac{6}{25})b$	$(\frac{27}{35}\beta^2 + \frac{13}{35}\beta^{-2} - \frac{6}{25})a$	$-\frac{156}{35}\beta^2 + \frac{54}{35}\beta^{-2} - \frac{72}{25}$	$[\frac{22}{35}\beta^2 - \frac{27}{35}\beta^{-2} + \frac{6}{25}(1 + 5\nu)]b$	$(\frac{78}{35}\beta^2 - \frac{13}{35}\beta^{-2} + \frac{6}{25})a$
$(\frac{13}{35}\beta^2 + \frac{27}{35}\beta^{-2} - \frac{6}{25})b$	$(\frac{3}{35}\beta^2 + \frac{9}{35}\beta^{-2} + \frac{2}{25})b^2$	$[-\frac{13}{70}(\beta^2 + \beta^{-2}) + \frac{1}{50}]ab$	$[\frac{22}{35}\beta^2 - \frac{27}{35}\beta^{-2} + \frac{6}{25}(1 + 5\nu)]b$	$(-\frac{4}{35}\beta^2 + \frac{18}{35}\beta^{-2} - \frac{8}{25})b^2$	$[-\frac{11}{35}\beta^2 + \frac{13}{70}\beta^{-2} - \frac{1}{50}(1 + 5\nu)]ab$
$(-\frac{27}{35}\beta^2 - \frac{13}{35}\beta^{-2} + \frac{6}{25})a$	$[-\frac{13}{70}(\beta^2 + \beta^{-2}) + \frac{1}{50}]ab$	$(\frac{9}{35}\beta^2 + \frac{3}{35}\beta^{-2} + \frac{2}{25})a^2$	$(-\frac{78}{35}\beta^2 + \frac{13}{35}\beta^{-2} - \frac{6}{25})a$	$[\frac{11}{35}\beta^2 - \frac{13}{70}\beta^{-2} + \frac{1}{50}(1 + 5\nu)]ab$	$(\frac{26}{35}\beta^2 - \frac{3}{35}\beta^{-2} - \frac{2}{25})a^2$
$-\frac{156}{35}\beta^2 + \frac{54}{35}\beta^{-2} - \frac{72}{25}$	$[-\frac{22}{35}\beta^2 + \frac{27}{35}\beta^{-2} - \frac{6}{25}(1 + 5\nu)]b$	$(\frac{78}{35}\beta^2 - \frac{13}{35}\beta^{-2} + \frac{6}{25})a$	$-\frac{54}{35}(\beta^2 + \beta^{-2}) + \frac{72}{25}$	$(\frac{13}{35}\beta^2 + \frac{27}{35}\beta^{-2} - \frac{6}{25})b$	$(\frac{27}{35}\beta^2 + \frac{13}{35}\beta^{-2} - \frac{6}{25})a$
$[-\frac{22}{35}\beta^2 + \frac{27}{35}\beta^{-2} - \frac{6}{25}(1 + 5\nu)]b$	$(-\frac{4}{35}\beta^2 + \frac{18}{35}\beta^{-2} - \frac{8}{25})b^2$	$[\frac{11}{35}\beta^2 - \frac{13}{70}\beta^{-2} + \frac{1}{50}(1 + 5\nu)]ab$	$(-\frac{13}{35}\beta^2 - \frac{27}{35}\beta^{-2} + \frac{6}{25})b$	$(\frac{3}{35}\beta^2 + \frac{9}{35}\beta^{-2} + \frac{2}{25})b^2$	$[\frac{13}{70}(\beta^2 + \beta^{-2}) - \frac{1}{50}]ab$
$(-\frac{78}{35}\beta^2 + \frac{13}{35}\beta^{-2} - \frac{6}{25})a$	$[-\frac{11}{35}\beta^2 + \frac{13}{70}\beta^{-2} - \frac{1}{50}(1 + 5\nu)]ab$	$(\frac{26}{35}\beta^2 - \frac{3}{35}\beta^{-2} - \frac{2}{25})a^2$	$(-\frac{27}{35}\beta^2 - \frac{13}{35}\beta^{-2} + \frac{6}{25})a$	$[\frac{13}{70}(\beta^2 + \beta^{-2}) - \frac{1}{50}]ab$	$(\frac{9}{35}\beta^2 + \frac{3}{35}\beta^{-2} + \frac{2}{25})a^2$

Table 5-4 Submatrix $\mathbf{k}_{II,II}$ of stiffness matrix for a rectangular plate in bending, all coefficients multiplied by $Et^3/(12(1 - \nu^2)ab)$, where a and b are the plate dimensions (Przemieniecki 1985).

$\frac{156}{35}(\beta^2 + \beta^{-2}) + \frac{72}{25}$					
$-\left[\frac{22}{35}\beta^2 + \frac{78}{35}\beta^{-2} + \frac{6}{25}(1 + 5\nu)\right]b$	$\left(\frac{4}{35}\beta^2 + \frac{52}{35}\beta^{-2} + \frac{8}{25}\right)b^2$				
$\left[\frac{78}{35}\beta^2 + \frac{22}{35}\beta^{-2} + \frac{6}{25}(1 + 5\nu)\right]a$	$-\left[\frac{11}{35}(\beta^2 + \beta^{-2}) + \frac{1}{50}(1 + 60\nu)\right]ab$	$\left(\frac{52}{35}\beta^2 + \frac{4}{35}\beta^{-2} + \frac{8}{25}\right)a^2$			Symmetric
$\frac{54}{35}\beta^2 - \frac{156}{35}\beta^{-2} - \frac{72}{25}$	$\left(-\frac{13}{35}\beta^2 + \frac{78}{35}\beta^{-2} + \frac{6}{25}\right)b$	$\left[\frac{27}{35}\beta^2 - \frac{22}{35}\beta^{-2} - \frac{6}{25}(1 + 5\nu)\right]a$	$\frac{156}{35}(\beta^2 + \beta^{-2}) + \frac{72}{25}$		
$\left(\frac{13}{35}\beta^2 - \frac{78}{35}\beta^{-2} - \frac{6}{25}\right)b$	$\left(-\frac{3}{35}\beta^2 + \frac{26}{35}\beta^{-2} - \frac{2}{25}\right)b^2$	$\left[\frac{13}{70}\beta^2 - \frac{11}{35}\beta^{-2} - \frac{1}{50}(1 + 5\nu)\right]ab$	$\left[\frac{22}{35}\beta^2 + \frac{78}{35}\beta^{-2} + \frac{6}{25}(1 + 5\nu)\right]b$	$\left(\frac{4}{35}\beta^2 + \frac{52}{35}\beta^{-2} + \frac{8}{25}\right)b^2$	
$\left[\frac{27}{35}\beta^2 - \frac{22}{35}\beta^{-2} - \frac{6}{25}(1 + 5\nu)\right]a$	$\left[-\frac{13}{70}\beta^2 + \frac{11}{35}\beta^{-2} + \frac{1}{50}(1 + 5\nu)\right]ab$	$\left(\frac{18}{35}\beta^2 - \frac{4}{35}\beta^{-2} - \frac{8}{25}\right)a^2$	$\left[\frac{78}{35}\beta^2 + \frac{22}{35}\beta^{-2} + \frac{6}{25}(1 + 5\nu)\right]a$	$\left[\frac{11}{35}(\beta^2 + \beta^{-2}) + \frac{1}{50}(1 + 60\nu)\right]ab$	$\left(\frac{52}{35}\beta^2 + \frac{4}{35}\beta^{-2} + \frac{8}{25}\right)a^2$

Table 5-5 Mass matrix **m** for a rectangular plate in bending, all coefficients multiplied by $\frac{\rho a b t}{176400}$, where *a* and *b* are the plate dimension (Przemieniecki 1985)

24336											
3432 b	624 b ²										
-3432 a	-484 ab	624 a ²				Symmetric					
8424	2028 b	-1188 a	24336								
-2028 b	-468 b ²	286 ab	-3432 b	624 b ²							
-1188 a	-286 ab	216 a ²	-3432 a	484 ab	624 a ²						
2916	702 b	-702 a	8424	-1188 b	-2028 a	24336					
-702 b	-162 b ²	169 ab	-1188 b	216 b ²	286 ab	-3432 b	624 b ²				
702 a	169 ab	-162 a ²	2028 a	-286 ab	-468 a ²	3432 a	-484 ab	624 a ²			
8424	1188 b	-2028 a	2916	-702 b	-702 a	8424	-2028 b	1188 a	24336		
1188 b	216 b ²	-286 ab	702 b	-162 b ²	-169 ab	2028 b	-468 b ²	286 ab	3432 b	624 b ²	
2028 a	286 ab	-468 a ²	702 a	-169 ab	-162 a ²	1188 a	-286 ab	216 a ²	3432 a	484 ab	624 a ²

5.2.2.2 Modified Stiffness Matrix with Arbitrary Crack

The previous section introduced the static stiffness and equivalent mass matrices for a rectangular plate element. For a plate containing an arbitrary crack the properties will be changed to produce a reduction of the stiffness. This study ignores any reduction of mass and damping factor as a result of the crack.

Figure 5-4 shows a portion of a cracked FE plate model, in which the crack runs along the line PQRS through the elements *I*, *II* and *IV*. The crack is simulated as a rotational spring with depth-dependent compliance C per unit length per element; details of the simulation will be presented in the next section. The compliance C is then resolved into rotational components along the x-axis and y-axis (C_x, C_y) respectively. The components in element *I* are integrated along PQ using shape functions to allocate the related compliances to nodes (1, 2, 4, 5). Similar allocation of the compliances occurring in elements *II* and *IV* are made to nodes (2, 3, 5, 6) and (5, 6, 8, 9).

The finite elements have three degrees of freedom at each node when intact: vertical displacement W and rotations θ_x and θ_y about the x and y axes respectively. The essential and challenging part is the modelling of the cracked element. Nodes to which rotational compliances (C_x, C_y) have been allocated are given additional rotational degrees of freedom. Using node 5 as an example shown in Figure 5-5, element *I* connects to $(W_5, \theta_{x5L}, \theta_{y5L})$ while element *II* connects to $(W_5, \theta_{x5U}, \theta_{y5U})$, and so on. Rotational springs of stiffness $(1/C_x, 1/C_y)$ add on degrees of freedom $(\theta_{x5L}, \theta_{x5U})$ and $(\theta_{y5L}, \theta_{y5U})$.

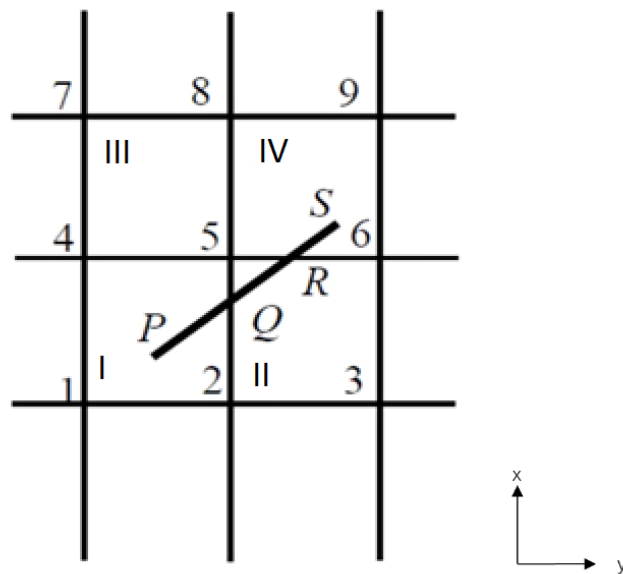


Figure 5-4 Detail of a portion of the FE cracked plate model.

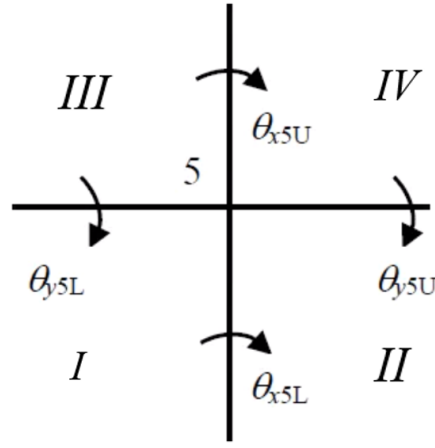


Figure 5-5 Rotational degrees of freedom at node 5 of the cracked portion.

5.2.2.3 Rotational Spring Crack Simulation

To determine the rotational compliances associated with the crack prior to their being allocated to their respective element nodes and thus incorporated into the element stiffness matrices and hence the global stiffness matrix, as shown in Figure 5-6, the concepts introduced in considering all through-the-length cracks are again used.

$C(d/h)$, a dimensionless function showing the relationship between the depth of crack and the compliance of crack in Eq. 5-5 (Caddemi and Caliò 2008; Labib et al. 2014). The compliance per plate element is generated from Eq. 5-1 which analogue from the beam-like structure (Labib et al. 2014):

$$KS_b = (E * I/L) * (1/\lambda) \quad \text{Eq. 5-15}$$

where KS_b is the rotational stiffness of the beam and L is the length of the beam. And the non-dimensional compliance factor λ is given by:

$$\lambda = (h/L) * C(d/h) \quad \text{Eq. 5-16}$$

Two factors $\cos \theta / a_e$ and $\sin \theta / b_e$ are introduced to allow the crack compliance to be allocated along the x and y directions at element level within the plates, θ is the crack angle between crack and x direction shown in Figure 5-6. Using a crack in the x-direction of the plate as an example, Eq. 5-17 gives the compliance C_{px} per unit length along the x-direction:

$$C_{px} = h * C(d/h) * \cos \theta / (D * a_e) \quad \text{Eq. 5-17}$$

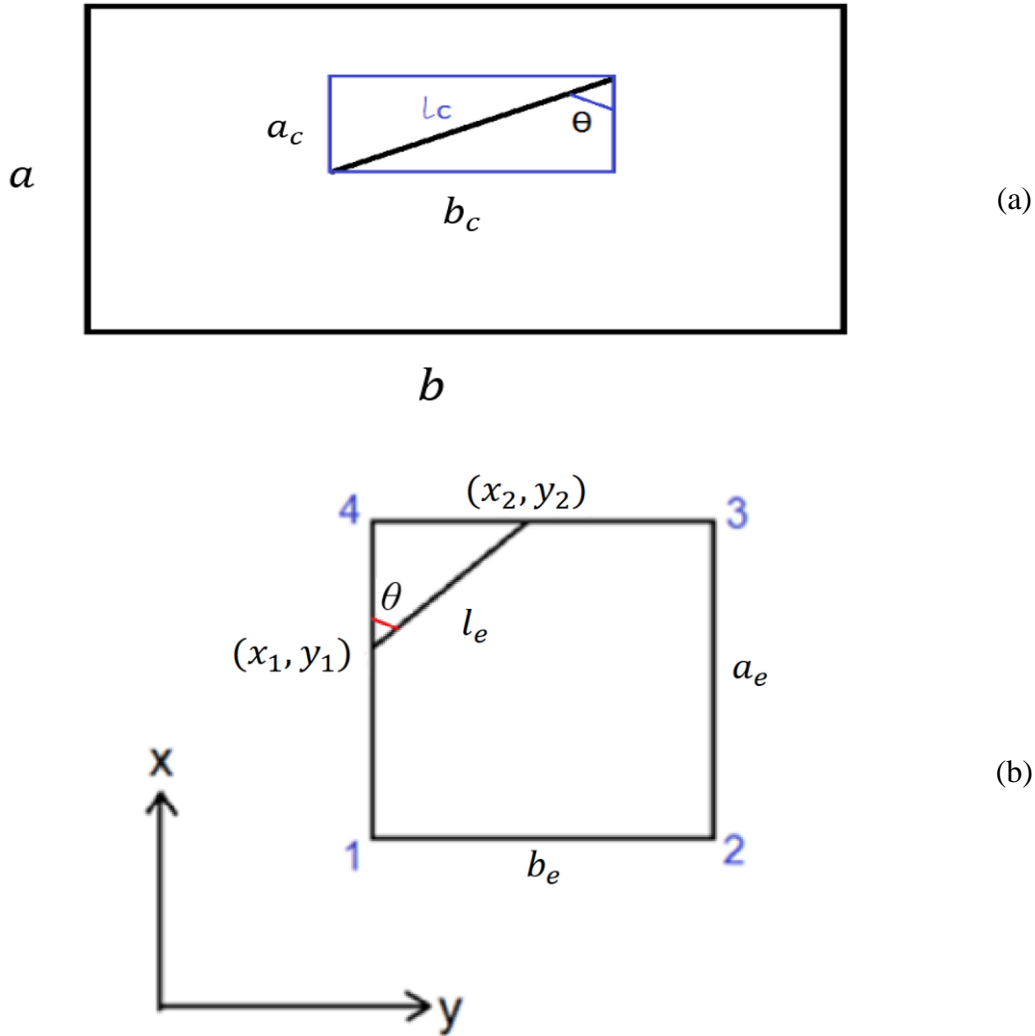


Figure 5-6 Arbitrary cracked plate and relative cracked element.

(a) Rectangular isotropic plate contains an arbitrary crack; (b) a cracked element.

In which $D * a_e$ possesses the same function as $E * I$ for a beam-like structure, where D is the flexural rigidity of a plate; a_e is the length of element along x direction; b_e is the width of element along y direction. For the compliance per element per unit length in a plate Ce_{px} :

$$Ce_{px} = h * C(d/h) * \cos \theta / (D * a_e * a_e) \tag{Eq. 5-18}$$

Similarly, the compliance per element per unit length along the y-direction is:

$$Ce_{py} = h * C(d/h) * \sin \theta / (D * b_e * b_e) \tag{Eq. 5-19}$$

While determining the compliance per element per unit along the x and y directions, shape functions are utilized to allocate the compliance to corresponding nodes by integration. At the element level, the shape functions are:

$$\begin{aligned} N_1 &= \left(1 - \frac{x}{a_e}\right) * \left(1 - \frac{y}{b_e}\right) \\ N_2 &= \left(1 - \frac{x}{a_e}\right) * \left(\frac{y}{b_e}\right) \\ N_3 &= \left(\frac{x}{a_e}\right) * \left(\frac{y}{b_e}\right) \\ N_4 &= \left(\frac{x}{a_e}\right) * \left(1 - \frac{y}{b_e}\right) \end{aligned} \quad \text{Eq. 5-20}$$

From Figure 5-6 (b), the crack extends from (x_1, y_1) to (x_2, y_2) . Assume the gradient is $\tan \theta$:

$$\tan \theta = (y_2 - y_1)/(x_2 - x_1) \quad \text{Eq. 5-21}$$

Hence, the crack in the element can be regarded as occurring at a set of points. For each point, the local coordinates are:

$$\begin{aligned} y &= y_1 + (x - x_1) * \tan \theta \\ x &= x_1 + (y - y_1) * \cot \theta \end{aligned} \quad \text{Eq. 5-22}$$

Then the compliance of each point in the x and y directions is integrated and allocated to the adjacent nodes at the element level.

$$\begin{aligned} C'_{px} &= \int_{x_1}^{x_2} (h * C(d/h) * \cos \theta * N_i(x, y)/(D * a_e * a_e)) dl_e \\ C'_{py} &= \int_{y_1}^{y_2} (h * C(d/h) * \sin \theta * N_i(x, y)/(D * b_e * b_e)) dl_e \end{aligned} \quad \text{Eq. 5-23}$$

Since $\cos \theta * dl_e = dx$ and $\sin \theta * dl_e = dy$, Eq. 5-23 can be simplified as:

$$\begin{aligned} C'_{px} &= \int_{x_1}^{x_2} (h * C(d/h) * N_i(x, y)/(D * a_e * a_e)) dx \\ C'_{py} &= \int_{y_1}^{y_2} (h * C(d/h) * N_i(x, y)/(D * b_e * b_e)) dy \end{aligned} \quad \text{Eq. 5-24}$$

Using the nodal sequence shown in Figure 5-3 (b), the compliances added to each node to model the crack are listed as follows:

$$\begin{aligned}
C'_{px1} &= h * \frac{C\left(\frac{d}{h}\right)}{D * a_e^3 * b_e} * ((a_e * (b_e - y_1) + a_e * x_1 \\
&\quad * \tan \theta) * (x_2 - x_1) \\
&\quad + (-a_e * \tan \theta - (b_e - y_1) - x_1 * \tan \theta) \\
&\quad * \frac{(x_2^2 - x_1^2)}{2} + \tan \theta * (x_2^3 - x_1^3)/3) \\
C'_{px2} &= h * \frac{C\left(\frac{d}{h}\right)}{D * a_e^3 * b_e} * ((a_e * y_1 - a_e * x_1 * \tan \theta) * (x_2 - x_1) \\
&\quad + (-y_1 + x_1 * \tan \theta + a_e * \tan \theta) * \frac{(x_2^2 - x_1^2)}{2} \\
&\quad - \tan \theta * (x_2^3 - x_1^3)/3) \\
C'_{px3} &= h * \frac{C\left(\frac{d}{h}\right)}{D * a_e^3 * b_e} * ((y_1 - x_1 * \tan \theta) * \frac{(x_2^2 - x_1^2)}{2} + \tan \theta \\
&\quad * (x_2^3 - x_1^3)/3) \\
C'_{px4} &= h * \frac{C\left(\frac{d}{h}\right)}{D * a_e^3 * b_e} * ((b_e - y_1 + x_1 * \tan \theta) * \frac{(x_2^2 - x_1^2)}{2} \\
&\quad - \tan \theta * (x_2^3 - x_1^3)/3) \\
C'_{py1} &= h * \frac{C\left(\frac{d}{h}\right)}{D * a_e * b_e^3} * ((b_e * (a_e - x_1) + b_e * y_1 \\
&\quad * \cot \theta) * (y_2 - y_1) \\
&\quad + (a_e - x_1 - y_1 * \cot \theta - b_e * \cot \theta) * \frac{(y_2^2 - y_1^2)}{2} \\
&\quad + \cot \theta * (y_2^3 - y_1^3)/3) \\
C'_{py2} &= h * \frac{C\left(\frac{d}{h}\right)}{D * a_e * b_e^3} * ((a_e - x_1 + y_1 * \cot \theta) * \frac{(y_2^2 - y_1^2)}{2} \\
&\quad - \cot \theta * (y_2^3 - y_1^3)/3) \\
C'_{py3} &= h * \frac{C\left(\frac{d}{h}\right)}{D * a_e * b_e^3} * ((x_1 - y_1 * \cot \theta) * \frac{(y_2^2 - y_1^2)}{2} + \cot \theta \\
&\quad * (y_2^3 - y_1^3)/3) \\
C'_{py4} &= h * \frac{C\left(\frac{d}{h}\right)}{D * a_e * b_e^3} * ((b_e * x_1 - b_e * y_1 * \cot \theta) * (y_2 - y_1) \\
&\quad + (b_e * \cot \theta - x_1 + y_1 * \cot \theta) * \frac{(y_2^2 - y_1^2)}{2} - \cot \theta \\
&\quad * (y_2^3 - y_1^3)/3)
\end{aligned}$$

Eq. 5-25

After the allocation of the crack compliances the element stiffness matrices are assembled, with appropriate sequencing of degrees of freedom, into a global stiffness matrix. MATLAB code related to assembly procedures are shown in the Appendix E, and the results for several cracked plate cases will be compared in Chapter 6.

5.2.3 Cracked Plate Modelling in ABAQUS

ABAQUS is a commercial finite element computer program which is used widely in various engineering areas. In this study ABAQUS is used to model the effects of a series of cracks in different locations to verify the results generated by VFM model.

The ABAQUS thin plate model in this study uses 4-node doubly curved thin shell S4R elements (20*20, 400 elements in total) to determine the vibration parameters (natural frequencies and mode shapes) of a simply supported isotropic rectangular plate. The predefined crack could be aligned horizontally or vertically and located at any position on the plate with arbitrary depth. Six degree of freedoms have been chosen for each node in the ABAQUS model of this study. We study the first six natural frequencies when solving the inverse problem, and so only out-of-plane behaviour will be discussed and all in-plane DOFs will be suppressed in the ABAQUS model. Hence, the simulated ABAQUS model could be regarded as equivalent to our pure FE model or VFM model. As with the previously described method, the difficulty in the ABAQUS modelling is the crack simulation. Three different modelling approaches have been proposed and compared with literature and the VFM model.

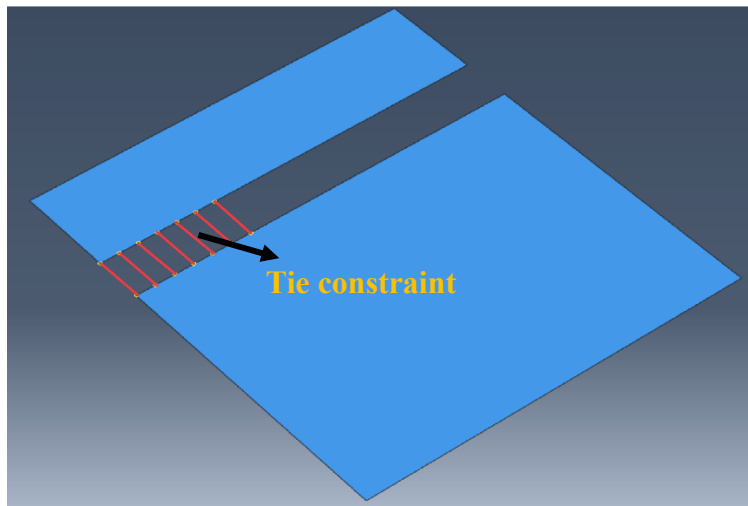
5.2.3.1 ABAQUS cracked plate modelling

The approach used to model the crack considered it as two separate plates, connected together along the length of the crack using suitable constraints (Figure 5-7).

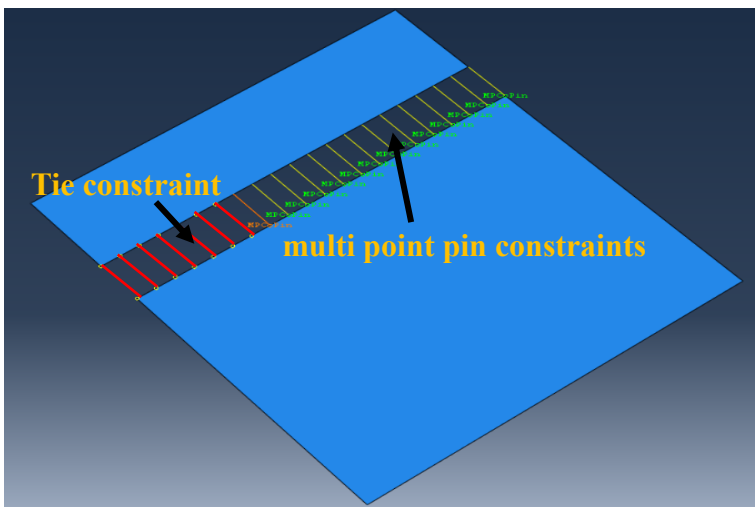
The models used are shown in Figure 5-7. For a simply supported plate, all three displacement degrees of freedom are constrained at the boundary and the rotational freedoms are free.

In order to validate the model, tie constraints were first used to couple all the nodes along the crack direction to check that the two plates would deform as a whole intact plate. Eq. 5-26 is applied to normalise the obtained natural frequencies into non-dimensional values, and a comparison with VIPASA and previously published results is shown in Table 5-6.

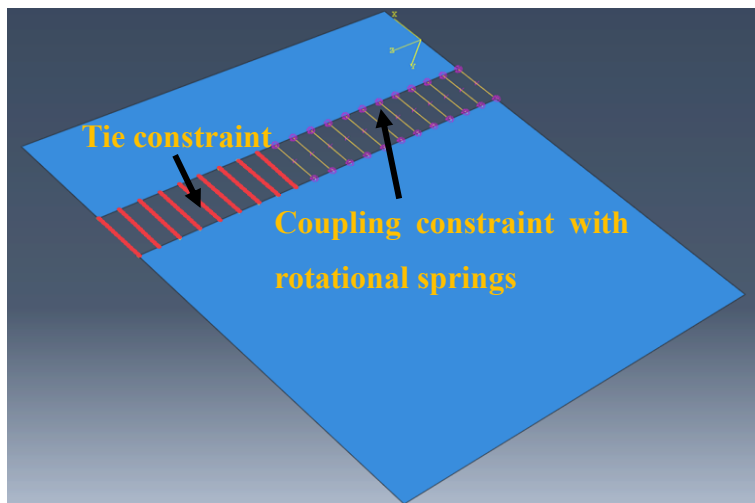
$$\Omega_{mn} = 2\pi l^2 \omega_{mn} \sqrt{\rho h / D} \quad \text{Eq. 5-26}$$



(a)



(b)



(c)

Figure 5-7 Different crack simulation techniques in ABAQUS.

(a) **AT** model, tie constraints used to connect the intact part, leave the damaged part to deform freely; (b) tie constraints used to connect the intact part, multi point pin constraints used to model the crack by constraining all three displacements whilst leaving rotational deformation free; (c) **ATCS** model, tie constraints used to connect the intact part, with a coupling constraint introduced into the damaged part to constrain all displacements and irrelevant rotational deformations, and an elastic spring used to constrain rotation about the crack direction.

Table 5-6 Comparison of the dimensionless natural frequencies of undamaged SSSS plate from ABAQUS with previous studies.

Mode	1,1	1,2	2,1	2,2	3,1	1,3
VIPASA	19.74	49.35	49.35	78.96	98.70	98.70
Liew et al. (1994)	19.74	49.35	49.35	78.96	98.70	98.70
Stahl and Keer (1972)	19.74	49.35	49.35	78.96	98.70	98.70
Huang et al. (2011)	19.74	49.35	49.35	78.96	98.70	98.70
ABAQUS	19.74	49.69	49.69	79.37	100.82	100.82

As shown in Table 5-6, the non-dimensional natural frequencies of the intact plate obtained from the ABAQUS model match well with previous research and VIPASA models, especially for lower modes. Hence, the model is validated and can be used as a comparative test for different cracked cases. The same material parameters are defined in both portions of the plate: $E = 110 * 10^9 \text{ N} \cdot \text{m}^{-2}$; $\rho = 4480 \text{ kg} \cdot \text{m}^{-3}$; $\nu = 0.3$; $a = 0.1\text{m}$; $b = 0.1\text{m}$; $h = 0.001\text{m}$ (Same as the plate used in Figure 6-1), and three different crack models are discussed below.

The first cracked model **AT** (ABAQUS tie constraint only model), shown in Figure 5-7 (a), uses tie constraints to ensure the intact parts deform together. All displacements are constrained at the boundary, leaving the two portions to move freely with respect to each other in the crack region. For the cracked model shown in Figure 5-7 (b), the difference is the added multiple points constraints (MPC) which are intended to restrain the displacements in the damaged region. The MPC pin constraints used here restrain all displacements and release the rotations. However, for this model, the certain value of reduced stiffness caused by the crack cannot be defined by MPC pin constraints. Thus the second model cannot simulate a partial through-the-depth crack (**PTDC**). Referring to Caddemi and Caliò (2008) and Labib et al. (2014), a rotational spring can be used to simulate a crack and the model **ATCS** (ABAQUS model with tie, coupling and rotational spring constraints) in Figure 5-7 (c) aims to do this. For the **ATCS** model, tie constraints are still used in the intact parts and coupling constraints are chosen to restrain all displacements and rotations, except for the rotation about the crack direction. A rotational spring with stiffness calculated using Eq. 5-27 is then used to simulate the degraded stiffness of each cracked plate element.

$$KS_p = D * l_e / (h * C(d/h)) \quad \text{Eq. 5-27}$$

Here l_e is the crack length in each cracked element. Because ABAQUS can always model a crack at the edge of the element by re-assembling or re-meshing, instead of the integration procedure in the pure FE model (Eq. 5-24 and Eq. 5-25), ABAQUS **ATCS** simply adopts Eq. 5-27 to allocate the corresponding rotational spring stiffness at two nodes. The results obtained from the **AT** and **ATCS** models are presented and compared in Chapter 6.

5.2.3.2 Further Remarks

ABAQUS is a commercial software that provides suitable results for researchers. However, due to the chosen element type and quantity as well as the methods chosen to simulate the crack, it still shows small differences in predicted behaviour for this particular problem compared with previous studies (shown in Table 5-6). Furthermore, similar problems will occur with the ABAQUS model as have been found in previous studies, mostly due to the degradation rates of different natural frequencies being different, resulting in sequencing problems which have been discussed further in section 4.2.2. For an intact square plate, different mode shapes (e.g. $(m, n) = (1, 2)$ or $(m, n) = (2, 1)$) will be associated with coincident natural frequencies. This problem will be automatically resolved when introducing a crack or changing the aspect ratio of the plate, since the symmetry of the problem is violated.

5.2.4 Cracked Plate Modelling in Hybrid Approach

Cracked plate modelling in VICONOPT has been introduced for all through-the-length cracks, with the VICONOPT cracked model showing high efficiency and convincing results. However, VICONOPT can only model prismatic structures. When arbitrary cracks result in a problem which is not prismatic, this method loses efficacy. Hence, the FE method is introduced to increase versatility when modelling arbitrary cracks, effectively compensating for the limitation of ESM. The resulting hybrid rectangular plate model containing an arbitrary crack is shown in Figure 4-1.

The rectangular hybrid plate model is divided into two parts, as shown in Figure 4-1. The cracked part is modelled by the FE method coupling with ESM for the intact part. The displacements and rotations at the boundaries are constrained by Lagrangian Multipliers as introduced in Chapter 3.4. The natural frequencies are determined by the Wittrick-Williams algorithm, and mode shapes are obtained by a random force vector method proposed by Hopper and Williams (1977). Suliman (2018) studied the hybrid modelling of delaminated composite plates, this study will focus on the hybrid modelling of cracks in isotropic plates.

5.2.4.1 Essential Derivation and Explicit Expressions of the Dynamic Stiffness Matrix of ESM

The stiffness matrix of the ESM part of the hybrid model was first proposed by Wittrick and Williams (1974), and constitutes an essential part of the software VIPASA. However, for in-plane shear loading or composite materials, the mode shapes will be skewed, and the end conditions will not be satisfied. In order to address this, Lagrangian Multipliers were introduced by Williams and Anderson (1983) to couple different wavelengths and extend the applicability of VIPASA as illustrated in Eq. 3-23 and Eq. 3-24 of Chapter 3.4. This new application, named VICON, comprised a series of VIPASA stiffness matrices coupled by Lagrangian Multipliers.

The VFM model comprises two different parts. The FE method is utilised to obtain the vibration characteristics of the damaged part, and details of the FE stiffness and equivalent mass matrices have been given in section 5.2.2. For efficiency, ESM is used to calculate the vibration parameters of the intact part. The FE and ESM matrices are merged to represent the whole plate. Section 3.5 gave a brief background to the dynamic stiffness matrix of ESM and presented the elastic properties of out-of-plane and in-plane systems individually. As mentioned before, only the out-of-plane stiffness matrix is considered in this study which is presented in Eq. 3-29. This equation allows the derivation of exact analytical expressions for all the elements in Eq. 3-28. When the plate has orthotropic bending properties, the k_{ij} in Eq. 3-27 can be then deduced as (Wittrick and Williams 1974):

$$\begin{aligned}
 \mathbf{k}_{11} &= \begin{bmatrix} S_{MM} & -S_{MQ} \\ -\bar{S}_{MQ} & S_{QQ} \end{bmatrix} \\
 \mathbf{k}_{22} &= \begin{bmatrix} S_{MM} & \bar{S}_{MQ} \\ S_{MQ} & S_{QQ} \end{bmatrix} \\
 \mathbf{k}_{12} = \bar{\mathbf{k}}_{21}^t &= \begin{bmatrix} f_{MM} & f_{MQ} \\ -f_{MQ} & -f_{QQ} \end{bmatrix}
 \end{aligned}
 \tag{Eq. 5-28}$$

Here a bar expresses the complex conjugate, and superscript t represents the transpose. S_{MM} , S_{QQ} are always real, while the elements S_{MQ} , f_{MM} , f_{MQ} and f_{QQ} are in general complex. If $D_{13} = D_{23} = 0$ and shear loading is zero, all the elements will be real.

The out-of-plane motion (Wittrick and Williams 1974) of the individual element shown in Figure 3-4 (b) and Figure 3-5 is given by:

$$q_x = \frac{\partial m_x}{\partial x} + \frac{\partial m_{xy}}{\partial y} \quad \text{Eq. 5-29}$$

$$q_y = \frac{\partial m_{xy}}{\partial x} + \frac{\partial m_y}{\partial y}$$

$$\frac{\partial q_x}{\partial x} + \frac{\partial q_y}{\partial y} = m \frac{\partial^2 w}{\partial t^2} \quad \text{Eq. 5-30}$$

Here q_x and q_y are the lateral shearing forces per unit length, and m is the mass per unit area of the plate. To eliminate the lateral shearing forces, Eq. 5-29 and Eq. 5-30 should satisfy the equation:

$$\frac{\partial^2 m_x}{\partial x^2} + 2 \frac{\partial^2 m_{xy}}{\partial x \partial y} + \frac{\partial^2 m_y}{\partial y^2} - m \frac{\partial^2 w}{\partial t^2} = 0 \quad \text{Eq. 5-31}$$

Substituting into Eq. 3-29, the differential equation for w is given as:

$$\frac{\partial^4 w}{\partial y^4} + 2(\alpha_{12} + 2\alpha_{33}) \frac{\partial^4 w}{\partial x^2 \partial y^2} + \alpha_{11} \frac{\partial^4 w}{\partial x^4} + \frac{1}{D_{22}} + m \frac{\partial^2 w}{\partial t^2} = 0 \quad \text{Eq. 5-32}$$

The parameters α_{11} , α_{12} and α_{33} are dimensionless ratios between the flexural rigidities:

$$\alpha_{11} = D_{11}/D_{22}, \alpha_{12} = D_{12}/D_{22}, \alpha_{33} = D_{33}/D_{22}, \alpha_{13} = 0, \alpha_{23} = 0 \quad \text{Eq. 5-33}$$

The underlying assumption of the ESM is that the mode is sinusoidal in the longitudinal x -direction. Dimensionless parameters T , S and L are defined as (Wittrick and Williams 1974):

$$\begin{aligned} T &= \alpha_{12} + 2\alpha_{33} \\ S &= 0 \\ L &= \frac{\lambda^2}{\pi^2 D_{22}} + (+4m\lambda^2\rho^2) + (T)^2 - \alpha_{11} \end{aligned} \quad \text{Eq. 5-34}$$

Here, ρ is the density per unit area, and explicit expressions for the above stiffness parameters need to be dealt with individually to avoid the appearance of indeterminacies as in the following cases: (a) $S = 0, L > 0$; (b) $S = 0, L < 0$; (c) $S = 0, L = 0$. The frequency is n and the half-wavelength is λ .

For free vibration of an orthotropic plate, $S = 0$ and the eigenvalue calculation will depend on L as for the following different cases (Wittrick and Williams 1974). The out-of-plane stiffness coefficients are given by Eq. 5-35:

$$\begin{aligned}
 S_{MM} &= \left(\pi D_{22} / \lambda \right) Z^{-1} R_1 \\
 S_{QQ} &= \left(\pi^3 D_{22} / \lambda^3 \right) Z^{-1} R_2 \\
 S_{MQ} &= \left(\pi^2 D_{22} / \lambda^2 \right) \{ (A - \hat{\nu} - Z^{-1} R_3) \} \\
 f_{MM} &= \left(\pi D_{22} / \lambda \right) Z^{-1} (R_4) \\
 f_{QQ} &= \left(\pi^3 D_{22} / \lambda^3 \right) Z^{-1} [A R_4 + F R_5] \\
 f_{MQ} &= \left(\pi^2 D_{22} / \lambda^2 \right) Z^{-1} R_6 \\
 \hat{\nu} &= \alpha_{12}
 \end{aligned}
 \tag{Eq. 5-35}$$

Case (a). $S = 0, L > 0$, The computational sequence of the parameters in the dynamic stiffness matrix is:

1. Calculate parameters α and γ ;

$$\begin{aligned}
 \alpha^2 &= T + L^{\frac{1}{2}}, \\
 \gamma^2 &= T - L^{\frac{1}{2}}
 \end{aligned}
 \tag{Eq. 5-36}$$

2. Calculate parameters s_1, c_1, s_3 and c_3 ;

$$\begin{aligned}
 s_1 &= (1/\alpha) \sinh \omega \alpha \\
 c_1 &= \cosh \omega \alpha \\
 s_3 &= (1/\gamma) \sinh \omega \gamma \\
 c_3 &= \cosh \omega \gamma
 \end{aligned}
 \tag{Eq. 5-37}$$

In Eq. 5-36, $\omega = \pi b / \lambda$ and b is the plate width.

3. Next obtain:

$$\begin{aligned}
 Z &= Ts_1s_3 - c_1c_3 + 1 \\
 R_1 &= L^{\frac{1}{2}}(c_1s_3 - c_3s_1) \\
 R_2 &= L^{\frac{1}{2}}(\alpha^2c_3s_1 - \gamma^2c_1s_3) \\
 R_3 &= Ls_1s_3 \\
 R_4 &= L^{\frac{1}{2}}(s_1 - s_3) \\
 R_5 &= (s_1 + s_3) \\
 R_6 &= L^{\frac{1}{2}}(c_1 - c_3)
 \end{aligned} \tag{Eq. 5-38}$$

4. The out-of-plane stiffness coefficients are then given as Eq. 5-35, for case (a):

$$\begin{aligned}
 A &= T, F = L \\
 I_3 &= I_4 = I_5 = I_6 = 0
 \end{aligned} \tag{Eq. 5-39}$$

Case (b). $S = 0, L < 0$,

1. Calculate parameters α , γ and β ;

$$\begin{aligned}
 \alpha &= \gamma = \left\{ \frac{1}{2} \left[\sqrt{(T^2 - L)} + T \right] \right\}^{\frac{1}{2}} \\
 \beta &= \left\{ \frac{1}{2} \left[\sqrt{(T^2 - L)} - T \right] \right\}^{\frac{1}{2}}
 \end{aligned} \tag{Eq. 5-40}$$

2. Calculate parameters s_1 , c_1 , s_3 and c_3 from Eq. 5-37, with

$$\begin{aligned}
 s_2 &= \sin \omega\beta \\
 c_2 &= \cos \omega\beta
 \end{aligned} \tag{Eq. 5-41}$$

3. It may be noted that $s_1 = s_3$ and $c_1 = c_3$ since $\alpha = \gamma$. Also, since $S = 0$, $B_1 = B_3$, so that $I_3 = I_4 = I_5 = I_6 = 0$. The next calculation is:

$$\begin{aligned}
 A &= T + 2\beta^2 \\
 F &= L + 8T\beta^2 + 12\beta^4 \\
 B_1 &= 2\beta^2 \\
 B_3 &= 2\beta^2
 \end{aligned} \tag{Eq. 5-42}$$

4. Then, calculate

$$\begin{aligned}
 Z &= (A + \beta^2)s_1s_3 - c_1c_3 + 2c_2^2 - 1 \\
 R_1 &= B_1c_1s_3 - B_3c_3s_1 + 4\beta c_2s_2 \\
 R_2 &= 4A\beta c_2s_2 + (F - AB_1)c_1s_3 + (F - AB_3)c_3s_1 \\
 R_3 &= F s_1 s_3 \\
 R_4 &= 2\beta s_2(c_1 - c_3) - c_2(B_1s_3 + B_3s_1)c_3s_1 \\
 R_5 &= c_2(s_3 + s_1) \\
 R_6 &= \beta s_2[(T + A + B_1) + s_3(T + A + B_3)]
 \end{aligned}
 \tag{Eq. 5-43}$$

5. The final out-of-plane stiffness coefficients use the same expressions as in equation Eq. 5-35.

Case (c). $S = 0, L = 0,$

1. The first calculation is:

$$\begin{aligned}
 s_4 &= \frac{\sinh \omega \sqrt{T}}{\omega \sqrt{T}} \\
 c_4 &= \cosh \omega \sqrt{T} \\
 Z &= \frac{1}{2} (s_4^2 - 1)
 \end{aligned}
 \tag{Eq. 5-44}$$

2. The out-of-plane stiffness parameters are then choosing the following equations:

$$\begin{aligned}
 S_{MM} &= \left(D_{22}/b \right) Z^{-1} (s_4 c_4 - 1) \\
 S_{QQ} &= \left(D_{22}/b^3 \right) \omega^2 Z^{-1} T (s_4 c_4 + 1) \\
 S_{MQ} &= - \left(D_{22}/b^2 \right) \omega^2 (\hat{v} + T + T Z^{-1}) \\
 f_{MM} &= \left(D_{22}/b \right) Z^{-1} (c_4 - s_4) \\
 f_{QQ} &= \left(D_{22}/b^3 \right) Z^{-1} \omega^2 T (c_4 + s_4) \\
 f_{MQ} &= - \left(D_{22}/b^2 \right) Z^{-1} \omega^2 T s_4
 \end{aligned}
 \tag{Eq. 5-45}$$

5.2.4.2 VICON Analysis with FEM---Global Stiffness Matrix

Since all the parameters of the out-of-plane stiffness matrix have been calculated for the intact part, the stiffness matrices for the different half-wavelengths can then be assembled as in Eq. 3-24 and Eq. 3-34. The last row of Eq. 3-24 is the global constraint matrix of the ESM part, where \mathbf{E}_i is the constraint matrix related to half-wavelength λ_i of the region $0 \leq x < l$ that contains the terms $e^{i\pi x/\lambda_i}$. Also, the static stiffness and equivalent mass matrix of a single element in the FE method are shown in Table 5-2, Table 5-3, Table 5-4

and Table 5-5 in section 5.2.2. These element stiffness and mass matrices are then assembled into a global FE dynamic stiffness matrix with additional spring stiffnesses to represent the damaged part:

$$\mathbf{K}_{FE} = \mathbf{k} - n^2 \mathbf{m} \quad Eq. 5-46$$

In this equation, n is the frequency in rad/s; \mathbf{k} is the static stiffness matrix and \mathbf{m} is the equivalent mass matrix. Then, the hybrid dynamic stiffness matrix comprises the global VIPASA stiffness matrix and dynamic FE stiffness matrix coupled by Lagrangian Multipliers as:

$$\mathbf{K}_{Global} = \begin{bmatrix} \mathbf{K}_{Global\ VIPASA} & \mathbf{0} & \mathbf{C}_1^H \\ \mathbf{0} & \mathbf{K}_{FE} & \mathbf{C}_2^T \\ \mathbf{C}_1 & \mathbf{C}_2 & \mathbf{0} \end{bmatrix} \quad Eq. 5-47$$

where \mathbf{C}_1 and \mathbf{C}_2 are constraint matrices that enforce equal displacements and rotations at the boundaries connecting the intact and damaged regions. \mathbf{C}_1 also contains any point support conditions in the intact region. The detail of the constraint matrices is introduced in section 3.4 and will be shown in the MATLAB code in the Appendix G. T denotes the transpose and H is the Hermitian operator. The Wittrick-Williams algorithm is then introduced in its simplified form Eq. 3-19 and used to calculate natural frequencies under any desired values.

5.2.4.3 Further Remarks

The new VFM method balances the efficiency, accuracy and versatility of its constituent components (VICONOPT and FE Method). Lagrangian Multipliers are used to ensure the compatibility between different modelling parts. VFM can analyse arbitrary cracks with any length, location, orientation or depth. It can thus solve more complicated structural eigenvalue problems while guaranteeing computational efficiency. The particular case of a simply supported plate containing an arbitrary crack is solved in Chapter 6 and the relevant MATLAB codes are listed in the Appendix B.

It should be noted that the Wittrick-Williams algorithm is used to calculate the natural frequencies while the target is to triangulate the global stiffness matrix and determine the negative sign count. It is noted that pairs of half-wavelengths λ_i and $-\lambda_i$ will produce the same diagonal terms and hence the same contributions to the sign count. For computational efficiency, only positive half-wavelengths are considered in the VICON part and their sign count contributions are doubled. Suliman (2018) also made this observation when he studied the vibration characteristics of delaminated composite plates.

5.3 Mode Shapes of Cracked Plates

Natural frequencies are the main parameters studied in the thesis. As discussed before, for coincident modes or as the length of a crack increases, it can be difficult to recognise the right sequence of corresponding natural frequencies. Mode shapes are then introduced as a reference to help sort related modes.

Hopper and Williams (1977) proposed an extension of the “random force” method, called the PRT method, to determine the modes, and this method is applied here. The plate is divided into two parts, one part is damaged, and another one is intact. The mode shapes are plotted according to the vertical displacements calculated from Eq. 3-11 by dividing the plate into elements depend on the size of elements chosen in the model simulation. The global stiffness matrix is obtained from Eq. 5-47; the bending properties of each half-wavelength stiffness matrix in VICON are obtained from Eq. 5-35 to Eq. 5-45; the bending stiffness parameters of the static stiffness and equivalent mass matrices are obtained from Table 5-2, Table 5-3, Table 5-4 and Table 5-5. The calculated natural frequencies are obtained and used as trial values. The complete global stiffness equations at any of these trial values have the form:

$$\mathbf{K}_{VFM} = \begin{bmatrix} \mathbf{K}_{ESM} & \mathbf{0} & \mathbf{C}_1^H \\ \mathbf{0} & \mathbf{K}_{FE} & \mathbf{C}_2^T \\ \mathbf{C}_1 & \mathbf{C}_2 & \mathbf{0} \end{bmatrix} \begin{bmatrix} \mathbf{D}_{ESM} \\ \mathbf{D}_{FE} \\ \mathbf{D}_R \end{bmatrix} = \begin{bmatrix} \mathbf{P}_{ESM} \\ \mathbf{P}_{FE} \\ \mathbf{P}_R \end{bmatrix} \quad Eq. 5-48$$

Applying random \mathbf{P}_{ESM} and \mathbf{P}_{FE} , the equations are solved to find \mathbf{D}_{ESM} , \mathbf{D}_{FE} and \mathbf{D}_R . The vertical displacements can thus be extracted, and the mode shapes plotted for each natural frequency. It should be noted that, for plotting the ESM mode shapes, the vertical displacement at any point along the longitudinal direction can be determined according to the displacements obtained at the ends and then calculated using the explicit trigonometric functions given in Eq. 3-31. The displacement \mathbf{D}_A is a complex quantity so the real part is considered. Then the vectors \mathbf{D}_m are real, and the summation of the real part \mathbf{D}_m of \mathbf{D}_A is $\sum \cos(\pi x/\lambda_m)$. A constraint at the boundary of the damaged region applies a particular displacement in \mathbf{D}_A equal to the corresponding displacement in the FE part vector \mathbf{D}_F . Suppose these displacements are the i^{th} element of \mathbf{D}_A and the j^{th} element of \mathbf{D}_F then they must satisfy the constraint equation:

$$\mathbf{D}_A(i) - \mathbf{D}_F(j) = 0 \quad Eq. 5-49$$

Then, for each of the vectors \mathbf{D}_m , the coefficient $\mathbf{D}_m(i)$ is $\cos(\pi x/\lambda_m)$ and the coefficient of $\mathbf{D}_F(j)$ is -1. For more details on the mode shape calculations, the numerical procedure and related MATLAB code, please refer to the Appendix H. Corresponding numerical results and mode shapes for related cases are presented in Chapter 6. Appropriate normalisation is performed to display all the different mode shapes to the same scale, by dividing all the displacements by the maximum vertical displacement of each mode.

5.4 Conclusions

This chapter describes different approaches for the free vibration modelling of different boundary conditions and materials while a simply supported isotropic plate is used for validation and preliminary study. Various modelling approaches have been illustrated and the advantages and disadvantages of each discussed. Necessary derivations of related stiffness matrices and corresponding calculations of the parameters in those matrices are presented. A finite element ABAQUS model is shown in Chapter 5.2.3 as a comparative study to validate the reliability of the new proposed model.

A simply supported isotropic plate with an arbitrarily located and aligned crack is chosen to illustrate the new hybrid method VFM, for which a global dynamic stiffness matrix is assembled from stiffness matrices prepared from ESM and FEM. An upper triangular stiffness matrix is obtained by an advanced bandwidth method with partial Gauss elimination which is mentioned in section 4.2.3. The Wittrick-Williams algorithm (Wittrick and Williams 1971) is then introduced to iteratively calculate the natural frequencies under any desired value with the required precision. Finally, mode shapes are plotted based on the automatic sign method introduced in section 4.2.2 to analyse the vibration response of different modes in the correct sequence. All obtained results for comparison and validation will be shown in Chapter 6, and a prepared database will be used for the inverse problem of damage detection elaborated in Chapter 7.

VFM could be extended to more complicated cases, such as composite plates, stiffened plate or plates with different boundary conditions. This new method can solve vibration eigenvalue problems accurately and effectively, so satisfying the requirements for preliminary design in practical aerospace applications.

Chapter 6--- Single predefined damage analysis in plates

6.1 Introduction

Chapter 5 introduced different modelling techniques to simulate damage in plates under a range of materials and boundary conditions. The DSM software VICONOPT and the finite element code ABAQUS utilized are widely used in various engineering areas, and it is not therefore required to validate the reliability of these methods. However, in order to improve accuracy and computational efficiency, a new hybrid method VFM has been proposed, and it is necessary to verify its applicability, and in particular that of the FE component used to model the damaged part of the plate.

In this chapter, vibration parameters obtained from the model of a simply supported isotropic damaged plate (SSSS) simulated in Chapter 5 (Figure 6-1) are discussed and compared with previous studies. The dimension and related properties are defined as: $E = 110 * 10^9 Nm^{-2}$; $\rho = 4480 kgm^{-3}$; $\nu = 0.3$; $b = 0.1m$; $a = 0.1m$; $h = 10^{-3}m$.

Different types of damage are considered, including: all through-the-length delamination (ATLD); all through-the-length crack (ATLC); parallel part through-the-length crack (PTLC) and arbitrary direction crack (ADC). For PTLC, two different cases are discussed, one is an all through-the-depth crack (ATDC), and the another one is a partial through-the-depth crack (PTDC). For the ADC, the effect of different parameters is examined and discussed including the length, depth and orientation.

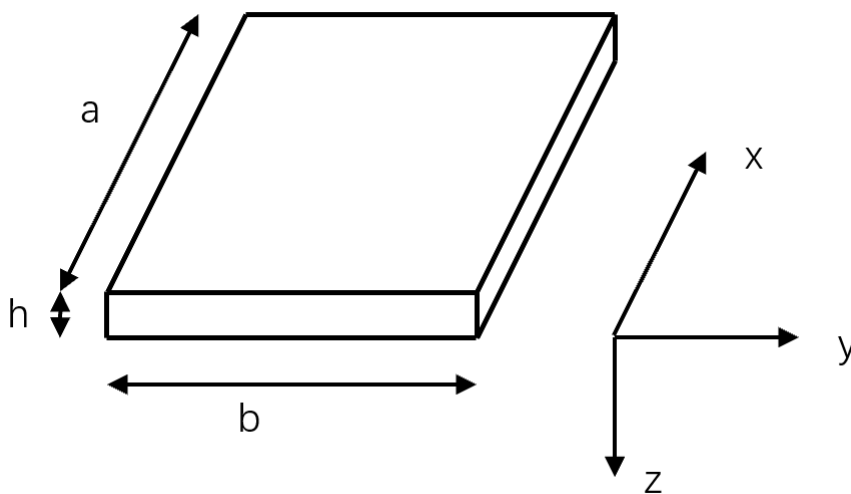


Figure 6-1 Simply supported isotropic square plate with corresponding notations.

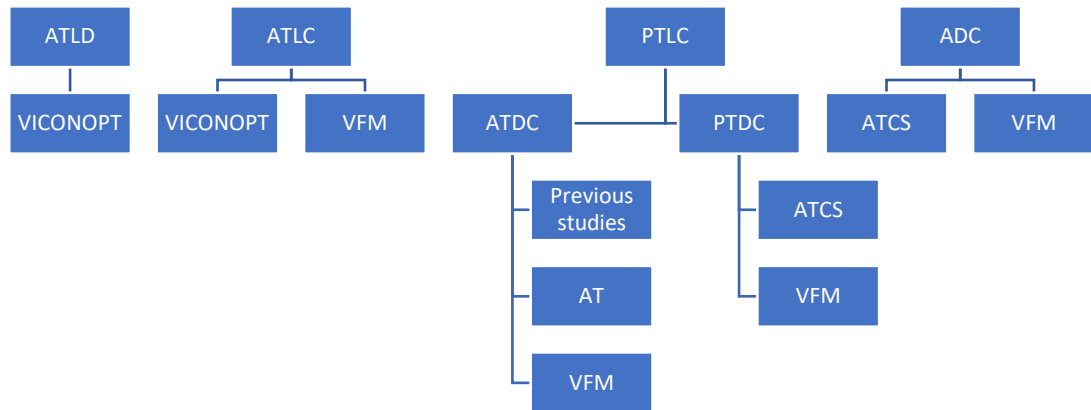


Figure 6-2 Different damaged cases studied by various approaches in the study.

AT is an ABAQUS cracked plate model which uses only tie constraints to simulate the crack; *ATCS* is an ABAQUS cracked plate model, which tie constraints are used to restrain displacements while a spring is used for the rotation along the crack direction and a coupling constraint is used to restrain the rotation for all other directions.

Figure 6-2 presents a flowchart of the different approaches included, and lists the comparative studies of the various damage cases. A proposed FE model will generate a damaged model for all cases, and so an ABAQUS model will be prepared for all cases except ATLD. Because ATLC retains the prismatic status in the longitudinal direction, VICONOPT can still be used and provides validation for the newly proposed FE model. Comparison studies will be discussed for PTLC, including Stahl and Keer (1972), Liew et al. (1994), and Huang et al. (2011). For ADC, such generality is absent from the literature, with results commonly restricted to cracks located at the centre, or the edge of the plate, running parallel to one of edges of the plate, over the full length of width, or through the full thickness. Hence, ABAQUS is chosen for ADC to verify the reliability of the proposed FE model and VFM.

Validation in this study will be based on a simply supported isotropic square plate as the most straightforward example to verify the feasibility of the proposed FE model and VFM technique. Suliman (2018) previously studied delaminations in isotropic and anisotropic plates using the VFM approach. This study therefore will focus on arbitrary cracks. Cracks with different locations, orientations, depths and lengths will be studied in order to prepare for the inverse problem of detecting damage. A series of numerical analyses are presented, and the related MATLAB codes are attached in the Appendix. The computational cost of different techniques will also be evaluated and discussed.

6.2 All through-the-length delamination

6.2.1 Model

Figure 6-3 (a) shows an example of a simply supported plate with an all through-the-length delamination. The delaminated region is shown in Figure 6-3 (b) and has width β , while the delamination location (the location of the widthwise delamination region β) may be different. The depth of the delamination is d , which divides the damaged region into two parts. The analysis ignores the damping factor, contact and penetration between the two parts. The upper and lower delaminated parts deform separately but coupled at the boundaries of the damaged region have equal deformations imposed by point constraints, as shown in Figure 6-3 (b). The plate dimensions are shown in Figure 6-3 (a); the mass per unit volume is $2.3 \times 10^{-6} \text{kg mm}^{-3}$; Young's modulus in the direction of the x axis is 130kN mm^{-2} ; Young's modulus perpendicular to the x axis is 10kN mm^{-2} ; in-plane shear modulus $G_{xy} = G_{yz} = G_{xz} = 5 \text{kN mm}^{-2}$ and the major Poisson's ratio is 0.3. The plate comprises 16 unidirectional layers each with uniform thickness 0.125mm. The sequence of those layers in the plate is $[0/+45/-45/90/0/+45/-45/90]$ s. This particular composite case is chosen from Damghani et al. (2011). The laminated plate in this study will only be discussed as a comparative case and used in the preliminary stage to understand the use of the VFM model. For more detail of different stacking sequences please refer to Suliman (2018). The modelling of an arbitrary crack in isotropic plate and related inverse problem is the main target of this study. The original VICONOPT data of the delamination case is attached in the Appendix I.

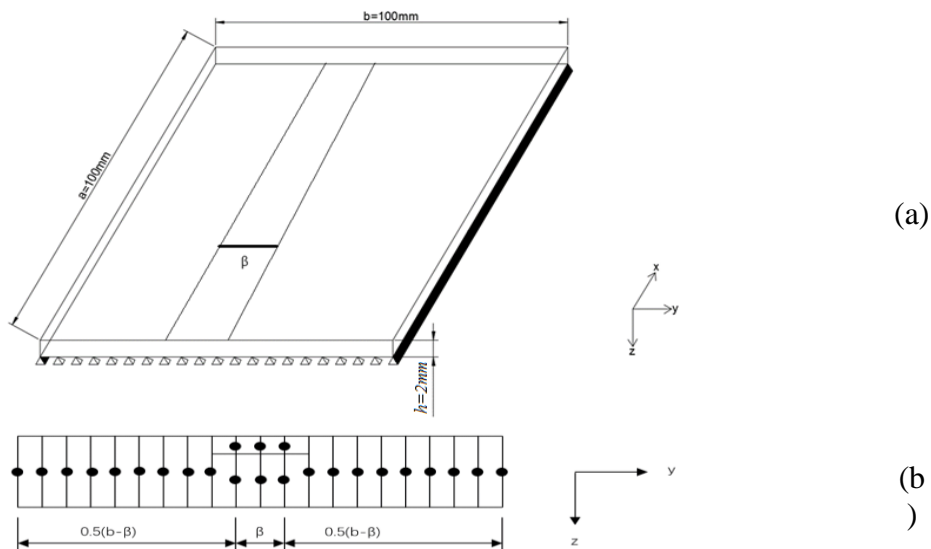


Figure 6-3 All through-the-length delamination plate model.

(a) All through-the-length delamination with damaged width β ; (b) the cross-section of the damaged plate, point supports are defined at the edge of each strip along the transverse direction except at the boundary.

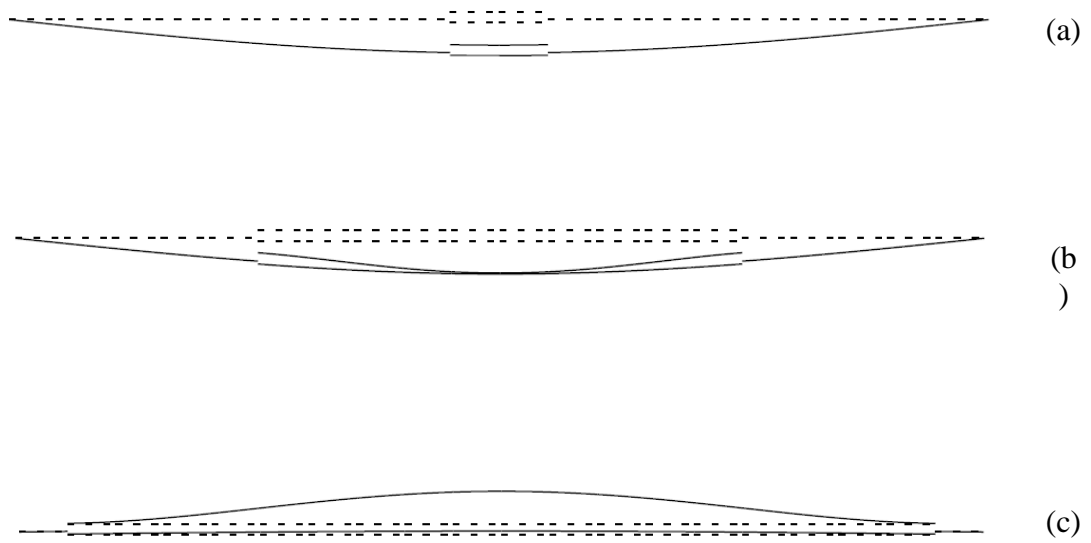


Figure 6-4 Three different transformation statuses which exist during the propagation of delamination.

(a) $\beta=0.2$; (b) $\beta=0.6$; (c) $\beta=0.9$.

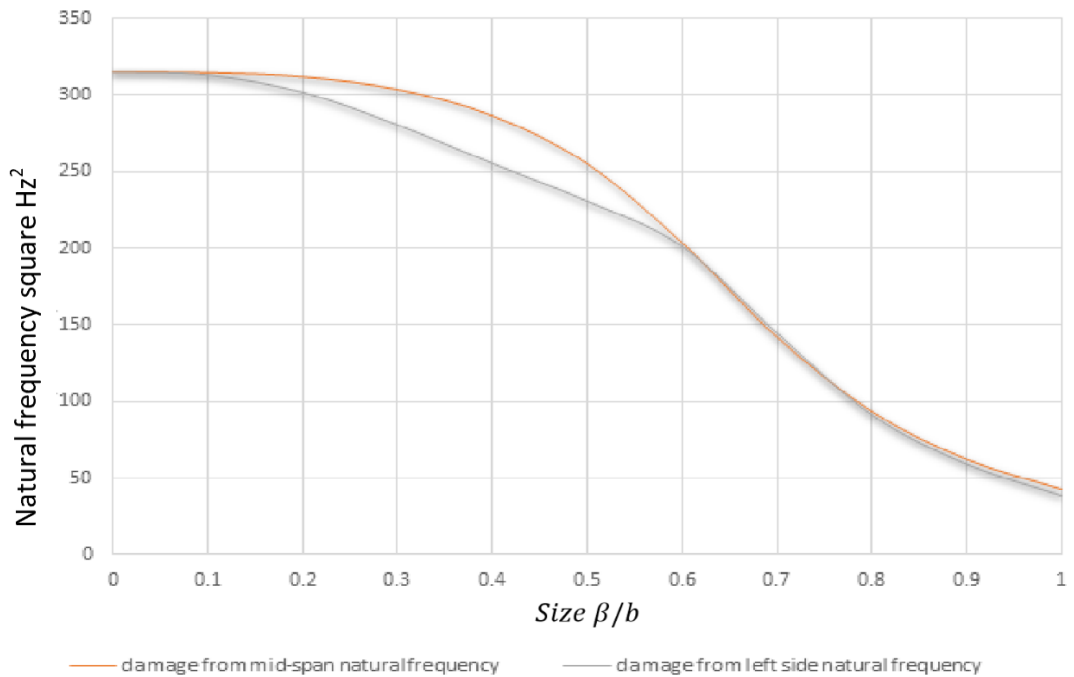


Figure 6-5 The propagation of delamination with different starting points.

6.2.2 Three different deformation statuses

Using the modelling strategy and parameters presented in Chapter 5.2.1 and repeated separately above, some useful numerical results can be obtained from the VICONOPT model. With the propagation of the delamination (by increasing the delamination width β), the deformations of the plate can be grouped into three stages (Figure 6-4): the global stage, the transition stage and the local stage. Figure 6-4 shows the mode shapes obtained from VICONOPT illustrating the development of a centrally located delamination. Figure 6-5 shows the reduction in natural frequencies which occurs as the delamination grows, for both central and edge delaminations.

For $\beta \leq 0.2b$, Figure 6-4 (a) shows the two parts in the damaged region deform together indicating global deformation behaviour. Figure 6-5 shows that the corresponding natural frequencies decrease only slightly in a near- linear way. They then show a rapid reduction as the delamination grows (with $0.2b$ as the limit), while the two parts in the damaged region start to deform separately (Figure 6-4 (b)). The deformation status then changes into the local state (Figure 6-4 (c)), when the severity of delamination is large (Figure 6-5). Figure 6-5 also indicates reductions in the natural frequencies during the propagation of an edge located delamination showing similar development trends as the delamination developing from the middle of plate.

6.2.3 Size effect and location effect

The development of a delamination will cause a degradation of the stiffness of the plate, and result in a change of vibration parameters. Generally, two main factors control the change in the natural frequencies: severity and location. Table 6-1 illustrates the effect of the severity of a delamination starting at different locations (OL), showing the original natural frequencies and change in squared natural frequencies, for delaminations starting from three different points with increasing delamination width. Simulations chosen in the study are not penetrated damage, thus the changes in natural frequencies caused by the limited damaged region are relatively small. Here, $\xi=0.01$ or 1 and Eigen=1-4 denote different modes, Eigen=1-2 is the combination of different half-wavelength modes in the VICONOPT model in chronological order; OL is the original location of the y-coordinate at the midpoint of the delamination region; DS is the width of delamination ; DLF is the natural frequency; CNF² is the difference of square natural frequencies between the intact and damaged cases; Δ_{ij} is the ratio of the change in CNF² {DS = 10: DS = 20} and {DS = 20: DS = 40}. Each value in Table 6-1 keeps four decimals for the natural frequencies and related change natural frequencies.

Table 6-1 All through-the-length delamination starting at different original locations with varying width, delamination depth $d=0.5\text{mm}$.

OL, $y=50\text{mm}$	$\xi=0.01$, EIGEN=1-2			$\xi=0.01$, EIGEN=3-4		
DS (β ,mm)	DLF (ω ,Hz)	CNF² (Ψ_{ij} ,Hz ²)	Ratio (Δ_{ij})	DLF (ω ,Hz)	CNF² (Ψ_{ij} ,Hz ²)	Ratio (Δ_{ij})
0	44.4189			74.0617		
10	44.1677	0.0113		73.7718	0.0078	
20	42.7989	0.0716	6.3490	71.9727	0.0556	7.1190
30	39.8370	0.1957		61.4693	0.3111	
40	33.9011	0.4175	5.8300	41.2081	0.6904	12.4100
OL, $y=50\text{mm}$	$\xi=1$, EIGEN=1			$\xi=1$, EIGEN=3		
DS (β ,mm)	DLF (ω ,Hz)	CNF² (Ψ_{ij} ,Hz ²)	Ratio (Δ_{ij})	DLF (ω ,Hz)	CNF² (Ψ_{ij} ,Hz ²)	Ratio (Δ_{ij})
0	28.1417			110.5251		
10	28.0978	0.0031		109.2139	0.0236	
20	27.7850	0.0252	8.0770	100.9893	0.1651	7.0000
30	26.9141	0.0854		70.4062	0.5942	
40	25.0794	0.2058	8.1700	45.7329	0.8288	5.0200
OL, $y=40\text{mm}$	$\xi=0.01$, EIGEN=1-2			$\xi=0.01$, EIGEN=3-4		
DS (β ,mm)	DLF (ω ,Hz)	CNF² (Ψ_{ij} ,Hz ²)	Ratio (Δ_{ij})	DLF (ω ,Hz)	CNF² (Ψ_{ij} ,Hz ²)	Ratio (Δ_{ij})
0	44.4189			74.0617		
10	44.1879	0.0104		73.7497	0.0084	
20	42.9151	0.0666	6.4170	71.8705	0.0583	6.9340
30	41.2994	0.1355		57.9506	0.3878	
40	34.1455	0.4091	6.1450	41.2571	0.6897	11.8300
OL, $y=40\text{mm}$	$\xi=1$, EIGEN=1			$\xi=1$, EIGEN=3		
DS (β ,mm)	DLF (ω ,Hz)	CNF² (Ψ_{ij} ,Hz ²)	Ratio (Δ_{ij})	DLF (ω ,Hz)	CNF² (Ψ_{ij} ,Hz ²)	Ratio (Δ_{ij})
0	28.1417			110.5251		
10	28.0993	0.0030		109.3205	0.0217	
20	27.7985	0.0243	8.0540	101.3852	0.1586	7.3140
30	25.0988	0.2046		72.5053	0.5697	
40	25.1998	0.1981	8.1730	44.7194	0.8363	5.2750

Table 6-1 (continued)

OL, y=35mm	$\xi=0.01$, EIGEN=1-2			$\xi=0.01$, EIGEN=3-4		
DS (β ,mm)	DLF (ω ,Hz)	CNF² (ψ_{ij} ,Hz ²)	Ratio (Δ_{ij})	DLF (ω ,Hz)	CNF² (ψ_{ij} ,Hz ²)	Ratio (Δ_{ij})
0	44.4189			74.0617		
10	44.2115	0.0093		73.7298	0.0089	
20	43.0538	0.0605	6.4960	71.7707	0.0609	6.8120
30	40.4041	0.1726		62.1506	0.2958	
40	34.4720	0.3977	6.5720	41.3278	0.6886	11.3100
OL, y=35mm	$\xi=1$, EIGEN=1			$\xi=1$, EIGEN=3		
DS (β ,mm)	DLF (ω ,Hz)	CNF² (ψ_{ij} ,Hz ²)	Ratio (Δ_{ij})	DLF (ω ,Hz)	CNF² (ψ_{ij} ,Hz ²)	Ratio (Δ_{ij})
0	28.1417			110.5251		
10	28.1011	0.0029		109.4474	0.0194	
20	27.8141	0.0232	8.0250	101.9154	0.1497	7.7150
30	27.0220	0.0780		70.5288	0.5928	
40	25.3452	0.1889	8.1580	44.7255	0.8362	5.5850

As Figure 6-5 shows, for small delaminations the relationship between the reduction of the natural frequencies square and the propagation of delamination width nearly remains linear. The ratio Δ_{ij} could then be analogous from Table 6-1 to the relationship of severity in Eq. 6-1.

$$\Delta_{ij+1}/\Delta_{ij} \approx \left(\frac{\beta_{ij+1}}{\beta_{ij}}\right)^\Delta \quad \text{Eq. 6-1}$$

Here i denotes the chronological sequence of the modes, and j is the chronological sequence of the delamination propagation of width. The severity factors Δ deduced from Table 6-1 show that as DS doubles, the Δ_{ij} increases by a factor of 8, hence the severity index Δ here is achieved as three by Eq. 6-1. The severity recovery procedure Eq. 6-1 could be used in the inverse problem to predict delamination severity according to the reduced natural frequencies.

Next the location effect is studied based on a delamination of fixed width which is located at different places along the y -axis as shown in Table 6-2. Each value in Table 6-2 keeps four significant decimals; DL is the delamination location; DLF and CNF² keep the same meaning as in Table 6-1; ω_{i0} is the natural frequency of the intact plate; i here represent different modes; ξ and EIGEN relates to different modes as in Table 6-1.

Table 6-2 All through-the-length delamination with fixed width ($\beta = 10\text{mm}$) at varying locations (depth $d=0.5\text{mm}$).

	$\omega_{10}=74.0617\text{Hz}$ $\xi = 0.01, \text{EIGEN}=3-4$		$\omega_{20}=110.5251\text{Hz}$ $\xi = 1, \text{EIGEN}=3$		$\omega_{30}=28.1417\text{Hz}$ $\xi = 1, \text{EIGEN}=1$	
DL (y, mm)	DLF (ω , Hz)	CNF² (Ψ_{ij}, Hz^2)	DLF (ω , Hz)	CNF² (Ψ_{ij}, Hz^2)	DLF (ω , Hz)	CNF² (Ψ_{ij}, Hz^2)
5	73.7660	0.0080	110.4060	0.0022	28.1133	0.0020
15	73.7323	0.0089	110.1750	0.0063	28.1105	0.0022
25	73.7081	0.0095	109.8010	0.0131	28.1058	0.0026
35	73.7298	0.0089	109.4470	0.0194	28.1011	0.0029
45	73.7657	0.0080	109.2410	0.0231	28.0982	0.0031
55	73.7657	0.0080	109.2410	0.0231	28.0982	0.0031
65	73.7298	0.0089	109.4470	0.0194	28.1011	0.0029
75	73.7081	0.0095	109.8010	0.0131	28.1058	0.0026
85	73.7323	0.0089	110.1750	0.0063	28.1105	0.0022
95	73.7660	0.0080	110.4060	0.0022	28.1133	0.0020

Figure 6-6 plots the value of change in squared natural frequencies square from Table 6-2 against delamination location. The natural frequency curve for each mode approximately matches a trigonometric function. Hence, Eq. 7-2 is introduced to normalise the size effect, and the location of a single delamination can then be detected by solving the inverse problem numerically. More detail on the normalisation procedure and delamination inverse problem analysis will be discussed in Section 7.3.1.

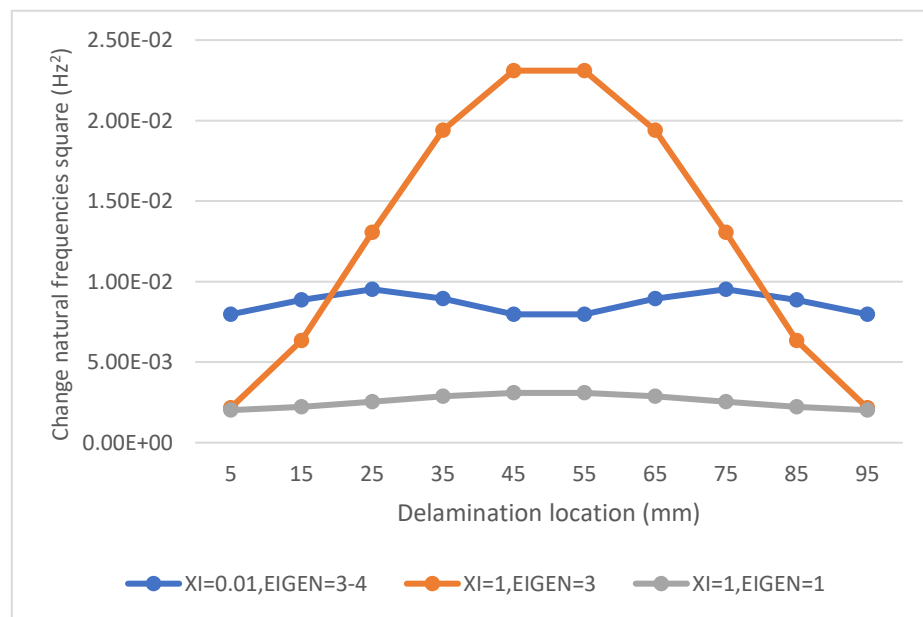


Figure 6-6 All through-the-length delamination with fixed damaged width at a different locations along the y-axis.

6.3 Parallel all through-the-length crack

6.3.1 Model

Since VICONOPT and the hybrid model for delaminations in composites (Suliman 2018) have been validated, the remainder of Chapter 6 will focus on validating the proposed FE crack modelling technique which will be incorporated into the hybrid method. This will be done through comparison with previous studies for different crack cases (Sections 6.3, 6.4 and 6.5). In section 6.3 for an all through-the-length crack, and the properties of the plate remain longitudinally invariant. Hence the damaged plate remains its prismatic status, and can be modelled using VICONOPT. A comparative study will therefore be made between the VICONOPT model and the advanced FE model (AFE) (the proposed FE model incorporating cracks presented in section 5.2.2), followed by a brief example for the case when the ATLC runs all through-the-depth. For partial through-the-length-crack cases (section 6.4), the natural frequencies obtained by VFM for an intact plate (Table 6-3) will be compared with one of the partial through-the-length crack cases (Table 6-14 to Table 6-16) to examine the hybrid model for the consistency of both ESM and FEM part.

Figure 6-1 shows the overall dimension and properties of the isotropic simply supported plate to be considered. Figure 6-7 (a) and (b) show the location of the crack in the VICONOPT model (crack angle 0°) and the AFE model (crack angle 90°), respectively. The VICONOPT model splits the plate into 10 strips with the same width and properties. Point supports are added to each strip along the transverse edge. The crack is simulated as a spring based on the same assumptions as in Chapter 5.2.1. All of the data produced from AFE will be normalised to provide non-dimensional results, which can simply be compared with previous studies regardless of the properties of the plates adopted by different researchers. It should be noted that the aspect ratio and boundary conditions will affect the non-dimensional results and same conditions need to be chosen in the comparative study. Eq. 6-2 expresses the normalisation procedure as:

$$\bar{\omega}_{mn} = \omega_{mn} * 2 * \pi * b^2 * \sqrt{\rho h / D} \quad \text{Eq. 6-2}$$

where ω is the natural frequency (Hz), b is the transverse dimension (y-axis) of the plate (m), ρ is the density (kg/m^3), h is the thickness of the plate (m) and D is the flexural rigidity of the plate ($\text{N} * \text{m}$).

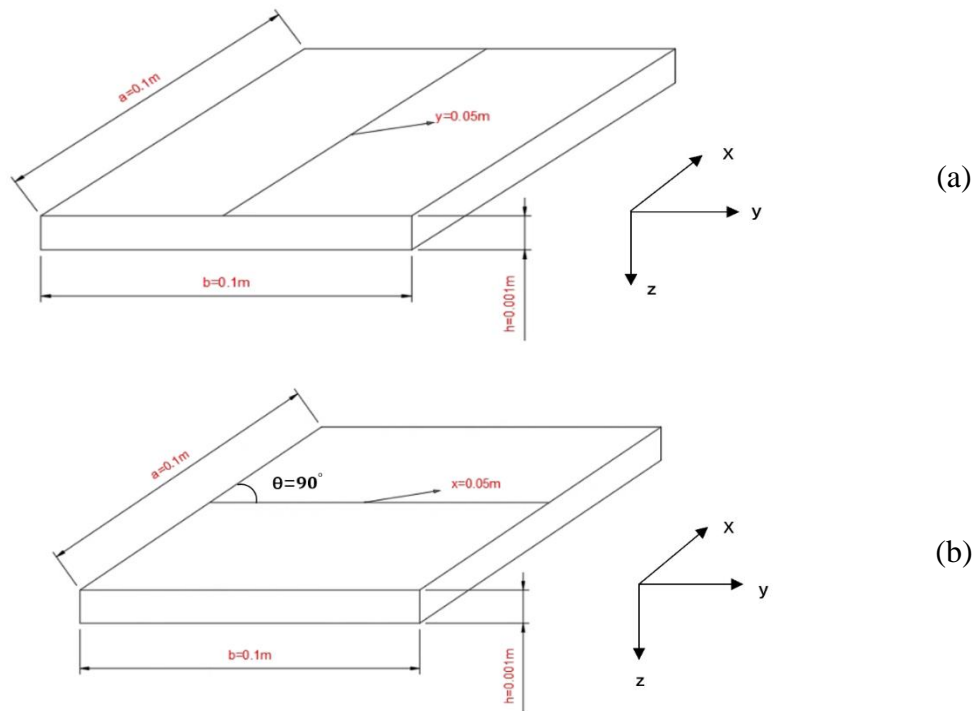


Figure 6-7 ATLC model simulated by different techniques at various location.
(a) VICONOPT model; (b) AFE model.

6.3.2 Results

For ATLC, two different cases are analysed. Table 6-4 to Table 6-7 show the original natural frequency (ONF) and the relative change in natural frequency (RCNF) for a crack located in the middle of the plate. Here RCNF is the difference between damaged natural frequency and the intact natural frequency as calculated from Eq. 6-3. Compared with delamination case, RCNF is used instead of the change natural frequencies square as the factor to detect the degradation of natural frequencies. ‘Change natural frequencies square’ is the difference of natural frequencies square between the intact plate and damaged plate. The reason choosing ‘Change natural frequency square’ is that for some small severity damage cases, the magnitude of RCNF may not be enough to detect the change in natural frequencies.

$$\delta_{ij} = (\omega_{0ij} - \omega_{ij}) / \omega_{0ij} \quad \text{Eq. 6-3}$$

where δ denotes the RCNF, ω_{0ij} are the natural frequencies of the intact plate. i, j are eigen-numbers representing different modes for both the VICONOPT model and the AFE model, i.e. the number of half waves in the x and y directions, respectively. The depth ratio denotes the crack depth divided by the plate thickness and the crack angle is the

angle between the crack and the x -axis shown in Figure 5-6, which is 90° for these cases. Mode (m, n) refers to the original mode for the uncracked case, where (m, n) are the number of half-wavelengths along each axis. The mode shape may transform into more complicated cases when there is a crack. If there is a crossover between a higher mode and a lower mode, it can be detected through the mode shape detection procedure described in section 4.2.2 to correct the sequence and continue to record the results in the appropriate place. For a simply supported isotropic square plate, theoretical results for an intact plate (Eq. 6-4), derived by Beards and Miao (1996) can be used as a reference.

$$\bar{\omega} = \pi^2 * (m^2 + n^2) \quad \text{Eq. 6-4}$$

According to Eq. 6-3, Table 6-3 contains the non-dimensional natural frequencies of the intact plate calculated using the theoretical model, VICONOPT, AFE and VFM. For the VFM model, the FE region is in the middle and the two strips of ESM at the two sides as shown in Figure 4-1. The size of elements for FE is $16*8$, while the dimensions and properties of the plate are the same as in Figure 6-1. For the AFE model, the plate is divided into 400 rectangular elements, i.e. the mesh has 20 rows and 20 columns. The crack is centrally located as shown in Figure 6-7 (b). Due to the use of compliance to simulate crack, when the depth ratio is 1, Eq. 5-15 will be null. Hence, a depth ratio of 0.9999 is used to avoid numerical problems for the all through-the-depth crack of AFE model in MATLAB.

Examining the results, those obtained from VICONOPT are the same as the theoretical values, but those acquired from AFE are slightly higher. The natural frequencies obtained by VFM match well with the others except for modes (2,1) and (2,2). This may be due to modelling assumptions such as:

1. The conservative plate model based on classical thin plate theory and an old version of the shape function;
2. The size of elements for both VICONOPT and AFE model;
3. The constraint matrices applied at the boundaries.

Also, a similar difference exists in the literature observed by crack simulation from Eq. 5-15. Natural frequencies from different modes for the intact plate are presented in Table 6-3 and these will be used in the following tables. The comparisons in this study will use relative change in natural frequencies as the parameter to analyse the change of vibration characteristics.

Table 6-3 Non-dimensional natural frequencies---comparison for intact plate.

	Mode 1,1	Mode 1,2	Mode 2,1	Mode 2,2	Mode 3,1	Mode 1,3
Theoretical	19.74	49.35	49.35	78.96	98.70	98.70
VICONOPT	19.74	49.35	49.35	78.96	98.7	98.7
AFE	20.18	50.07	50.07	80.78	99.53	99.54
VFM	19.80	49.73	49.44	79.93	98.78	99.24

Table 6-4 The ONF of an ATLC located at the middle of the plate using the VICONOPT model.

VICONOPT model		ONF of different modes (non-dimensional results)					
Crack angle	Depth ratio	1,1	1,2	2,1	2,2	3,1	1,3
90°	0	19.7392	49.3480	49.3480	78.9568	98.6960	98.6960
Centrally located	0.2	19.6878	49.2896	49.3480	78.9568	98.1739	98.6142
	0.4	19.5816	49.1719	49.3480	78.9568	97.1182	98.4533
	0.5	19.4811	49.0640	49.3480	78.9568	96.1471	98.3106
	0.6	19.3104	48.8883	49.3480	78.9568	94.5618	98.0875
	0.8	18.3635	48.0566	49.3480	78.9568	87.0297	97.1648
	1	16.1348	46.7381	49.3480	78.9568	75.2834	96.0405

Table 6-5 The ONF of an ATLC located at the middle of the plate by AFE model.

AFE 20*20 model		ONF of different modes (non-dimensional results)					
Crack angle	Depth ratio	1,1	1,2	2,1	2,2	3,1	1,3
90°	0	20.1782	50.0664	50.0664	80.7773	99.5317	99.5350
Centrally located	0.2	20.1282	50.0097	50.0664	80.7773	99.0166	99.4545
	0.4	20.0249	49.8955	50.0664	80.7772	97.9724	99.2999
	0.5	19.9272	49.7910	50.0664	80.7772	97.0122	99.1631
	0.6	19.7617	49.6217	50.0664	80.7772	95.4460	98.9502
	0.8	18.8510	48.8309	50.0664	80.7772	88.0232	98.0806
	0.9999	16.7606	47.6122	50.0664	80.7773	76.5197	97.0438

Table 6-6 The RCNF of an ATLC located at the middle of the plate by VICONOPT model.

VICONOPT model		RCNF of different modes (non-dimensional results)					
Crack angle	Depth ratio	1,1	1,2	2,1	2,2	3,1	1,3
90°	0	0.0000	0.0000	0.0000	0.0000	0.0000	0.0000
Centrally located	0.2	0.0026	0.0012	0.0000	0.0000	0.0053	0.0008
	0.4	0.0080	0.0036	0.0000	0.0000	0.0160	0.0025
	0.5	0.0131	0.0058	0.0000	0.0000	0.0258	0.0039
	0.6	0.0217	0.0093	0.0000	0.0000	0.0419	0.0062
	0.8	0.0697	0.0262	0.0000	0.0000	0.1182	0.0155
	1	0.1826	0.0529	0.0000	0.0000	0.2372	0.0269

Table 6-7 The RCNF of an ATLC located at the middle of the plate by AFE model.

AFE 20*20 model		RCNF of different modes (non-dimensional results)					
Crack angle	Depth ratio	1,1	1,2	2,1	2,2	3,1	1,3
90°	0	0.0000	0.0000	0.0000	0.0000	0.0000	0.0000
Centrally located	0.2	0.0025	0.0011	0.0000	0.0000	0.0052	0.0008
	0.4	0.0076	0.0034	0.0000	0.0000	0.0157	0.0024
	0.5	0.0124	0.0055	0.0000	0.0000	0.0253	0.0037
	0.6	0.0206	0.0089	0.0000	0.0000	0.0410	0.0059
	0.8	0.0658	0.0247	0.0000	0.0000	0.1156	0.0146
	0.9999	0.1694	0.0490	0.0000	0.0000	0.2312	0.0250

It should be noted that mode 2,1 and mode 2,2 are anti-symmetric about the y-axis in the VICONOPT cracked model, because only rotational stiffness is affected by the crack. If the crack occurs in the centre line of the plate, the curvature of the mode shapes will be zero there as can be seen from the contour plots for the intact plate in Figure 6-8. In these figures, symmetric and antisymmetric modes are shown respectively when an ATLC is all through-the-depth. For antisymmetric modes about the y-axis, the mode shapes remain the same with and without the crack and the natural frequencies of these modes are unchanged. The proposed AFE model and VFM adopt the same assumptions as VICONOPT, and similar phenomena are shown in Table 6-6 and Table 6-7 which will

be indicated in the mode shapes. The shapes of antisymmetric and symmetric modes for a depth ratio of 0.2 from AFE model are shown in Figure 6-9. Then, Figure 6-10 (a) to (c) compare ATLC model with VICONOPT and AFE for symmetrical modes. Figure 6-10 shows a good match of RCNF between VICONOPT and AFE when the crack is all through-the-length and located at the middle of the plate.

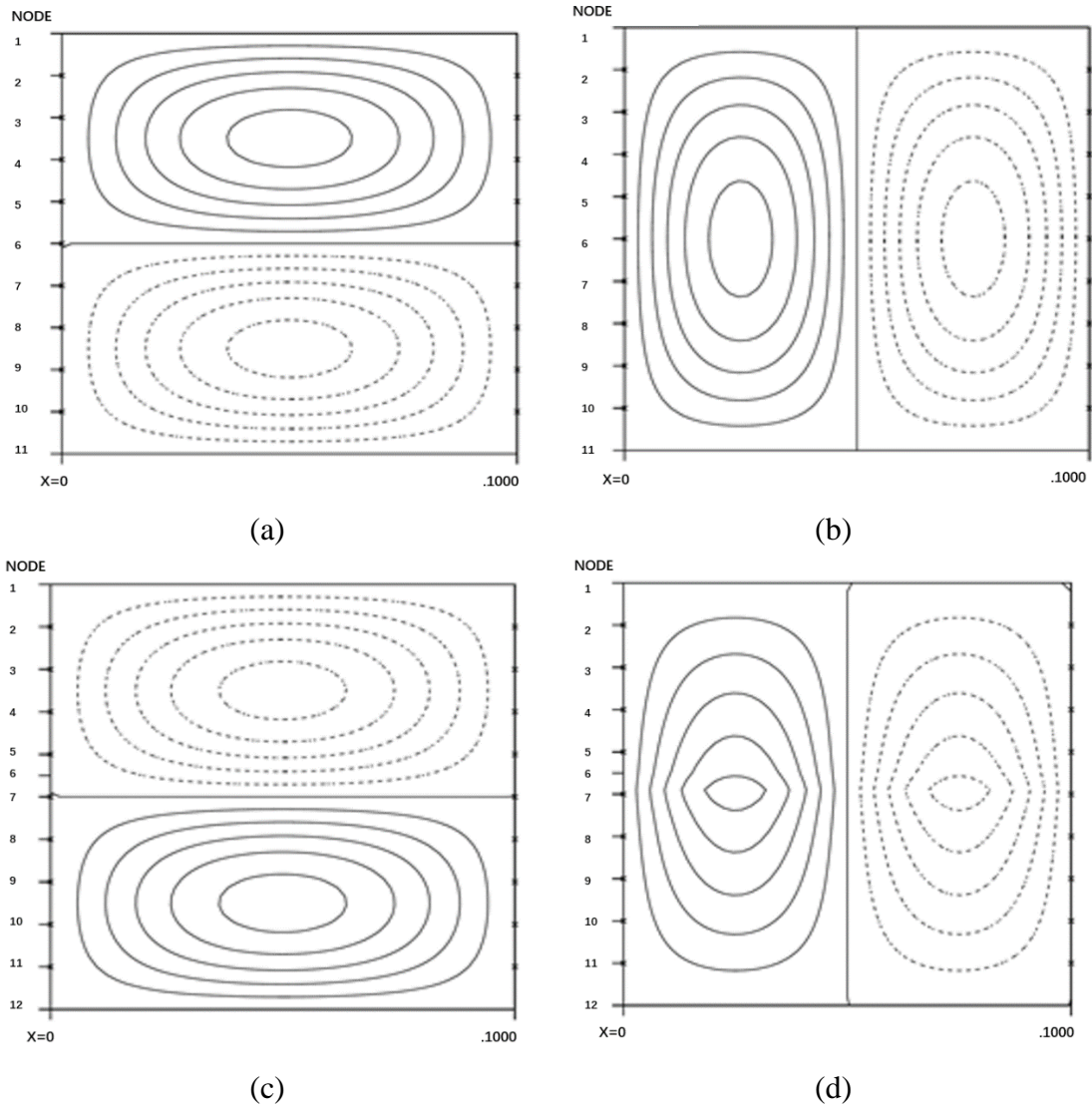


Figure 6-8 Mode shapes reproduced from VICONOPT.

(a) mode 2,1 of the intact plate; (b) mode 1,2 of the intact plate; (c) mode 2,1 of an ATLC (Figure 6-7 (a)) at the middle when depth ratio is 1; (d) mode 1,2 of an ATLC (Figure 6-7 (a)) at the middle when depth ratio is 1.

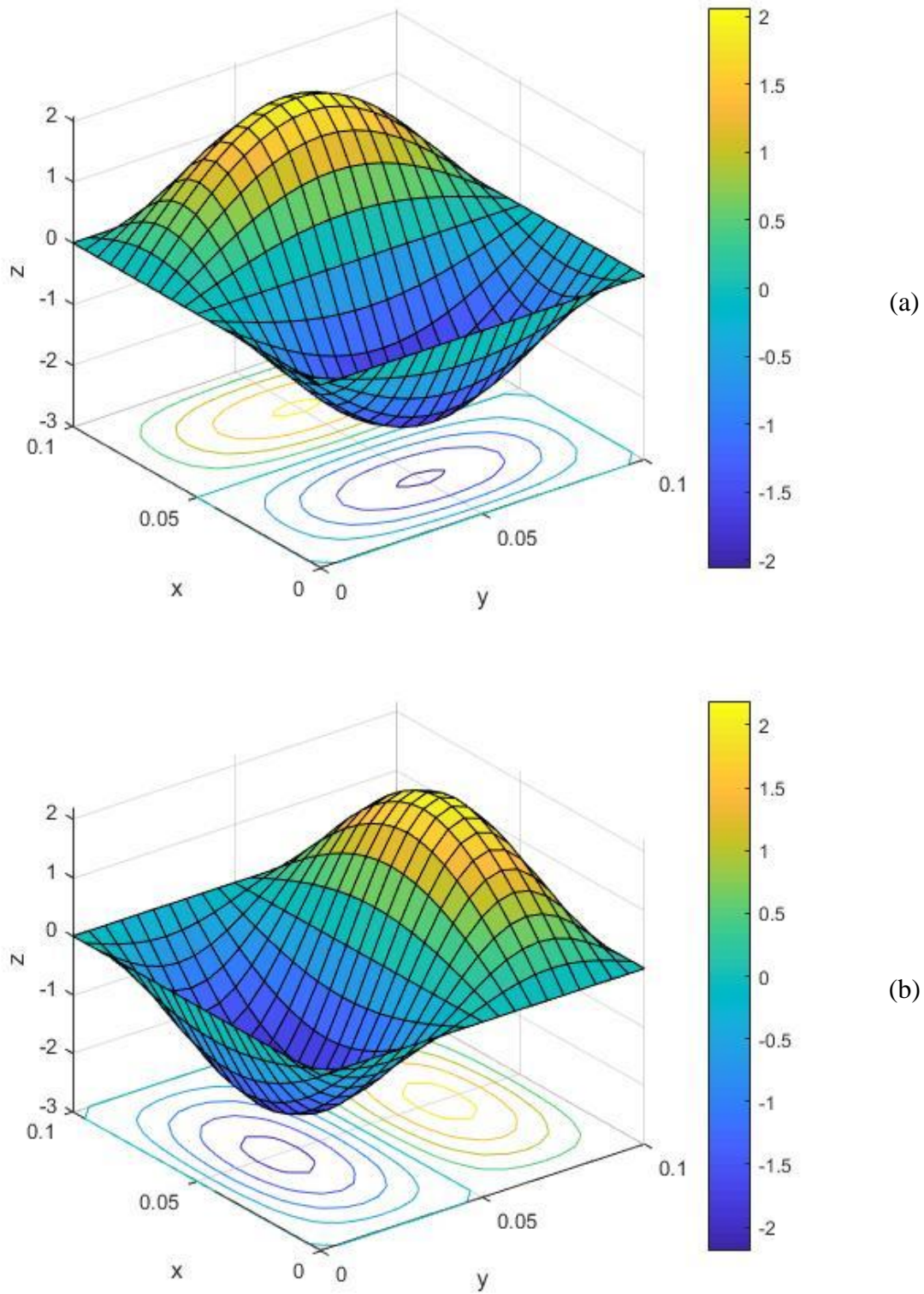


Figure 6-9 Mode shapes reproduced from AFE.

(a) mode 2,1 of the cracked plate, symmetric about the x-axis; (b) mode 1,2 of cracked plate, anti-symmetric about the y-axis.

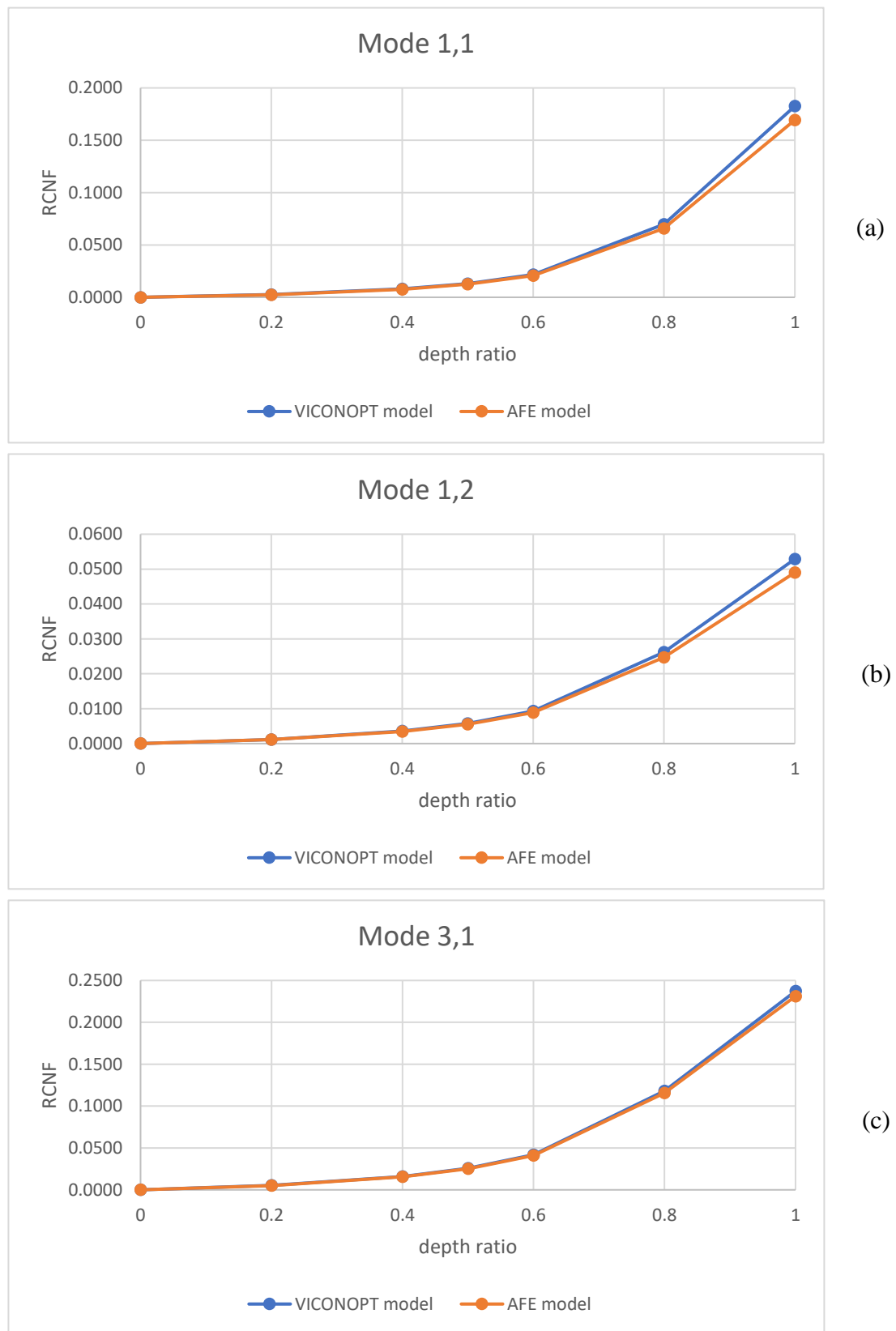


Figure 6-10 Comparison of RCNF for centrally located ATLC for VICONOPT and AFE.

(a) mode 1,1; (b) mode 1,2; (c) mode 3,1.

Because of the symmetric peculiarity, more general cracked plate cases need to be presented and discussed. Hence, an ATLC located at an arbitrary location ($y=0.075m$) is considered and the natural frequencies obtained from AFE are compared with those from VICONOPT in Figure 6-11. Table 6-8 to Table 6-11 show the ONF and RCNF data produced from VICONOPT and AFE.

Table 6-8 The ONF of an ATLC located at an arbitrary point of the plate using the VICONOPT model.

VICONOPT model		ONF of different modes (non-dimensional results)					
Crack angle	Depth ratio	1,1	1,2	2,1	2,2	3,1	1,3
90°	0	19.7392	49.3480	49.3480	78.9568	98.6960	98.6960
Location $y=0.075$	0.2	19.7134	49.1238	49.3187	78.7534	98.4361	98.6549
	0.4	19.6593	48.6648	49.2589	78.3458	97.9178	98.5732
	0.5	19.6070	48.2356	49.2033	77.9751	97.4493	98.4996
	0.6	19.5162	47.5202	49.1110	77.3788	96.7011	98.3823
	0.8	18.9561	43.8532	48.6436	74.6862	93.4147	97.8688
	1	17.1780	37.2168	47.7889	70.9137	89.0919	97.1762

Table 6-9 The ONF of an ATLC located at an arbitrary point of the plate using the AFE model.

AFE 20*20 model		ONF of different modes (non-dimensional results)					
Crack angle	Depth ratio	1,1	1,2	2,1	2,2	3,1	1,3
90°	0	20.1782	50.0664	50.0664	80.7773	99.5317	99.5350
location $x=0.075$	0.2	20.1530	49.8459	50.0378	80.5802	99.2763	99.4936
	0.4	20.1003	49.3950	49.9796	80.1862	98.7639	99.4148
	0.5	20.0494	48.9737	49.9257	79.8287	98.3008	99.3442
	0.6	19.9613	48.2724	49.8367	79.2551	97.5616	99.2325
	0.8	19.4249	44.6944	49.3950	76.6861	94.3166	98.7523
	1	17.7965	38.2789	48.6225	73.1339	90.0542	98.1271

Table 6-10 The RCNF of an ATLC located at an arbitrary point of the plate using the VICONOPT model.

VICONOPT model		RCNF of different modes (non-dimensional results)					
Crack angle	Depth ratio	1,1	2,1	1,2	2,2	3,1	1,3
90°	0	0.00	0.00	0.00	0.00	0.00	0.00
location y=0.075	0.2	0.0013	0.0045	0.0006	0.0026	0.0026	0.0004
	0.4	0.0040	0.0138	0.0018	0.0077	0.0079	0.0012
	0.5	0.0067	0.0225	0.0029	0.0124	0.0126	0.0020
	0.6	0.0113	0.0370	0.0048	0.0200	0.0202	0.0032
	0.8	0.0397	0.1113	0.0143	0.0541	0.0535	0.0084
	1	0.1298	0.2458	0.0316	0.1019	0.0973	0.0154

Table 6-11 The RCNF of an ATLC located at an arbitrary point of the plate using the AFE model.

AFE 20*20 model		RCNF of different modes (non-dimensional results)					
Crack angle	Depth ratio	1,1	2,1	1,2	2,2	3,1	1,3
90°	0	0.00	0.00	0.00	0.00	0.00	0.00
location x=0.075	0.2	0.0013	0.0044	0.0006	0.0024	0.0026	0.0004
	0.4	0.0039	0.0134	0.0017	0.0073	0.0077	0.0012
	0.5	0.0064	0.0218	0.0028	0.0117	0.0124	0.0019
	0.6	0.0108	0.0358	0.0046	0.0188	0.0198	0.0030
	0.8	0.0373	0.1073	0.0134	0.0506	0.0524	0.0079
	0.9999	0.1180	0.2354	0.0288	0.0946	0.0952	0.0141

In Figure 6-11, the RCNF data from Table 6-10 and Table 6-11 are plotted to compare VICONOPT and AFE. Because the arbitrary crack location removes the symmetric status of plate, all modes in Figure 6-11 show changes in natural frequencies and these have different magnitudes.

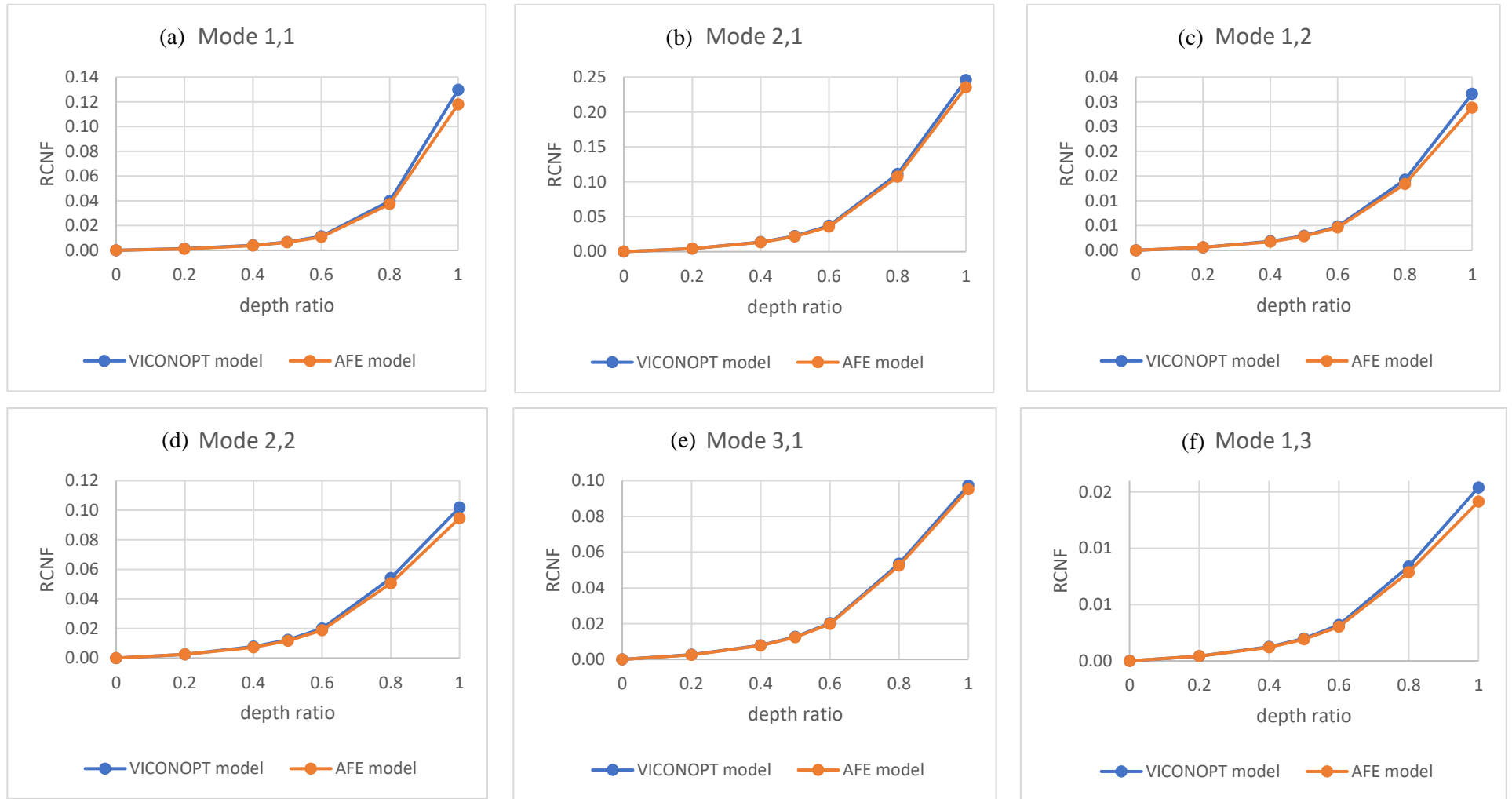


Figure 6-11 Comparison of RCNF for an arbitrary located ($y=0.075\text{m}$, quarter located) ATLC based on VICONOPT and AFE. (a) mode 1,1; (b) mode 2,1; (c) mode 1,2; (d) mode 2,2; (e) mode 3,1; (f) mode 1,3.

From Figure 6-11 (a) to (f), it is seen that the difference between the RCNF obtained from the VICONOPT and AFE models is small. The most significant difference is 0.01 among six modes, which is an acceptable level of noise in comparison. For partial through-the-depth and arbitrarily located cracks, relevant results are largely absent from previous studies. Table 6-12 and Table 6-13 show the comparison of natural frequencies with the literature when the ATLC is at the middle of plate and the depth ratio of the crack is 1.

Table 6-12 The ONF of an ATLC located at the mid-point of the plate using different approaches, depth ratio 1.

Centrally located, ONF of different modes (non-dimensional)								
Method	Crack angle	Depth ratio	1,1	1,2	2,1	2,2	3,1	1,3
VICONOPT	90°	0	19.74	49.35	49.35	78.96	98.70	98.70
(Liew et al. 1994)	90°	0	19.74	49.35	49.35	78.96	98.70	98.70
(Stahl and Keer 1972)	90°	0	19.74	49.35	49.35	78.96	98.70	98.70
(Bose and Mohanty 2013)	90°	0	19.74	49.35	49.35	78.96		
AFE	90°	0	20.18	50.07	50.07	80.78	99.53	99.54
VICONOPT	90°	1	16.13	46.74	49.35	78.96	75.28	96.04
(Liew et al. 1994)	90°	1	16.13	46.74	16.13	46.74	75.28	96.04
(Stahl and Keer 1972)	90°	1	16.13	46.74	16.13	46.74	75.29	96.03
(Bose and Mohanty 2013)	90°	1	16.13	47.00	27.36	64.51		
AFE	90°	0.9999	16.76	47.61	50.07	80.78	76.52	97.04

Table 6-13 The RCNF of an ATLC located at the mid-point of the plate using different approaches, depth ratio 1.

Centrally located, RCNF of different modes (non-dimensional)								
Method	Crack angle	Depth ratio	1,1	1,2	2,1	2,2	3,1	1,3
VICONOPT	90°	1	0.18	0.05	0.00	0.00	0.24	0.03
(Liew et al. 1994)	90°	1	0.18	0.05	0.67	0.41	0.24	0.03
(Stahl and Keer 1972)	90°	1	0.18	0.05	0.67	0.41	0.24	0.03
(Bose and Mohanty 2013)	90°	1	0.18	0.05	0.45	0.18		
AFE	90°	0.9999	0.17	0.05	0.00	0.00	0.23	0.03

As shown by the results in Table 6-13, even for an all through-the-depth crack, apart from the antisymmetric modes, the ONF and RCNF obtained from VICONOPT match well with other approaches. Since the results obtained from the AFE for a partial through-the-depth ATLC agree with VICONOPT, the applicability of the AFE method in the hybrid VFM model can now be preliminarily validated. However, for an all through-the-depth ATLC crack, the value of RCNF from AFE is slightly different compared with previous studies. Possible reasons for the difference are as follows.

1. The depth ratio chosen for AFE is 0.9999, not the whole depth.
2. Only a rotational spring is used to simulate the crack for the ATDC case, while other studies also include vertical and horizontal displacements because the vertical displacements at either side of the crack can be different for all through the depth cracks whereas the proposed AFE model assumes the vertical displacements are same (which is appropriate for partial through the depth cracks but not all through the depth). The AFE model only releases the degree of freedom of the rotation about the crack direction and constrains all others. The difference caused by these different constraints is shown in the mode shapes especially when the severity of crack is large.
3. The assumptions of the AFE model may differ from those in other research, e.g. shape function, stiffness matrix, mass matrix and constitutive law. The stiffness and mass matrix in the AFE model were chosen from Przemieniecki (1985) for a certain problem and used for validation purposes.

The primary target of this study is to solve the inverse problem, which can be used in damage detection. The main research object is the partial through-the-depth crack, and a good match has been observed through comparison with VICONOPT model. Even for the all through-the-depth crack, the accuracy of RCNF results is acceptable for use in the inverse problem.

6.4 Parallel partial through-the-length crack

6.4.1 Modelling Preparation

In this section, more crack cases are presented and modelled with AFE to validate with other approaches for a simply supported isotropic plate (SSSS) of length 0.1m and width 0.1m. Three main cases are considered. Figure 6-12 shows a crack partial through-the-length while all through-the-depth and parallel to one of the axes (ATDC) starting at various points (with the mid-point of the crack at $(x_c, y_c = 0.05\text{m}, 0.05\text{m})$). Figure 6-13 shows the results for the case when the right end of the crack is at $(x_e, y_e = 0.05\text{m}, 0.1\text{m})$ with different crack length ratios ($l_c/b = 0.1$ to 1) and Figure 6-22 shows a partial through-the-depth crack (PTDC) with varying crack length ($l_c/b = 0.1$ to 1) at an arbitrary edge location (for example, the right end of the crack is $(x_e, y_e = 0.075\text{m}, 0.1\text{m})$). The ATDC example is compared with Liew et al. (1994), Stahl and Keer (1972), Huang and Leissa (2009) and an ABAQUS ‘AT’ model (ABAQUS with tie constraint only model); the PTDC case will be examined alongside ABAQUS ‘ATCS’ model (ABAQUS with tie, coupling and rotational spring constraints model). The properties and transverse sectional dimensions of the cracked plate shown in Figure 6-12 are the same as for the previous model in section 6.3. The modelling concepts and methods of AFE are elaborated in section 5.2.2.

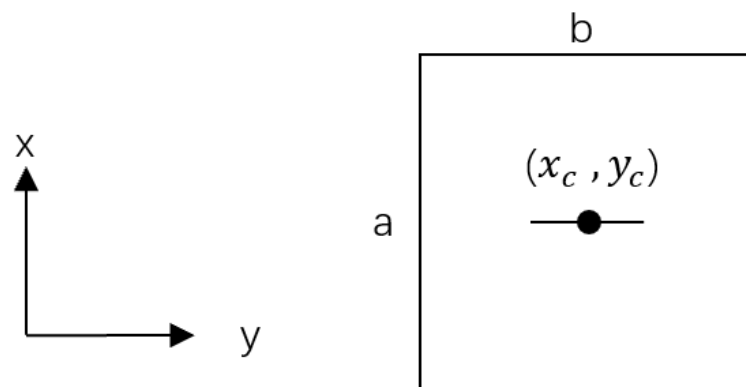


Figure 6-12 The dimensions ($a = 100\text{mm}, b = 100\text{mm}$) of the plate and the location of ATDC ($x_c, y_c = 0.05\text{m}, 0.05\text{m}$) when crack locates at the middle of plate.

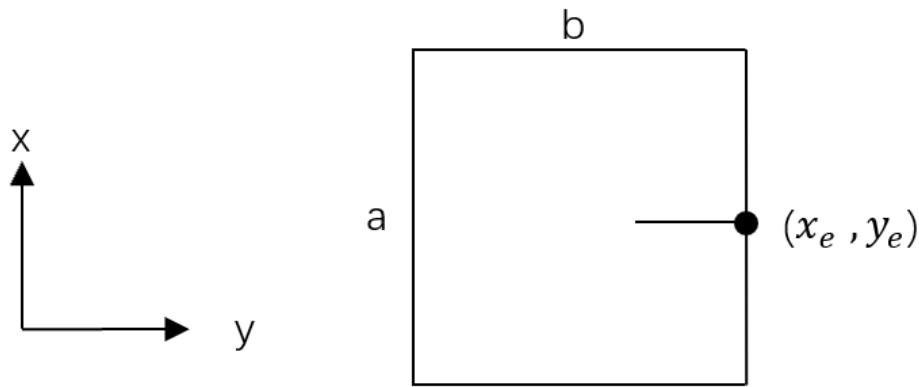


Figure 6-13 The dimension ($a = 100\text{mm}$, $b = 100\text{mm}$) of plate and the location of ATDC ($x_e, y_e = 0.05\text{m}, 0.1\text{m}$) when crack develop from the middle edge of plate with various length ratio.

6.4.2 Results

6.4.2.1 ATDC Located at the Middle of Plate ($x_c, y_c = 0.05\text{m}, 0.05\text{m}$)

For the ATDC modelled using AFE, the centrally located through-thickness crack in an isotropic square plate with length $a = 0.1\text{m}$ and width $b = 0.1\text{m}$ running parallel to the y -axis (Figure 6-12) with edges simply supported (SSSS), results are shown for the lowest six natural frequencies $\omega = \omega_{mn}$ whose modes have m and n half-waves in the x and y directions, respectively. Original natural frequencies (ONF) are normalised using Eq. 6-2 for comparison with other studies. The relative changes in natural frequencies (RCNF) are normalised by Eq. 6-3.

For the first comparison, two different ABAQUS models are presented to attempt to simulate the same crack case as other studies and the AFE model separately. The ABAQUS models chosen from section 5.2.3 are the AT (Figure 5-7 (a)) and ATCS (Figure 5-7 (b)) models respectively. The same modelling and element assumptions are applied. AT is used to compare with previous studies for the ATDC case, while ATCS is used to simulate the AFE model for the PTDC case. For both AT and ATCS models, the crack is located at the edge of an element to minimise the effect caused by an inaccurate damage region. The plate model in ABAQUS is divided into 400 square elements (20 in each direction), while the plate model in AFE is divided into 1600 square elements (40 in each direction). The AFE 40*40 model is mainly used for comparison with the literature. Other meshes in the AFE model, namely AFE 20*20, AFE 21*21, AFE 30*30, AFE 31*31 and AFE 41*41, were run in a convergence study and used to analyse the effect of element size on accuracy.

In the following tables, the depth ratio is the crack depth divided by the plate thickness; the length ratio is the crack length l_c divided by the plate length b ; the crack angle is the angle between the crack and the x -axis, with a 90° angle chosen for the parallel to y -axis crack problem. Non-dimensional natural frequencies and normalised relative changes in natural frequencies are tabulated for each study from the literature, the proposed AFE model and the ABAQUS model. The RCNF and the ONF data is given to two decimal places to match the previous studies.

Table 6-14 The ONF of intact plate obtained from different studies.

*Reference a: Stahl and Keer (1972); Reference b: Liew et al. (1994); Reference c: Bose and Mohanty (2013); Case a: AFE (21*21); Case b: AFE (41*41); Case c: AFE (40*40); Case d: AT model; Case e: ATCS model, Case f: VFM (16*8). All notations will represent the same model until further notification.*

Crack case: Crack angle= 90° ; Centrally located;						
	ONF of different modes (non-dimensional results)					
	1,1	1,2	2,1	2,2	3,1	1,3
Reference a	19.74	49.35	49.35	78.96	98.7	98.7
Reference b	19.74	49.35	49.35	78.96	98.7	98.7
Reference c	19.74	49.35	49.35	78.96		
Case a	20.18	50.07	50.07	80.78	99.53	99.53
Case b	20.19	50.08	50.08	80.80	99.53	99.53
Case c	20.19	50.08	50.08	80.80	99.53	99.53
Case d	19.74	49.69	49.69	79.37	100.82	100.82
Case e	19.74	49.69	49.69	79.37	100.82	100.82
Case f	19.80	49.73	49.43	79.93	98.78	99.24

Table 6-15 The ONF and RCNF of an ATDC located at the plate's midpoint reproduced from different studies, length ratio 0.2.

Crack case: Crack angle=90°; Centrally located; Depth ratio=1; Length ratio=0.2						
	ONF of different modes (non-dimensional results)					
	1,1	1,2	2,1	2,2	3,1	1,3
Reference a	19.3	49.33	49.17	78.96	93.96	98.7
Reference b	19.38	49.31	49.16	78.81	94.69	98.69
Reference c	18.31	48.38	41.55	73.24		
Case a	19.00	49.88	49.66	80.75	88.46	99.50
Case b	19.41	50.00	49.99	80.79	91.35	99.52
Case c	19.63	50.04	50.08	80.80	93.38	99.53
Case d	19.31	49.67	49.55	79.34	95.70	100.82
Case e	19.31	49.67	49.69	79.37	95.70	100.82
Case f	18.68	49.55	49.43	79.93	89.08	99.16
	RCNF of different modes (non-dimensional results)					
Reference a	0.02	0.00	0.00	0.00	0.05	0.00
Reference b	0.02	0.00	0.00	0.00	0.04	0.00
Reference c	0.07	0.02	0.16	0.07		
Case a	0.06	0.00	0.01	0.00	0.11	0.00
Case b	0.04	0.00	0.00	0.00	0.08	0.00
Case c	0.03	0.00	0.00	0.00	0.06	0.00
Case d	0.02	0.00	0.00	0.00	0.05	0.00
Case e	0.02	0.00	0.00	0.00	0.05	0.00
Case f	0.06	0.00	0.00	0.01	0.10	0.00

Table 6-16 The ONF and RCNF of an ATDC located at the plate's midpoint reproduced from different studies, length ratio 0.4.

Crack case: Crack angle=90°; Centrally located; Depth ratio=1; Length ratio=0.4						
	ONF of different modes (non-dimensional results)					
	1,1	1,2	2,1	2,2	3,1	1,3
Reference a	18.27	49.03	46.62	78.6	85.51	98.68
Reference b	18.44	49.04	46.44	78.39	86.71	98.58
Reference c	18.18	48.29	40.82	72.73		
Case a	17.90	49.20	48.77	80.59	82.10	99.10
Case b	18.33	49.52	49.66	80.75	83.81	99.30
Case c	18.61	49.67	50.08	80.80	85.41	99.38
Case d	18.27	49.39	47.05	79.02	86.67	100.73
Case e	18.27	49.39	49.69	79.37	86.67	100.73
Case f	17.96	49.15	49.43	79.93	89.08	98.91
	RCNF of different modes (non-dimensional results)					
Reference a	0.07	0.01	0.06	0.00	0.13	0.00
Reference b	0.07	0.01	0.06	0.01	0.12	0.00
Reference c	0.08	0.02	0.17	0.08		
Case a	0.11	0.02	0.03	0.00	0.18	0.00
Case b	0.09	0.01	0.01	0.00	0.16	0.00
Case c	0.08	0.01	0.00	0.00	0.14	0.00
Case d	0.07	0.01	0.05	0.00	0.14	0.00
Case e	0.07	0.01	0.00	0.00	0.14	0.00
Case f	0.09	0.01	0.00	0.06	0.10	0.00

Table 6-17 The ONF and RCNF of an ATDC located at the plate's midpoint reproduced from different studies, length ratio 0.5.

Crack case: Crack angle=90°; Centrally located; Depth ratio=1; Length ratio=0.5						
	ONF of different modes (non-dimensional results)					
	1,1	1,2	2,1	2,2	3,1	1,3
Reference a	17.71	48.7	43.03	77.73	82.15	98.4
Reference b	17.85	48.72	42.82	77.44	83.01	98.35
Case a	17.42	48.67	48.12	80.43	80.01	98.59
Case b	17.82	49.07	49.39	80.69	81.16	98.94
Case c	18.08	49.30	50.08	80.80	82.40	99.12
Case d	17.70	49.04	43.44	78.20	83.11	100.53
Case e	17.70	49.04	49.69	79.37	83.11	100.53
	RCNF of different modes (non-dimensional results)					
Reference a	0.10	0.01	0.13	0.02	0.17	0.00
Reference b	0.10	0.01	0.13	0.02	0.16	0.00
Case a	0.14	0.03	0.04	0.00	0.20	0.01
Case b	0.12	0.02	0.01	0.00	0.18	0.01
Case c	0.10	0.02	0.00	0.00	0.17	0.00
Case d	0.10	0.01	0.13	0.01	0.18	0.00
Case e	0.10	0.01	0.00	0.00	0.18	0.00

Table 6-18 The ONF and RCNF of an ATDC located at the plate's midpoint reproduced from different studies, length ratio 0.6.

Crack case: Crack angle=90°; Centrally located; Depth ratio=1; Length ratio=0.6						
	ONF of different modes (non-dimensional results)					
	1,1	1,2	2,1	2,2	3,1	1,3
Reference a	17.19	48.22	37.98	75.58	79.59	97.99
Reference b	17.33	48.26	37.75	75.23	80.32	97.96
Reference c	17.53	47.87	36.95	70.14		
Case a	17.04	48.12	47.35	80.20	78.49	97.90
Case b	17.37	48.56	49.05	80.60	79.19	98.39
Case c	17.61	48.83	50.08	80.80	80.10	98.67
Case d	17.16	48.56	38.33	76.19	80.41	100.13
Case e	17.16	48.56	49.69	79.37	80.41	100.13
	RCNF of different modes (non-dimensional results)					
Reference a	0.13	0.02	0.23	0.04	0.19	0.01
Reference b	0.12	0.02	0.24	0.05	0.19	0.01
Reference c	0.11	0.03	0.25	0.11		
Case a	0.16	0.04	0.05	0.01	0.21	0.02
Case b	0.14	0.03	0.02	0.00	0.20	0.01
Case c	0.13	0.03	0.00	0.00	0.20	0.01
Case d	0.13	0.02	0.23	0.04	0.20	0.01
Case e	0.13	0.02	0.00	0.00	0.20	0.01

Table 6-19 The ONF and RCNF of an ATDC located at the plate's midpoint reproduced from different studies, length ratio 0.8.

Crack case: Crack angle=90°; Centrally located; Depth ratio=1; Length ratio=0.8						
	ONF of different modes (non-dimensional results)					
	1,1	1,2	2,1	2,2	3,1	1,3
Reference a	16.4	47.26	27.77	65.73	76.37	96.76
Reference b	16.47	47.27	27.43	65.19	76.6	96.78
Reference c	16.28	47.11	28.51	65.12		
Case a	16.59	47.32	45.69	79.66	76.80	96.60
Case b	16.79	47.66	48.21	80.36	76.83	97.10
Case c	16.96	47.93	50.08	80.80	77.27	97.50
Case d	16.38	47.53	27.93	66.50	77.02	98.86
Case e	16.38	47.53	49.69	79.37	77.02	98.86
	RCNF of different modes (non-dimensional results)					
Reference a	0.17	0.04	0.44	0.17	0.23	0.02
Reference b	0.17	0.04	0.44	0.17	0.22	0.02
Reference c	0.18	0.05	0.42	0.18		
Case a	0.18	0.05	0.09	0.01	0.23	0.03
Case b	0.17	0.05	0.04	0.01	0.23	0.02
Case c	0.16	0.04	0.00	0.00	0.22	0.02
Case d	0.17	0.04	0.44	0.16	0.24	0.02
Case e	0.17	0.04	0.00	0.00	0.24	0.02

Table 6-20 The ONF and RCNF of an ATDC located at the plate's mid-point reproduced from different studies, length ratio 1.

Crack case: Crack angle=90°; Centrally located; Depth ratio=1; Length ratio=1						
	ONF of different modes (non-dimensional results)					
	1,1	1,2	2,1	2,2	3,1	1,3
Reference a	16.13	46.74	16.13	46.74	75.29	96.03
Reference b	16.13	46.74	16.13	46.74	75.28	96.04
Reference c	16.13	47	27.36	64.51		
Case a	16.53	47.20	45.11	79.47	76.57	96.37
Case b	16.66	47.42	47.62	80.20	76.32	96.69
Case c	16.79	47.64	50.08	80.80	76.57	97.05
Case d	16.10	47.05	16.10	47.05	75.89	98.11
Case e	16.10	47.05	49.69	79.36	75.89	98.11
	RCNF of different modes (non-dimensional results)					
Reference a	0.18	0.05	0.67	0.41	0.24	0.03
Reference b	0.18	0.05	0.67	0.41	0.24	0.03
Reference c	0.18	0.05	0.45	0.18		
Case a	0.18	0.06	0.10	0.02	0.23	0.03
Case b	0.17	0.05	0.05	0.01	0.23	0.03
Case c	0.17	0.05	0.00	0.00	0.23	0.02
Case d	0.18	0.05	0.68	0.41	0.25	0.03
Case e	0.18	0.05	0.00	0.00	0.25	0.03

In Table 6-14 to Table 6-20, the natural frequencies obtained from eight different models with different length ratio are tabulated. Normalised changes in the natural frequencies are also calculated and listed. Figure 6-14 will plot the RCNF data to compare results achieved from AFE with other studies and ABAQUS models. For the first PTLC case, since the AFE model chosen in the study ignores the effects caused by displacement in the damaged region, antisymmetric modes will show a constant zero change when the crack is located at the middle of the square plate. This is because the crack is on a line of zero curvature. Hence, only four modes will be plotted to compare with results in the literature, namely $(m, n) = (1,1); (1,2); (3,1); (1,3)$. Eigenvalues obtained from different meshes (441, 1681 and 1600 elements) are plotted in Figure 6-16 to show the effect caused by mesh size.

The changes in the natural frequencies obtained by ATCS in In Table 6-14 to Table 6-20 show a good match with the AFE model, particularly for antisymmetric modes about the y -axis. This shows that the ATCS model successfully simulates the same cracked model as the AFE model, which can now be used to analyse PTDC cases since there is an absence of previous partial through-the-thickness crack studies. Since the aim of damage identification, is to detect a crack in its early stages, being able to model partial through-the-depth cracks is essential. After the relationship between the change in natural frequencies and the crack location is observed, the data is normalised to eliminate the effect of severity. Relative changes in the natural frequencies (RCNF) can then be used in the inverse problem, allowing the location to be determined as will be shown in Chapter 7.

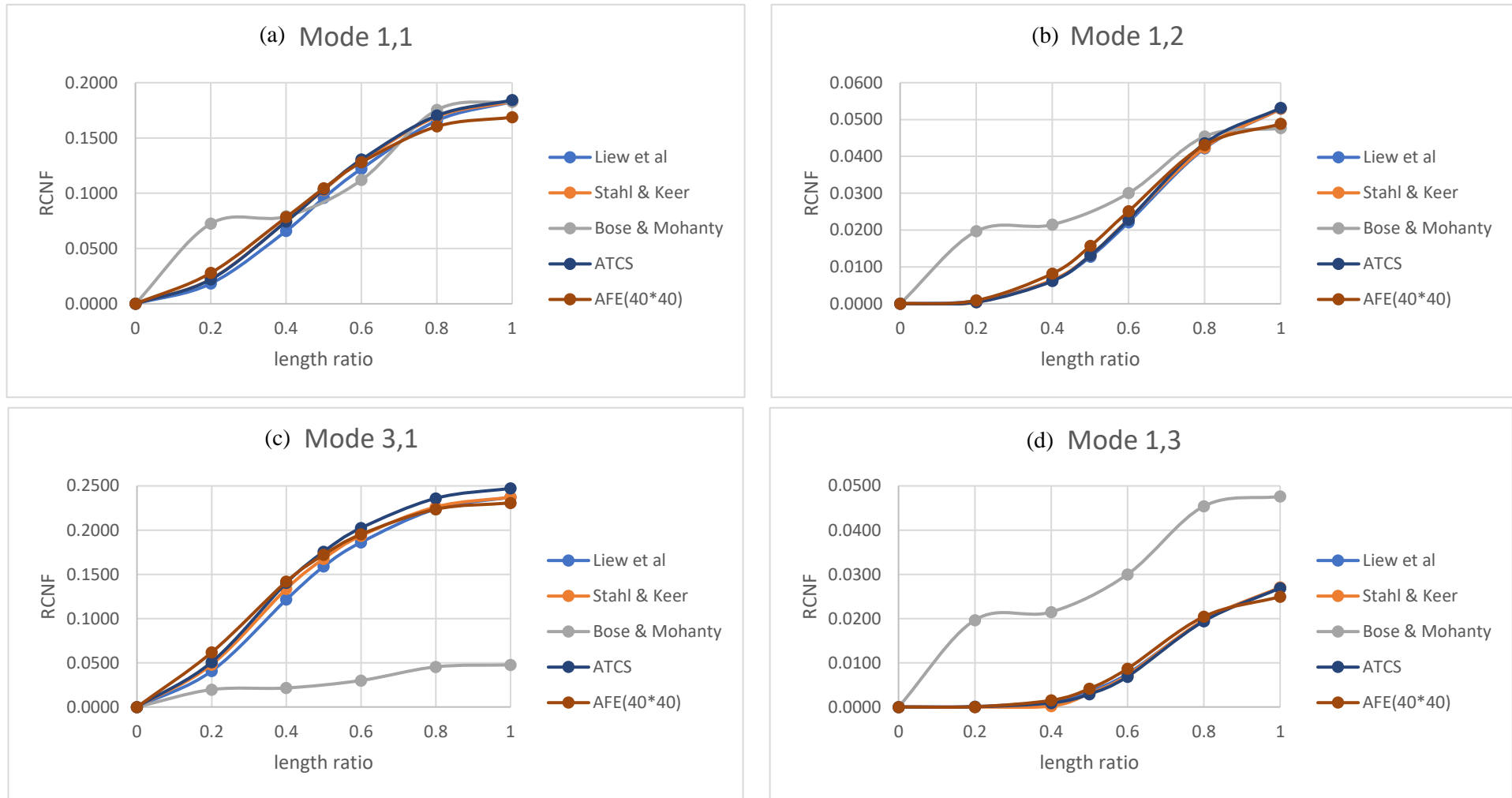


Figure 6-14 Comparative figures of centrally located ATDC with various length ratio between AFE and previous studies.

(a) mode 1,1; (b) mode 1,2; (c) mode 3,1; (d) mode 1,3.

As mentioned in Chapter 6.3, the natural frequencies obtained from the proposed AFE model are slightly higher than the theoretical results due to the different modelling assumptions made and the way the elements are meshed. (Although a finer mesh of 80*80 was applied, this came with a significantly higher computational cost due to the larger matrix whilst offering a relatively small improvement, and was not therefore adopted).

Figure 6-14, shows a small reduction in natural frequencies with increasing crack severity. For a single crack, even when it penetrates through the length and depth of the plate, the maximum decrease for symmetric modes is 25%. When the length ratio of an ATDC is smaller than 0.4, the average reduction of natural frequencies is no more than 10%. A good agreement is seen in the plots of RCNF for all modes when the crack is parallel to one of the axes, especially when the length ratio is smaller than 0.8. When the ATDC penetrates the whole length of plate, the difference in the values of RCNF is noticeable when comparing AFE with other studies because the displacement in the damaged part will dominate the behaviour of vibration response when the ATDC is severe enough. If the displacement degree of freedom is considered, the change in natural frequencies is shown to be more significant for antisymmetric modes (when the mode is antisymmetric about the y -axis and when the crack parallel to the y -axis). However, when only the rotational degree of freedom is considered, the natural frequencies of antisymmetric modes remain constant with increasing length of crack.

Based on the above comparative figures and previously mentioned assumptions about AT and ATCS, the fundamental mode (1,1) shows a good match between AT, ATCS, AFE and previous studies for ATDC (Figure 6-15). Notably, for the antisymmetric mode (2,1), the ATCS model shows an entirely satisfactory agreement with the proposed AFE model proving the equivalence of these two models (Figure 6-15). Validation of the AT and ATCS models is in preparation for the PTDC cases. Figure 6-16 shows the influence of different element sizes on the RCNF for an ATDC with different crack length ratios.

Figure 6-16 firstly shows a better match with AFE and a previous study from the literature when more finite elements are used to model the plate. For AFE 20*20, the mesh comprises 400 elements equally distributed in the two directions. For AFE 40*40, a finer mesh is used containing 1600 elements. Compared with the results presented by Liew et al. (1994), the results obtained from the finer mesh are within 1%. In the following comparison, an AFE 40*40 mesh is therefore chosen for all of the models.

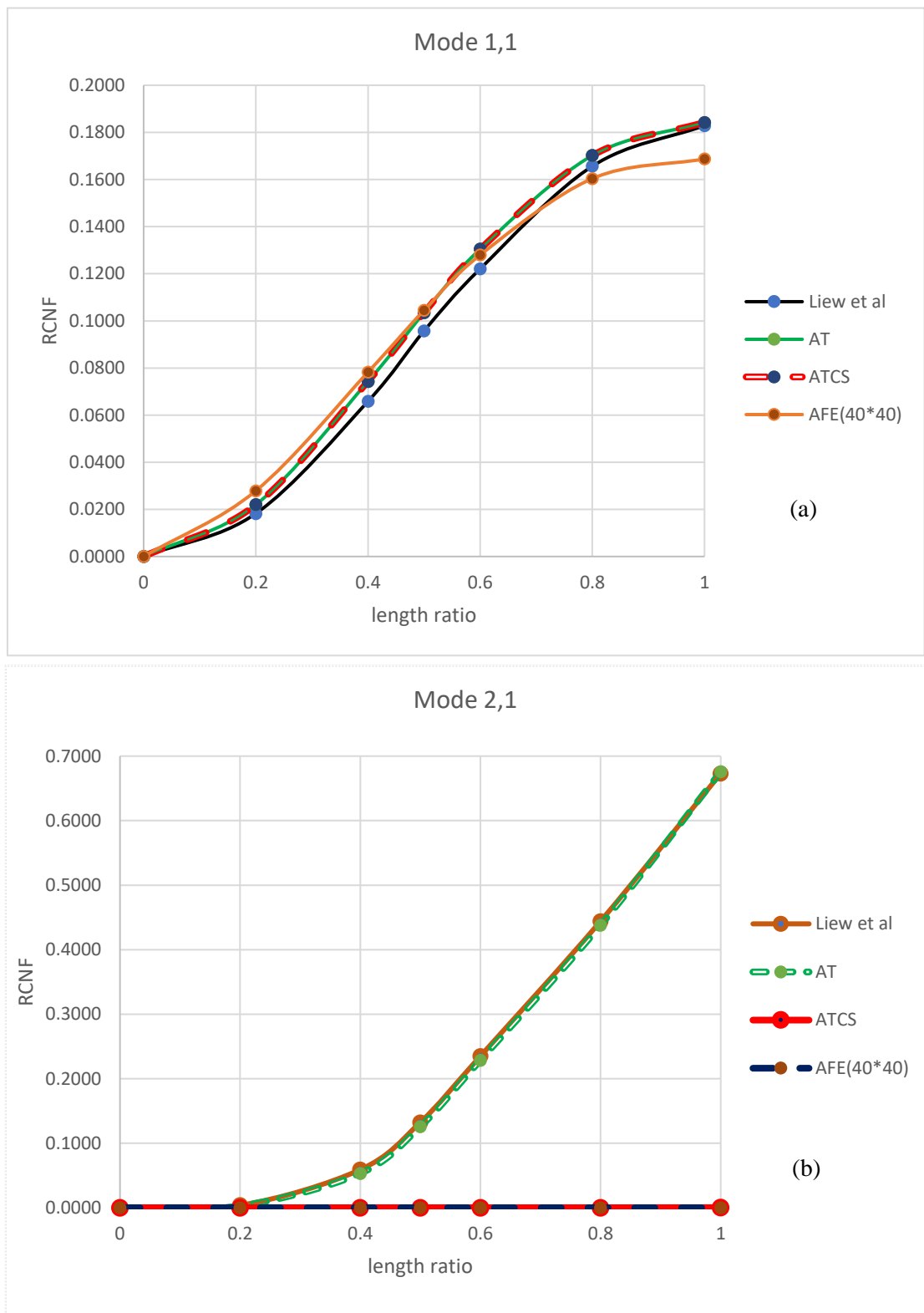


Figure 6-15 Comparison of AT, ATCS and approaches from the literature predicted values of RCNF for centrally located ATDC with various length ratio.

(a) mode 1,1; (b) mode 2,1.

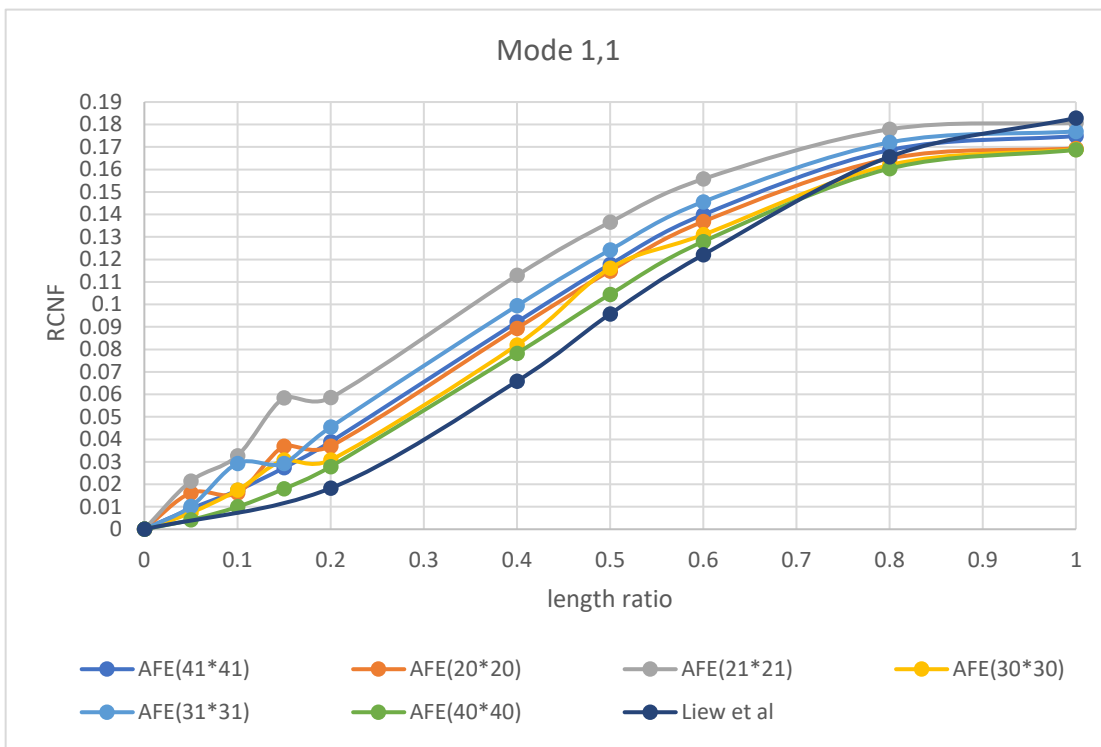


Figure 6-16 Relative change in fundamental natural frequency, ATDC centrally located from AFE model with various mesh sizes.

A perturbation is also seen in the curves in Figure 6-16 for particular length ratios. Coarser meshes are seen to result in larger perturbations particularly when the ATDC is located within an element instead of at its edge. This is due to the way the rotational compliance is allocated in the proposed AFE model. When assembling the global stiffness matrix, the additional compliance induced by the crack is distributed to the corresponding nodes by the integrated shape function presented in Eq. 5-25 and explained in section 5.2.2. If the crack is all through-the-depth of the plate, this compliance is infinite. So when the crack is located anywhere inside an element, even if it is a short crack, it will cause zero rotational stiffness to be added to all four nodes of the element. Thus a higher reduction in natural frequencies will occur compared with that only when the crack ends exactly at the edge of the element. This perturbation phenomenon only occurs in the ATDC case; in the PTDC case the rotational compliance is finite and a smooth RCNF curve will be generated, again accuracy is improved by using a finer mesh.

6.4.2.2 ATDC Locates at the Middle Edge of Plate ($x_e, y_e = 0.05m, 0.1m$)

In the second ATDC case shown in Figure 6-13, the crack starts from the middle of one edge of the plate ($y_e = 0.1m$), parallel to the y -axis and has various crack length ratios l_c/b . The dimension and properties of the plate are same as in Figure 6-1. Results obtained from AFE are compared with Huang and Leissa (2009), the AT and ATCS ABAQUS models. The same assumptions and element sizes for the cracked plate model are chosen as for the previous ABAQUS model.

Table 6-21 The ONF of the intact plate obtained from different studies.

	ONF of different modes (non-dimensional results)				
	1,1	1,2	2,1	2,2	3,1
(Huang and Leissa 2009)	19.74	49.35	49.35	78.96	98.7
AFE 40*40	20.19	50.08	50.08	80.80	99.53
AT 20*20	19.74	49.69	49.69	79.37	100.82
ATCS 20*20	19.74	49.69	49.69	79.37	100.82

Table 6-22 The ONF and RCNF of an ATDC starting at the middle of one edge of the plate, data reproduced from different studies. Crack case: Length ratio=0.1; Crack angle= 90° ; Depth ratio=1.

	ONF of different modes (non-dimensional results)				
	1,1	1,2	2,1	2,2	3,1
(Huang and Leissa 2009)	19.74	49.34	49.35	78.95	98.63
AFE 40*40	20.19	50.06	50.08	80.80	99.41
AT 20*20	19.74	49.68	49.69	79.35	100.76
ATCS 20*20	19.74	49.68	49.69	79.37	100.76
	RCNF of different modes (non-dimensional results)				
(Huang and Leissa 2009)	0.00	0.00	0.00	0.00	0.00
AFE 40*40	0.00	0.00	0.00	0.00	0.00
AT 20*20	0.00	0.00	0.00	0.00	0.00
ATCS 20*20	0.00	0.00	0.00	0.00	0.00

Table 6-23 The ONF and RCNF of an ATDC starting at the middle of one edge of the plate, data reproduced from different studies. Crack case: Length ratio=0.2; Crack angle=90°; Depth ratio=1.

	ONF of different modes (non-dimensional results)				
	1,1	1,2	2,1	2,2	3,1
(Huang and Leissa 2009)	19.7	49.19	49.33	78.78	97.88
AFE 40*40	20.14	49.88	50.08	80.80	98.46
AT 20*20	19.70	49.54	49.66	79.20	99.97
ATCS 20*20	19.70	49.54	49.69	79.37	99.97
	RCNF of different modes (non-dimensional results)				
(Huang and Leissa 2009)	0.00	0.00	0.00	0.00	0.01
AFE 40*40	0.00	0.00	0.00	0.00	0.01
AT 20*20	0.00	0.00	0.00	0.00	0.01
ATCS 20*20	0.00	0.00	0.00	0.00	0.01

Table 6-24 The ONF and RCNF of an ATDC starting at the middle of one edge of the plate, data reproduced from different studies. Crack case: Length ratio=0.3; Crack angle=90°; Depth ratio=1.

	ONF of different modes (non-dimensional results)				
	1,1	1,2	2,1	2,2	3,1
(Huang and Leissa 2009)	19.54	48.77	49.09	77.18	95.69
AFE 40*40	19.96	49.44	50.08	80.80	96.14
AT 20*20	19.54	49.12	49.43	77.72	97.58
ATCS 20*20	19.54	49.12	49.69	79.37	97.58
	RCNF of different modes (non-dimensional results)				
(Huang and Leissa 2009)	0.01	0.01	0.01	0.02	0.03
AFE 40*40	0.01	0.01	0.00	0.00	0.03
AT 20*20	0.01	0.01	0.01	0.02	0.03
ATCS 20*20	0.01	0.01	0.00	0.00	0.03

Table 6-25 The ONF and RCNF of an ATDC starting at the middle of one edge of the plate, data reproduced from different studies. Crack case: Length ratio=0.4; Crack angle=90°; Depth ratio=1.

	ONF of different modes (non-dimensional results)				
	1,1	1,2	2,1	2,2	3,1
(Huang and Leissa 2009)	19.2	47.8	48.24	71.27	92.23
AFE 40*40	19.60	48.96	50.08	80.80	92.71
AT 20*20	19.20	48.58	48.16	71.97	93.76
ATCS 20*20	19.20	48.58	49.69	79.37	93.76
	RCNF of different modes (non-dimensional results)				
(Huang and Leissa 2009)	0.03	0.03	0.02	0.10	0.07
AFE 40*40	0.03	0.02	0.00	0.00	0.07
AT 20*20	0.03	0.02	0.03	0.09	0.07
ATCS 20*20	0.03	0.02	0.00	0.00	0.07

Table 6-26 The ONF and RCNF of an ATDC starting at the middle of one edge of the plate, data reproduced from different studies. Crack case: Length ratio=0.5; Crack angle=90°; Depth ratio=1.

	ONF of different modes (non-dimensional results)				
	1,1	1,2	2,1	2,2	3,1
(Huang and Leissa 2009)	18.65	43.42	47.92	64.4	88.08
AFE 40*40	19.05	48.71	50.08	80.80	88.59
AT 20*20	18.64	48.25	43.77	64.99	89.26
ATCS 20*20	18.64	48.25	49.69	79.37	89.26
	RCNF of different modes (non-dimensional results)				
(Huang and Leissa 2009)	0.06	0.12	0.03	0.18	0.11
AFE 40*40	0.06	0.03	0.00	0.00	0.11
AT 20*20	0.06	0.03	0.12	0.18	0.11
ATCS 20*20	0.06	0.03	0.00	0.00	0.11

Table 6-27 The ONF and RCNF of an ATDC starting at the middle of one edge of the plate, data reproduced from different studies. Crack case: Length ratio=0.6; Crack angle=90°; Depth ratio=1.

	ONF of different modes (non-dimensional results)				
	1,1	1,2	2,1	2,2	3,1
(Huang and Leissa 2009)	17.96	36.45	47.86	62.24	83.78
AFE 40*40	18.39	48.68	50.08	80.80	84.35
AT 20*20	17.94	48.19	36.70	62.74	84.72
ATCS 20*20	17.94	48.19	49.69	79.37	84.72
	RCNF of different modes (non-dimensional results)				
(Huang and Leissa 2009)	0.09	0.26	0.03	0.21	0.15
AFE 40*40	0.09	0.03	0.00	0.00	0.15
AT 20*20	0.09	0.03	0.26	0.21	0.16
ATCS 20*20	0.09	0.03	0.00	0.00	0.16

According to Table 6-21 to Table 6-27, the natural frequencies for antisymmetric modes remain constant because the crack occurs on the centre line of a square isotropic plate where there is zero curvature in the mode shape. Hence, the Figure 6-17 only show the symmetric modes (about the y -axis) to make a comparison between the results of AFE, AT, ATCS and Huang and Leissa (2009).

The relative changes in natural frequencies seen in Figure 6-17 show similar degradation to the earlier results where the ATDC starts from the centre of the plate. The RCNF data for modes (1,1) and (3,1) presents a good match between all the proposed methods. However, mode (1,2) reveals a difference in trends between the data from Huang and Leissa (2009) and other approaches when the length ratio exceeds 0.4. Figure 6-18 explains the difference by reference to the mode shape plots. When the crack length ratio approaches 0.4, the magnitudes of mode (1,2) and mode (2,1) swap in Huang and Leissa's data (2009). Since the authors recorded the natural frequencies in ascending order and this results in modes (1,2) and (2,1) being swapped. As shown in Figure 6-18, therefore Figure 6-17 (b) plots a higher mode from Huang and Leissa (2009) when the crack length ratio is over 0.4. This also explains the sudden change in gradient in the plot at this point.

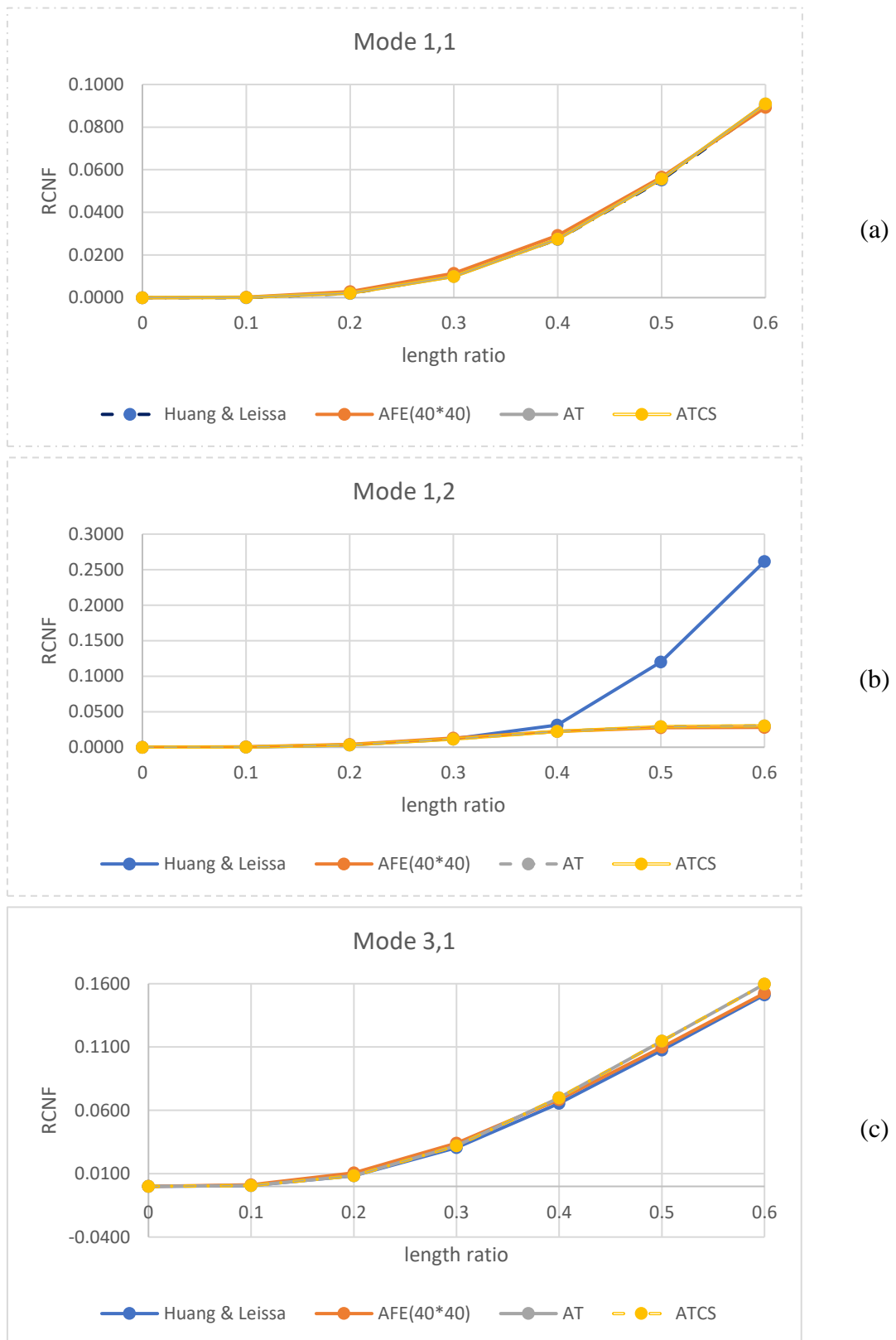


Figure 6-17 Comparison of the values of RCNF for different techniques for modelling an ATDC starting from the middle edge with various length ratio from various approaches.

(a) mode 1,1; (b) mode 1,2; (c) mode 3,1.

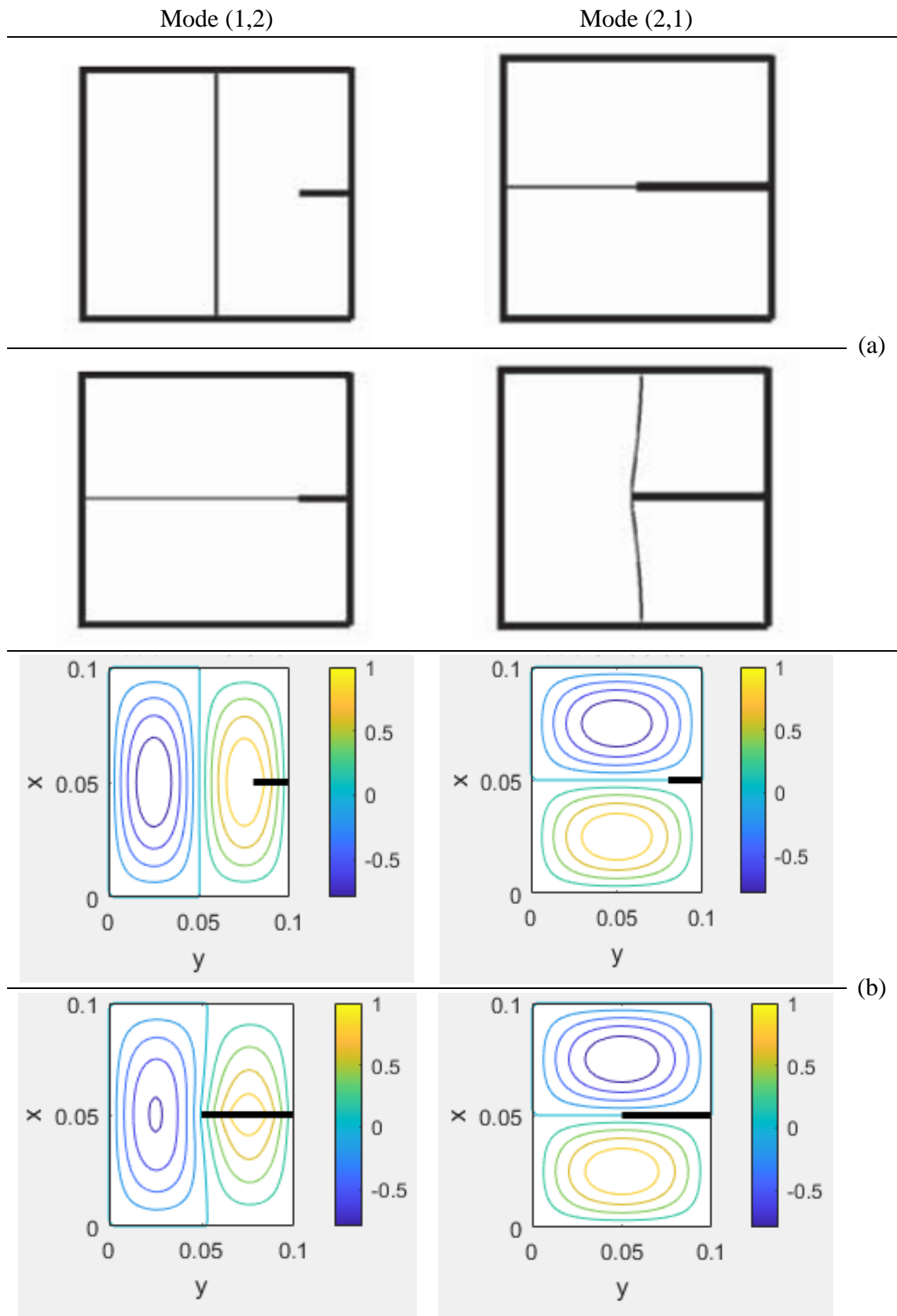


Figure 6-18 Mode shape comparison between AFE and Huang and Leissa (2009).
 Model from (a) Huang and Leissa (2009); (b) AFE model.

6.4.2.3 ATDC Locates at an Arbitrary Point of Plate ($x_e, y_e = 0.075m, 0.1m$)

The next ATDC case in Figure 6-19 shows a crack arbitrarily located and parallel to the y -axis. An arbitrary start point at $(x, y) = (0.075, 1)$ is chosen with various crack length ratios. The results are validated for the AFE 40*40 model against the study by Huang and Leissa (2009). The properties and cross-sectional dimensions are the same as for the previous cracked plate model, and the same ABAQUS 20*20 models are used for comparison. Table 6-28 to Table 6-31 show non-dimensional natural frequencies and normalised relative change in natural frequencies from the different approaches. By choosing to examine an ATDC located at an arbitrary place, it will break the symmetric characteristics about one of the axes.

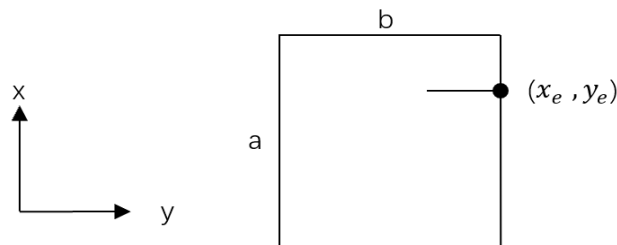


Figure 6-19 The dimensions ($a = 100mm, b = 100mm$) of the plate and the location of ATDC ($x_e, y_e = 0.075m, 0.1m$) when crack locates an arbitrary point of plate.

Table 6-28 The ONF and RCNF of ATDC starting at an arbitrary point of the plate, data reproduced from Huang and Leissa (2009).

	Crack angle=90°; Depth ratio=1; Crack initial location (0.075,0.1)				
	ONF of different modes (non-dimensional results)				
Length ratio	1,1	1,2	2,1	2,2	3,1
0	19.74	49.35	49.35	78.96	98.7
0.1	19.74	49.33	49.35	78.91	98.67
0.2	19.72	49.08	49.34	78.4	98.3
0.3	19.62	48.15	49.23	76.96	96.95
0.4	19.38	46.34	48.74	75.18	87.28
0.5	18.88	44.07	47.32	68.85	76.03
0.6	18.1	41.65	44.52	58.84	75.3
Length ratio	RCNF of different modes (non-dimensional results)				
0	0.00	0.00	0.00	0.00	0.00
0.1	0.00	0.00	0.00	0.00	0.00
0.2	0.00	0.01	0.00	0.01	0.00
0.3	0.01	0.02	0.00	0.03	0.02
0.4	0.02	0.06	0.01	0.05	0.12
0.5	0.04	0.11	0.04	0.13	0.23
0.6	0.08	0.16	0.10	0.25	0.24

Table 6-29 The ONF and RCNF of ATDC starting at an arbitrary point, data reproduced from AT 20*20 model.

	Crack angle=90°; Depth ratio=1; Crack initial location (0.075,0.1)					
	ONF of different modes (non-dimensional results)					
Length ratio	1,1	2,1	1,2	2,2	3,1	1,3
0	19.74	49.69	49.69	79.37	100.82	100.82
0.1	19.74	49.67	49.69	79.33	100.79	100.81
0.2	19.71	49.42	49.68	78.80	100.41	100.71
0.3	19.62	48.46	49.58	77.32	98.97	99.91
0.4	19.37	46.59	49.11	75.51	88.82	99.31
0.5	18.88	44.24	47.73	69.36	76.45	99.18
0.6	18.09	41.73	44.91	59.06	75.64	98.40
Length ratio	RCNF of different modes (non-dimensional results)					
0	0.00	0.00	0.00	0.00	0.00	0.00
0.1	0.00	0.00	0.00	0.00	0.00	0.00
0.2	0.00	0.01	0.00	0.01	0.00	0.00
0.3	0.01	0.02	0.00	0.03	0.02	0.01
0.4	0.02	0.06	0.01	0.05	0.12	0.02
0.5	0.04	0.11	0.04	0.13	0.24	0.02
0.6	0.08	0.16	0.10	0.26	0.25	0.02

Table 6-30 The ONF and RCNF of ATDC starting at an arbitrary point, data reproduced from the ATCS 20*20 model.

	Crack angle=90°; Depth ratio=1; Crack initial location (0.075,0.1)					
	ONF of different modes (non-dimensional results)					
Length ratio	1,1	2,1	1,2	2,2	3,1	1,3
0	19.74	49.69	49.69	79.37	100.82	100.82
0.1	19.74	49.67	49.69	79.33	100.79	100.82
0.2	19.72	49.42	49.69	78.80	100.41	100.82
0.3	19.64	48.49	49.69	77.33	99.42	100.80
0.4	19.45	46.65	49.67	75.71	98.19	100.65
0.5	19.12	44.25	49.62	75.01	96.74	100.29
0.6	18.66	41.91	49.45	74.97	94.75	100.00
Length ratio	RCNF of different modes (non-dimensional results)					
0	0.00	0.00	0.00	0.00	0.00	0.00
0.1	0.00	0.00	0.00	0.00	0.00	0.00
0.2	0.00	0.01	0.00	0.01	0.00	0.00
0.3	0.01	0.02	0.00	0.03	0.01	0.00
0.4	0.01	0.06	0.00	0.05	0.03	0.00
0.5	0.03	0.11	0.00	0.05	0.04	0.01
0.6	0.05	0.16	0.00	0.06	0.06	0.01

Table 6-31 The ONF and RCNF of ATDC starting at an arbitrary point of the plate, data reproduced from the AFE 40*40 model.

		Crack angle=90°; Depth ratio=0.9999; Crack initial location (0.075,0.1)				
		ONF of different modes (non-dimensional results)				
Length ratio	1,1	2,1	1,2	2,2	3,1	1,3
0	20.19	50.08	50.08	80.80	99.53	99.53
0.1	20.19	50.05	50.08	80.72	99.47	99.53
0.2	20.17	49.73	50.08	80.07	99.02	99.53
0.3	20.08	48.72	50.08	78.59	98.11	99.50
0.4	19.88	46.90	50.06	77.19	97.02	99.32
0.5	19.55	44.66	49.99	76.66	95.63	98.98
0.6	19.12	42.50	49.81	76.62	93.71	98.77
Length ratio	RCNF of different modes (non-dimensional results)					
0	0.00	0.00	0.00	0.00	0.00	0.00
0.1	0.00	0.00	0.00	0.00	0.00	0.00
0.2	0.00	0.01	0.00	0.01	0.01	0.00
0.3	0.01	0.03	0.00	0.03	0.01	0.00
0.4	0.02	0.06	0.00	0.04	0.03	0.00
0.5	0.03	0.11	0.00	0.05	0.04	0.01
0.6	0.05	0.15	0.01	0.05	0.06	0.01

The results in Table 6-28 to Table 6-31 show a more obvious difference between the results obtained from the AFE model and those from previous studies which is caused by the different modelling assumptions and the size of the element mesh. Figure 6-20 plots the RCNF curves from the different models. Unlike the previous cases, the natural frequencies associated with asymmetric modes will have a non-zero RCNF due to the presence of the crack.

From Figure 6-20, it is evident that results obtained from the AT model match well with Huang and Leissa (2009) while results from the ATCS model agree well with AFE. The reason for this is that the modelling assumptions for the AT model are more representative of those made in previous studies (e.g. Huang and Leissa (2009)) and the ATCS model is closer to the proposed AFE model. Only mode (1,2) shows a good match for all four models across the full range of crack lengths; however, all RCNF data match well when the crack length ratio is smaller than 0.3. This difference in behaviour is also reflected in the mode shapes. As shown in Figure 6-21, mode shapes reproduced from Huang and Leissa (2009) show similar trends to the mode shapes plotted by AFE for initial crack. With increasing crack length ratio, the mode shapes from different models are become more dissimilar. This difference in mode shapes is caused by the crack simulation: AFE only adopts a rotational spring to simulate the crack while other approaches consider changes in the vertical displacement across the damaged region. For a small crack, additional rotational springs are always validated and can be extended to the PTDC and ADC cases.

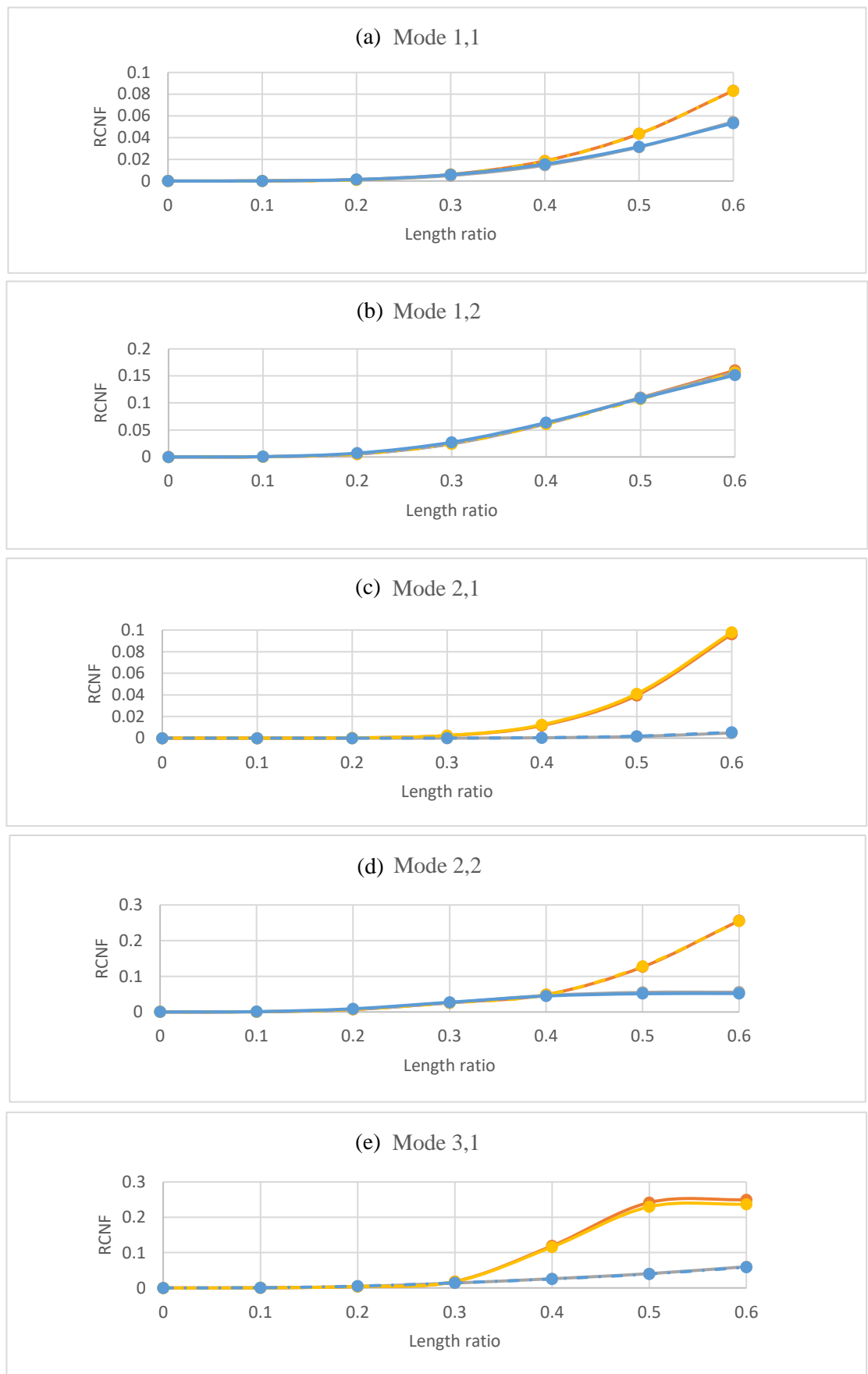


Figure 6-20 Comparison of the values of RCNF for different techniques for modelling an ATDC starting from an arbitrary point with various length ratio from different approaches, — AT — ATCS — Huang & Leissa — AFE(40*40).

(a) mode 1,1; (b) mode 1,2; (c) mode 2,1; (d) mode 2,2; (e) mode 3,1.

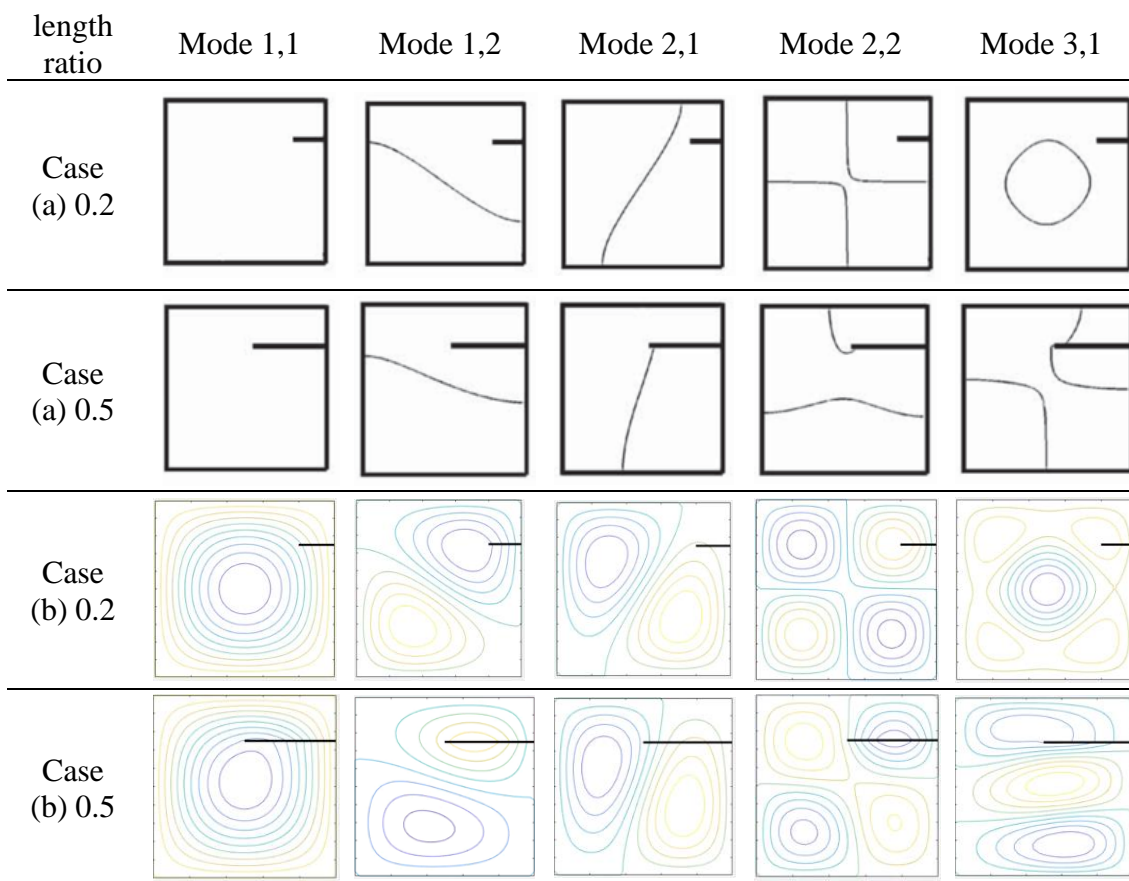


Figure 6-21 Comparison of mode shapes for different modes when the crack length ratio is 0.2 and 0.5; crack angle is 90°; crack start point $(x, y) = (0.075, 0.1)$.

(a) Huang and Leissa (2009); (b) AFE 40*40 model.

6.4.2.4 PTDC with Fixed Length Ratio starting at Different Point

Sections 6.4.2.1 to 6.4.2.3 have discussed the PTLC with all through the depth crack cases, and a good match has been shown between AFE and previous studies. Further validation is needed to examine the feasibility of AFE for modelling arbitrary crack conditions (arbitrary crack location, depth, length and orientation). The next set of results are for a part through-the-depth crack (PTDC). Because the study of PTDC is essentially absent from previous literature, the validated ATCS model will be used to compare with the AFE model in these specific cases, which concern an isotropic simply supported square plate with the same properties and dimensions as the previous cracked plate cases. Three different PTDC cases will be illustrated to analyse the vibration behaviour. The first two PTDC cases will present a fixed-length ratio ($\frac{l_c}{b} = 0.5$) crack with various depth ratios at different locations. Figure 6-22 (a) shows a parallel crack starting at $(x, y) = (0.075, 0.05)$ and finishing at $(x, y) = (0.075, 0.1)$; Figure 6-22 (b) demonstrates a parallel crack starting at $(x, y) = (0.05, 0.05)$ and finishing at $(x, y) = (0.05, 0.1)$. Then,

the last case in section 1.4.2.5 shows a crack with a fixed depth ratio ($\frac{d}{h} = 0.5$) with different length ratios starting at the point $(x, y) = (0.075, 0.1)$. The results are shown in tables using the same data processing methodology as previous cracked cases. Furthermore, comparative RCNF results are plotted for the first six modes.

Table 6-32 and Table 6-33 show ONF and RCNF results for the first case shown in Figure 6-22 (a) and plotted in Figure 6-23. A good match is seen for all six modes, the maximum difference being less than 1%.

The next case moves the PTDC crack of the same length ratio to a different crack location (Figure 6-22) and looks at the effect of increasing the depth ratio. The same non-dimensional data is presented in Table 6-34 and Table 6-35.

However, because the crack is located on the centre line of the plate, antisymmetric mode shapes will appear for several modes, leading to zero curvature at the crack location and no change in the corresponding natural frequencies. Hence, the RCNF plots in Figure 6-24 only considers the remaining modes. A nearly perfect match is observed between the two approaches, the maximum difference between the RCNF being less than 0.1%.

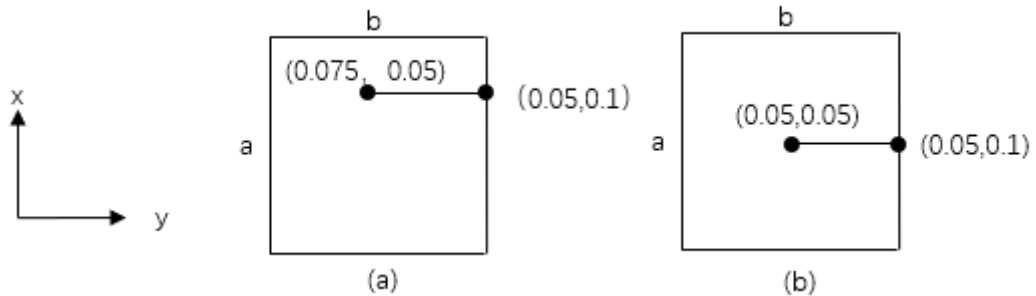


Figure 6-22 The plate dimensions ($a = 100\text{mm}$, $b = 100\text{mm}$) and the location of a PTDC with fixed length ratio 0.5.

Parallel crack locates at an arbitrary point of the plate, (a) crack starts at $(x, y) = (0.075, 0.05)$; (b) crack starts at $(x, y) = (0.05, 0.05)$.

Table 6-32 The ONF and RCNF of the PTDC shown in Figure 6-22 (a), data reproduced from AFE 40*40.

Depth ratio	Crack angle=90°; Crack length ratio=0.5					
	ONF of different modes (non-dimensional results)					
Depth ratio	1,1	1,2	2,1	2,2	3,1	1,3
0	20.1943	50.0828	50.0828	80.7956	99.5322	99.5328
0.1	20.1890	50.0319	50.0813	80.7536	99.4782	99.5240
0.2	20.1818	49.9625	50.0792	80.6963	99.4047	99.5125
0.3	20.1716	49.8644	50.0764	80.6153	99.3023	99.4965
0.4	20.1566	49.7204	50.0724	80.4964	99.1548	99.4738
0.5	20.1333	49.4985	50.0665	80.3136	98.9343	99.4403
0.6	20.0949	49.1375	50.0578	80.0173	98.5916	99.3892
0.7	20.0276	48.5157	50.0445	79.5127	98.0462	99.3102
0.8	19.9038	47.4185	50.0254	78.6477	97.2074	99.1928
Depth ratio	RCNF of different modes (non-dimensional results)					
0	0	0	0	0	0	0
0.1	0.0002	0.0010	0.0000	0.0005	0.0005	0.0001
0.2	0.0006	0.0024	0.0001	0.0012	0.0013	0.0002
0.3	0.0011	0.0044	0.0001	0.0022	0.0023	0.0004
0.4	0.0019	0.0072	0.0002	0.0037	0.0038	0.0006
0.5	0.0030	0.0117	0.0003	0.0060	0.0060	0.0009
0.6	0.0049	0.0189	0.0005	0.0096	0.0095	0.0014
0.7	0.0083	0.0313	0.0008	0.0159	0.0149	0.0022
0.8	0.0144	0.0532	0.0011	0.0266	0.0234	0.0034

Table 6-33 The ONF and RCNF of the PTDC shown in Figure 6-22 (a), data reproduced from ATCS 20*20.

Depth ratio	Crack angle=90° ; Crack length ratio=0.5					
	ONF of different modes (non-dimensional results)					
Depth ratio	1,1	1,2	2,1	2,2	3,1	1,3
0	19.7392	49.6915	49.6915	79.3664	100.8160	100.8202
0.1	19.7341	49.6412	49.6915	79.3245	100.7657	100.8076
0.2	19.7274	49.5742	49.6873	79.2658	100.6903	100.7992
0.3	19.7182	49.4820	49.6873	79.1820	100.5897	100.7867
0.4	19.7040	49.3437	49.6831	79.0605	100.4431	100.7657
0.5	19.6826	49.1300	49.6789	78.8678	100.2252	100.7364
0.6	19.6466	48.7780	49.6705	78.5619	99.8774	100.6903
0.7	19.5829	48.1662	49.6621	78.0339	99.3201	100.6191
0.8	19.4651	47.0810	49.6454	77.1247	98.4485	100.5059
Depth ratio	RCNF of different modes (non-dimensional results)					
0	0	0	0	0	0	0
0.1	0.0003	0.0010	0.0000	0.0005	0.0005	0.0001
0.2	0.0006	0.0024	0.0001	0.0013	0.0012	0.0002
0.3	0.0011	0.0042	0.0001	0.0023	0.0022	0.0003
0.4	0.0018	0.0070	0.0002	0.0039	0.0037	0.0005
0.5	0.0029	0.0113	0.0003	0.0063	0.0059	0.0008
0.6	0.0047	0.0184	0.0004	0.0101	0.0093	0.0013
0.7	0.0079	0.0307	0.0006	0.0168	0.0148	0.0020
0.8	0.0139	0.0525	0.0009	0.0282	0.0235	0.0031

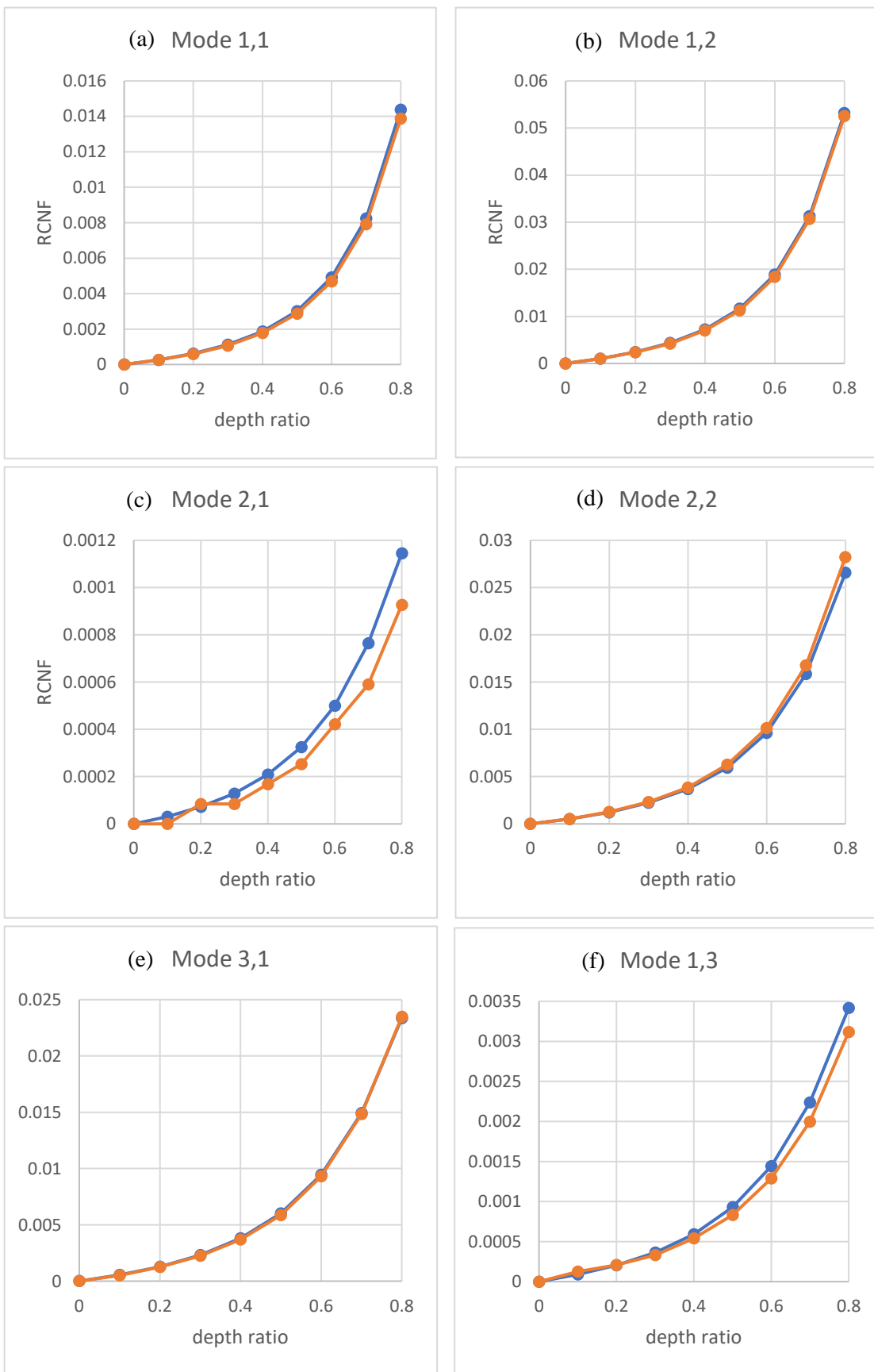


Figure 6-23 Different modes of comparative figures, PTDC starts from arbitrary point with various depth ratio from different approaches.

(a) mode 1,1; (b) mode 1,2; (c) mode 2,1; (d) mode 2,2; (e) mode 3,1; (f) mode 1,3.

—●— AFE(40*40) —●— ATCS

Table 6-34 The ONF and RCNF of PTDC shown in Figure 6-22 (b), data reproduced from AFM 40*40.

		Crack angle=90°; Crack length ratio=0.5				
		ONF of different modes (non-dimensional results)				
Depth ratio	1,1	1,2	2,1	2,2	3,1	1,3
0	20.1943	50.0828	50.0828	80.7956	99.5322	99.5328
0.1	20.1838	50.0708	50.0828	80.7955	99.4234	99.5155
0.2	20.1694	50.0542	50.0828	80.7955	99.2746	99.4925
0.3	20.1492	50.0307	50.0828	80.7955	99.0647	99.4607
0.4	20.1196	49.9962	50.0828	80.7955	98.7570	99.4153
0.5	20.0739	49.9428	50.0828	80.7955	98.2844	99.3482
0.6	19.9997	49.8554	50.0828	80.7955	97.5183	99.2459
0.7	19.8717	49.7034	50.0828	80.7955	96.2097	99.0873
0.8	19.6445	49.4307	50.0828	80.7955	93.9434	98.8518
Depth ratio	RCNF of different modes (non-dimensional results)					
0	0.0000	0.0000	0.0000	0.0000	0.0000	0.0000
0.1	0.0005	0.0002	0.0000	0.0000	0.0011	0.0002
0.2	0.0012	0.0006	0.0000	0.0000	0.0026	0.0004
0.3	0.0022	0.0010	0.0000	0.0000	0.0047	0.0007
0.4	0.0037	0.0017	0.0000	0.0000	0.0078	0.0012
0.5	0.0060	0.0028	0.0000	0.0000	0.0125	0.0019
0.6	0.0096	0.0045	0.0000	0.0000	0.0202	0.0029
0.7	0.0160	0.0076	0.0000	0.0000	0.0334	0.0045
0.8	0.0272	0.0130	0.0000	0.0000	0.0562	0.0068

Table 6-35 The ONF and RCNF of PTDC shown in Figure 6-22 (b), data reproduced from ATCS 20*20.

		Crack angle=90°; Crack length ratio=0.5				
		ONF of different modes (non-dimensional results)				
Depth ratio	1,1	1,2	2,1	2,2	3,1	1,3
0	19.7392	49.6915	49.6915	79.3664	100.8160	100.8202
0.1	19.7295	49.6789	49.6915	79.3664	100.7112	100.8034
0.2	19.7161	49.6621	49.6915	79.3664	100.5646	100.7825
0.3	19.6973	49.6370	49.6915	79.3664	100.3551	100.7532
0.4	19.6700	49.6035	49.6915	79.3664	100.0492	100.7154
0.5	19.6273	49.5490	49.6915	79.3664	99.5757	100.6568
0.6	19.5577	49.4610	49.6915	79.3664	98.8005	100.5646
0.7	19.4366	49.3060	49.6915	79.3664	97.4555	100.4221
0.8	19.2200	49.0210	49.6915	79.3664	95.0796	100.2000
Depth ratio	RCNF of different modes (non-dimensional results)					
0	0.0000	0.0000	0.0000	0.0000	0.0000	0.0000
0.1	0.0005	0.0003	0.0000	0.0000	0.0010	0.0002
0.2	0.0012	0.0006	0.0000	0.0000	0.0025	0.0004
0.3	0.0021	0.0011	0.0000	0.0000	0.0046	0.0007
0.4	0.0035	0.0018	0.0000	0.0000	0.0076	0.0010
0.5	0.0057	0.0029	0.0000	0.0000	0.0123	0.0016
0.6	0.0092	0.0046	0.0000	0.0000	0.0200	0.0025
0.7	0.0153	0.0078	0.0000	0.0000	0.0333	0.0039
0.8	0.0263	0.0135	0.0000	0.0000	0.0569	0.0062

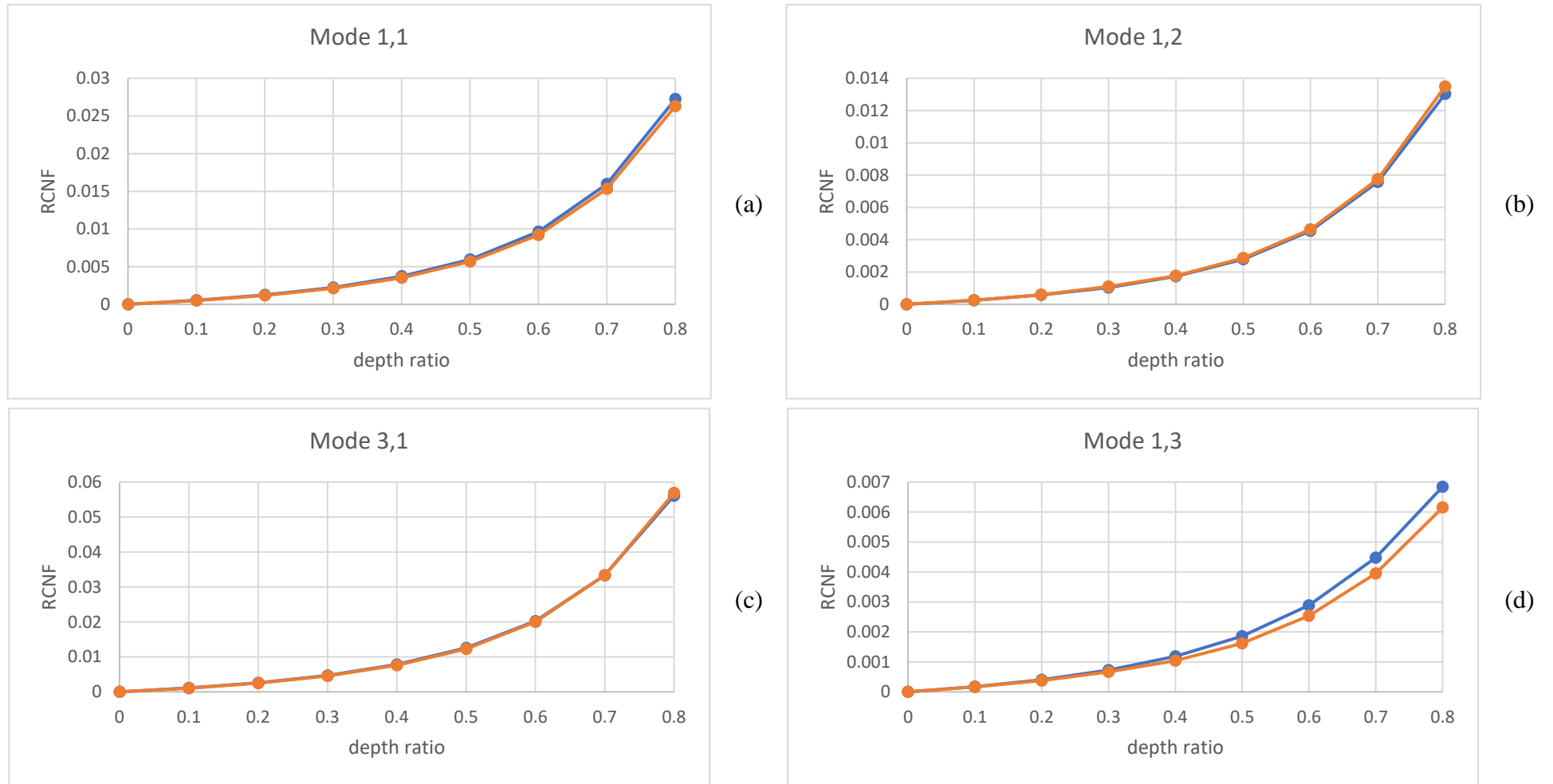


Figure 6-24 Different modes of comparative figures, PTDC starts from arbitrary point with various depth ratio from different approaches.

(a) mode 1,1; (b) mode 1,2; (c) mode 3,1; (d) mode 1,3. —●— AFE(40*40) —●— ATCS

6.4.2.5 PTDC with Fixed Depth Ratio starting at an Arbitrary Point

The final validation for a PTDC considers the cracked plate in Figure 6-25, having the same properties and dimensions as the previous cases. The crack starts at $(x, y) = (0.075, 0.1)$ and has a fixed depth ratio ($\frac{d}{h} = 0.5$) but different length ratios and remains parallel to the y -axis. Natural frequencies obtained from the AFE model are normalised and compared with the ATCS model. As before A 40×40 element mesh is used for the AFE model, and a 20×20 element mesh is applied for ATCS. ONF and RCNF results are shown in Table 6-36 and Table 6-37, while Figure 6-26 compares the RCNF from the two models. The crack starts a quarter of the way along one edge, disrupting the symmetry of the mode shape. However, as shown in Figure 6-26, the RCNF obtained from the AFE model still agrees well with the ATCS model as the length ratio increases.

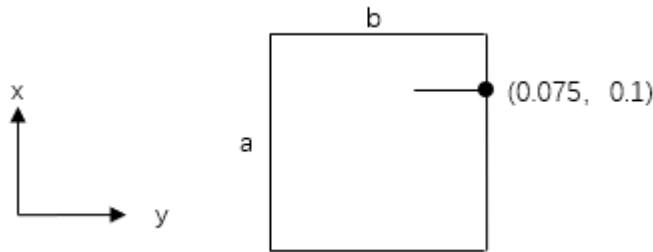


Figure 6-25 The plate dimensions ($a = 100\text{mm}$, $b = 100\text{mm}$) and the location of PTDC with a fixed depth ratio 0.5.

A parallel crack starts from an arbitrary point of the plate: $(x, y) = (0.075, 0.1)$.

Table 6-36 The ONF and RCNF of PTDC shown in Figure 6-25, data reproduced from AFE 40*40.

Length ratio	Crack angle=90°; Crack depth ratio=0.5					
	ONF of different modes (non-dimensional results)					
	1,1	1,2	2,1	2,2	3,1	1,3
0	20.1943	50.0828	50.0828	80.7956	99.5322	99.5328
0.1	20.1936	50.0741	50.0828	80.7756	99.5176	99.5322
0.2	20.1889	50.0161	50.0828	80.6608	99.4366	99.5316
0.3	20.1772	49.8859	50.0822	80.4755	99.3053	99.5234
0.4	20.1578	49.7012	50.0785	80.3433	99.1472	99.4893
0.5	20.1333	49.4985	50.0665	80.3136	98.9343	99.4403
0.6	20.1081	49.3092	50.0408	80.2952	98.6842	99.4189
Length ratio	RCNF of different modes (non-dimensional results)					
0	0	0	0	0	0	0
0.1	0.0000	0.0002	0.0000	0.0002	0.0001	0.0000
0.2	0.0003	0.0013	0.0000	0.0017	0.0010	0.0000
0.3	0.0008	0.0039	0.0000	0.0040	0.0023	0.0001
0.4	0.0018	0.0076	0.0001	0.0056	0.0039	0.0004
0.5	0.0030	0.0117	0.0003	0.0060	0.0060	0.0009
0.6	0.0043	0.0154	0.0008	0.0062	0.0085	0.0011

Table 6-37 The ONF and RCNF of PTDC shown in Figure 6-25, data reproduced from ATCS 20*20.

Length ratio	Crack angle=90°; Crack depth ratio=0.5					
	ONF of different modes (non-dimensional results)					
	1	2	3	4	5	6
0	19.7392	49.6915	49.6915	79.3664	100.8160	100.8202
0.1	19.7387	49.6873	49.6915	79.3580	100.8118	100.8160
0.2	19.7354	49.6412	49.6915	79.2658	100.7448	100.8160
0.3	19.7253	49.5239	49.6915	79.0815	100.6107	100.8118
0.4	19.7069	49.3395	49.6873	78.9181	100.4431	100.7867
0.5	19.6826	49.1300	49.6789	78.8678	100.2252	100.7364
0.6	19.6562	48.9247	49.6580	78.8594	99.9528	100.7071
Length ratio	RCNF of different modes (non-dimensional results)					
0	0	0	0	0	0	0
0.1	0.0000	0.0001	0.0000	0.0001	0.0000	0.0000
0.2	0.0002	0.0010	0.0000	0.0013	0.0007	0.0000
0.3	0.0007	0.0034	0.0000	0.0036	0.0020	0.0001
0.4	0.0016	0.0071	0.0001	0.0056	0.0037	0.0003
0.5	0.0029	0.0113	0.0003	0.0063	0.0059	0.0008
0.6	0.0042	0.0154	0.0007	0.0064	0.0086	0.0011

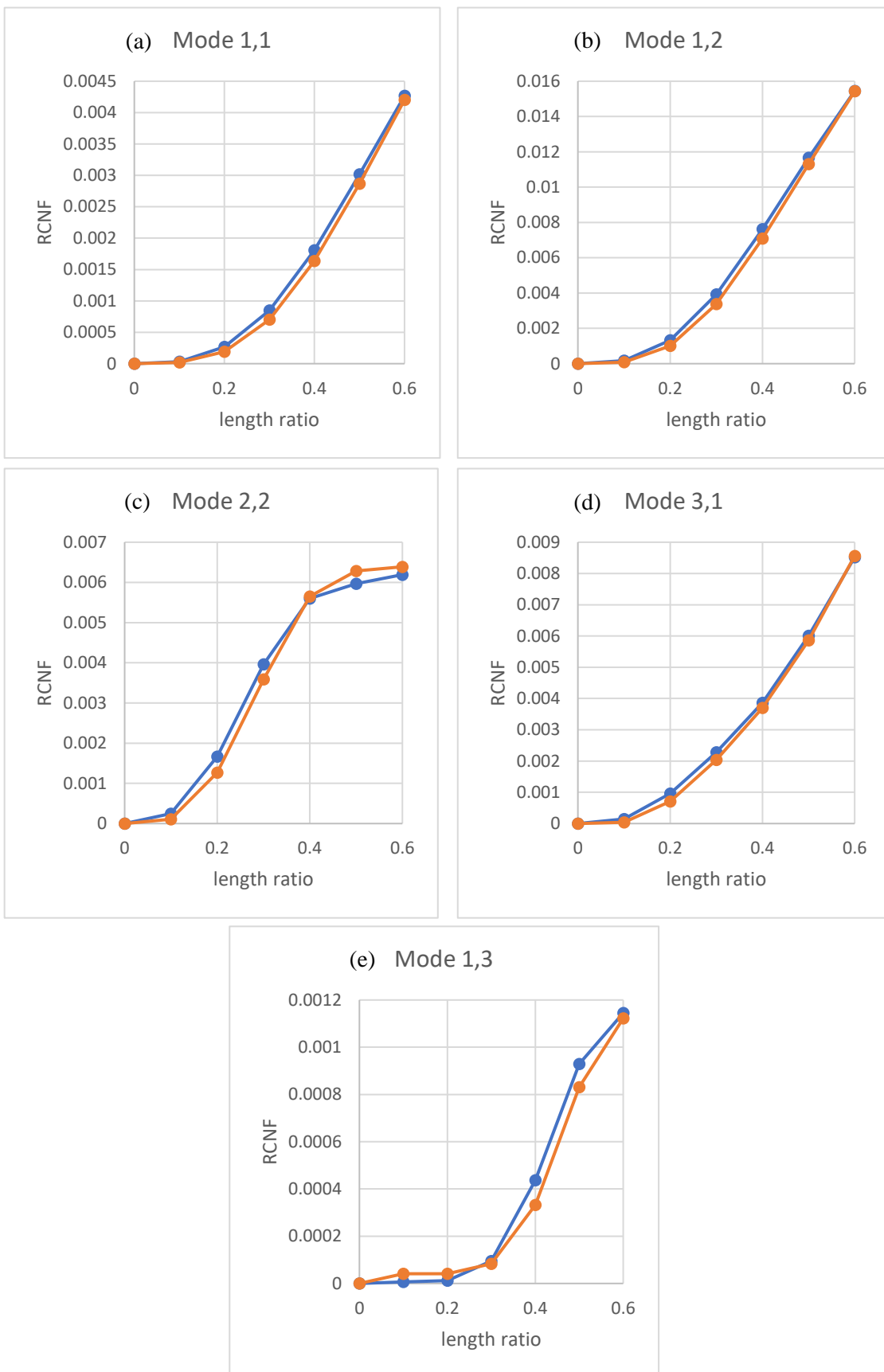


Figure 6-26 Different modes of comparative figures, PTDC starting from an arbitrary point with various length ratio from different approaches.

(a) mode 1,1; (b) mode 1,2; (c) mode 2,2; (d) mode 3,1; (e) mode 1,3. The value of RCNF from mode (2,1) is too small to plot as shown in Table 6-36 and Table 6-37.

—●— AFE(40*40) —●— ATCS

6.4.3 Discussion

In this section, eigenfrequencies obtained from the proposed AFE model have been compared with the literature and relevant ABAQUS models. The parallel partial through-the-length crack has been used for comparison based on different depth ratios and locations. Most of cracked cases show a good agreement with other studies especially when the crack is small (for ATDC, when the length ratio is smaller than 0.5). A good agreement with ABAQUS models has also been shown for PTDC. Natural frequencies for intact plates and the ATDC case when crack starts from the middle point have also been obtained using the hybrid model. A good agreement is shown when coupling the proposed FE model with ESM. The validations in this section will be a preliminary study for the arbitrary crack case (ADC), and an arbitrary direction crack will be studied in the next section.

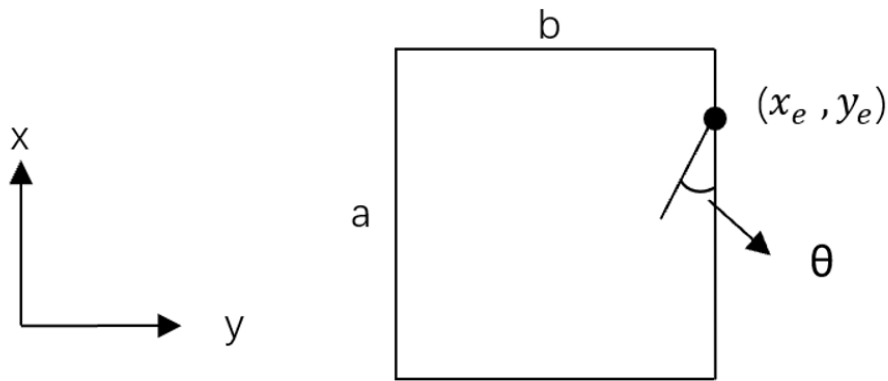


Figure 6-27 The dimension of the plate and the location of ADC with through crack depth at orientation $\theta = 15^\circ$ or 30° with various crack lengths, which ADC arbitrarily locates starting at $(x, y) = (0.075, 0.1)$.

6.5 Arbitrary direction crack

This chapter has introduced several crack cases for comparison with previous approaches. All through-the-length or all through-the-depth, parallel part through-the-depth and part through-the-length cracks have been analysed and compared with the ABAQUS ‘ATCS’ model. However, in reality not all cracks are parallel to the edges of the plate. Randomly located cracks with various shapes, directions and lengths will also occur in plate structures. Few methods possess the ability to analyse arbitrary cracks (with random direction, length, location and depth). AFE (which could be coupled with ESM in the hybrid VFM model) provides an attractive method to simulate an arbitrary direction crack (ADC) as a rotational spring whose stiffness is allocated to the nodes of the elements through which the crack passes. Detailed crack simulation concepts have been introduced in Chapter 5, and vibration results obtained from this and alternative models are presented in this section. The dimensions and materials of the analysed cracked plate are same as Figure 6-1.

Figure 6-27 shows an arbitrary cracked plate which has the same dimensions and properties as previous cases. The ADC case will be validated against results from Huang and Leissa (2009) and the ATCS model. The ADC starts at $(x, y) = (0.075, 0.1)$ with different crack length ratios $\frac{l_c}{b}$ varying from 0.1 to 0.6, and the orientation of the crack is 15° or 30° to the x -axis. The first five modes will be compared with Huang and Leissa (2009), and the first six modes will be compared with the ATCS model. For the AFE model, a rectangular 48×20 mesh is used giving a total of 960 elements. For the ABAQUS model, an adjustable mesh is used so that the crack runs along element boundaries with

its ends at nodes, and a combination of quadratic and triangular elements will be applied in ATCS model. Thus it should be noted that the mesh of elements in the ATCS model will be irregular and will cause a distinct difference in the relevant mode shapes. Non-dimensional natural frequencies and normalised relative changes in natural frequencies for the crack angle 15° are shown in Table 6-38 to Table 6-42. The following simulated case of crack angle 30° are listed in Table 6-43 and Table 6-44 for further validation with Huang and Leissa (2009).

Table 6-38 The ONF and RCNF of ADC shown in Figure 6-27, data reproduced from Huang and Leissa (2009).

	Crack angle= 15° ; Crack depth ratio=1				
	ONF of different modes (non-dimensional results)				
Length ratio	1,1	1,2	2,1	2,2	3,1
0	19.74	49.35	49.35	78.96	98.7
0.1	19.73	49.32	49.35	78.92	98.66
0.2	19.68	49.04	49.34	78.5	98.36
0.3	19.51	48.24	49.29	77.23	97.17
0.4	19.15	46.97	48.88	74.82	86.37
0.5	18.56	45.47	47.09	65.76	77.42
0.6	17.79	40.54	45.61	58.76	76.03
Length ratio	RCNF of different modes (non-dimensional results)				
0	0.00	0.00	0.00	0.00	0.00
0.1	0.00	0.00	0.00	0.00	0.00
0.2	0.00	0.01	0.00	0.01	0.00
0.3	0.01	0.02	0.00	0.02	0.02
0.4	0.03	0.05	0.01	0.05	0.12
0.5	0.06	0.08	0.05	0.17	0.22
0.6	0.10	0.18	0.08	0.26	0.23

Table 6-39 The ONF and RCNF of ADC shown in Figure 6-27, data reproduced from ABAQUS AT 24*20 model.

	Crack angle=15° ; Crack depth ratio=1					
	ONF of different modes (non-dimensional results)					
Length ratio	1,1	1,2	2,1	2,2	3,1	1,3
0	19.75	49.58	49.72	79.36	100.13	100.87
0.1035	19.74	49.57	49.70	79.32	100.12	100.82
0.2071	19.67	49.31	49.64	78.85	100.04	100.49
0.3106	19.48	48.41	49.58	77.44	98.43	100.05
0.4141	19.08	47.02	49.09	74.58	85.44	100.00
0.5176	18.44	45.17	47.06	64.44	77.55	99.45
0.6212	17.61	39.23	45.84	58.37	76.23	97.50
Length ratio	RCNF of different modes (non-dimensional results)					
0	0.00	0.00	0.00	0.00	0.00	0.00
0.1035	0.00	0.00	0.00	0.00	0.00	0.00
0.2071	0.00	0.01	0.00	0.01	0.00	0.00
0.3106	0.01	0.02	0.00	0.02	0.02	0.01
0.4141	0.03	0.05	0.01	0.06	0.15	0.01
0.5176	0.07	0.09	0.05	0.19	0.23	0.01
0.6212	0.11	0.21	0.08	0.26	0.24	0.03

Table 6-40 The ONF and RCNF of ADC shown in Figure 6-27, data reproduced from ABAQUS ATCS 24*20 model.

	Crack angle=15° ; Crack depth ratio=1					
	ONF of different modes (non-dimensional results)					
Length ratio	1,1	1,2	2,1	2,2	3,1	
0	19.75	49.58	49.72	79.36	100.13	
0.1035	19.74	49.57	49.70	79.32	100.12	
0.2071	19.67	49.31	49.64	78.85	100.04	
0.3106	19.48	48.41	49.58	77.44	98.43	
0.4141	19.08	47.02	49.09	74.58	85.44	
0.5176	18.44	45.17	47.06	64.44	77.55	
0.6212	17.61	39.23	45.84	58.37	76.23	
Length ratio	RCNF of different modes (non-dimensional results)					
0	0.00	0.00	0.00	0.00	0.00	
0.1035	0.00	0.00	0.00	0.00	0.00	
0.2071	0.00	0.01	0.00	0.01	0.00	
0.3106	0.01	0.02	0.00	0.02	0.00	
0.4141	0.03	0.05	0.00	0.04	0.00	
0.5176	0.06	0.08	0.00	0.05	0.01	
0.6212	0.10	0.10	0.01	0.05	0.02	

Table 6-41 The ONF of ADC shown in Figure 6-27, data reproduced from the AFE 48*20 model.

Four decimals are considered in the table to analyse the degradation of natural frequencies of ADC by a small increment of length ratio.

Length ratio	Crack angle=15°; Crack depth ratio=0.9999				
	ONF of different modes (non-dimensional results)				
	1,1	1,2	2,1	2,2	3,1
0	20.6731	50.8488	50.9159	82.8279	100.3853
0.1035	20.6607	50.7229	50.8758	82.5119	100.1769
0.2071	20.5882	49.9917	50.8279	81.2813	99.3301
0.3106	20.4073	48.7566	50.7549	80.0066	98.9672
0.4141	20.0039	47.2693	50.6367	79.3813	98.4088
0.5	19.5404	46.4884	50.4497	79.3336	96.6492
0.51	19.5404	46.4884	50.4497	79.3336	96.6492
0.5176	19.5404	46.4884	50.4497	79.3336	96.6492
0.52	19.3385	46.3049	50.3033	79.2751	95.8868
0.53	19.3385	46.3049	50.3033	79.2751	95.8868
0.54	19.3385	46.3049	50.3033	79.2751	95.8868
0.55	19.3385	46.3049	50.3033	79.2751	95.8868
0.56	19.3385	46.3049	50.3033	79.2751	95.8868
0.57	19.0931	46.2253	50.0707	79.1350	94.6552
0.58	19.0931	46.2253	50.0707	79.1350	94.6552
0.59	19.0931	46.2253	50.0707	79.1350	94.6552
0.6	19.0931	46.2253	50.0707	79.1350	94.6552
0.6212	19.0931	46.2253	50.0707	79.1350	94.6552
0.63	18.8730	46.1180	49.7390	78.9465	94.1061
0.64	18.8730	46.1180	49.7390	78.9465	94.1061
0.65	18.8233	46.1069	49.6164	78.9190	93.9134
0.67	18.8233	46.1069	49.6164	78.9190	93.9134
0.68	18.6681	46.0827	49.2984	78.7729	93.4966

If this study uses the same length ratios of ADC as Huang and Leissa (2009), the crack cannot be guaranteed to start and finish at the element boundaries. Hence, because the crack is all through-the-depth (for comparison with Huang and Leissa (2009)), a plot of RCNF against length ratio will show perturbations (Figure 6-31), as explained for a centrally located ATDC (Figure 6-16). Therefore additional value of crack length ratios have been used to calculated to show the ‘wobble’ effect for ATDC, while it can be avoided by ensuring the crack always starts and finishes at a node according to Figure 6-31.

Table 6-42 The RCNF of ADC shown in Figure 6-27, data reproduced from the AFE 48*20 model.

	Crack angle=15°; Crack depth ratio=0.9999				
	RCNF of different modes (non-dimensional results)				
Length ratio	1,1	1,2	2,1	2,2	3,1
0	0.0000	0.0000	0.0000	0.0000	0.0000
0.1035	0.0006	0.0025	0.0008	0.0038	0.0021
0.2071	0.0041	0.0169	0.0017	0.0187	0.0105
0.3106	0.0129	0.0411	0.0032	0.0341	0.0141
0.4141	0.0324	0.0704	0.0055	0.0416	0.0197
0.5	0.0548	0.0858	0.0092	0.0422	0.0372
0.51	0.0548	0.0858	0.0092	0.0422	0.0372
0.5176	0.0548	0.0858	0.0092	0.0422	0.0372
0.52	0.0646	0.0894	0.0120	0.0429	0.0448
0.53	0.0646	0.0894	0.0120	0.0429	0.0448
0.54	0.0646	0.0894	0.0120	0.0429	0.0448
0.55	0.0646	0.0894	0.0120	0.0429	0.0448
0.56	0.0646	0.0894	0.0120	0.0429	0.0448
0.57	0.0764	0.0909	0.0166	0.0446	0.0571
0.58	0.0764	0.0909	0.0166	0.0446	0.0571
0.59	0.0764	0.0909	0.0166	0.0446	0.0571
0.6	0.0764	0.0909	0.0166	0.0446	0.0571
0.6212	0.0764	0.0909	0.0166	0.0446	0.0571
0.63	0.0871	0.0930	0.0231	0.0469	0.0626
0.64	0.0871	0.0930	0.0231	0.0469	0.0626
0.65	0.0895	0.0933	0.0255	0.0472	0.0645
0.67	0.0895	0.0933	0.0255	0.0472	0.0645
0.68	0.0970	0.0937	0.0318	0.0490	0.0686

Figure 6-28 shows a good match for the same modelling assumptions i.e. the AT model agrees with Huang and Leissa (2009) for all the chosen modes. The RCNFs for the ATCS and proposed AFE model match well with those from the previous study for the fundamental mode, and also for the higher modes when the crack length ratio is small. But significant differences arise for larger crack ratios, which is explained by differences in the mode shapes of different modes shown in Figure 6-29. A potential swapped data recording exists for the higher modes, similar to that for a parallel arbitrary crack described earlier (Figure 6-18). For another arbitrary crack case when the crack angle is 30°, a similar phenomenon is shown of different fundamental mode cases in Figure 6-30.

Table 6-43 The ONF and RCNF of ADC shown in Figure 6-27, data reproduced from Huang and Leissa (2009).

Length ratio	Crack angle=30°; Crack depth ratio=1				
	ONF of different modes (non-dimensional results)				
Length ratio	1,1	1,2	2,1	2,2	3,1
0	19.74	49.35	49.35	78.96	98.70
0.1	19.72	49.35	49.31	78.94	98.61
0.2	19.64	49.35	49.03	78.69	98.03
0.3	19.44	49.30	48.33	77.78	96.12
0.4	19.07	48.89	47.39	75.12	87.14
0.5	18.50	46.67	46.50	66.22	79.56
0.6	17.78	46.38	39.99	60.77	77.66
Length ratio	RCNF of different modes (non-dimensional results)				
0	0.00	0.00	0.00	0.00	0.00
0.1	0.00	0.00	0.00	0.00	0.00
0.2	0.01	0.00	0.01	0.00	0.01
0.3	0.02	0.00	0.02	0.01	0.03
0.4	0.03	0.01	0.04	0.05	0.12
0.5	0.06	0.05	0.06	0.16	0.19
0.6	0.10	0.06	0.19	0.23	0.21

Table 6-44 The ONF and RCNF of ADC shown in Figure 6-27, data reproduced from the AFE 48*20 model.

Length ratio	Crack angle=30°; Crack depth ratio=0.9999				
	ONF of different modes (non-dimensional results)				
Length ratio	1,1	1,2	2,1	2,2	3,1
0	20.67	50.85	50.92	82.83	100.39
0.1	20.66	50.71	50.87	82.51	100.13
0.2	20.57	49.97	50.81	81.49	98.87
0.3	20.29	48.61	50.70	80.56	97.87
0.4	20.05	48.06	50.63	80.47	97.56
0.5	19.60	47.78	50.53	80.42	94.12
0.6	19.05	47.61	50.37	80.36	89.91
Length ratio	RCNF of different modes (non-dimensional results)				
0	0.00	0.00	0.00	0.00	0.00
0.1	0.00	0.00	0.00	0.00	0.00
0.2	0.00	0.02	0.00	0.02	0.02
0.3	0.02	0.04	0.00	0.03	0.03
0.4	0.03	0.05	0.01	0.03	0.03
0.5	0.05	0.06	0.01	0.03	0.06
0.6	0.08	0.06	0.01	0.03	0.10

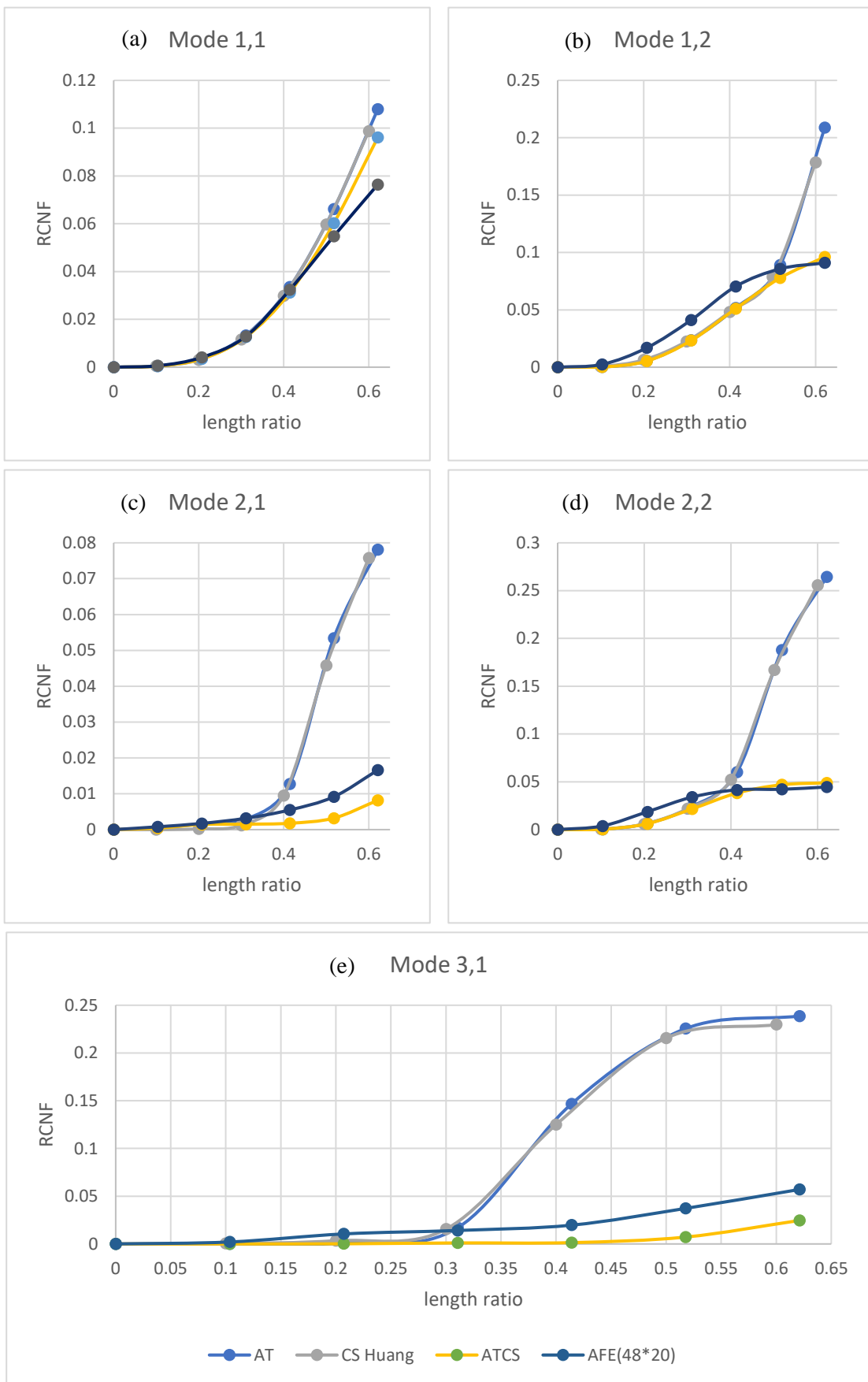


Figure 6-28 Comparison of RCNF for different modes for an ADC starting from an arbitrary point with various length ratios from different approaches, Crack angle=15°. (a) mode 1,1; (b) mode 1,2; (c) mode 2,1; (d) mode 2,2; (e) mode 3,1.

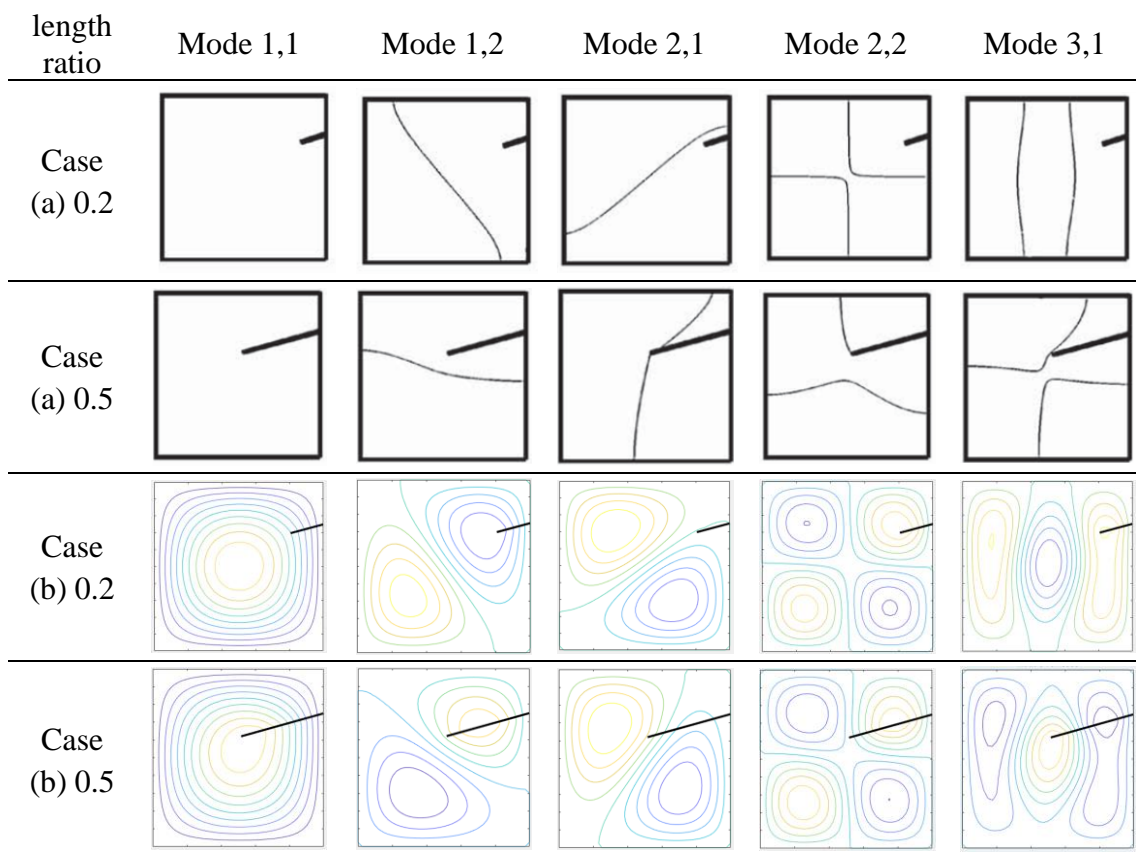


Figure 6-29 Comparison of mode shapes for different modes when the crack length ratio is 0.2 and 0.5; crack angle is 15° ; crack start point $(x, y) = (0.075, 0.1)$.

Model from (a) Huang and Leissa (2009) and (b) AFE model.

Whilst the AFE results match well with those obtained from the ATCS model for most of the results, some slight differences are seen in Figure 6-28. The crack simulation approach of AFE distributes the rotational stiffness to the nodes of all the elements through which the crack passes. Comparing the results using different sizes of element for AFE, 48×20 (48 elements per row and 20 elements per column) gives the best comparison with the ATCS model. As discussed in Figure 6-16, for an all through-the-thickness crack, a zero rotational stiffness is applied to each node of the damaged element even the crack does not extend completely through the whole element. Figure 6-31 shows a similar perturbation phenomenon to that seen in Figure 6-16, and a better match is obtained when the crack starts and ends at element boundaries (or preferably at nodes).

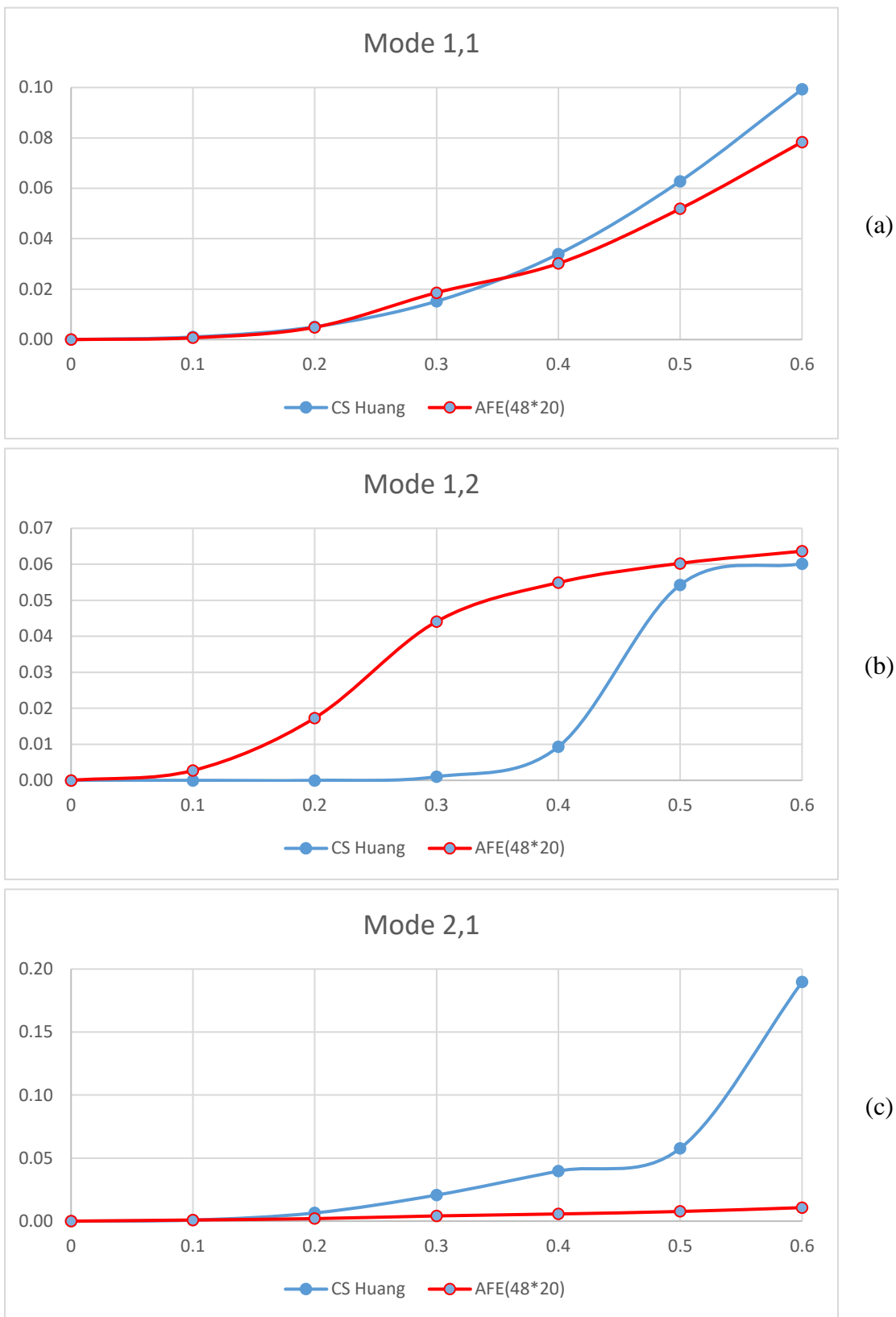


Figure 6-30 Comparison of RCNF for different modes for an ADC starting from an arbitrary point with various length ratios from different approaches, Crack angle=30°. (a) mode 1,1; (b) mode 1,2; (c) mode 2,1.

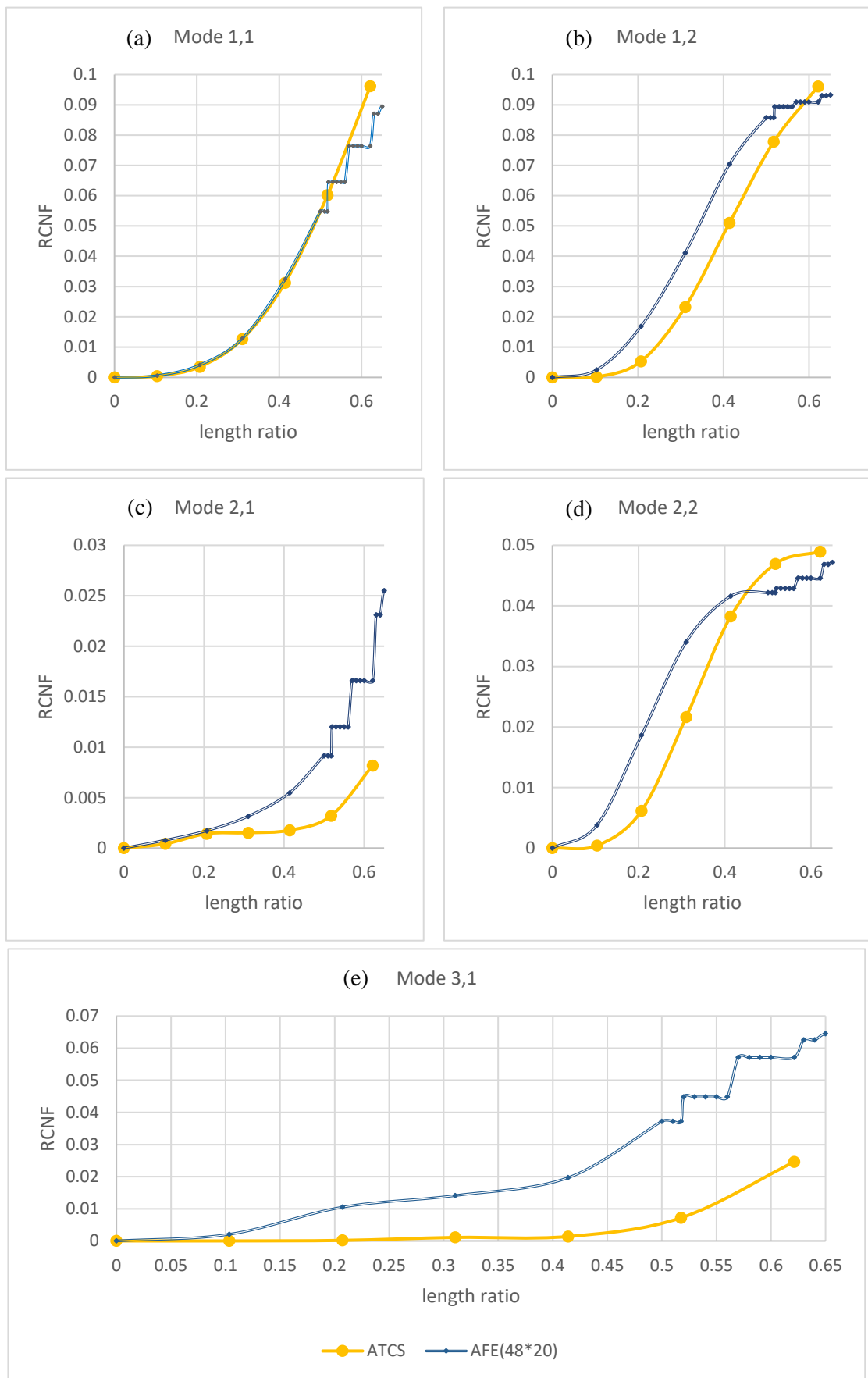


Figure 6-31 The influence of a small increment in crack length on the change natural frequencies for different modes, ADC starts from the arbitrary point with various length ratios.

(a) mode 1,1; (b) mode 1,2; (c) mode 2,1; (d) mode 2,2; (e) mode 3,1.

6.6 Summary of results and discussion

Natural frequencies have been obtained in this chapter for a square plate containing two types of damage: delaminations and cracks. For delaminations, a square composite plate of 16 layers with different angles was analysed. Because of the prismatic status limitation of the VICONOPT software, an all through-the-length delamination was studied first to explore the different degradation stages (Figure 6-4) as the delamination develops. All through-the-length delamination can be regarded as a one-dimensional problem, so that a plate containing an all through the length delamination can be simplified as a wide beam structure. Figure 6-5 shows the degradation of the stiffness of the plate in terms of the magnitude of the reduction in (natural frequencies)², as the width of the delamination increases for different damage locations. Delaminations in different locations follow the same pattern in that when the size ratio β/b (β is the delamination width, b is the plate width) is smaller than 0.2, the mode shapes exhibit global behaviour. The degradation of the natural frequencies is primarily affected by location and severity factors. Table 6-1 shows the severity effect for a single delamination and Eq. 6-1 indicates the relationship between the change in natural frequencies and the width of delamination. Table 6-2 shows the location effect using a set of uniformly spaced delaminations with a fixed delamination width 10mm, and the unnormalised squared changes in natural frequencies for different modes are plotted into Figure 6-6. The normalisation methodology applied in the inverse problem to eliminate the influence caused by the severity of the delamination is based on that given by Labib et al. (2015).

Crack detection is the primary research aim in this thesis. Damage needs to be detectable before it has caused catastrophic failure or irreparable damage to the structure. For simplicity, an additional rotational spring is used to simulate a non-severe crack (Caddemi and Caliò 2008; Labib et al. 2014). The main difference compared with other approaches is the number of degrees of freedom assumed in the crack region. Besides the rotational spring, shear effects, displacement and stretch effects are considered in other studies (Stahl and Keer 1972; Liew et al. 1994; Banerjee and Guo 2009; Huang and Leissa 2009; Bose and Mohanty 2013; Ismail 2013). For a single crack in an isotropic, simply supported plate, the primary effect of damage on the degradation of stiffness is represented by the rotational spring (Labib et al. 2014), while other factors could be considered as secondary effects. This is true when the crack is not severe (Labib 2015), however, more effects need to be taken into consideration for a more complicated structure or a severe crack. Based on the validated underlying concept of the hybrid model,

an extension of the stiffness matrix for additional different types of spring (like translational springs) to apply on other degrees of freedom is not difficult and could be studied in the future. For the validation of the cracked plate model, two ABAQUS models are introduced to simulate the AFE model and other methods separately. The ATCS model is similar to AFE while the AT model is closer to the models from literature. The crack analyses in this chapter can be grouped into two parts: parallel cracks and arbitrary direction cracks.

For a crack parallel to one of the axes the following cases were considered: all through-the-length crack, partial through-the-length crack, all through-the-depth crack and partial through-the-depth crack.

The first cracked plate case was an all through-the-length crack placed at different locations. For cracks in the middle of the plate and at an arbitrary point, close agreement of the obtained natural frequencies from VICONOPT model and AFE mode was shown in Figure 6-10 and Figure 6-11. The maximum difference between the relative changes in natural frequencies was less than 0.3%. Table 6-12 and Table 6-13 show a good match of the convergence of natural frequencies obtained for an intact plate and an all through-the-depth crack, validating the VICONOPT model so that its results could be then used as a reference for the proposed AFE model.

The next comparison was a parallel partial through-the-length, all through-the-depth crack, located at the middle of plate and increased in length in 20% increments of the plate width. Results obtained from AFE compared well with Stahl and Keer (1972), Liew et al. (1994), Bose and Mohanty (2013) and the ATCS model. A good comparison of the relative change in natural frequencies is shown in Figure 6-13 for symmetric modes (about the y-axis), with the maximum difference (occurring in mode 5), being around 2%. Due to the symmetry and isotropic material, there is zero curvature at the crack location in the anti-symmetric modes (about the y-axis) when the crack is located along the centre line of the plate and the natural frequency will then be constant as shown in Table 6-15 to Table 6-20.

There is an absence of studies in the literature for arbitrarily aligned cracks, especially for partial through-the-depth cracks, and a validation model is needed to examine the proposed AFE method. Hence, Figure 6-15 shows a plot comparing the results from an ABAQUS model, AFE and the literature (Liew et al. (1994)). A perfect match is shown for the ATDC when it is located in the middle of the plate. The AT model uses the same

crack simulation assumptions as previous studies and the ATCS model uses a rotational spring to represent the crack. Based on this, the ATCS model is chosen to validate the AFE when analysing a partial through-the-depth crack or arbitrarily located crack.

The results for a centrally located crack in an isotropic square plate obtained for different finite element meshes using the AFE model show the same trends in Figure 6-16, with a slight difference between a coarser mesh (20*20) and a finer mesh (40*40). For different mesh sizes, if the crack occurs precisely on the edge of elements there is better agreement with previous studies than when the crack passes through the elements. Moreover, for the ATDC case, a perturbation phenomenon is shown in Figure 6-16 for different sizes of element. This is because the crack is represented by an infinite additional compliance applied to all nodes of the elements through which the crack passes, even if it only encroaches a small way into the element. If more length ratio points are inserted between 0 and 0.2 as shown in Figure 6-16, the same natural frequencies will be obtained for these different length ratios for several element sizes. However, the perturbation will vanish when a partial through-the-depth crack is analysed because only a finite compliance is added to the nodes. For a non-severe crack, the AFE provides convenient solutions with acceptable accuracy. Considering the computational efficiency and calculation accuracy, a 40*40 element mesh is chosen and is applied in further cracked plate analysis.

In the next crack case, an ATDC starts from the middle of one edge of the plate, and the results obtained from AFE are compared with Huang and Leissa (2009) and related ABAQUS models. A good match is shown in Figure 6-17 except for mode (1,2). By studying the mode shapes of Figure 6-18, a swap is observed in the modes recorded by Huang and Leissa (2009) when the length ratio is greater than 0.4. To address this sequencing problem, the automatic mode shape sign method proposed in Chapter 4 is used to modify the problem by numerical comparison of the mode shapes. When the ATDC starts from the quarter edge of the plate ($(x,y) = (0.075,1)$), the natural frequencies obtained from AFE compare well with Huang and Leissa (2009) and related ABAQUS models. An arbitrarily located crack will break the symmetry of the plate, so that every mode will show a change in natural frequencies. The relative changes in natural frequencies match well for all modes when the crack length ratio is smaller than 0.4. With further increases in crack length ratio, due to the differences in crack simulation and recording methodologies, AFE only complies with the ATCS model for severe crack as shown in Figure 6-20.

The final parallel case is a partial through-the-depth crack, and further validation is made using the ATCS model. The PTDC case starts from the middle of one edge or a quarter of the way along one edge as shown in Figure 6-22. Plots of the relative changes in natural frequencies show satisfactory agreement between AFE model and ATCS model. The maximum difference between the two is less than 0.2% for cracks starting at different locations and having varying depth ratios (see Figure 6-23 and Figure 6-24). For a fixed depth ratio with different length ratios, when the crack starts at a point a quarter of the way along one edge, the curves of related change natural frequencies obtained from AFE and ATCS model still match.

Besides the parallel crack, a crack with an arbitrary orientation angle is analysed in Section 6.5, and the results are compared with those from Huang and Leissa (2009). The crack starts a quarter of the way along one edge and has a 15° orientation to the x -axis. Results show a good comparison when the crack is small. As with the parallel crack, differences in crack simulation and mode recording mean that only the ATCS model agrees with AFE results when the crack length ratio is greater than 0.3 (mode (3,1)). Figure 6-29 shows that differences exist in each mode shape between AFE and Huang and Leissa (2009). As for ATCS (described in section 5.2.3), the model requires the crack to start and finish at the nodes. Hence, for an arbitrary direction crack, the mesh in ATCS requires the use of both quadratic and triangular elements. Because different meshes have been chosen for the AFE model and ATCS models, different mode shapes will occur between these two models. However, reasonable agreement is shown in Figure 6-31 where the maximum difference is less than 4%.

6.7 Conclusion

This chapter tabulates and plots the natural frequencies obtained from the proposed AFE model and compares them with previous studies (Stahl and Keer 1972; Liew et al. 1994; Huang and Leissa 2009; Bose and Mohanty 2013) and ABAQUS models. The Wittrick-Williams algorithm (Wittrick and Williams 1971) and Lagrangian Multipliers (Williams and Anderson 1983) are introduced to calculate the natural frequencies from an assembled global dynamic stiffness matrix. Natural frequencies of a single cracked plate structure are calculated by a hybrid approach which combines the computational efficiency of the exact strip method with the versatility of the finite element analysis. The proposed method can fill gaps in the literature for arbitrary crack models (arbitrary length, depth, location and orientation). Good agreement has been shown for a parallel crack modelled using VICONOPT, Stahl and Keer (1972), Liew et al. (1994), Huang and Leissa (2009) and an ABAQUS model.

The proposed AFE model improves the computational efficiency by using an advanced bandwidth method in the Gaussian elimination, resulting in a time of 248s for a 40*40 FE model calculation as shown in Figure 6-32. The AFE model shows a greater advantage in element meshing when preparing a cracked model. Here once the mesh is determined, the model will automatically add corresponding rotational spring stiffnesses to the nodes of damaged elements, and it is not necessary to re-mesh. The AFE model shows the benefits of accuracy and convenience and could be well coupled with the Exact Strip Method by Lagrangian Multipliers.

In preparation for the inverse problem, an all through-the-length delamination shows the size and location effects respectively in Table 6-1 and Table 6-2. The relative sensitivities of different natural frequencies to the crack location and severity could be used for crack identification. The applicability of the AFE for modelling a single delaminations and cracks in isotropic plate-like structures has been examined in this chapter, while the location effect and severity effect have been discussed individually for the partial through-the-thickness cases. Moreover, as the central part of the VFM hybrid approach, the AFE model has been examined and compares well with previous studies and ABAQUS models.

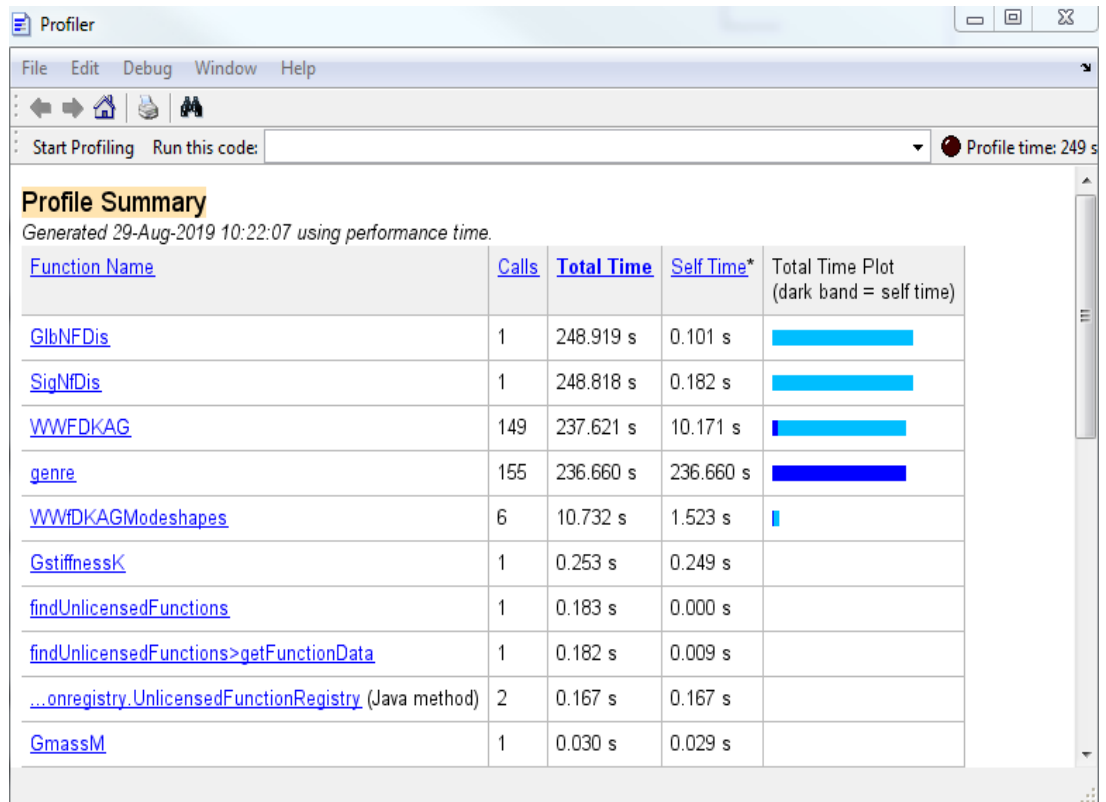


Figure 6-32 Time consumption for AFE 40*40 model.

Chapter 7--- Damage Detection in Plate Structures

7.1 Introduction

Plate-type structures are used widely in many different engineering sectors and are particularly important in aerospace structures. Damage caused by impact or arising from stress concentrations (e.g. around rivet holes), both during manufacture and in operation, can lead to significant reductions in strength and stability. This is further complicated by the fact that in many cases, for example when composite materials are used, this damage is invisible from the surface. The ability to detect damage using non-destructive detection techniques (NDT) and to understand its effects on the behaviour of structures is therefore essential to ensure safe operation. In this chapter a method for detecting cracks based on the resulting changes to the structure's natural frequencies is presented. The method consists of two stages: crack location and severity prediction.

Chapter 4 presented the data processing methodologies used in this study including the Wittrick-Williams algorithm, the automatic mode shape sign method and the bandwidth method for iterative calculations. Chapter 5 developed the hybrid VFM model and the primary AFE model, in which cracks are simulated based on the addition of a rotational spring. Finally, Chapter 6 compared the natural frequencies obtained from the AFE model with previous studies for different crack cases (ATLD, ATLC, PTLC, ATDC, PTDC and ADC). Good agreement between the obtained vibration parameters was presented as well as data on the effect of cracks with different locations / severities on the natural frequencies of a series of plates plotted for different vibration modes.

In this chapter, the method proposed by Labib et al. (2015) in which crack localisation is dependent on normalising the variation between a structure's uncracked and cracked natural frequencies, is used to solve a one-dimensional cracked structure problem. This approach, which Labib (2015) applied to beam and frame structures, is extended to study the effect of single through-the-length delaminations / cracks on the vibration parameters (natural frequencies and mode shapes) of plates. A set of discrete points is chosen along the transverse direction of the plate. The vibration parameters are obtained first for undamaged plates and then for those which have had damage introduced at each of these points at different depths and having different lengths and orientations. The consequent degradations in each of the natural frequencies as the damage is introduced are normalised to obtain curves which are independent of the damage severity. The crack severity is

determined by comparing with the unnormalized data through the severity relative index Δ from reference set. The curves are then used to solve the inverse problem of locating the damage with simulated noise-free and contaminated natural frequency measurements considered.

The two-dimensional problem of part through-the-length cracks is then briefly introduced in Chapter 8 as a topic for future work. The effect, in terms of the changes in natural frequencies and mode shapes, of damage in plate-like structures with different boundary conditions will be then studied using the VFM model as the first stage of extending damage detection to two dimensional structures. A general degradation algorithm for the vibration parameters could be then achieved, and the inverse problem of damage detection could be then proposed and applied in the non-destructive detection. The results in the chapter will demonstrate the efficiency, reliability and accuracy of the methods developed for the one-dimensional problem.

7.2 Severity and location effects

As discussed in Chapter 6 and in the literature reviewed in Chapter 2, the presence of damage in a plate member causes a degradation in its natural frequencies that is mainly related to the damage location and severity. Figure 7-1 uses a crack of depth $0.4h$ of simply supported isotropic square plate of length and width l as an example of the relationship between the natural frequencies of undamaged and damaged structures. The crack runs from $(x, y) = (\alpha l, 0)$ to $(\alpha l, \beta l)$ where α is a location parameter in the range $0.1 \leq \alpha \leq 0.9$ and β is a length parameter in the range $0.2 \leq \beta \leq 0.8$. The four lowest non-dimensional natural frequencies are shown in Figure 7-1. This relationship can be written (Adam et al. 1978; Hearn and Testa 1991; Morassi 1993; Morassi et al. 2008; Labib 2015):

$$\omega_{ic} = \omega_{io}(1 - \tilde{s}f_i(x/l)) \quad \text{Eq. 7-1}$$

where ω_{io} and ω_{ic} are the natural frequencies in the undamaged and damaged cases individually, i is the mode number, \tilde{s} is a non-dimensional function of the crack severity that is independent of the mode number, x is the damage location along the transverse axis of the structure and $f_i(x/l)$ is a dimensionless function of the crack location x/l . Eq. 7-1 is derived from the first order natural frequency and validated for small severity cracks (generally defined as having a crack depth to section height ratio $d/h \leq 0.4$) (Morassi et al. 2008). The relative change in natural frequencies (RCNF) uses the form of Eq. 6-3, $\delta_{ij} = \tilde{s}f_i(x/l)$. As the RCNF is related to both the severity and the location of the damage, the change in natural frequencies is normalised to eliminate the severity effect (Adam et al. 1978; Hearn and Testa 1991; Morassi et al. 2008; Labib et al. 2015) for different vibration modes:

$$\bar{\delta}_l\left(\frac{x}{l}\right) = \frac{\delta_i}{\sqrt{\sum_i \delta_i^2}} = \frac{f_i(x/l)}{\sqrt{\sum_i (f_i(x/l))^2}} \quad \text{Eq. 7-2}$$

The summation of the relative changes in natural frequencies is dependent on the number of natural frequencies chosen. The range of the normalised relative changes in natural frequencies is $0 \leq \bar{\delta}_l\left(\frac{x}{l}\right) \leq 1$.

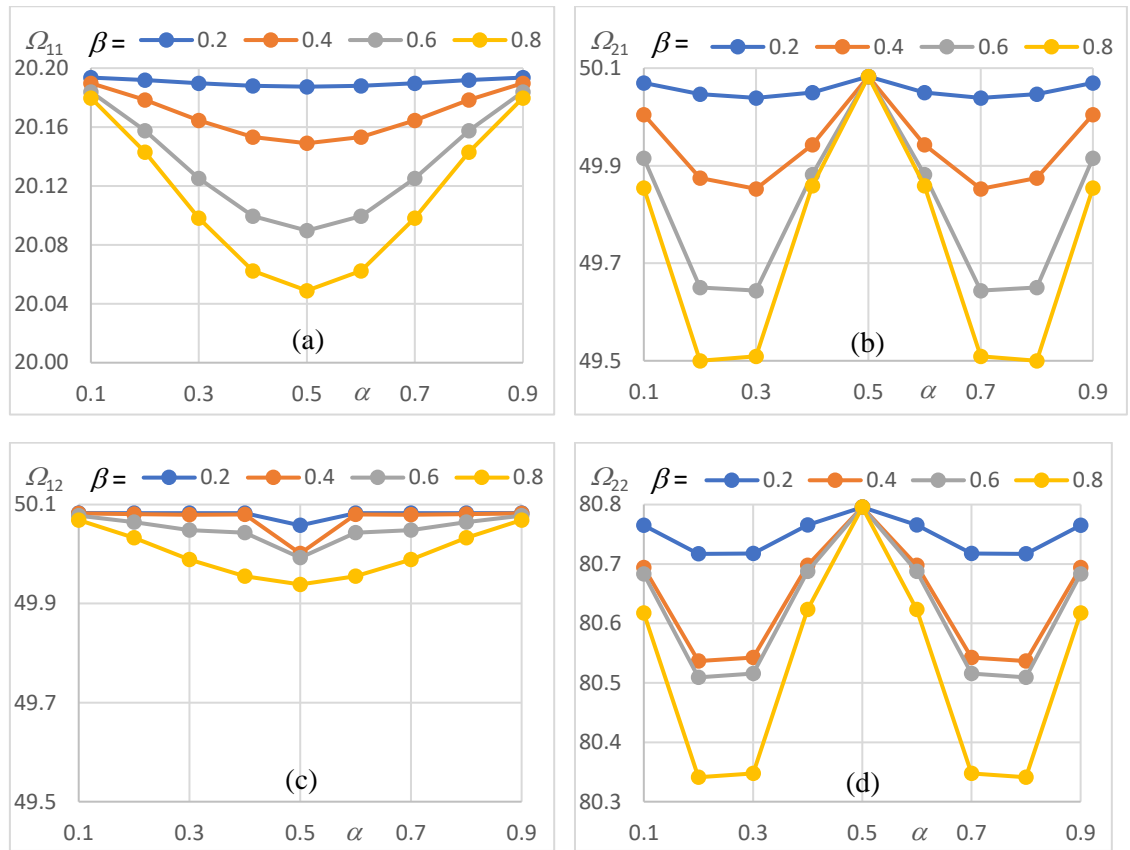


Figure 7-1 Degradation of natural frequencies with crack location and length (Luo et al. 2019).

(a) mode Ω_{11} ; (b) mode Ω_{21} ; (c) mode Ω_{12} ; (d) mode Ω_{22} .

For the severity problem, the dimensionless function $C\left(\frac{d}{h}\right)$ which is related to the crack depth to the section thickness ratio, can be used to generate a compliance equation (Eq. 5-5) to represent the severity of a crack. Table 6-1 to Table 6-5 show the changes in natural frequencies for different types of damage in different types of structures obtained by applying the dimensionless compliance formula.

During the validation and comparison of the VFM model with other approaches, the degradation of higher natural frequencies was sometimes found to be greater than that of lower modes causing the potential mode swapping. According to Figure 6-18 and Figure 6-21, this mode swapping problem occurs when the crack length ratio propagates to 0.5. This causes problems for the damage detection analysis, particularly in the normalisation procedure when the natural frequencies for different modes may be incorrectly grouped together. The noted trend for mode shapes of different modes to change gradually as crack severity increases (demonstrated in sections 6.4 and 7.3.3) and the automatic mode shape sign method described in section 4.2.2 can be utilised to avoid this. Using the partial through-the-length crack case in Figure 4-4 as an example, for a crack starting at $(x, y) =$

(0.04,0), the zero contour in mode 2 is parallel to the x -axis when the crack length ratio is 0.1. This zero contour rotates slightly as the crack length increases. The mode shapes of mode 2 would show a 90-degree rotation as the crack length ratio approaches 0.8. It appears to have rotated 90 degrees because it has been incorrectly identified and in fact this 90-degree mode is a higher mode which has swapped over. The automatic mode shapes sign method can solve the recording problem based on location and crack length ratio, respectively (see section 4.2.2). It solves the main sequencing problem except for cracks located in the middle of the plate, which are affected by the symmetry of their location and the zero curvature. Hence, manual adjustment of relevant vibration parameter recording is needed when cracks are located at the middle of a symmetric plate-type structures.

7.3 Single damage detection in plate-like structures using noise-free simulation

7.3.1 All through-the-length delamination

The natural frequencies of plates containing through-the-length delaminations can be obtained from VICONOPT models. These models are able to show the effect of the severity and location of a single source of damage introduced into the plate on these natural frequencies. In this chapter, the procedure for detecting damage in the all through-the-delamination (ATLD) case including normalisation and linear interpolation will be described first and can be regarded as a reference for the remaining cracked plate cases.

7.3.1.1 Normalisation procedure

The process will be described in relation to the detection of damage in a square composite plate having the same properties and dimensions as the case shown in section 6.2, with a delamination added which is 10mm wide and located at a depth of 0.5mm. A set of discrete points $\bar{\delta}_i \left(\frac{x}{l} \right)$ is chosen along the transverse direction (y-axis) as the reference points. The distance between the mid-points of consecutive delaminations is 10mm. Case 1 ($\xi = 0.01, \theta = 3 - 4$), 2 ($\xi = 1, \theta = 1$) and 3 ($\xi = 1, \theta = 3$) represent different modes of simulate case, ξ and θ here are in terms of XI and EIGEN in Figure 7-3.

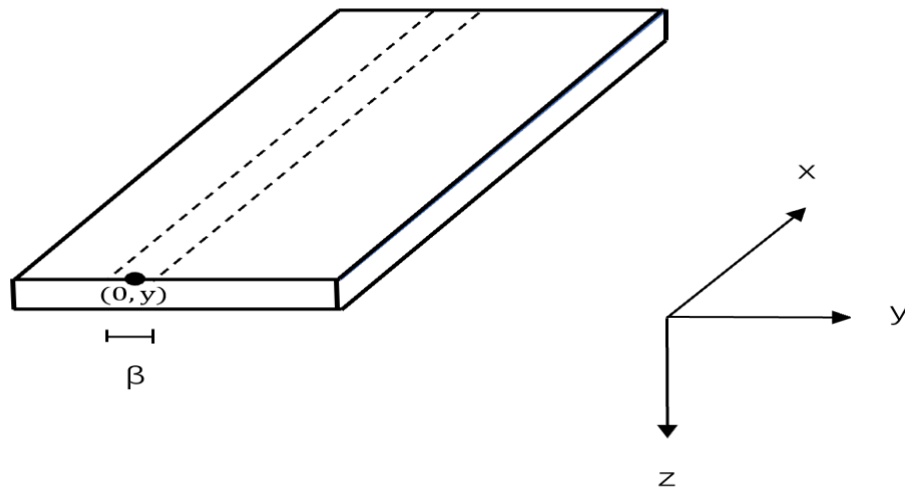


Figure 7-2 ATLD case geometry.

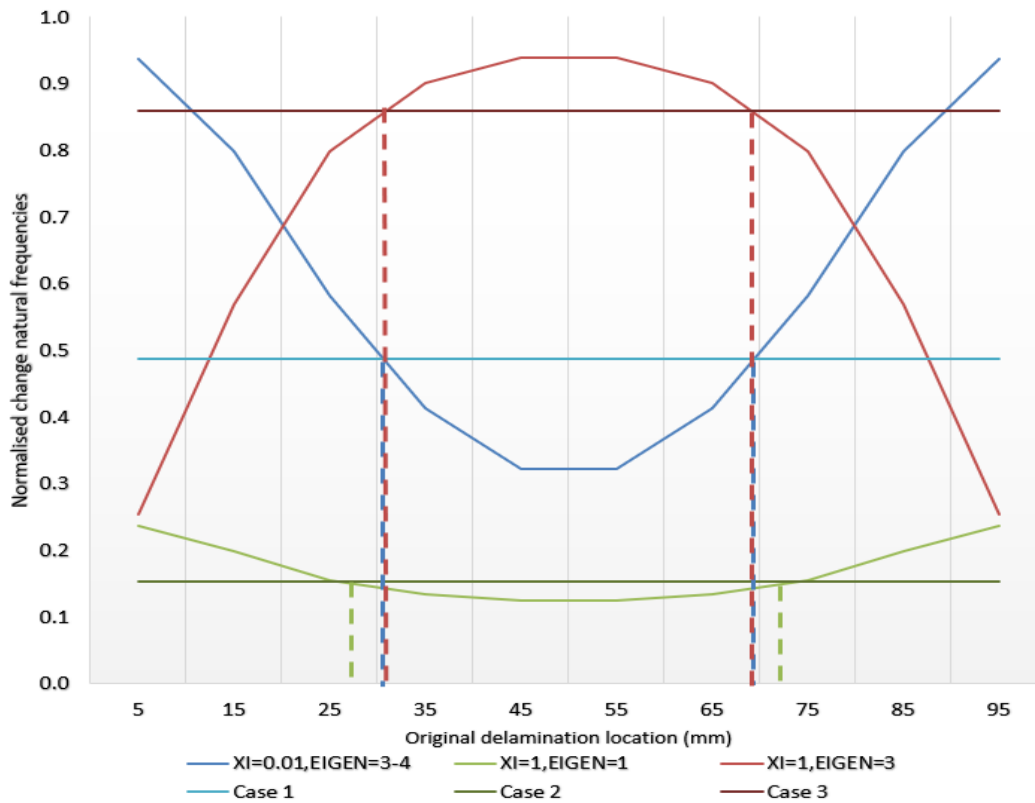


Figure 7-3 Normalised reference frequency and simulated frequency, from three chosen modes.

Table 7-1 Changes in natural frequencies for a fixed width delamination ($\beta = 10mm$).

Change natural frequencies (δ_i)				Normalised natural frequencies ($\bar{\delta}_i$)			
DL, y (mm)	$\xi=0.01, \theta=3-4$	$\xi=1, \theta=3$	$\xi=1, \theta=1$	Mag (r_w)	$\xi=0.01, \theta=3-4$	$\xi=1, \theta=3$	$\xi=1, \theta=1$
5	0.0040	0.0011	0.0010	0.0043	0.9378	0.2535	0.2373
15	0.0045	0.0032	0.0011	0.0056	0.7979	0.5690	0.1991
25	0.0048	0.0066	0.0013	0.0082	0.5818	0.7983	0.1556
35	0.0045	0.0098	0.0014	0.0108	0.4138	0.9006	0.1333
45	0.0040	0.0116	0.0016	0.0124	0.3227	0.9382	0.1249
55	0.0040	0.0116	0.0016	0.0124	0.3227	0.9382	0.1249
65	0.0045	0.0098	0.0014	0.0108	0.4138	0.9006	0.1333
75	0.0048	0.0066	0.0013	0.0082	0.5818	0.7983	0.1556
85	0.0045	0.0032	0.0011	0.0056	0.7979	0.5690	0.1991
95	0.0040	0.0011	0.0010	0.0043	0.9378	0.2535	0.2373

The following steps are then taken:

1. The number of modes to be examined is chosen (in this example 3). A set of normalised natural frequencies $\overline{\delta_{im}}$ (one for each mode) is calculated based on measured (or simulated) data using Eq. 7-1 and Eq. 7-2.
2. Normalised natural frequencies and changes in natural frequencies based on delaminations positioned at each of the reference points are then calculated (based on the data presented in Table 6-2 and plotted in Figure 6-6. These are presented in Table 7-1 and the reference curves plotted in Figure 7-3.
3. The normalised measured (or simulated) changes in natural frequencies for each of the modes are drawn as horizontal lines in Figure 7-3.
4. These lines will cross the reference curves. For each mode, there will be at least two crossover points due to the symmetry of the problem.
5. The delamination location is the point at which all the intersections occur at the same place, with two potential damage locations detected if the plate is symmetric.

In Table 7-1, DL (mm) is the distance to the mid- point of the delamination along the y-axis; δ_i are the changes natural frequencies between the intact status and the damaged case; $\overline{\delta}_i$ are the normalised natural frequencies based on δ_i ; r_w is the magnitude of the chosen modes; ξ and θ are the eigenvalues which represent different modes.

For real engineering cases, the actual damage location is hard to predict as it is likely to occur between two successive discrete points. Hence, the crossover points for each of the modes examined may not coincide but will be close to the correct crack location. The intersections of the chosen mode must then be obtained by a process of linear interpolation. This process is outlined here.

7.3.1.2 Linear interpolation

The first stage is to estimate the damage location:

$$\dot{y}_i = y_1 + \left[\frac{y_2 - y_1}{\overline{\delta}_{i2} - \overline{\delta}_{i1}} * (\dot{\delta}_i - \overline{\delta}_{i1}) \right] \quad \text{Eq. 7-3}$$

Here \dot{y}_i is an estimate of the damage location, $\dot{\delta}_i$ is the normalised measured natural frequency of the specific mode. The expected natural frequencies are then calculated by another linear interpolation (Eq. 7-4) based on the width ratio defined in the reference set.

$$\delta_i = \delta_{i1} + \left[\frac{\delta_{i2} - \delta_{i1}}{y_2 - y_1} \right] * (\dot{y}_i - y_1) \quad \text{Eq. 7-4}$$

where δ_l is the natural frequency based on the expectation from the reference points with a defined severity ratio (the width of the delamination). The crack severity is then recovered by applying a specific severity ratio based on different damaged plate cases. For example, the specific severity ratio of ATLD case is obtained from Table 6-1 and formalised in Eq. 6-1. Finally, the recovered severity β_l of the measured damage can be obtained from Eq. 7-5.

$$\beta_l = \beta * \left(\frac{\delta_l}{\delta_l}\right)^\Delta \tag{Eq. 7-5}$$

where β is the defined width (10mm) of the delamination region of the reference point, and δ_l is the change natural frequencies of the measured data (Table 7-2). The index Δ ($\frac{1}{3}$ for the ATLD case) can be altered when the dimensions and properties of the plate change. Five different simulated cases with different severities and/or locations which will be used to demonstrate/validate this approach are listed in Table 7-2. The results of the linear interpolation process for each case are presented in Table 7-3, where, c is the ratio of the changes in natural frequencies from the expected value and the measured value. The data recorded retains four decimal places.

Table 7-2 Changes in natural frequencies with varying width delaminations at arbitrary locations.

Change in natural frequencies (δ_l)						Normalised frequencies (δ_l)		
DL, y (mm)	DS, β (mm)	$\xi=0.01,$ $\theta=3-4$	$\xi=1,$ $\theta=3$	$\xi=1,$ $\theta=1$	Mag (r_w)	$\xi=0.01,$ $\theta=3-4$	$\xi=1,$ $\theta=3$	$\xi=1,$ $\theta=1$
28	8	0.0025	0.0039	0.0007	0.0047	0.5325	0.8339	0.1455
28	16	0.0174	0.0307	0.0055	0.0357	0.4868	0.8600	0.1528
34	6	0.0010	0.0020	0.0003	0.0022	0.4464	0.8843	0.1366
18	10	0.0045	0.0036	0.0011	0.0059	0.7622	0.6174	0.1947
14	12	0.0072	0.0048	0.0019	0.0089	0.8174	0.5354	0.2128

Table 7-3 Location based on calculated data from the inverse problem compared with actual data.

Simulated Cases	DL: Y=28mm; DS: $\beta=8\text{mm}$			DL: Y=34mm; DS: $\beta=6\text{mm}$		
	$\xi=0.01,$ $\theta=3-4$	$\xi=1, \theta=3$	$\xi=1, \theta=1$	$\xi=0.01,$ $\theta=3-4$	$\xi=1, \theta=3$	$\xi=1, \theta=1$
y_1	25	25	25	25	25	25
y_2	35	35	35	35	35	35
$\overline{\delta}_{l1}$	0.5818	0.7983	0.1556	0.5818	0.7983	0.1556
$\overline{\delta}_{l2}$	0.4138	0.9006	0.1333	0.4138	0.9006	0.1333
$\dot{\delta}_l$	0.5325	0.8339	0.1455	0.4464	0.8843	0.1366
\dot{y}_l	27.9368	28.4759	29.5155	33.0583	33.4133	33.5110
Difference	0.23%	1.70%	5.41%	2.77%	1.73%	1.44%
$\ddot{\delta}_l$	0.0047	0.0077	0.0014	0.0045	0.0092	0.0014
δ_l	0.0025	0.0039	0.0007	0.0010	0.0020	0.0003
c	0.5310	0.5087	0.5032	0.2187	0.2127	0.2141
β	8.0977	7.9827	7.9538	6.0250	5.9691	5.9823
Difference	1.22%	0.22%	0.58%	0.42%	0.51%	0.29%
Simulated Cases	DL: Y=28mm; DS: $\beta=16\text{mm}$			DL: Y=18mm; DS: $\beta=10\text{mm}$		
	$\xi=0.01,$ $\theta=3-4$	$\xi=1, \theta=3$	$\xi=1, \theta=1$	$\xi=0.01,$ $\theta=3-4$	$\xi=1, \theta=3$	$\xi=1, \theta=1$
y_1	25	25	25	15	15	15
y_2	35	35	35	25	25	25
$\overline{\delta}_{l1}$	0.5818	0.7983	0.1556	0.7979	0.5690	0.1991
$\overline{\delta}_{l2}$	0.4138	0.9006	0.1333	0.5818	0.7983	0.1556
$\dot{\delta}_l$	0.4868	0.8600	0.1528	0.7622	0.6174	0.1947
\dot{y}_l	30.6546	31.0372	26.2303	16.6525	17.1121	16.0264
Difference	9.48%	10.85%	6.32%	7.49%	4.93%	10.96%
$\ddot{\delta}_l$	0.0046	0.0085	0.0013	0.0045	0.0039	0.0011
δ_l	0.0174	0.0307	0.0054	0.0045	0.0036	0.0011
c	3.7658	3.6141	4.2003	0.9908	0.9299	1.0107
β	15.5579	15.3461	16.1347	9.9693	9.7606	10.0354
Difference	2.76%	4.09%	0.84%	0.31%	2.39%	0.35%

Table 7-3 (continued)

Simulated Cases	DL: Y=14mm; DS: $\beta=12\text{mm}$		
	$\xi=0.01, \theta=3-4$	$\xi=1, \theta=3$	$\xi=1, \theta=1$
y_1	5	5	5
y_2	15	15	15
$\overline{\delta_{l1}}$	0.9378	0.2535	0.2373
$\overline{\delta_{l2}}$	0.7979	0.5690	0.1991
$\dot{\delta}_l$	0.8174	0.5354	0.2128
\dot{y}_l	13.6064	13.9348	11.4254
Difference	2.81%	0.47%	18.39%
$\ddot{\delta}_l$	0.0044	0.0029	0.0011
$\dot{\delta}_l$	0.0072	0.0047	0.0019
c	1.6528	1.6096	1.7558
β	11.8234	11.7194	12.0640
Difference	1.47%	2.34%	0.53%

When the delamination occurs at $y=28\text{mm}$ with a width factor of 8mm, the estimated locations based on the three modes are 27.9368mm, 28.4759mm and 29.5155mm respectively. The maximum difference between the expected and actual damage locations is less than 5%. In terms of severity, the result is more accurate, achieving from the different modes widths of 8.0977mm, 7.9827mm, and 7.9538mm, giving a maximum difference of less than 2%. A good match between the expected and actual values is also shown for the rest of the delamination cases with various locations and severity (Table 7-3).

7.3.2 All through-the-length crack

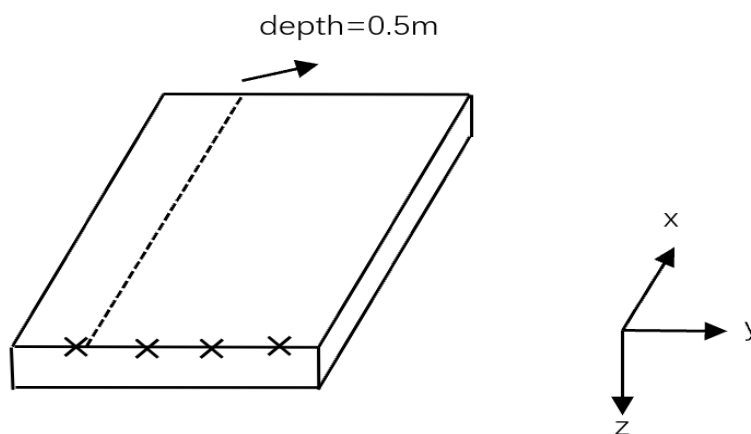


Figure 7-4 ATLC case geometry.

The validated damage detection method described above is next applied to the through-the-length crack case shown in Figure 7-4. Again, the dimensions and properties of the cracked plate are the same as those in section 5.2.1 for a composite simply supported square plate. An equally spaced reference set of crack locations is chosen along the y-axis and the same normalisation data processing and damage detection procedure are applied. The depth of the crack is 0.5mm and the distance between adjacent cracks is 10mm. Table 7-4 shows the natural frequencies of six different modes obtained from the VICONOPT model using rotational springs to simulate the crack (Caddemi and Caliò 2009; Labib et al. 2014). The modelling idea and relevant assumptions have been introduced in section 5.2.1. Frequencies are calculated to four decimal places.

The changes in natural frequencies and the normalised data for these modes are listed in Table 7-5. Four decimal places are considered for the original change natural frequencies and the normalised data, and the same value will be used in the following tables.

The magnitudes r_w of the six chosen modes for the ATLC case for $y = [5, 10, 15, 20, 25, 30, 35, 40, 45, 50]$ are [0.0004, 0.0016, 0.0029, 0.0041, 0.0045, 0.0044, 0.0035, 0.0028, 0.0024, 0.0026]. Four different measured cases for ATLC are shown in Table 7-6 to validate the method.

Table 7-4 Natural frequencies of through-the-length cracks with depth 0.5mm.

Natural frequencies of different modes (Hz)						
Intact	110.3599	63.8852	28.1436	77.5457	73.2854	44.3553
DL, y (mm)	$\xi = 1, \theta = 3$	$\xi = 1, \theta = 2$	$\xi = 1, \theta = 1$	$\xi = 0, \theta = 3$	$\xi = 0, \theta = 2$	$\xi = 0, \theta = 1$
5	110.3581	63.8631	28.1422	77.5405	73.2689	44.3541
10	110.3496	63.8053	28.1380	77.5250	73.2230	44.3499
15	110.3454	63.7353	28.1322	77.5085	73.1719	44.3456
20	110.3236	63.6791	28.1248	77.4890	73.1211	44.3363
25	110.3249	63.6583	28.1166	77.4785	73.1113	44.3320
30	110.2914	63.6802	28.1084	77.4707	73.1190	44.3195
35	110.3045	63.7367	28.1011	77.4739	73.1672	44.3184
40	110.2657	63.8062	28.0953	77.4787	73.2151	44.3060
45	110.2920	63.8630	28.0916	77.4854	73.2589	44.3100
50	110.2559	63.8844	28.0903	77.4878	73.2746	44.3008

Table 7-5 Changes in natural frequencies for ATLC from the reference set.

Changes in natural frequencies (δ_i)						
DL, y (mm)	$\xi=1, \theta=3$	$\xi=1, \theta=2$	$\xi=1, \theta=1$	$\xi=0, \theta=3$	$\xi=0, \theta=2$	$\xi=0, \theta=1$
5	0.0000	0.0004	0.0001	0.0001	0.0002	0.0000
10	0.0001	0.0013	0.0002	0.0003	0.0009	0.0001
15	0.0001	0.0024	0.0004	0.0005	0.0016	0.0002
20	0.0003	0.0032	0.0007	0.0007	0.0022	0.0004
25	0.0003	0.0036	0.0010	0.0009	0.0024	0.0005
30	0.0006	0.0032	0.0013	0.0010	0.0023	0.0008
35	0.0005	0.0023	0.0015	0.0009	0.0016	0.0008
40	0.0009	0.0012	0.0017	0.0009	0.0010	0.0011
45	0.0006	0.0004	0.0019	0.0008	0.0004	0.0010
50	0.0009	0.0000	0.0019	0.0008	0.0002	0.0012
Normalised changes in natural frequencies ($\bar{\delta}_i$)						
5	0.0375	0.8184	0.1201	0.1604	0.5337	0.0620
10	0.0596	0.8038	0.1284	0.1716	0.5464	0.0773
15	0.0455	0.8113	0.1405	0.1660	0.5354	0.0753
20	0.0804	0.7892	0.1641	0.1791	0.5484	0.1045
25	0.0704	0.7882	0.2130	0.1924	0.5270	0.1166
30	0.1424	0.7366	0.2870	0.2219	0.5209	0.1850
35	0.1444	0.6688	0.4343	0.2662	0.4639	0.2393
40	0.2998	0.4344	0.6028	0.3037	0.3369	0.3903
45	0.2578	0.1459	0.7745	0.3261	0.1516	0.4279
50	0.3678	0.0052	0.7394	0.2914	0.0577	0.4794

Table 7-6 Changes in natural frequencies for ATLC from simulated cracked cases.

Changes in natural frequencies (δ_i) of different modes							
DL, y (mm)	Depth, d (mm)	$\xi=1, \theta=3$	$\xi=1, \theta=2$	$\xi=1, \theta=1$	$\xi=0, \theta=3$	$\xi=0, \theta=2$	$\xi=0, \theta=1$
26	0.15	0.0001	0.0007	0.0002	0.0002	0.0005	0.0001
15	0.06	0.0000	0.0002	0.0000	0.0000	0.0001	0.0000
33	0.34	0.0003	0.0015	0.0008	0.0005	0.0010	0.0004
46	0.53	0.0006	0.0002	0.0019	0.0008	0.0003	0.0010
Normalised changes in natural frequencies ($\bar{\delta}_i$) of different modes							
DL, y (mm)	Depth, d (mm)	$\xi=1, \theta=3$	$\xi=1, \theta=2$	$\xi=1, \theta=1$	$\xi=0, \theta=3$	$\xi=0, \theta=2$	$\xi=0, \theta=1$
26	0.15	0.0764	0.7837	0.2247	0.2000	0.5235	0.1245
15	0.06	0.0461	0.8116	0.1404	0.1689	0.5341	0.0757
33	0.34	0.1276	0.7113	0.3673	0.2471	0.4890	0.2063
46	0.53	0.2636	0.0962	0.7834	0.3223	0.1202	0.4351

The magnitudes r_w of six chosen modes for each measured case [26, 15, 33, 46] are [0.0009, 0.0002, 0.0020, 0.0024]. After the determination of the natural frequencies and normalisation of the reference set and the simulated cracked cases, the inverse problem can be solved based on the data from Table 7-5 and Table 7-6, as documented in Table 7-7.

In each case shown in Table 7-7, for damage determination, the same procedure is applied as in section 7.3.1 for the one-dimensional problem. For example, when the actual measured crack location is 26mm, and the depth of crack is 0.15mm, the linear interpolation of Eq. 7-3 is used to calculate the expected crack locations based on the first six modes which are [25.4126mm, 25.4398mm, 25.7872mm, 26.2861mm, 27.8848mm, 25.5818mm]. The maximum difference occurs for mode (0, 2). Using the expected location and Eq. 7-4, while the estimated crack depths can be calculated as [0.1499mm, 0.1497mm, 0.1501mm, 0.1504mm, 0.1515mm, 0.1500mm]. The maximum difference between the expected and actual crack depths also occurs at mode (0, 2) and is 1.01%. The most discrepancy occurs when the measured location is 33mm and the depth is 0.34mm. In this case the maximum difference is seen for mode (1, 1) with the difference for location is 12.2% and crack depth is 25.62%.

Linear interpolation is then shown to provide accurate damage and severity information for one-dimensional problems, and has been shown to be effective in this study of ATLD and ATLC plates, although it could be improved by using a polynomial fitting curve or other advanced interpolation method.

The next stage therefore is to move to two dimensional problems, using the hybrid method to provide accurate and efficient natural frequencies for arbitrary cracked plate problems containing cracks at any location, orientation, length and depth. For fixed severity cracks (fixed length, depth and orientation) running parallel to either the x or y axis and uniformly distributed in the plate, the natural frequencies and normalised results can be obtained using VFM. This two-dimensional damage detection problem is briefly introduced in Chapter 8.

Table 7-7 The damage detection procedure for four different cases.

Simulated Damaged Case: DL: Y=26mm; Depth: d=0.15mm						
	$\xi=1, \theta=3$	$\xi=1, \theta=2$	$\xi=1, \theta=1$	$\xi=0, \theta=3$	$\xi=0, \theta=2$	$\xi=0, \theta=1$
y_1	25	25	25	25	25	25
y_2	30	30	30	30	30	30
$\bar{\delta}_1$	0.0704	0.7882	0.2130	0.1924	0.5270	0.1166
$\bar{\delta}_2$	0.1424	0.7366	0.2870	0.2219	0.5209	0.1850
$\dot{\delta}_i$	0.0764	0.7837	0.2247	0.2000	0.5235	0.1245
\dot{y}_i	25.4126	25.4398	25.7872	26.2861	27.8848	25.5818
Difference	2.26%	2.15%	0.82%	1.10%	7.25%	1.61%
$\ddot{\delta}_i$	0.0003	0.0035	0.0010	0.0009	0.0023	0.0006
$\dot{\delta}_i$	0.0001	0.0007	0.0002	0.0002	0.0005	0.0001
c	0.2007	0.2002	0.2010	0.2016	0.2036	0.2008
β	0.1499	0.1497	0.1501	0.1504	0.1515	0.1500
Difference	0.05%	0.23%	0.07%	0.28%	1.01%	0.00%
Simulated Damaged Case: DL: Y=15mm; Depth: d=0.06mm						
	$\xi=1, \theta=3$	$\xi=1, \theta=2$	$\xi=1, \theta=1$	$\xi=0, \theta=3$	$\xi=0, \theta=2$	$\xi=0, \theta=1$
y_1	15	15	10	15	15	15
y_2	20	20	15	20	20	20
$\bar{\delta}_1$	0.0455	0.8113	0.1284	0.1660	0.5354	0.0753
$\bar{\delta}_2$	0.0805	0.7892	0.1405	0.1791	0.5484	0.1045
$\dot{\delta}_i$	0.0461	0.8116	0.1404	0.1689	0.5341	0.0757
\dot{y}_i	15.0907	14.9471	14.9711	16.1089	14.4775	15.0645
Difference	0.60%	0.35%	0.19%	7.39%	3.48%	0.43%
$\ddot{\delta}_i$	0.0001	0.0023	0.0004	0.0005	0.0015	0.0002
$\dot{\delta}_i$	0.0000	0.0002	0.0000	0.0000	0.0001	0.0000
c	0.0729	0.0742	0.0741	0.0673	0.0773	0.0733
β	0.0701	0.0711	0.0710	0.0661	0.0733	0.0704
Difference	16.88%	18.42%	18.32%	10.10%	22.12%	17.38%

Table 7-7 (continued)

Simulated Damaged Case: DL: Y=33mm; Depth: d=0.34mm						
	$\xi=1, \theta=3$	$\xi=1, \theta=2$	$\xi=1, \theta=1$	$\xi=0, \theta=3$	$\xi=0, \theta=2$	$\xi=0, \theta=1$
y_1	25	30	30	30	30	30
y_2	30	35	35	35	35	35
$\bar{\delta}_1$	0.0704	0.7366	0.2870	0.2219	0.5209	0.1850
$\bar{\delta}_2$	0.1424	0.6688	0.4343	0.2662	0.4639	0.2393
$\dot{\delta}_t$	0.1276	0.7113	0.3673	0.2471	0.4890	0.2063
\dot{y}_t	28.9753	31.8617	32.7261	32.8460	32.7931	31.9646
Difference	12.20%	3.45%	0.83%	0.47%	0.63%	3.14%
$\ddot{\delta}_t$	0.0006	0.0029	0.0014	0.0009	0.0019	0.0008
$\dot{\delta}_t$	0.0003	0.0015	0.0008	0.0005	0.0010	0.0004
c	0.4030	0.5026	0.5370	0.5331	0.5230	0.5144
β	0.2529	0.2985	0.3136	0.3119	0.3075	0.3037
Difference	25.62%	12.22%	7.75%	8.26%	9.56%	10.68%
Simulated Damaged Case: DL: Y=46mm; Depth: d=0.53mm						
	$\xi=1, \theta=3$	$\xi=1, \theta=2$	$\xi=1, \theta=1$	$\xi=0, \theta=3$	$\xi=0, \theta=2$	$\xi=0, \theta=1$
y_1	45	45	45	45	45	45
y_2	50	50	50	50	50	50
$\bar{\delta}_1$	0.2578	0.1459	0.7745	0.3261	0.1516	0.4279
$\bar{\delta}_2$	0.3678	0.0052	0.7394	0.2914	0.0577	0.4794
$\dot{\delta}_t$	0.2636	0.0962	0.7834	0.3223	0.1202	0.4351
\dot{y}_t	45.2617	46.7677	43.7335	45.5494	46.6711	45.6971
Difference	1.60%	1.67%	4.93%	0.98%	1.46%	0.66%
$\ddot{\delta}_t$	0.0006	0.0002	0.0018	0.0008	0.0003	0.0011
$\dot{\delta}_t$	0.0006	0.0002	0.0019	0.0008	0.0003	0.0010
c	0.9851	0.9890	1.0081	0.9832	0.9789	0.9794
β	0.4944	0.4959	0.5030	0.4937	0.4921	0.4922
Difference	6.72%	6.44%	5.09%	6.85%	7.16%	7.12%

7.4 Single damage detection in plate-like structure with noisy simulated measurement

7.4.1 All through-the-length delamination

The problem of detecting all through-the-length damage introduced in section 7.3 will now be extended to examine the effect of noise on the accuracy of the calculation. A noise factor ε will be applied to the simulated measurement data, and interval arithmetic (Moore 1979) will be introduced to model the resulting uncertainty. For two ranges of positive real numbers X and Y :

$$X \in [X_{LL}, X_{UL}], Y \in [Y_{LL}, Y_{UL}] \quad \text{Eq. 7-6}$$

where X_{LL} and Y_{LL} are the lower limits of X and Y , and X_{UL} and Y_{UL} are the upper limits, the following equations can be shown to apply:

$$\begin{aligned} X + Y &\in [X_{LL} + Y_{LL}, X_{UL} + Y_{UL}], \\ X - Y &\in [X_{LL} - Y_{UL}, X_{UL} - Y_{LL}], \\ \frac{1}{Y} &\in \left[\frac{1}{Y_{UL}}, \frac{1}{Y_{LL}} \right], \\ \frac{X}{Y} &\in \left[\frac{X_{LL}}{Y_{UL}}, \frac{X_{UL}}{Y_{LL}} \right]. \end{aligned} \quad \text{Eq. 7-7}$$

These equations can be used to converge on the possible damage intervals in the presence of noise. If the simulated variables ω^{HP} and ω^{DP} are the natural frequencies of the undamaged and damaged plate respectively, their intervals are $[\omega_{imin}^{HP}, \omega_{imax}^{HP}]$ and $[\omega_{imin}^{DP}, \omega_{imax}^{DP}]$, where the subscripts *min* and *max* denote the lower and upper limits respectively and the subscript *i* denotes the modes can be used to describe the range of possible values. Here the limits depend on the noise factor: ω_{imin}^{HP} or $\omega_{imax}^{HP} = \omega^{HP} \pm \varepsilon$. Interval arithmetic operations can then be introduced into Eq. 7-7, and the related minimum and maximum changes in natural frequencies are obtained as:

$$\delta_{imin} = \frac{\omega_{imin}^{HP} - \omega_{imax}^{DP}}{\omega_{imin}^{HP}} \quad \text{Eq. 7-8}$$

$$\delta_{imax} = \frac{\omega_{imax}^{HP} - \omega_{imin}^{DP}}{\omega_{imax}^{HP}} \quad \text{Eq. 7-9}$$

where δ_{imin} and δ_{imax} are the lower and upper limits of the change in natural frequency. When the values of uncracked and cracked natural frequencies are close, the value of δ_{imin} can become negative in which case the lower limit should be set to zero. The normalised limits on the changes in natural frequencies for each mode $\overline{\delta_{imin}}$ and $\overline{\delta_{imax}}$ can then be evaluated based on Eq. 7-2 as:

$$\overline{\delta_{imin}} = \frac{\delta_{imin}}{\sqrt{\delta_{imin}^2 + \sum_{j \neq i} \delta_{jmax}^2}} \quad \text{Eq. 7-10}$$

$$\overline{\delta_{imax}} = \frac{\delta_{imax}}{\sqrt{\delta_{imax}^2 + \sum_{j \neq i} \delta_{jmin}^2}} \quad \text{Eq. 7-11}$$

leading to a converged interval $[\overline{\delta_{imin}}, \overline{\delta_{imax}}]$ of possible normalised changes in natural frequencies.

Table 7-8 will first be applied to the same measured delamination cases as examined in section 7.3.1, with the dimensions and properties of the plate shown in Figure 7-2. Three modes ($\xi=0.01, \theta=3-4$; $\xi=1, \theta=3$; $\xi=1, \theta=1$) are selected for normalisation, and two noise factors ε (0.05 and 0.01) are compared to determine the reasonable noise factors. The resulting changes in natural frequency are presented in Table 7-8. Four decimal places are considered for the obtained natural frequencies, with the same precision applied to the following operations.

In this study, $\varepsilon = \pm 0.01\text{Hz}$ will be chosen as the noise factor for a reasonable changed natural frequency region. The possible intervals for the simulated cases $[\overline{\delta_{imin}}, \overline{\delta_{imax}}]$, obtained using Eq. 7-10 and Eq. 7-11 and tabulated in Table 7-8, are plotted as two horizontal lines in Figure 7-5 against the reference δ data for the delaminated case, which was tabulated in Table 7-1. Case 1 ($\xi = 0.01, \theta = 3 - 4$), 2 ($\xi = 1, \theta = 1$) and 3 ($\xi = 1, \theta = 3$) represent different modes of simulate case, ξ and θ here are in terms of XI and EIGEN in Figure 7-5. Applying the linear interpolation of Eq. 7-12:

$$\begin{aligned} y_{imin} &= y_1 + \left[\frac{y_2 - y_1}{\overline{\delta_{i2}} - \overline{\delta_{i1}}} * (\overline{\delta_{imin}} - \overline{\delta_{i1}}) \right] \\ y_{imax} &= y_1 + \left[\frac{y_2 - y_1}{\overline{\delta_{i2}} - \overline{\delta_{i1}}} * (\overline{\delta_{imax}} - \overline{\delta_{i1}}) \right] \end{aligned} \quad \text{Eq. 7-12}$$

where y_{imin} and y_{imax} are the lower limit and upper limit of the expected damage location according to the related normalised change natural frequencies $[\overline{\delta_{imin}}, \overline{\delta_{imax}}]$,

enables the range of the delamination locations to be calculated for each mode, and the coinciding ranges of intersections in the plotted curves are then the possible delamination location intervals.

The delamination severity in terms of the delamination width β can be recovered using a similar procedure as Eq. 7-5. Eq. 7-13 is first applied to obtain the expected lower and upper normalised changes in natural frequencies δ_i^L and δ_i^U .

$$\begin{aligned} \delta_i^L &= \delta_1 + \left[\frac{\delta_2 - \delta_1}{y_2 - y_1} * (y^L - y_1) \right] \\ \delta_i^U &= \delta_1 + \left[\frac{\delta_2 - \delta_1}{y_2 - y_1} * (y^U - y_1) \right] \end{aligned} \quad \text{Eq. 7-13}$$

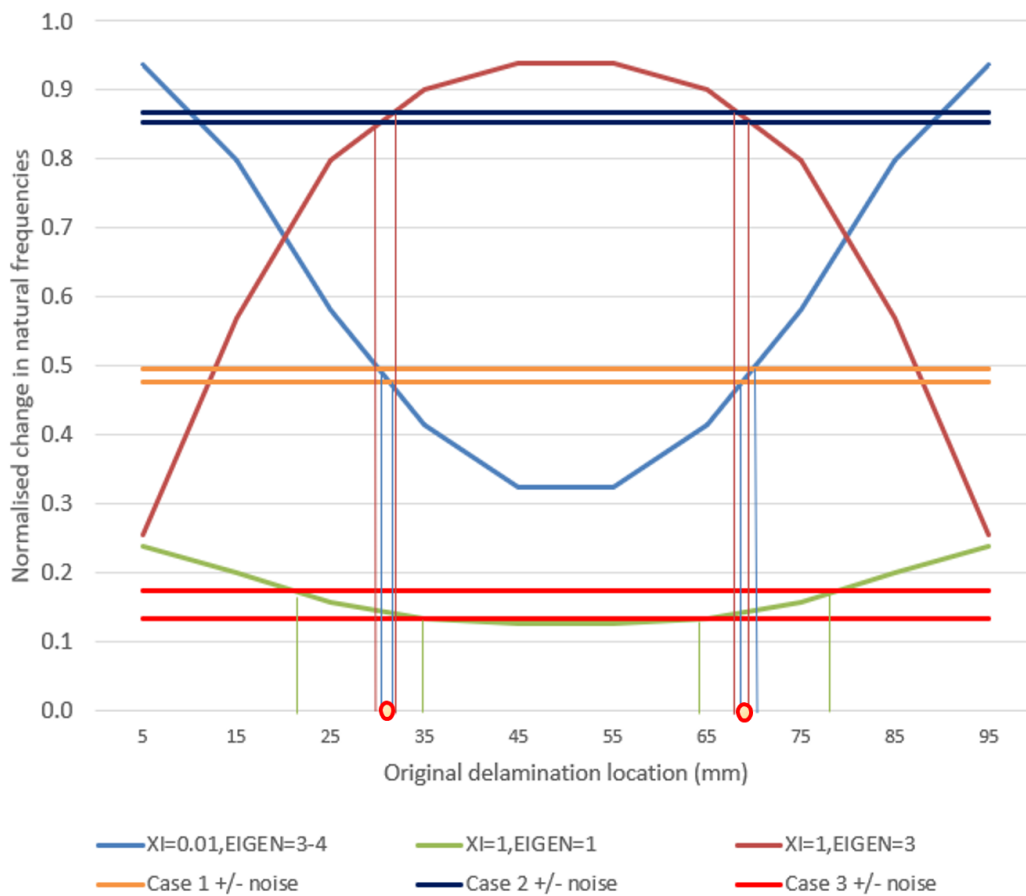


Figure 7-5 The normalised change natural frequencies of three chosen modes from the referred set for discrete points along the y-axis and simulated cases.

Table 7-8 Normalised changes in natural frequencies for simulated cases within noise effect.

Simulated Damaged Case: DL: Y=28mm, DS: $\beta=8\text{mm}$, $\varepsilon=0.05$						
	$\xi=0.01, \theta=3-4$		$\xi=1, \theta=3$		$\xi=1, \theta=1$	
	$-\varepsilon$	$+\varepsilon$	$-\varepsilon$	$+\varepsilon$	$-\varepsilon$	$+\varepsilon$
ω_i^{HP}	74.0117	74.1117	110.4751	110.5751	28.0917	28.1917
ω_i^{DP}	73.8273	73.9273	110.0443	110.1443	28.0726	28.1726
$\delta_{imin}/\delta_{imax}$	0.0011/0.0038		0.0030/0.0048		0.0000/0.0042	
$\overline{\delta_{imin}}/\overline{\delta_{imax}}$	0.1754/0.7883		0.4646/0.9730		0.0000/0.7969	
Simulated Damaged Case: DL: Y=28mm, DS: $\beta=8\text{mm}$, $\varepsilon=0.01$						
ω_i^{HP}	74.0517	74.0717	110.5151	110.5351	28.1317	28.1517
ω_i^{DP}	73.8673	73.8873	110.0843	110.1043	28.1126	28.1326
$\delta_{imin}/\delta_{imax}$	0.0022/0.0028		0.0037/0.0041		0.0000/0.0014	
$\overline{\delta_{imin}}/\overline{\delta_{imax}}$	0.4579/0.5959		0.7691/0.8784		0.0000/0.3058	
Simulated Damaged Case: DL: Y=28mm, DS: $\beta=16\text{mm}$, $\varepsilon=0.01$						
ω_i^{HP}	74.0517	74.0717	110.5151	110.5351	28.1317	28.1517
ω_i^{DP}	72.7665	72.7865	107.1267	107.1467	27.9784	27.9984
$\delta_{imin}/\delta_{imax}$	0.0171/0.0176		0.0305/0.0308		0.0047/0.0062	
$\overline{\delta_{imin}}/\overline{\delta_{imax}}$	0.4774/0.4960		0.8528/0.8669		0.1323/0.1735	
Simulated Damaged Case: DL: Y=34mm, DS: $\beta=6\text{mm}$, $\varepsilon=0.01$						
ω_i^{HP}	74.0517	74.0717	110.5151	110.5351	28.1317	28.1517
ω_i^{DP}	73.9782	73.9982	110.2978	110.3178	28.1232	28.1432
$\delta_{imin}/\delta_{imax}$	0.0007/0.0013		0.0018/0.0021		0.0000/0.0010	
$\overline{\delta_{imin}}/\overline{\delta_{imax}}$	0.2911/0.5773		0.7407/0.9478		0.0000/0.4659	
Simulated Damaged Case: DL: Y=18mm, DS: $\beta=10\text{mm}$, $\varepsilon=0.01$						
ω_i^{HP}	74.0517	74.0717	110.5151	110.5351	28.1317	28.1517
ω_i^{DP}	73.7214	73.7414	110.1159	110.1359	28.0997	28.1197
$\delta_{imin}/\delta_{imax}$	0.0042/0.0047		0.0034/0.0038		0.0004/0.0018	
$\overline{\delta_{imin}}/\overline{\delta_{imax}}$	0.7046/0.8072		0.5600/0.6692		0.0705/0.3231	
Simulated Damaged Case: DL: Y=14mm, DS: $\beta=12\text{mm}$, $\varepsilon=0.01$						
ω_i^{HP}	74.0517	74.0717	110.5151	110.5351	28.1317	28.1517
ω_i^{DP}	73.5151	73.5351	109.9907	110.0107	28.0786	28.0986
$\delta_{imin}/\delta_{imax}$	0.0070/0.0075		0.0046/0.0049		0.0012/0.0026	
$\overline{\delta_{imin}}/\overline{\delta_{imax}}$	0.7816/0.8471		0.4979/0.5714		0.1298/0.2973	

Table 7-9 The delamination location interval and severity of the simulated ATLD cases with noise effect.

Simulated Damaged Case		DL: Y=28mm; DS: $\beta=8\text{mm}$; $\varepsilon=0.01$			DL: Y=28mm; DS: $\beta=16\text{mm}$; $\varepsilon=0.01$		
		$\xi=0.01, \theta=3-4$	$\xi=1, \theta=3$	$\xi=1, \theta=1$	$\xi=0.01, \theta=3-4$	$\xi=1, \theta=3$	$\xi=1, \theta=1$
min	y_1	25	15		25	25	35
	y_2	35	25		35	35	45
	$\overline{\delta_{l1}}$	0.5818	0.5690		0.5818	0.7983	0.1333
	$\overline{\delta_{l2}}$	0.4138	0.7983		0.4138	0.9006	0.1249
	$\overline{\delta_{min}}$	0.4579	0.7691	0	0.4774	0.8528	0.1323
	y_{imin}	32.3763	23.7254	0	31.2128	30.3290	36.2387
max	y_1	15	25		25	25	15
	y_2	25	35		35	35	25
	$\overline{\delta_{l1}}$	0.7979	0.7983		0.5818	0.7983	0.1991
	$\overline{\delta_{l2}}$	0.5818	0.9006		0.4138	0.9006	0.1556
	$\overline{\delta_{max}}$	0.5959	0.8784	0.3058	0.4960	0.8669	0.1735
	y_{imax}	24.3454	32.8309	100	30.1058	31.7093	20.8791
	y^L	24.3454	23.7254	0.0000	30.1058	30.3290	20.8791
	y^U	32.3763	32.8309	100	31.2128	31.7093	36.2387
Expected Delamination Region		[24.3454, 32.3763]			[30.1058, 31.2128]		
Lower	δ_i^L	0.0048	0.0063		0.0043	0.0115	0.0012
	δ_i^L/δ_i^U	0.0028	0.0037		0.0171	0.0305	0.0047
	d	0.5805	0.5912		3.9508	2.6603	3.9540
	EDS	8.3419	8.3930		15.8087	13.8561	15.8130
Upper	δ_i^U	0.0046	0.0077		0.0047	0.0078	0.0013
	δ_i^L/δ_i^U	0.0022	0.0041		0.0171	0.0305	0.0047
	d	0.4870	0.5299		3.6641	3.9264	3.5373
	EDS	7.8674	8.0921		15.4167	15.7761	15.2366
Expected Severity Region		[8.0921, 8.3419]			[15.4167, 15.8087]		

Table 7-9 (continued)

Simulated Damaged Case		DL: Y=18mm; DS: $\beta=10\text{mm}$; $\varepsilon=0.01$			DL: Y=14mm; DS: $\beta=12\text{mm}$; $\varepsilon=0.01$		
		$\xi=0.01$, $\theta=3-4$	$\xi=1, \theta=3$	$\xi=1, \theta=1$	$\xi=0.01$, $\theta=3-4$	$\xi=1, \theta=3$	$\xi=1, \theta=1$
min	y_1	15	5		15	5	35
	y_2	25	15		25	15	45
	$\overline{\delta_{t1}}$	0.7979	0.2535		0.7979	0.2535	0.1333
	$\overline{\delta_{t2}}$	0.5818	0.5690		0.5818	0.5690	0.1249
	$\overline{\delta_{min}}$	0.7046	0.5600	0.0705	0.7816	0.4979	0.1298
	y_{imin}	19.3168	14.7150	0.0000	15.7552	12.7488	39.2189
max	y_1	5	15		5	15	
	y_2	15	25		15	25	
	$\overline{\delta_{t1}}$	0.9378	0.5690		0.9378	0.5690	
	$\overline{\delta_{t2}}$	0.7979	0.7983		0.7979	0.7983	
	$\overline{\delta_{max}}$	0.8072	0.6692	0.3231	0.8471	0.5714	0.2973
	y_{imax}	14.3364	19.3702	10.0000	11.4809	15.1069	0.0000
	y^L	14.3364	14.7150	0.0000	11.4809	12.7488	0.0000
	y^U	19.3168	19.3702	10.0000	15.7552	15.1069	39.2189
Expected Delamination Region		[14.7150, 19.3168]			[12.7488, 15.1069]		
Lower	δ_i^L	0.0044	0.0031		0.0043	0.0027	
	δ_i^L/δ_i^U	0.0042	0.0034		0.0070	0.0046	0.0012
	d	0.9450	1.1030		1.6057	1.6906	
	EDS	9.8132	10.3322		11.7101	11.9129	
Upper	δ_i^U	0.0046	0.0046		0.0045	0.0032	
	δ_i^L/δ_i^U	0.0042	0.0034		0.0075	0.0049	0.0026
	d	0.9133	0.7412		1.6884	1.5359	
	EDS	9.7021	9.0501		11.9077	11.5377	
Expected Severity Region		[9.7021, 9.8132]			[11.7101, 11.9077]		

Table 7-9 (continued)

Simulated Damaged Case		DL: Y=34mm; DS: β=6mm; ε=0.01		
		ξ=0.01, θ=3-4	ξ=1,θ=3	ξ=1,θ=1
min	y ₁	45	15	
	y ₂	55	25	
	$\overline{\delta_{i1}}$	0.3227	0.5690	
	$\overline{\delta_{i2}}$	0.3227	0.7983	
	$\overline{\delta_{min}}$	0.2911	0.7407	0.0000
	y _{imin}	0.0000	22.4881	0.0000
max	y ₁	25	45	
	y ₂	35	55	
	$\overline{\delta_{i1}}$	0.5818	0.9382	
	$\overline{\delta_{i2}}$	0.4138	0.9382	
	$\overline{\delta_{max}}$	0.5773	0.9478	0.4659
	y _{imax}	25.2647	0.0000	10.0000
	y ^L	0.0000	0.0000	0.0000
	y ^U	25.2647	22.4881	10.0000
Expected Delamination Region		[25.2647, 74.7353]		

where y^L and y^U are the lowest and highest estimations for all the different modes respectively. The severity range is then calculated based on δ_i^L and δ_i^U using Eq. 7-14:

$$\beta_i^L = \beta * \left(\frac{\delta_i^L}{\dot{\delta}_i^L}\right)^\Delta$$

$$\beta_i^U = \beta * \left(\frac{\delta_i^U}{\dot{\delta}_i^U}\right)^\Delta$$

Eq. 7-14

where β is the fixed predefined width used to calculate the discrete reference points (10mm); δ_i^L and δ_i^U are the lowest and highest value of the measured changes in natural frequencies (from Table 7-8) and the severity index Δ ($\frac{1}{3}$ for the ATLD case) depends on the dimensions and properties of the damaged plate (an example is shown in section 6.2). In Table 7-9, the process is applied to five simulated cases with noise effect factor 0.01 and ‘EDS’ is the expected severity factor of delamination width β .

From Table 7-9, when the simulated delamination is located at $y=28\text{mm}$ with a delamination width $\beta=8\text{mm}$ and a noise factor 0.01, the expected damage location is [24.3454, 32.3763], while the estimated severity region is [8.0921, 8.3419]. The expected location interval covers the actual damage location while the severity exists a difference at 1.15%. For the same location with the more severe case $\beta=16\text{mm}$, the expected damage location is [30.1058, 31.2128], while the estimated severity region is [15.4167, 15.7761]. This gives a predicted damage location interval close to the actual simulated case with a maximum difference of 7.5% while the difference for severity is 1.4%. For other simulated cases, a similar difference exists except for the delamination located at $y=34\text{mm}$ with a delamination width of 6mm, the expected location interval covers half the width of the plate. This may be related to the number of nodes chosen in the reference data. In this study, only ten discrete points are chosen along the y -axis for the reference curve. Because the curve could resemble a high order polynomial, if the number of sample points is not enough, the data plot could lose some values, and hence a discrepancy will occur. More discrete points need to be applied to the reference plot to generate a more accurate referred curve.

7.4.2 All through-the-length crack

The effect of noise on the detection of an all through the length crack will be considered next. In comparison with a delamination, the reduction of natural frequencies due to a single crack of increasing severity in a plate structure is much smaller as shown in Table 7-4. Hence the value of the introduced noise factor ε will need to be significantly smaller to make detection feasible. In this study a value $\varepsilon = 0.001$ is used. Furthermore, in comparison with delamination cases, more discrete points need to be chosen as reference points to give a more accurate estimation of the crack location and severity.

In this example, a plate with dimensions and properties the same as in Figure 7-4 will be used. Four decimal places will be considered in the damage detection for the ATLC case, with the first six modes selected to converge on the intervals of the possible crack location and depth. The solution of the inverse problem of plate structure is analogous to that of Labib et al. (2015), where three modes were chosen for damage region convergence. According to previous studies and the results obtained from ATLD, extra modes could provide more accurate results. Four decimal places precision is enough to show the change in natural frequencies. For ATLC, the same normalisation procedure and interval arithmetic processing will be applied as for the through-the-length delamination in Table 7-10. Table 7-10 shows the minimum and maximum normalised changes in natural frequencies ($\overline{\delta_{imin}}/\overline{\delta_{imax}}$) of four simulated crack cases with a noise factor $\varepsilon = 0.001$.

Table 7-10 Maximum/minimum normalised changes in natural frequencies of the first six modes with noise factor $\varepsilon = 0.001$.

Simulated Damaged Case: DL: Y=26mm; d=0.15mm; $\varepsilon=0.001$												
	$\xi=1, \theta=3$		$\xi=1, \theta=2$		$\xi=1, \theta=1$		$\xi=0, \theta=3$		$\xi=0, \theta=2$		$\xi=0, \theta=1$	
	$-\varepsilon$	$+\varepsilon$	$-\varepsilon$	$+\varepsilon$	$-\varepsilon$	$+\varepsilon$	$-\varepsilon$	$+\varepsilon$	$-\varepsilon$	$+\varepsilon$	$-\varepsilon$	$+\varepsilon$
ω_i^{HP}	110.3589	110.3609	63.8842	63.8862	28.1426	28.1446	77.5447	77.5467	73.2844	73.2864	44.3543	44.3563
ω_i^{DP}	110.3513	110.3533	63.8392	63.8412	28.1370	28.1390	77.5308	77.5328	73.2499	73.2519	44.3493	44.3513
δ_{imin}	0.0001		0.0007		0.0001		0.0002		0.0004		0.0001	
δ_{imax}	0.0001		0.0007		0.0003		0.0002		0.0005		0.0002	
$\overline{\delta_{imin}}$	0.0523		0.7302		0.1396		0.1606		0.4708		0.0698	
$\overline{\delta_{imax}}$	0.1035		0.8300		0.3141		0.2429		0.5752		0.1853	
Simulated Damaged Case: DL: Y=15mm; d=0.06mm; $\varepsilon=0.001$												
	$\xi=1, \theta=3$		$\xi=1, \theta=2$		$\xi=1, \theta=1$		$\xi=0, \theta=3$		$\xi=0, \theta=2$		$\xi=0, \theta=1$	
	$-\varepsilon$	$+\varepsilon$	$-\varepsilon$	$+\varepsilon$	$-\varepsilon$	$+\varepsilon$	$-\varepsilon$	$+\varepsilon$	$-\varepsilon$	$+\varepsilon$	$-\varepsilon$	$+\varepsilon$
ω_i^{HP}	110.3589	110.3609	63.8842	63.8862	28.1426	28.1446	77.5447	77.5467	73.2844	73.2864	44.3543	44.3563
ω_i^{DP}	110.3578	110.3598	63.8732	63.8752	28.1418	28.1438	77.5419	77.5439	73.2760	73.2780	44.3535	44.3555
δ_{imin}	0.0001		0.0007		0.0001		0.0002		0.0004		0.0001	
δ_{imax}	0.0001		0.0007		0.0003		0.0002		0.0005		0.0002	
$\overline{\delta_{imin}}$	0.0523		0.7302		0.1396		0.1606		0.4708		0.0698	
$\overline{\delta_{imax}}$	0.1035		0.8300		0.3141		0.2429		0.5752		0.1853	

Table 7-10 (continued)

Simulated Damaged Case: DL: Y=34mm; d=0.34mm; $\varepsilon=0.001$												
	$\xi=1, \theta=3$		$\xi=1, \theta=2$		$\xi=1, \theta=1$		$\xi=0, \theta=3$		$\xi=0, \theta=2$		$\xi=0, \theta=1$	
	- ε	+ ε	- ε	+ ε	- ε	+ ε	- ε	+ ε	- ε	+ ε	- ε	+ ε
ω_i^{HP}	110.3589	110.3609	63.8842	63.8862	28.1426	28.1446	77.5447	77.5467	73.2844	73.2864	44.3543	44.3563
ω_i^{DP}	110.3302	110.3322	63.7917	63.7937	28.1216	28.1236	77.5057	77.5077	73.2114	73.2134	44.3356	44.3376
δ_{imin}	0.0002		0.0014		0.0007		0.0005		0.0010		0.0004	
δ_{imax}	0.0003		0.0015		0.0008		0.0005		0.0010		0.0005	
$\overline{\delta_{imin}}$	0.1145		0.6835		0.3276		0.2269		0.4632		0.1787	
$\overline{\delta_{imax}}$	0.1417		0.7387		0.4072		0.2684		0.5154		0.2354	
Simulated Damaged Case: DL: Y=46mm; d=0.53mm; $\varepsilon=0.001$												
	$\xi=1, \theta=3$		$\xi=1, \theta=2$		$\xi=1, \theta=1$		$\xi=0, \theta=3$		$\xi=0, \theta=2$		$\xi=0, \theta=1$	
	- ε	+ ε	- ε	+ ε	- ε	+ ε	- ε	+ ε	- ε	+ ε	- ε	+ ε
ω_i^{HP}	110.3589	110.3609	63.8842	63.8862	28.1426	28.1446	77.5447	77.5467	73.2844	73.2864	44.3543	44.3563
ω_i^{DP}	110.2901	110.2921	63.8697	63.8717	28.0905	28.0925	77.4857	77.4877	73.2636	73.2656	44.3086	44.3106
δ_{imin}	0.0006		0.0002		0.0018		0.0007		0.0003		0.0010	
δ_{imax}	0.0006		0.0003		0.0019		0.0008		0.0003		0.0011	
$\overline{\delta_{imin}}$	0.2469		0.0799		0.7580		0.3013		0.1048		0.4063	
$\overline{\delta_{imax}}$	0.2813		0.1136		0.8071		0.3444		0.1368		0.4648	

Table 7-11 Crack location region and severity for ATLC at $y=26\text{mm}$, $d=0.15\text{mm}$ with noise factor $\varepsilon = 0.001$.

Simulated Damaged Case: DL: $Y=26\text{mm}$; $d=0.15\text{mm}$; $\varepsilon = 0.001$							
		$\xi = 1,$ $\theta = 3$	$\xi = 1,$ $\theta = 2$	$\xi = 1,$ $\theta = 1$	$\xi = 0,$ $\theta = 3$	$\xi = 0,$ $\theta = 2$	$\xi = 0,$ $\theta = 1$
min	y_1	15	30	10	5	30	5
	y_2	20	35	15	10	35	10
	$\overline{\delta_{i1}}$	0.0455	0.7366	0.1284	0.1604	0.5209	0.0620
	$\overline{\delta_{i2}}$	0.0804	0.6688	0.1405	0.1716	0.4639	0.0773
	$\overline{\delta_{min}}$	0.0523	0.7302	0.1396	0.1606	0.4708	0.0698
	y_{imin}	15.9800	30.4695	14.6219	5.0945	34.3923	7.5651
max	y_1	25	10	30	30	15	30
	y_2	30	15	35	35	20	35
	$\overline{\delta_{i1}}$	0.0704	0.8038	0.2870	0.2219	0.5354	0.1850
	$\overline{\delta_{i2}}$	0.1424	0.8113	0.4343	0.2662	0.5484	0.2393
	$\overline{\delta_{max}}$	0.1035	0.8300	0.3141	0.2429	0.5752	0.1853
	y_{imax}	27.2970	27.2909	30.9204	32.3676	30.3703	30.0230
	y^L	15.9800	27.2909	14.6219	5.0945	30.3703	7.5651
	y^U	27.2970	30.4695	30.9204	32.3676	34.3923	30.0230
Expected crack region: [30.3703, 27.2970]							
Lower	$\ddot{\delta}_i^L$	0.0005	0.0034	0.0011	0.0009	0.0023	0.0007
	$\dot{\delta}_i^L / \dot{\delta}_i^U$	0.0001	0.0007	0.0003	0.0002	0.0005	0.0002
	c	0.1902	0.2170	0.2499	0.2254	0.2142	0.2402
	EDS	0.1440	0.1589	0.1767	0.1636	0.1574	0.1715
Upper	$\ddot{\delta}_i^U$	0.0006	0.0031	0.0013	0.0010	0.0022	0.0008
	$\dot{\delta}_i^L / \dot{\delta}_i^U$	0.0001	0.0007	0.0003	0.0002	0.0005	0.0002
	c	0.1420	0.2343	0.2152	0.2135	0.2244	0.1945
	EDS	0.1156	0.1684	0.1580	0.1570	0.1630	0.1464
	d^L	0.1156	0.1589	0.1580	0.1570	0.1574	0.1464
	d^U	0.1440	0.1684	0.1767	0.1636	0.1630	0.1715
Expected depth region: [0.1589, 0.1440]							

After the regions of normalised changes in natural frequencies have been calculated, the linear interpolation stages laid out in Eq. 7-12, Eq. 7-13 and Eq. 7-14 can be performed to explore the estimated damage region according to the set of reference crack points. The values of the normalised changes in the natural frequencies of the simulated cracked plate should be located between two adjacent reference points. Because ATLC causes only a small reduction in natural frequencies compared to delamination, the regions of normalised natural frequencies may be located at different intervals which will lead to inconsistent values. Choosing the case where $y=26\text{mm}$ and the depth of crack is 0.15mm as an example, Table 7-11 shows the expected crack location region and severity of the simulated ATLC cases with a noise effect $\varepsilon = 0.001$. Compared with the reference set of the normalised changes in natural frequency, the normalised change in natural frequencies from the measured case of different modes may not be located at the same region caused by the introduced noise factor and limited number of selected reference points.

From Table 7-11, 'EDS' is the expected severity factor of crack depth d . The expected region of crack location and severity is seen to be close to the actual value, but the value of the lower limit is higher than the upper limit. The contradiction is caused firstly by the fact that the value of the natural frequency is quite sensitive, so that a crack may reduce the value of natural frequency by only a small magnitude. Considering the efficiency of computation, limited reference points are recorded and then the normalised measured change in natural frequency may be located in several adjacent intervals of the reference set. If only one interval is chosen in the damage detection procedure, this will result in an unreasonable region for the final estimation. Secondly, too many modes have been chosen to obtain the converged region. Generally, the more modes selected, the more accurate a value can be achieved. However, when more modes are chosen to solve the inverse problem, it may lead to contradictory results as shown in Table 7-11. The following operations solve this contradiction problem in two ways.

Table 7-12 shows the common location regions based on the intervals of the normalised changes in natural frequencies from the first six modes. The potential cracked region should be located at a coincident interval within the noise effect. Here '>LB' is a check to see whether the value is between the upper and lower bounds of the normalised change in natural frequencies from the reference set. The reference normalised frequencies are compared with the lower limit of the obtained interval of the simulated case, and '<UB' is another check to see whether the value is between the upper and lower bounds, again the normalised reference frequencies are compared with $\overline{\delta_{max}}$. 'RL' represents the location of the reference set points.

According to Table 7-12, the potential crack location is in the region [15, 30]. Linear interpolation is applied in [15, 20] and [25, 30] separately to determine the lower limit and upper limit of a possible crack location. Table 7-13 show the expected location region within those chosen intervals.

According to Table 7-13, a lower limit of 15.98 is thus obtained from interval [15, 20], while the upper limit is 27.297 from interval [25, 30]. A final crack location region is determined as [15.9800, 27.2970]. After the first optimisation, the region of the crack location still needs to narrow. Hence, a second optimisation is used with a different combination of modes. In Table 7-14, modes $\xi=1, \theta=3$; $\xi=1, \theta=2$; $\xi=0, \theta=3$ are chosen to converge the region of crack location, ECR is the expected crack region.

Table 7-12 The selection of crack location region.

Simulated Damaged Case: DL: Y=26mm; d=0.15mm; $\epsilon=0.001$												
$\xi=1, \theta=3$		$\xi=1, \theta=2$		$\xi=1, \theta=1$		$\xi=0, \theta=3$		$\xi=0, \theta=2$		$\xi=0, \theta=1$		RL
>LB	<UB	>LB	<UB	>LB	<UB	>LB	<UB	>LB	<UB	>LB	<UB	
N				N		N				N		5
				N								10
N												15
												20
												25
	N											30
	N	N			N		N	N			N	35
	N	N			N		N	N			N	40
	N	N			N		N	N			N	45
	N	N			N		N	N			N	50

Table 7-13 Crack location region and severity for simulated ATLC at $y=26\text{mm}$, $d=0.15\text{mm}$, noise factor $\varepsilon = 0.001$, chosen interval of the reference set is $[15, 20]$ and $[25, 30]$.

Simulated Damaged Case: DL: Y=26mm; d=0.15mm; $\varepsilon = 0.001$							
		$\xi = 1,$ $\theta = 3$	$\xi = 1,$ $\theta = 2$	$\xi = 1,$ $\theta = 1$	$\xi = 0,$ $\theta = 3$	$\xi = 0,$ $\theta = 2$	$\xi = 0,$ $\theta = 1$
min	y_1	15	15	15	15	15	15
	y_2	20	20	20	20	20	20
	$\overline{\delta_{t1}}$	0.0455	0.8113	0.1405	0.1660	0.5354	0.0753
	$\overline{\delta_{t2}}$	0.0804	0.7892	0.1641	0.1791	0.5484	0.1045
	$\overline{\delta_{min}}$	0.0523	0.7302	0.1396	0.1606	0.4708	0.0698
	y_{imin}	15.9800	33.3487	14.8062	12.9503	-9.9546	14.0573
max	y_1	15	15	15	15	15	15
	y_2	20	20	20	20	20	20
	$\overline{\delta_{t1}}$	0.0455	0.8113	0.1405	0.1660	0.5354	0.0753
	$\overline{\delta_{t2}}$	0.0804	0.7892	0.1641	0.1791	0.5484	0.1045
	$\overline{\delta_{max}}$	0.1035	0.8300	0.3141	0.2429	0.5752	0.1853
	y_{imax}	23.2925	10.7820	51.8251	44.3532	30.3703	33.8547
	y^L	15.9800	10.7820	14.8062	12.9503	-9.9546	14.0573
	y^U	23.2925	33.3487	51.8251	44.3532	30.3703	33.8547
Simulated Damaged Case: DL: Y=26mm; d=0.15mm; $\varepsilon = 0.001$							
		$\xi = 1,$ $\theta = 3$	$\xi = 1,$ $\theta = 2$	$\xi = 1,$ $\theta = 1$	$\xi = 0,$ $\theta = 3$	$\xi = 0,$ $\theta = 2$	$\xi = 0,$ $\theta = 1$
min	y_1	25	25	25	25	25	25
	y_2	30	30	30	30	30	30
	$\overline{\delta_{t1}}$	0.0704	0.7882	0.2130	0.1924	0.5270	0.1166
	$\overline{\delta_{t2}}$	0.1424	0.7366	0.2870	0.2219	0.5209	0.1850
	$\overline{\delta_{min}}$	0.0523	0.7302	0.1396	0.1606	0.4708	0.0698
	y_{imin}	23.7425	30.6170	20.0358	19.6072	70.7330	21.5876
max	y_1	25	25	25	25	25	25
	y_2	30	30	30	30	30	30
	$\overline{\delta_{t1}}$	0.0704	0.7882	0.2130	0.1924	0.5270	0.1166
	$\overline{\delta_{t2}}$	0.1424	0.7366	0.2870	0.2219	0.5209	0.1850
	$\overline{\delta_{max}}$	0.1035	0.8300	0.3141	0.2429	0.5752	0.1853
	y_{imax}	27.2970	20.9536	31.8325	33.5598	-14.1972	30.0183
	y^L	23.7425	20.9536	20.0358	19.6072	-14.1972	21.5876
	y^U	27.2970	30.6170	31.8325	33.5598	70.7330	30.0183

Table 7-14 Converged natural frequencies with a selected combination of different modes.

Simulated Damaged Case: DL: Y=26mm; d=0.15mm; $\varepsilon = 0.001$							
		$\xi = 1, \theta = 3$	$\xi = 1, \theta = 2$	$\xi = 0, \theta = 3$	$\xi = 1, \theta = 3$	$\xi = 1, \theta = 2$	$\xi = 0, \theta = 3$
min	y_1	5	5	5	10	10	10
	y_2	10	10	10	15	15	15
	$\overline{\delta_{l1}}$	0.0449	0.9803	0.1922	0.0723	0.9754	0.2082
	$\overline{\delta_{l2}}$	0.0723	0.9754	0.2082	0.0548	0.9782	0.2002
	$\overline{\delta_{min}}$	0.0660	0.9492	0.2036	0.0660	0.9492	0.2036
	y_{imin}	8.8526	36.5514	8.5509	11.7970	-36.3139	12.8817
max	y_1	5	5	5	10	10	10
	y_2	10	10	10	15	15	15
	$\overline{\delta_{l1}}$	0.0449	0.9803	0.1922	0.0723	0.9754	0.2082
	$\overline{\delta_{l2}}$	0.0723	0.9754	0.2082	0.0548	0.9782	0.2002
	$\overline{\delta_{max}}$	0.1246	0.9766	0.2913	0.1246	0.9766	0.2913
	y_{imax}	19.5543	8.8148	35.8582	-4.9640	12.0674	-41.4200
	y^L	8.8526	8.8148	8.5509	-4.9640	-36.3139	-41.4200
	y^U	19.5543	36.5514	35.8582	11.7970	12.0674	12.8817
ECR		[8.8526, 19.5543]			[-4.9640, 11.7970]		
min	y_1	15	15	15	25	25	25
	y_2	20	20	20	30	30	30
	$\overline{\delta_{l1}}$	0.0548	0.9782	0.2002	0.0865	0.9678	0.2363
	$\overline{\delta_{l2}}$	0.0989	0.9704	0.2202	0.1820	0.9415	0.2836
	$\overline{\delta_{min}}$	0.0660	0.9492	0.2036	0.0660	0.9492	0.2036
	y_{imin}	16.2699	33.5703	15.8525	23.9296	28.5324	21.5470
max	y_1	15	15	15	25	25	25
	y_2	20	20	20	30	30	30
	$\overline{\delta_{l1}}$	0.0548	0.9782	0.2002	0.0865	0.9678	0.2363
	$\overline{\delta_{l2}}$	0.0989	0.9704	0.2202	0.1820	0.9415	0.2836
	$\overline{\delta_{max}}$	0.1246	0.9766	0.2913	0.1246	0.9766	0.2913
	y_{imax}	22.9149	16.0613	37.7045	26.9971	23.3396	30.8063
	y^L	16.2699	16.0613	15.8525	23.9296	23.3396	21.5470
	y^U	22.9149	33.5703	37.7045	26.9971	28.5324	30.8063
ECR		[16.2699, 22.9149]			[23.9296, 26.9971]		

7.5 Discussion

The crack detection method presented in Chapter 7 makes predictions for damage locations based on natural frequency simulations. The non-destructive damage detection procedure proposed is based on solving an inverse problem using changes in natural frequencies corresponding to a number of modes to determine the location and severity of the damage from which these changes result. Damage is detected based on a set of reference data for known damage at specific locations and a linear interpolation method and severity recovery procedure. The expected damage location may change slightly depending on the severity ratio (the width of delamination or the crack depth to thickness ratio) used to calculate the natural frequencies of the reference set along with the discretisation points.

The method shows a good match with actual values for noise-free simulations where four decimal places of accuracy are considered. For the detection of all through-the-length delaminations and cracks, vibration parameters (frequencies and modes) are obtained using VICONOPT. This demonstrates the feasibility of the method which has the potential to be extended to partial through-the-length damage, a two-dimensional problem which will be mentioned briefly in Chapter 8. For noise-free simulation, the maximum difference for ATLD is less than 2% for both delamination location prediction and severity. A good match is also found for ATLC in most cases, with a maximum difference of less than 5%. By using VICONOPT the method saves significantly the computational cost. However, for symmetric structures, it cannot distinguish between symmetric locations, and two potential locations will therefore be estimated.

To examine the effect of noisy data on the successful location of damage, different noise factors are considered, chosen based on the severity of the damage, and interval arithmetic methodology is applied (Moore 1979).

For delaminations, a noise factor of $\varepsilon=0.01$ is introduced, and the converged interval $[\overline{\delta_{imin}}, \overline{\delta_{imax}}]$ is then obtained through a normalisation procedure to eliminate the severity factors. With increasing levels of noise, a wider range of possible damage locations is predicted, eventually reaching a point at which the damage location cannot be predicted to a specific range. To improve the prediction, additional modes can be combined with previously used modes to narrow down the crack region. Moreover, more discretisation points can be chosen to provide a more accurate damage location region. Besides, a high quality laboratory environment could reduce the noise effect and improve the accuracy of measurement.

For an all through-the-length crack, the changes in natural frequencies are much smaller than for delaminations, and so a much smaller level of noise can be tolerated. In this chapter a noise factor $\varepsilon=0.001$ is chosen for the ATLC case. Compared to the expected damage location region for ATLD, the prediction for ATLC provides a much wider range of locations. Optimisation processes then need to be applied to narrow down this range to give a more accurate region. In the first stage this consists of comparing the normalised change in natural frequencies interval $[\overline{\delta_{imin}}, \overline{\delta_{imax}}]$ with the reference set (Table 7-12) to generate a new crack location range. Due to the modelling assumptions (crack simulation, plate modelling, and stiffness matrix), some modes may not provide accurate simulated data, especially when the damage is in the middle of the plate. A selected mode set is then used to solve the inverse problem (Table 7-14). A 2% enhancement of the accuracy is obtained by the second optimisation. For severity recovery, the effect caused by the severity has been explained in section 6.2.3, and Eq. 6-1 shows the relationship between severity and location. Hence, the severity index factor calculation Eq. 7-5 is varied based on the properties of the plate and type of damage which need to be firstly determined according to the change in natural frequencies before the normalisation procedure. For ATLD, the index factor of severity is 0.3333 for a square composite simply supported plate (16 plies); for ATLC, the index factor is 0.75 for a square isotropic plate.

All the damage detection analyses ignore the influence of the loss of axial stiffness through the damaged area, and also neglect the damping factors of the adjacent parts in the damaged region.

7.6 Conclusion

This study uses natural frequency measurements to estimate single damage locations in composite/isotropic plates based on the methods proposed by Labib (2015) for beams. This forms the first stage in preparation for the solution of two-dimensional damage detection problems.

VICONOPT models are used to obtain changes in selected natural frequencies for damage located at discrete points along the y -axis of a plate member to provide reference data with which measured data from damaged panels can be compared for location. Changes in frequency are normalised to enable location and severity to be inferred individually. Noise-free simulations converge to point damage predictions approaching actual locations, and a severity recovery process is demonstrated for through-the-length damage.

With the introduction of measurement errors, the prediction of damage location is in terms of intervals instead of single points. Using interval arithmetic, additional natural frequency modes and different combinations of modes are able to eliminate some false ranges and narrow down the predictions when the measurement noise is greater than the difference between intact and damaged cases. Increasing the number of discrete reference points would also provide a more accurate potential damage region for the linear interpolation. Furthermore, a linear interpolation approach is used in the inverse problem of this study, but quadratic or other polynomial curve fitting could be applied to increase the accuracy of prediction.

The method is applicable and efficient for one-dimensional problems when the noise factor is less than the variation of at least one of the chosen natural frequencies. However, the procedure only provides a validated methodology for one-dimensional structures. A more complex normalisation procedure (standard deviation) will need to be applied for a two-variable (x and y) controlled problem, which will be briefly introduced in Chapter 8 as future work.

Chapter 8--- Conclusions and Further Work

8.1 Conclusions

In this thesis a damage detection process has been proposed based on two stages: solution of the forward problem (modelling the effects of damage on a structure's vibration characteristics) followed by solution of the inverse problem (using changes in vibration characteristics to detect and locate damage and assess its severity).

Referred back to thesis aim and objectives in section 1.3. Related literature about the damage modelling and inverse problem have been reviewed in Chapter 2 about beam structure and plate structure, respectively. A basic study about the exact strip method are shown in Chapter 3. Consequently, several data analysis methods are presented in Chapter 4, which could improve the computational behaviour and efficiency.

Chapter 5 presented a novel method for the simulation of cracks with arbitrary location, depth, length and orientation in plate-type structures. An advanced cracked plate model was developed based on the equivalent dynamic stiffness matrix of an FE model programmed in MATLAB with additional degrees of freedom added to represent the crack. The method allowed the crack to pass through any part of an element by simulating it as a rotational spring resolved about the x and y axes with shape functions before assigning these rotational spring stiffness to the corresponding nodes of the element to generate the global stiffness matrix of the cracked plate structure. A hybrid model (based on that introduced in Chapter 3) was then assembled by coupling an exact strip model for the undamaged part with this FE model for the damaged part using Lagrangian Multipliers to equate the deflections at the boundary. The Wittrick-Williams algorithm (Wittrick and Williams 1971) was applied to obtain the natural frequencies to the required accuracy whilst avoiding missing any values. For the simply supported square plate (SSSS) used in this study, only the first six natural frequencies were needed to solve the inverse problem. Hence, in the first stage a modified Wittrick-Williams algorithm could be utilised (described in Chapter 4) without the need to consider the effect of fixed-end natural frequencies. A bandwidth method was used to achieve the required Gaussian elimination, significantly saving on computational cost whilst maintaining an acceptable calculation accuracy. Furthermore, by using the newly proposed crack simulation method re-meshing was avoided by introducing additional degrees of freedom.

The case of a simply supported isotropic square plate has been used to validate the proposed model against previous studies and corresponding ABAQUS models in Chapter 6. Different types of cracks (all or part through the length, all or part through the depth, parallel to the plate sides or with an arbitrary orientation) were modelled and their effects on the vibration response of the plate were compared. Due to the limitations created by utilising a classical plate theory and using rotational spring stiffness for crack simulation, changes in natural frequencies were selected as the variable to be compared. For a single crack parallel to one side and starting in the middle of the plate, the maximum difference between the resulting predictions of changes in natural frequencies for each mode and those found in the literature was less than 3%. This showed a good match for the hybrid model even when the crack was severe (all through-the-depth). Due to the symmetry of the square plate structure, lines of zero curvature exist for several modes, for example at the centre of the plate. When the crack runs along one of these lines, it has no effect on the local stiffness of the plate and the change in natural frequencies therefore becomes zero. When the crack runs elsewhere in the plate, it will break the symmetry and checks on the mode shapes are then needed for further identification of the natural frequencies. Mode shapes are calculated and plotted in Chapter 5 based on the obtained natural frequencies for given loading conditions (Hopper and Williams 1977). These mode shapes are used when a parallel crack starts from a random place or in the case of an arbitrary crack. Chapter 6 includes an investigation of the effect of cracks starting at different locations or having different orientations. The changes in natural frequencies are found to match with previous studies (Huang and Leissa 2009) when the length ratio of all through-the-depth cracks is less than 0.4, but not when the crack becomes more severe, except in the case of mode 2. Using the hybrid model with a rotational spring to simulate a crack based on fracture mechanics, accuracy will be lost at high natural frequencies or when the crack severity is high (Fan and Qiao 2011).

When examining the various mode shapes, a significant difference is found to exist between the proposed method and Huang and Leissa (2009). Moreover, Huang and Leissa (2009) recorded the sequence of different modes based on the magnitude of natural frequencies. However, mode swapping will occur when the crack become severe based on the chronological order of recording. With increasing crack severity, there is a sharp reduction in the differences in frequencies of some modes while the change in natural frequencies decreases gradually for other modes. When the ATDC starts from the middle of the plate, the results obtained by Liew et al. (1994), show the natural frequency of mode 3 reduces much more quickly than that of mode 2.

One of the primary aims of this study is to use the changes in the vibration characteristics of plates for damage detection. This is addressed in Chapter 7. First the effect of damage placed at a set of reference points, e.g. equally spaced locations along the lower edge of the plate, in terms of changes in the natural frequencies of the plate needs to be determined. The automatic mode shape sign method (presented in Chapter 4) is used to reduce errors. Using the start point (the initial damage location and severity) as the first reference, and choosing location or severity as the controlled variable, the next point is then obtained and determined as the following reference until all the required cases are allocated. The detailed procedure is illustrated in Chapter 4 and forms the basis of a preliminary study of two-dimensional damage detection problems. These natural frequencies are then used to detect damage in the plate structures (Labib 2015). Generally, the first three natural frequencies are sufficient to converge on the estimated location intervals. The changes in natural frequencies between the undamaged and damaged cases are first normalised. For a one-dimensional problem, the normalised change in natural frequency is not related to the crack severity ratio, only to the location. Selected natural frequencies are then chosen and calculated for the intact case and for a crack located at the discretisation points. Hence, curves of normalised changes in natural frequencies against location can be plotted for use in the detection procedure.

First, the all through-the-length delamination modelled in Chapters 5 and 6 is used to validate the damage detection procedure. Then, an all through-the-length crack is examined to compare with the all through-the-length delamination. Noise free and then noisy measurements are considered. Noise free methodologies converge on the damage location by approaching to the actual location. However, the precision of predicted damage location cannot be guaranteed because of the linear interpolation used. The success of the quadratic/polynomial fitted curve used to predict changes in natural frequencies will depend on the number of discretisation points chosen. The spline fitting curve may also vary slightly due to the severity of the crack modelled (Labib 2015). Once the estimated damage location is recovered, the damage severity can be assessed based on the dimensions and properties of selected plate structure.

Noisy measurements converge on intervals of the damage location and severity. Interval arithmetic and noise factors are also introduced in Chapter 7. Because a single damage in a plate generally causes a small change in its natural frequencies and they may also be affected by environmental or operational conditions, most damage identification problems have only been validated at laboratory scale. In this work a noise factor ϵ is

introduced to examine the effects of noise in measurements. Values of 0.01Hz for ATLD and 0.001Hz for ATLC are demonstrated to be the limit of the level that can be successfully handled. A more confident damage location region and severity would be obtained with more severe damage. Comparing all through-the-length delaminations and cracks, the detection of delaminations can generally be predicted more accurately with at least 5% greater precision. For a less severe damage such as a crack, Chapter 7 suggests several methods to optimise the estimation. Table 7-12 presents all possible crack locations based on the obtained interval of normalised changes in natural frequencies from a simulated case. Selected additional natural frequencies are chosen, combined with the previous optimisation and normalised to obtain a better prediction of the damaged region.

Compared with noise-free measurement, a small amount of noise results in a much wider range of possible damage locations, but gives more realistic results than the point prediction provided from noise free simulation. For a symmetric structure, a further complication is that identical frequency changes will be seen when the damage occurs symmetrically. Furthermore, damage occurring at a different location with a different severity may also cause identical frequency changes (Fan and Qiao 2011) while multiple damage detection will cause more severe problems.

8.2 Scope for future work

Chapter 7 presents a natural frequency-based method for damage detection, which can be applied to one-dimensional problems. As shown in Eq. 7-1 and Eq. 7-2, the change in natural frequencies corresponding to different vibration modes due to the presence of damage is dependent on a combination of its severity and its location, where location is defined in terms of the x variable which is along the transverse axis. An acceptable accuracy is shown for different damage cases in Chapter 7. The next step would be to extend this to a two-dimensional problem.

For a one-dimensional problem, the reference discretisation set is only needed along the transverse axis. For a two-dimensional problem more discrete points are needed in both the transverse and longitudinal directions. To achieve this two-dimensional crack detection in an isotropic simply supported plate, two different damage detection procedures are proposed.

The degradation of natural frequencies in a structure increases with the progressive development of damage. A damage detection procedure for two dimensional plate problems could be developed based on that for beam-type structures proposed by Labib (2015). Assuming that the magnitude of the degradation depends on the crack location and severity, for a small crack, the relationship between corresponding natural frequencies in intact and cracked plates can be written:

$$\omega_{ic} = \omega_{io}(1 - \tilde{s}f_i(x, y)) \quad \text{Eq. 8-1}$$

where ω_{ic} and ω_{io} represent the natural frequencies in the intact and cracked plate respectively; i is the mode number; \tilde{s} is a function of the crack severity which is independent of the vibration mode; and x, y are the crack location variables along the longitudinal and transverse axes of the plate. The changes in natural frequency can be normalised for selected vibration modes to eliminate the effect of severity (Adam et al. 1978; Hearn and Testa 1991; Morassi 1993). The normalised changes in frequencies for different crack locations and modes can be expressed as:

$$\bar{\delta}_i(x, y) = \frac{\delta_i}{\sqrt{\sum_i \delta_i^2}} = \frac{f_i(x, y)}{\sqrt{\sum_i (f_i(x, y))^2}} \quad \text{Eq. 8-2}$$

with the summation extending over the selected number of modes. Choosing an array of discrete points with the same spacing along the longitudinal and transverse axes, the natural frequencies of damage placed at each of these points in turn can be obtained using the automatic mode shape methodology proposed in Chapter 4 with the correct ordering of natural frequencies. Then the corresponding normalised changes for the simulated crack $\overline{\delta_{im}}$ can be obtained using Eq. 8-2. Comparison of the reference and simulated values gives the functions:

$$G_i(x, y) = \overline{\delta_i}(x, y) - \overline{\delta_{im}} \quad \text{Eq. 8-3}$$

Plotting $G_i(x, y)$ on a 3D curve against the transverse and longitudinal axes of the plate, the predicted crack location will be at a point where the curves corresponding to different modes pass through zero. Multiple points will be detected if the structure is symmetric. In practice, the predicted damage locations for each mode may not coincide due to the discretisation set chosen. If a small amount of noise is introduced, a possible damage interval will be achieved around the exact damage location instead of an exact point. Linear interpolation could then be applied to obtain the potential damage point. This preliminary approach is valid for simple structures, although advanced interpolation techniques are still needed for further development.

The second proposed approach of proposed is based on the evaluation of the first-order variation of the natural frequencies which is verified for small intensity cracks. An equation similar to Eq. 8-1 could be written:

$$\omega_{io} - \omega_{ic} = \tilde{s}_i(x, y) * f_i(x, y) \quad \text{Eq. 8-4}$$

where $\tilde{s}_i(x, y)$ is a dimensionless function relating to severity. The same normalisation procedure can be applied as for the first method from the hybrid VFM model. The severity factor has a consistent effect on all modes of natural frequencies for each vibration mode and can therefore be generated as a reference to identify the crack location by isolating the severity factor $\tilde{s}_i(x, y)$.

$$\tilde{s}_i(x, y) = \frac{f_i(x, y)}{\omega_{io} - \omega_{ic}} \quad \text{Eq. 8-5}$$

When the crack occurs at a particular location (x, y) , $\tilde{s}_i(x, y)$ will be an independent variable which is consistent for different vibration modes.

$$\tilde{s}_1(x, y) = \tilde{s}_2(x, y) = \tilde{s}_3(x, y) = \dots = \tilde{s}_i(x, y) \quad \text{Eq. 8-6}$$

The damage location can thus be determined by finding the least variance between different vibration modes. For any location (x, y) , calculate the mean value:

$$\bar{s}(x, y) = \frac{1}{n} \sum_{i=1}^n \tilde{s}_i(x, y) \quad \text{Eq. 8-7}$$

The variance of $\tilde{s}_i(x, y)$ is

$$V(x, y) = \sum_{i=1}^n (\tilde{s}_i(x, y) - \bar{s}(x, y))^2 \quad \text{Eq. 8-8}$$

Minimising $V(x, y)$ would obtain the location point where the severity factor has the least variance, which is close to the actual crack location.

The first approach could be used for single arbitrary cracks. For a single crack, the severity factor is same wherever the crack is located. However, multiple crack detection should only consider the second approach because different cracks have different severity factors. Dealing with multiple damage locations is another area of research interest for future work and could also be solved by the proposed hybrid method.

As mentioned in section 8.1, using rotational springs can only simulate small intensity damage and classical thin bending plate theory provides conservative results. Other alternative damage models would need to be used to develop a more general forward approach.

Appendix

Appendix A

Function file for bandwidth Gaussian elimination without row interchange:

```
function [ge]=genre (x,WBw)
for i=1:(length(x)-1);
  ilast=min (i+WBw(i), length(x));
  for j=(i+1): ilast;
    mult=x(j,i)/x(i,i);
    x(j,i:ilast)=x(j,i:ilast)-mult*x(i,i:ilast);
  end;
end;
ge=x;
```

% code to be stored in a file named 'genre.m'; WBw is the bandwidth used in the elimination.

Appendix B

Code for calculating the natural frequencies and mode shapes based on the automatic mode shape sign method:

```
clear; clear all; format long;
lex=40; ley=40;

%number of elements along each axis

reqmodes= [1:6];

%reqmodes: required mode number

w=0.001; La=0.1; Lb=0.1; ro=4480; E=110*10^9; t=10^(-3); vu=0.3; d=0.99*10^(-3);
nnodex=lex+1; nnodey=ley+1;
nodes=nnodex*nnodey;

%w: the trial natural frequency; La/Lb: plate length along each axis; ro: mass kg/m3; E:
Youngs modulus; t: thickness; vu: poisson's ratio; d: the crack depth

gloInix=[0.07241181]; gloFinx=[0.075];
gloIniy=[0.090340742]; gloFiny=[0.1];

%the global coordinates of the initial and final point of the crack

for i=1:length(gloFiny)

%determine the length ratio by the y-axis

    for j=1:length(gloFinx)

%determine the location along x-axis

        GloIniy=gloIniy(i); GloFiny=gloFiny(i);
        GloInix=gloInix(j); GloFinx=gloFinx(j);
[NorNF(i,j,:),NorDis(i,j,:,:)]=SigNfDis(lex,ley,reqmodes,w,La,Lb,ro,E,t,vu,d,GloInix,G
loFinx,GloIniy,GloFiny);

        %NorNF(i,j,r):i is the length variable, j is the location variable, r is the mode variable.
        NorDis(i,j,r,node): node is the node variable depends on the mesh.

    end
end
RefValue(1,1,1:length(reqmodes),:)=NorDis(1,1,1:length(reqmodes),:);

%Reference mode chosen

for i=1:length(gloFiny)
```

%length ratio

for j=1:length (gloFinx)

%location ratio

if j==1

for r=1:(length(reqmodes)-1)

DifSameOrder(i,j,r)=min([sum(abs(NorDis(i,j,r,:)-
RefValue(i,j,r,:))),sum(abs(NorDis(i,j,r,:)+RefValue(i,j,r,:)))]);

DifAscOrder(i,j,r)=min([sum(abs(NorDis(i,j,r+1,:)-
RefValue(i,j,r,:))),sum(abs(NorDis(i,j,r+1,:)+RefValue(i,j,r,:)))]);

*%this comparison is based on the initial crack length ratio 0.1 of the previous location,
for the start, use the first location and first crack length ratio as a reference. For the start
point, use length family curve as a standard.*

if DifSameOrder(i,j,r)<DifAscOrder(i,j,r)

RigOrdNorNF(i,j,r)=NorNF(i,j,r);

RigOrdNorNF(i,j,r+1)=NorNF(i,j,r+1);

RigOrdNorDis(i,j,r,:)=NorDis(i,j,r,:);

RigOrdNorDis(i,j,r+1,:)=NorDis(i,j,r+1,:);

else

RigOrdNorNF(i,j,r)=NorNF(i,j,r+1);

RigOrdNorNF(i,j,r+1)=NorNF(i,j,r);

RigOrdNorDis(i,j,r,:)=NorDis(i,j,r+1,:);

RigOrdNorDis(i,j,r+1,:)=NorDis(i,j,r,:);

end

NorNF(i,j,r)=RigOrdNorNF(i,j,r);

NorNF(i,j,r+1)=RigOrdNorNF(i,j,r+1);

NorDis(i,j,r,:)=RigOrdNorDis(i,j,r,:);

NorDis(i,j,r+1,:)=RigOrdNorDis(i,j,r+1,:);

end

else

for r=1:(length(reqmodes)-1)

DifSameOrder(i,j,r)=min([sum(abs(NorDis(i,j,r,:)-NorDis(i,j-
1,r,:))),sum(abs(NorDis(i,j,r,:)+NorDis(i,j-1,r,:)))]);

DifAscOrder(i,j,r)=min([sum(abs(NorDis(i,j,r+1,:)-NorDis(i,j-
1,r,:))),sum(abs(NorDis(i,j,r+1,:)+NorDis(i,j-1,r,:)))]);

*%from the second length ratio from 0.2, mainly discuss the family curve based on the
previous location ratio with the same length. In a conclude, discuss the family curve focus
on the location ratio family.*

if DifSameOrder(i,j,r)<DifAscOrder(i,j,r)

RigOrdNorNF(i,j,r)=NorNF(i,j,r);

RigOrdNorNF(i,j,r+1)=NorNF(i,j,r+1);

```

        RigOrdNorDis(i,j,r,:)=NorDis(i,j,r,:);
        RigOrdNorDis(i,j,r+1,:)=NorDis(i,j,r+1,:);
    else
        RigOrdNorNF(i,j,r)=NorNF(i,j,r+1);
        RigOrdNorNF(i,j,r+1)=NorNF(i,j,r);
        RigOrdNorDis(i,j,r,:)=NorDis(i,j,r+1,:);
        RigOrdNorDis(i,j,r+1,:)=NorDis(i,j,r,:);
    end
    NorNF(i,j,r)=RigOrdNorNF(i,j,r);
    NorNF(i,j,r+1)=RigOrdNorNF(i,j,r+1);
    NorDis(i,j,r,:)=RigOrdNorDis(i,j,r,:);
    NorDis(i,j,r+1,:)=RigOrdNorDis(i,j,r+1,:);
end
end
end
RefValue(i+1,1,1:length(reqmodes),:)=RigOrdNorDis(i,1,1:length(reqmodes),:);
end

%for the first reference value, the next location reference value will be the previous length
at the same location ratio

for j=1:length(gloFinx)
    for i=1:length(gloFiny)
        name=strcat('Modeshapes of crack start location: ',num2str(gloInix(j)),
num2str(gloIniy(j)), ',' , 'Crack Length: ',num2str(sqrt((gloFiny(i)-gloIniy(i))^2-
(gloFinx(i)-gloInix(i))^2)));
        figure('Name',name);
        for r=reqmodes
            Dz=zeros(nnodex,nnodey);
            for m=1:nnodex:(nodes-nnodex+1)
                Dz(1:nnodex,ceil(m/nnodex))=RigOrdNorDis(i,j,r,m:(m+nnodex-1));
            end
        end

%Dz is the final displacement for each node; reassigned the vertical displacement of each
of the node in the right place of mesh point

        x=linspace(0,La,nnodex);
        y=linspace(0,Lb,nnodey);
        [yy,xx]=meshgrid(y,x);
        %mesh the plate in correct scale
        zz=Dz;
        subplot(2,3,r)
        contour(yy,xx,zz)
        title(['Mode ',num2str(r), ' : ',num2str(RigOrdNorNF(i,j,r))])
        xlabel('y')
        ylabel('x')
    end
end

```

```
    xlabel('z')
    colorbar
    hold on
    LocaX=[gloIniy(i), gloFinny(i)];
    LocaY=[gloInix(j), gloFinx(j)];
    line (LocaX,LocaY,'Color','k','LineStyle','-','LineWidth',3)
    hold off
end
end
end
```

Appendix C

Function file for applying the Wittrick-Williams algorithm to obtain natural frequencies and mode shapes for a single cracked case:

```
% code to be stored in a file named 'SigNfDis.m'.

function [norNF,norDis] = SigNfDis (lex, ley, reqmodes, w, La, Lb, ro, E, t, vu, d,
GloInix, GloFinx, GloIniy, GloFiny)
a=La/lex; be=Lb/ley;
beta=(be/a);

%a/be: element dimension along the x/y axis; beta: the aspect ratio;

IniCord=[GloInix GloIniy];
FinCord=[GloFinx GloFiny];
VectCrack=FinCord-IniCord;

%initial and final point of the crack; VectCrack is the vector quantity of the crack;

alpha=atan((GloFiny-GloIniy)/(GloFinx-GloInix));

%the angle of the crack with x-axis;

TElem=lex*ley;

%total element number;

nnodex=lex+1; nnodey=ley+1;

%number of nodes along each axis;

nodes=nnodex*nnodey;

%total number of nodes of the whole structure

Enodes=zeros(nodes,1);
ii=0;
for i=[1:(nodes-nnodex)]
    if mod(i,nnodex)~=0
        ii=ii+1;
        Enodes(ii)=i;
    end
end
Efnodes=Enodes(Enodes~=0);

%Initial node of each element (bottom left) matrix; length (Efnodes) is the total number
of elements;
```



```
TElement=zeros(lex,ley);

%element number matrix of plates;

for i=1:lex:(TElem-lex+1)
    TElement(1:lex,ceil(i/lex))=Efnodes(i:(i+lex-1));
end

%arrange the initial bottom left nodes to corresponding element;

Clength=norm(VectCrack);
Seca=fix(sec(alpha)*1000)/1000; Coseca=fix(csc(alpha)*1000)/1000;
Cota=fix(cot(alpha)*1000)/1000; Tana=fix(tan(alpha)*1000)/1000;
Cosa=fix(cos(alpha)*1000)/1000; Sina=fix(sin(alpha)*1000)/1000;

%angle and length of the crack;

FGloInix=fix((GloInix/a)*1000)/1000; FGloIniy=fix((GloIniy/be)*1000)/1000;
FFinElex=fix((GloFinx/a)*1000)/1000; FFinEley=fix((GloFiny/be)*1000)/1000;

%the way we keep three decimal accuracy;

if Cota>0

%Cota here is used to determine which equation will be used to determine the global
coordinate number;

IniElex=fix(FGloInix)+1; IniEley=fix(FGloIniy)+1;
FinElex=ceil(FFinElex); FinEley=ceil(FFinEley);
elseif Cota<0
    IniElex=ceil(FGloInix); IniEley=fix(FGloIniy)+1;
    FinElex=fix(FFinElex)+1; FinEley=ceil(FFinEley);
    else
    IniElex=fix(FGloInix)+1; IniEley=fix(FGloIniy)+1;
    FinElex=fix(FFinElex)+1; FinEley=ceil(FFinEley);
end
MaxTotE=fix(abs(FinElex-IniElex)+abs(FinEley-IniEley))+1;

%MaxTotE: the maximum number of element the crack may across;

tCElement=zeros(MaxTotE+1,2);
tCElement(1,1)=IniElex; tCElement(1,2)=IniEley;

%the coordinate of the x and y in global scale to determine the CraE;

reqelement=[1:MaxTotE];

%maximum requirement element number from 1:MaxTotE;

reqEleLength=MaxTotE+1;
```

```
CLength=zeros(reqEleLength,1);
Aelement=2*MaxTotE;
x=zeros(Aelement,1);
y=zeros(Aelement,1);
x(1)=GloInix-(IniElex-1)*a;
y(1)=GloIniy-(IniEley-1)*be;

%the first point's local coordinate;

fCLength=zeros (MaxTotE,1);

%the accumulation crack length;

for e=requelement
240elta=(a-x(2*e-1))*Seca;
deltaB=(be-y(2*e-1))*Coseca;
Delta=240elta-deltaB;

%the virtual crack length caused by x-axis and y-axis in the specific element to compare;

if ClengthI<CLength
    if Delta>0
        x(2*e)=x(2*e-1)+(be-y(2*e-1))*Cota; y(2*e)=be;
        x(2*e+1)=x(2*e-1)+(be-y(2*e-1))*Cota; y(2*e+1)=0;
        Clength(e+1)=ClengthI+(be-y(2*e-1))*Coseca;

%the final local coordinate of this element and the next element;

        tCElement(e+1,1)=tCElement(e,1); tCElement(e+1,2)=tCElement(e,2)+1;
        elseif Delta<0
            x(2*e)=a; y(2*e)=y(2*e-1)+(a-x(2*e-1))*Tana;
            x(2*e+1)=0; y(2*e+1)=y(2*e-1)+(a-x(2*e-1))*Tana;
            Clength(e+1)=ClengthI+(a-x(2*e-1))*Seca;
            tCElement(e+1,1)=tCElement(e,1)+1; tCElement(e+1,2)=tCElement(e,2);
        else
            x(2*e)=a; y(2*e)=be;
            x(2*e+1)=0; y(2*e+1)=0;
            Clength(e+1)=ClengthI+(be-y(2*e-1))*Coseca;
            tCElement(e+1,1)=tCElement(e,1)+1; tCElement(e+1,2)=tCElement(e,2)+1;
        end
    end
fCLengthI=Clength(e+1);
else break
end
end
FCLength=fCLength(fCLength~=0);

%the final accumulation crack length;
```

```
X=x(1:length(FCLength)*2,1);
Y=y(1:length(FCLength)*2,1);
X(end)=GloFinx-(FinElex-1)*a;
Y(end)=GloFiny-(FinEley-1)*be;
TCElement=tCElement(1:length(FCLength));
for i=1:length(FCLength)
    craE(i)=Telement(TCElement(I,1),TCElement(I,2));
end
CraE=craE;

%element number start from left bottom node;

for i=1:length(FCLength)
    locaMx(I,1)=X(2*i-1); locaMx(I,2)=X(2*i);
    locaMy(I,1)=Y(2*i-1); locaMy(I,2)=Y(2*i);
end

%the local coordinate of the two points in single element;

LocaMx=locamx; LocaMy=locamy;

%the local coordinate in each element;

lengM=zeros(length(CraE),1);
for is=1:length(CraE)
    lengM(is,1)=sqrt(((LocaMx(is,2)-LocaMx(is,1))^2)+((LocaMy(is,2)-
LocaMy(is,1))^2));
end
LengM=lengM;

%the crack length in each element;

DD=E*t^3/(12*(1-vu^2));

%the flexural rigidity of plate;

CC=((d/t)*(2-(d/t)))/(0.9*((d/t)-1)^2);

%the dimensionless function about the d and t;

Iu=[1 0 0;
    0 1 0;
    0 0 1];
Ccsx=zeros(nodes,1); Ccsy=zeros(nodes,1);

%Compliance matrix;

XCompi=zeros(length(CraE),1);
XCompj=zeros(length(CraE),1);
XCompm=zeros(length(CraE),1);
```

```

XCompp=zeros(length(CraE),1);
YCompi=zeros(length(CraE),1);
YCompj=zeros(length(CraE),1);
YCompm=zeros(length(CraE),1);
YCompp=zeros(length(CraE),1);

%the additional compliance at element level;

MM=t*CC/(DD*(a^3)*be);
NN=t*CC/(DD*a*(be^3));
for is=1:length(CraE)
    XCompi(is)=XCompi(is)+MM*((a*(be-
LocaMy(is,1))+a*LocaMx(is,1)*Tana)*(LocaMx(is,2)-LocaMx(is,1))+(-a*Tana-(be-
LocaMy(is,1))-LocaMx(is,1)*Tana)*(((LocaMx(is,2)^2)-
(LocaMx(is,1)^2))/2)+Tana*(((LocaMx(is,2)^3)-(LocaMx(is,1)^3))/3));
    XCompj(is)=XCompj(is)+MM*((a*LocaMy(is,1)-
a*LocaMx(is,1)*Tana)*(LocaMx(is,2)-LocaMx(is,1))+(-
LocaMy(is,1)+LocaMx(is,1)*Tana+a*Tana)*(((LocaMx(is,2)^2)-(LocaMx(is,1)^2))/2)-
Tana*(((LocaMx(is,2)^3)-(LocaMx(is,1)^3))/3));
    XCompm(is)=XCompm(is)+MM*((LocaMy(is,1)-
LocaMx(is,1)*Tana)*(((LocaMx(is,2)^2)-
(LocaMx(is,1)^2))/2)+Tana*(((LocaMx(is,2)^3)-(LocaMx(is,1)^3))/3));
    XCompp(is)=XCompp(is)+MM*(((be-
LocaMy(is,1)+LocaMx(is,1)*Tana)*(((LocaMx(is,2)^2)-(LocaMx(is,1)^2))/2))-
Tana*(((LocaMx(is,2)^3)-(LocaMx(is,1)^3))/3));
    YCompi(is)=YCompi(is)+NN*((be*(a-
LocaMx(is,1))+be*LocaMy(is,1)*Cota)*(LocaMy(is,2)-LocaMy(is,1))+(-be*Cota-(a-
LocaMx(is,1))-LocaMy(is,1)*Cota)*(((LocaMy(is,2)^2)-
(LocaMy(is,1)^2))/2)+Cota*(((LocaMy(is,2)^3)-(LocaMy(is,1)^3))/3));
    YCompj(is)=YCompj(is)+NN*(((a-
LocaMx(is,1))+LocaMy(is,1)*Cota)*(((LocaMy(is,2)^2)-(LocaMy(is,1)^2))/2)-
Cota*(((LocaMy(is,2)^3)-(LocaMy(is,1)^3))/3));
    YCompm(is)=YCompm(is)+NN*((LocaMx(is,1)-
LocaMy(is,1)*Cota)*(((LocaMy(is,2)^2)-
(LocaMy(is,1)^2))/2)+Cota*(((LocaMy(is,2)^3)-(LocaMy(is,1)^3))/3));
    YCompp(is)=YCompp(is)+NN*((be*LocaMx(is,1)-
be*LocaMy(is,1)*Cota)*(LocaMy(is,2)-LocaMy(is,1))+be*Cota-
LocaMx(is,1)+LocaMy(is,1)*Cota)*(((LocaMy(is,2)^2)-(LocaMy(is,1)^2))/2)-
Cota*(((LocaMy(is,2)^3)-(LocaMy(is,1)^3))/3));
end

% the integral shape function which could let each point in the crack of single element
distributed into the four nodes on the right place;

for is=1:length(CraE)
    i=CraE(is); j=i+nnodex; m=i+nnodex+1; p=i+1;
    Ccsx(i)=Ccsx(i)+XCompi(is);
    Ccsx(j)=Ccsx(j)+XCompj(is);
    Ccsx(m)=Ccsx(m)+XCompm(is);

```

```
Ccsx(p)=Ccsx(p)+XCompp(is);
Ccsy(i)=Ccsy(i)+YCompi(is);
Ccsy(j)=Ccsy(j)+YCompj(is);
Ccsy(m)=Ccsy(m)+YCompm(is);
Ccsy(p)=Ccsy(p)+YCompp(is);
end
Csx=Ccsx; Csy=Ccsy;
Index=zeros(nodes*5,1);
Lastindex=0;
for i=[1:nodes]
    Index(5*i-4)=Lastindex+1;
    if Csx(i)==0
        Index(5*i-3)=Index(5*i-4)+1;
        Index(5*i-2)=Index(5*i-3);
    else Csx(i)~=0;
        Index(5*i-3)=Index(5*i-4)+1;
        Index(5*i-2)=Index(5*i-3)+1;
    end
    if Csy(i)==0
        Index(5*i-1)=Index(5*i-2)+1;
        Index(5*i)=Index(5*i-1);
    else Csy(i)~=0;
        Index(5*i-1)=Index(5*i-2)+1;
        Index(5*i)=Index(5*i-1)+1;
    end
    Lastindex=Index(5*i);
end
FIndex=Index;

%the index for each of the degree of freedom to corresponding node;

Fnode=FIndex(end);

% Bandwidth of matrix

bw=zeros(nodes,1);
for i=1:nodes
    ilast=min(i+nnodex+1,nodes);
    bw(i)=FIndex(5*ilast)-FIndex(5*i-4)+1;
end
Bw=zeros(Fnode,1);
for i=1:nodes
    Bw(FIndex(5*i-4):FIndex(5*i),1)=bw(i);
end
WBw=Bw;
KT=GstiffnessK (Fnode, nodes, nnodex, E, t, vu, a, be, beta, Efnodes, FIndex, Csx,
Csy);
```

%KT: global stiffness;

MT=GmassM (Fnode, ro, a, be, t, nnodex, Efnodes, FIndex);

%MT: global mass matrix;

J= WWFDKAG(w,KT,MT,WBw);

%J: the sign count from W-W algorithm

fr=length(reqmodes);

for r=reqmodes

 while r>J

 wl=w; w=2*w; wu=w;

 J= WWFDKAG(w,KT,MT,WBw);

 end

 while (wu-wl)>0.001

 w=(wu+wl)/2;

 J= WWFDKAG(w,KT,MT,WBw);

 if r>J

 wl=w;

 else

 wu=w;

 end

 end

 wr(r)=w;

 modeshape(r,:)= WWfDKAGModeshapes(w,Fnode,KT,MT,WBw);

end

%bisection method to calculate the NF(w)

EufHz(1,1:fr)=wr(reqmodes);

NondimenHz(1,1:fr)=EufHz*2*pi*(Lb^2)*(sqrt(ro*t/(DD)))

for mode=reqmodes

 for i=1:nodes

 DOF(1)=5*i-4;

 dz(mode,i)=modeshape(mode,FIndex(DOF(1)));

 end

 maxDis=max(abs(dz(mode,:)));

 for i=1:nodes

 dzNor(mode,i)=dz(mode,i)/maxDis;

 end

%normalise the mode shape by divide the maximum absolute vertical displacement; for each mode, transfer the three-dimensional matrix into one-dimensional matrix under the default sequence; and choose the vertical displacement from the total mode shape matrix;

```
    for i=[1:nnodex,(nodes-nnodex+1):nodes,(nnodex+1):nnodex:(nodes-  
2*nnodex+1),2*nnodex:nnodex:(nodes-nnodex)]  
        dzNor(mode,i)=0;  
    end  
end  
norNF=NondimenHz;  
norDis=dzNor;  
end
```

Appendix D

Code when ‘parfor’ code is applied for a set of different crack cases occurring in the same plate structure:

```
for i=1:length(gloFiny)
```

```
%firstly, we determine the length ratio by the y-axis
```

```
    parfor j=1:length(gloFinx)
```

```
%secondly, we determine the location along x-axis by introducing the parfor code
```

```
        GloIniy=gloIniy(i); GloFiny=gloFiny(i);
```

```
        GloInix=gloInix(j); GloFinx=gloFinx(j);
```

```
[NorNF(i,j,:),NorDis(i,j,:,:)]=SigNfDis(lex,ley,reqmodes,w,La,Lb,ro,E,t,vu,d,GloInix,GloFinx,GloIniy,GloFiny);
```

```
    end
```

```
end
```


Appendix E

Function file for assembly of the global stiffness matrix:

```

function [GSM]= GstiffnessK (Fnode, nodes, nnodex, E, t, vu, a, be, beta, Efnodes,
FIndex, Csx, Csy)
KEe= zeros (Fnode);
ww = 10^10;

for i=[1:nnodex,(nodes-nnodex+1):nodes,(nnodex+1):nnodex:(nodes-
2*nnodex+1),2*nnodex:nnodex:(nodes-nnodex)];
    DOF(1)=5*i-4; DOF(2)=5*i-4;
    KEe(FIndex(DOF(1)),FIndex(DOF(2)))=KEe(FIndex(DOF(1)),FIndex(DOF(2)))+ww;
End

KE=KEe;
Kke=EstiffnessK(E,t,vu,a,be,beta);

for is=1:length(Efnodes);
    i=Efnodes(is); j=i+nnodex; m=i+nnodex+1; p=i+1;
    DOF(1)=5*i-4; DOF(2)=5*i-2; DOF(3)=5*i-1;
    DOF(4)=5*j-4; DOF(5)=5*j-3; DOF(6)=5*j-1;
    DOF(7)=5*m-4; DOF(8)=5*m-3; DOF(9)=5*m;
    DOF(10)=5*p-4; DOF(11)=5*p-2; DOF(12)=5*p;

    %5*i-4 is the out-of-plane deflection; 5*i-3 is the left rotation about x-axis, 5*i-2 is the
    right rotation about x-axis; 5*i-1 is the top rotation about y-axis, 5*i is the bottom about
    y-axis

    for nn1=1:12;
        for nn2=1:12;
            KE(FIndex(DOF(nn1)),FIndex(DOF(nn2)))=KE(FIndex(DOF(nn1)),FIndex(DOF(nn2))
            )+Kke(nn1,nn2);
        end
    end
end
KE1=KE;
for i=[1:nodes];
    if Csx(i)~=0;
        nnx1=5*i-3;
        nnx2=5*i-2;
        KE1(FIndex(nnx1),FIndex(nnx1))=KE1(FIndex(nnx1),FIndex(nnx1))+1/Csx(i);
        KE1(FIndex(nnx1),FIndex(nnx2))=KE1(FIndex(nnx1),FIndex(nnx2))-1/Csx(i);
        KE1(FIndex(nnx2),FIndex(nnx1))=KE1(FIndex(nnx2),FIndex(nnx1))-1/Csx(i);
        KE1(FIndex(nnx2),FIndex(nnx2))=KE1(FIndex(nnx2),FIndex(nnx2))+1/Csx(i);
    end
end

```

```
if Csy(i)~=0;
    nny1=5*i-1;
    nny2=5*i;
    KE1(FIndex(nny1),FIndex(nny1))=KE1(FIndex(nny1),FIndex(nny1))+1/Csy(i);
    KE1(FIndex(nny1),FIndex(nny2))=KE1(FIndex(nny1),FIndex(nny2))-1/Csy(i);
    KE1(FIndex(nny2),FIndex(nny1))=KE1(FIndex(nny2),FIndex(nny1))-1/Csy(i);
    KE1(FIndex(nny2),FIndex(nny2))=KE1(FIndex(nny2),FIndex(nny2))+1/Csy(i);
end
end
```

%Csx is the compliance about x-axis, Csy is the compliance about y-axis; the additional spring stiffness added on the nodes both sides.

```
KE2=KE1;
GSM=KE2;
end
```

Appendix F

Function file for assembly of the global mass matrix:

```
function [GMM]= GmassM(Fnode,ro,a,be,t,nnodex,Efnodes,FIndex)
Mme=EmassM(ro,a,be,t);
MEe=zeros(Fnode);

for is=1:length(Efnodes);
    i=Efnodes(is); j=i+nnodex; m=i+nnodex+1; p=i+1;
    DOF(1)=5*i-4; DOF(2)=5*i-2; DOF(3)=5*i-1;
    DOF(4)=5*j-4; DOF(5)=5*j-3; DOF(6)=5*j-1;
    DOF(7)=5*m-4; DOF(8)=5*m-3; DOF(9)=5*m;
    DOF(10)=5*p-4; DOF(11)=5*p-2; DOF(12)=5*p;
    for nn1=1:12;
        for nn2=1:12;
            MEe(FIndex(DOF(nn1)),FIndex(DOF(nn2)))=MEe(FIndex(DOF(nn1)),FIndex(DOF(n
n2)))+Mme(nn1,nn2);
        end
    end
end

ME=MEe;
GMM=ME;
end
```

Appendix G

Function file for the constraint matrices used in the VFM model:

```
function [ConVICONOPT,ConFE]=Constraint (pi, Lambda, La, nnodex, nnodey, lex,
icomplex, FIndex)
```

```
LambdaRatio=zeros(length(Lambda)*2);
for i=1:length(Lambda)
LambdaRatio(2*i-1)=Lambda(i)/La;
LambdaRatio(2*i)=-Lambda(i)/La;
end
```

```
% positive and negative wavelength;
```

```
xLa=zeros(1,nnodex);
for i=1:nnodex
xLa(i)=(i-1)/lex;
end
```

```
% location based on the nodes we chosen;
```

```
ConLeftRo=cell(nnodex,length(Lambda)*2);
ConLeftDi=cell(nnodex,length(Lambda)*2);
ConRightRo=cell(nnodex,length(Lambda)*2);
ConRightDi=cell(nnodex,length(Lambda)*2);
```

```
for i=1:(length(Lambda)*2)
for j=1:nnodex
ConLeftRo{j,i}=[0 0 exp(icomplex*pi*xLa(j)/LambdaRatio(i)) 0 0 0 0 0];
ConRightRo{j,i}=[0 0 0 0 exp(icomplex*pi*xLa(j)/LambdaRatio(i)) 0 0 0];
ConLeftDi{j,i}=[0 0 0 exp(icomplex*pi*xLa(j)/LambdaRatio(i)) 0 0 0 0];
ConRightDi{j,i}=[0 0 0 0 0 exp(icomplex*pi*xLa(j)/LambdaRatio(i)) 0 0];
end
end
```

```
conVICONOPT=cell(4*nnodex-2,(length(Lambda)*2));
```

```
%% VICONOPT rotation connections at all nodes
```

```
for i=1:nnodex
for j=1:(length(Lambda)*2)
conVICONOPT{2*i-1,j}=ConLeftRo{i,j};
conVICONOPT{2*(nnodex+i)-2,j}= ConRightRo{i,j};
end
end
```

```
%% VICONOPT displacement connections at interior nodes
```

```
for i=1:nnodex-1
    for j=1:(length(Lambda)*2)
        conVICONOPT{2*i,j}=ConLeftDi{i,j};
        conVICONOPT{2*(nnodex+i)-1,j}=ConRightDi{i,j};
    end
end

% constrain all rotation, just leave far end displacement free

%% VICONOPT displacements set to zero at end nodes

ConVICONOPT=cell2mat(conVICONOPT);

% transfer cell to matrix, make the constraint to be fitted in the global stiffness matrix

ConFE=zeros(2*nnodex*2-2,FIndex(end));

%% FE rotation connections at all nodes

for i=1:nnodex
    ConFE(2*i-1,FIndex(5*i-2))=-1;
    ConFE(2*(nnodex+i)-2,FIndex(5*(nnodex*(nnodey-1)+i)-3))=-1;
end

%% FE displacement connections at interior nodes

for i=2:nnodex-1
    ConFE(2*i,FIndex(5*i-4))=-1;
    ConFE(2*(nnodex+i)-1,FIndex(5*(nnodex*(nnodey-1)+i)-4))=-1;
end
end

% 1. set the first node's displacement constraint to zero, leave the far end displacement
constraint free; 2. 2*nnodex: the total nodes along the VICONOPT boundary between
the FE and VICONOPT; 3. *2:the total degree of freedom in VICONOPY need to
constrain, which is the rotation about x axis and displacement. only out-of-plane problem
considered. 4. nnodex*nnodey: the total nodes in the FE part; 5. *3:the total degree of
freedom in the FE part. 6. the -1 comes from the Williams and Anderson (1983); 7. the
size of the constraint matrix: the number of column is the number of different half
wavelength we choose (include the positive and negative one). the number of row is the
number of different degree of freedoms for different nodes (left and right side plate
included).
```

Appendix H

Function file for calculating the mode shapes:

```
function [WTWLfDKAGModeshapes]=  
WWfDKAGModeshapes(w,Fnode,KT,MT,WBw)  
  
K2=KT-(MT*(w*2*pi)^2);  
K2=genre(K2,WBw);  
Dis=zeros(Fnode,1);  
Pn=rand(Fnode,1);  
Dis(Fnode)=Pn(Fnode)/K2(Fnode,Fnode);  
  
for i=1:(Fnode-1);  
Sum=K2(Fnode-i,Fnode-i+1:Fnode)*Dis(Fnode-i+1:Fnode);  
Dis(Fnode-i)=-Sum/K2(Fnode-i,Fnode-i);  
end  
  
WTWLfDKAGModeshapes=Dis;  
end
```

Appendix I

Data used in VICONOPT to calculate the natural frequencies and mode shapes:

TITLE

Simply supported, through length delamination, Nx, vary width

VICON 2 10

WAVELENGTH

XI 0.01 1.0 0.99

VIBRATION

ANALYSIS

EIGENVALUE

1 2 3

LENGTH 100.

PFAST

MATERIALS

1 130.E3 0.3 2.3E-6 5.E3 10.E3

LAYERS

1 0.125 1 0.

2 0.125 1 45.

3 0.125 1 90.

WALLS

1 1 2 -2 3 1 2 -2 3 3 -2 2 1 3 2 -2 1

2 1 2 -2 3

3 1 2 -2 3 3 -2 2 1 3 2 -2 1

PLATE

1 2. 1

2 2. 2

3 2. 3

ALIGNMENT

OFF 4 2 0. 0.75 0. 0.75

OFF 5 3 0. -0.25 0. -0.25

CONNECTION

1 2 1

=(1)(1)(0)

==(50)

ATTACHMENT

1 901 51 901

LONGITUDINAL LINE SUPPORT

123

PLOT

2 3 1.

POINT SUPPORTS

3

2 3 4 5 6 7 8 9 10 11 12 13 14 15 16 17 18 19 20 21 22 23 24 25

$X=0.$

3

26 27 28 29 30 31 32 33 34 35 36 37 38 39 40 41 42 43 44 45 46 47 48 49 50

NODES

1 2 3 4 5 6 7 8 9 10 11 12 13 14 15 16 17 18 19 20 21 22 23 24 25 26 27 28 29 30 31
32 33 34 35 36 37 38 39 40 41 42 43 44 45 46 47 48 49 50 51

CROSS

0

END

References

- Adams, R.D., Cawley, P., Pye, C.J. and Stone, B.J. 1978. A vibration technique for non-destructively assessing the integrity of structures. *Journal of Mechanical Engineering Science* 20(2), pp. 93–100. doi: 10.1243/JMES.
- Anderson, M.S. and Kennedy, D. 1993. Transverse shear deformation in exact buckling and vibration of composite plate assemblies. *AIAA Journal* 31(10), pp. 1963–1965.
- Anderson, M.S., Williams, F.W. and Wright, C.J. 1983. Buckling and vibration of any prismatic assembly of shear and compression loaded anisotropic plates with an arbitrary supporting structure. *International Journal of Mechanical Sciences* 25(8), pp. 585–596. doi: 10.1016/0020-7403(83)90050-4.
- ASNT.2011. Introduction to Nondestructive Testing. Available at: <https://asnt.org/MinorSiteSections/AboutASNT/Intro-to-NDT.aspx> [Accessed: 20 May 2019].
- Bachene, M., Tiberkak, R. and Rechak, S. 2009. Vibration analysis of cracked plates using the extended finite element method. *Archive of Applied Mechanics* 79(3), pp. 249–262.
- Banerjee, J.R. 1997. Dynamic stiffness formulation for structural elements: a general approach. *Computers and Structures* 63(1), pp. 101–103. doi: 10.1016/S0045-7949(96)00326-4.
- Banerjee, J.R., Papkov, S.O., Liu, X. and Kennedy, D. 2015. Dynamic stiffness matrix of a rectangular plate for the general case. *Journal of Sound and Vibration* 342, pp. 177–199.
- Banerjee, J.R. and Guo, S. 2009. On the dynamics of cracked beams. *Proceedings of 50th AIAA/ASME/ASCE/AHS/ASC Structures, Structural Dynamics, and Materials Conference*, pp. 2429. Palm Springs, California, 04 May 2009 - 07 May 2009. Available at: <https://doi.org/10.2514/6.2009-2429> [Accessed at: 19 July 2019].
- Banerjee, J.R. and Williams, F.W. 1994. An exact dynamic stiffness matrix for coupled extensional-torsional vibration of structural members. *Computers and Structures* 50(2), pp. 161–166.
- Beards, C.F. and Miao, M. 1996. *Structural Vibration: Analysis and Damping*. Oxford: Butterworth-Heinemann.
- Berger, H.M. 1954. A new approach to the analysis of large deflections of plates. (Doctoral dissertation, California Institute of Technology: Williams, Max L)
- Berger, J. and Wilson, D. 2011. Hole in Southwest jet attributed to cracks. *The New York Times*. Available at: <https://www.nytimes.com/2011/04/04/business/04plane.html> [Accessed: 20 May 2019]
- Birman, V. 2011. *Plate Structures*: Springer Science and Business Media. New York: SPI Publisher Services.
- Bogner, F.K., Mallett, R.H., Minich, M.D. and Scmit, L.A. 1965. *Development and Evaluation of Energy Search Methods of Nonlinear Structural Analysis*. Case Institute of

Technology, Cleveland OH. National Institute of Standards and Technology: U.S. Department of Commerce.

Bolotin, V. V. 2001. Mechanics of delamination in laminate composite structures. *Mechanics of Composite Materials* 37(5–6), pp.367–380. doi: 10.1023/A:1014210527476.

Boscolo, M. and Banerjee, J.R. 2011. Dynamic stiffness elements and their applications for plates using first order shear deformation theory. *Computers and structures* 89(3–4), pp. 395–410.

Boscolo, M. and Banerjee, J.R. 2012a. Dynamic stiffness formulation for composite Mindlin plates for exact modal analysis of structures. Part I: Theory. *Computers and Structures* 96, pp. 61–73.

Boscolo, M. and Banerjee, J.R. 2012b. Dynamic stiffness formulation for composite Mindlin plates for exact modal analysis of structures. Part II: Results and applications. *Computers and Structures* 96, pp. 74–83.

Boscolo, M. and Banerjee, J.R. 2014. Layer-wise dynamic stiffness solution for free vibration analysis of laminated composite plates. *Journal of Sound and Vibration* 333(1), pp. 200–227.

Bose, T. and Mohanty, A.R. 2013. Vibration analysis of a rectangular thin isotropic plate with a part-through surface crack of arbitrary orientation and position. *Journal of Sound and Vibration* 332(26), pp. 7123–7141.

Bourne, R. 2013. BIS Aerospace, Marine and Defence Sector Team. Available at: <https://www.gov.uk/government/groups/bis-aerospace-marine-and-defence-sector-team#aerospace> [Accessed: 13 May 2019].

Butler, R. and Williams, F.W. 1992. Optimum design using VICONOPT, a buckling and strength constraint program for prismatic assemblies of anisotropic plates. *Computers and Structures* 43(4), pp. 699–708. doi: 10.1016/0045-7949(92)90511-W.

Caddemi, S. and Caliò, I. 2008. Exact solution of the multi-cracked Euler-Bernoulli column. *International Journal of Solids and Structures* 45(5), pp. 1332–1351. doi: 10.1016/j.ijsolstr.2007.09.022.

Caddemi, S. and Caliò, I. 2009. Exact closed-form solution for the vibration modes of the Euler-Bernoulli beam with multiple open cracks. *Journal of Sound and Vibration* 327(3–5), pp. 473–489. doi: 10.1016/j.jsv.2009.07.008.

Caddemi, S. and Caliò, I. 2013. The exact explicit dynamic stiffness matrix of multi-cracked Euler–Bernoulli beam and applications to damaged frame structures. *Journal of Sound and Vibration* 332(12), pp. 3049–3063.

Caddemi, S. and Caliò, I. 2014. Exact reconstruction of multiple concentrated damages on beams. *Acta Mechanica* 225(11), pp. 3137–3156.

Caddemi, S. and Greco, A. 2006. The influence of instrumental errors on the static identification of damage parameters for elastic beams. *Computers and Structures* 84(26–27), pp. 1696–1708. doi: 10.1016/j.compstruc.2006.03.010.

Caddemi, S. and Morassi, A. 2007. Crack detection in elastic beams by static measurements. *International Journal of Solids and Structures* 44(16), pp. 5301–5315. doi: 10.1016/j.ijsolstr.2006.12.033.

- Cappello, F. and Tumino, D. 2006. Numerical analysis of composite plates with multiple delaminations subjected to uniaxial buckling load. *Composites Science and Technology* 66(2), pp. 264–272.
- Carden, E.P. and Fanning, P. 2004. Vibration based condition monitoring: a review. *Structural health monitoring* 3(4), pp. 355–377. doi: 10.1007/978-94-007-6422-4_11.
- Carrera, E., Fazzolari, F. and Cinefra, M. 2017. *Thermal Stress Analysis of Beams, Plates and Shells*, Elsevier, pp. 91–116.
- Cawley, P. and Adams, R.D. 1979. The location of defects in structures from measurements of natural frequencies. *Journal of Strain Analysis for Engineering Design* 14(2), pp. 49–57. doi: 10.1243/03093247V142049.
- Cerri, M.N. and Vestroni, F. 2000. Detection of damage in beams subjected to diffused cracking. *Journal of Sound and Vibration* 234(2), pp. 259–276. doi: 10.1006/jsvi.1999.2887.
- Cerri, M.N. and Vestroni, F. 2003. Use of frequency change for damage identification in reinforced concrete beams. *Modal Analysis* 9(3–4), pp. 475–491. doi: 10.1177/107754603030787.
- Chang, C.-C. and Chen, L.-W. 2004. Damage detection of a rectangular plate by spatial wavelet based approach. *Applied Acoustics* 65(8), pp. 819–832.
- Chang, F.K. 1998. *Structural Health Monitoring: Current Status and Perspectives*. Western Hemisphere: Technomic Publishing Company.
- Chatzi, E.N., Hiriyyur, B., Waisman, H. and Smyth, A.W. 2011. Experimental application and enhancement of the XFEM-GA algorithm for the detection of flaws in structures. *Computers and Structures* 89(7–8), pp. 556–570.
- Chen, H.-P. and Bicanic, N. 2000. Assessment of damage in continuum structures based on incomplete modal information. *Computers and Structures* 74(5), pp. 559–570.
- Cheung, Y.K. 1968. The finite strip method in the analysis of elastic plates with two opposite simply supported ends. *Proc. Am. Soc. Civ. Eng.*, pp. 1365–1378.
- Cheung, Y.K. 2013. *Finite Strip Method in Structural Analysis*. New York: Pergamon Press.
- Chinchalkar, S. 2001. Determination of crack location in beams using natural frequencies. *Journal of Sound and vibration* 247(3), pp. 417–429.
- Chondros, T.G., Dimarogonas, A.D. and Yao, J. 1998. A continuous cracked beam vibration theory. *Journal of sound and vibration* 215(1), pp. 17–34.
- Christides, S. and Barr, A.D.S. 1984. One-dimensional theory of cracked Bernoulli-Euler beams. *International Journal of Mechanical Sciences* 26(11–12), pp. 639–648. doi: 10.1016/0020-7403(84)90017-1.
- Clough, R.W. 1965. Finite element stiffness matrices for analysis of plate bending. *Proceedings of 1st Conference on Matrix Methods in Structural Mechanics*, pp. 515–546.
- CNBC. 2007. Air Travellers Seen Doubling by 2025. Available at: <https://www.cnn.com/id/16882170> [Accessed: 17 September 2019].

- Colakoglu, M. 2003. Material damping in 6061-T6511 aluminium to assess fatigue damage. *Fatigue and Fracture of Engineering Materials and Structures* 26(1), pp. 79–84.
- Cordes, R.D. and Joseph, P.F. 1994. Crack surface contact of surface and internal cracks in a plate with residual stresses. *International journal of fracture* 66(1), pp. 1–17.
- Cornwell, P., Doebbling, S.W. and Farrar, C.R. 1999. Application of the strain energy damage detection method to plate-like structures. *Journal of Sound and Vibration* 224(2), pp. 359–374. doi: 10.1006/jsvi.1999.2163.
- Cusido, J., Romeral, L., Ortega, J.A., Rosero, J.A. and Espinosa, A.G. 2008. Fault detection in induction machines using power spectral density in wavelet decomposition. *IEEE Transactions on Industrial Electronics* 55(2), pp. 633–643.
- Damghani, M., Kennedy, D. and Featherston, C. 2011. Critical buckling of delaminated composite plates using exact stiffness analysis. *Computers and Structures* 89(13–14), pp. 1286–1294.
- Damghani, M., Kennedy, D. and Featherston, C. 2014. Global buckling of composite plates containing rectangular delaminations using exact stiffness analysis and smearing method. *Computers and Structures* 134, pp.32–47.
- Danai, K., Civjan, S.A. and Styckiewicz, M.M. 2012. Direct method of damage localization for civil structures via shape comparison of dynamic response measurements. *Computers and Structures* 92, pp. 297–307.
- Dawe, D.J. 2002. Use of the finite strip method in predicting the behaviour of composite laminated structures. *Composite Structures* 57(1–4), pp. 11–36. doi: 10.1016/S0263-8223(02)00059-4.
- Delale, F. and Erdogan, F. 1981. Line-spring model for surface cracks in a Reissner plate. *International Journal of Engineering Science* 19(10), pp. 1331–1340.
- Dems, K. and Mróz, Z. 2001. Identification of damage in beam and plate structures using parameter-dependent frequency changes. *Engineering Computations* 18(1/2), pp. 96–120.
- Diaferio, M. and Sepe, V. 2016. Modal identification of damaged frames. *Structural Control and Health Monitoring* 23(1), pp. 82–102.
- Dimarogonas, A.D. 1996. Vibration of cracked structures: A state of the art review. *Engineering Fracture Mechanics* 55(5), pp. 831–857. doi: 10.1016/0013-7944(94)00175-8.
- Ding, W. 2000. Delamination Analysis of Composite Laminates. Canada: Acquisitions and Bibliographic Services.
- Dinh-Cong, D., Vo-Duy, T., Ho-Huu, V., Dang-Trung, H. and Nguyen-Thoi, T. 2017. An efficient multi-stage optimization approach for damage detection in plate structures. *Advances in Engineering Software* 112, pp. 76–87. doi: 10.1016/j.advengsoft.2017.06.015.
- Doebbling, S.W., Farrar, C.R. and Prime, M.B. 1998. A summary review of vibration-based damage identification methods. *Shock and Vibration Digest* 30(2), pp. 91–105. doi: 10.1177/058310249803000201.

- Escobar, J.A., Jesús Sosa, J. and Gómez, R. 2005. Structural damage detection using the transformation matrix. *Computers and Structures* 83(4–5), pp. 357–368. doi: 10.1016/j.compstruc.2004.08.013.
- Fan, W. and Qiao, P. 2011. Vibration-based damage identification methods: a review and comparative study. *Structural health monitoring* 10(1), pp. 83–111.
- Fang, X., Luo, H. and Tang, J. 2005. Structural damage detection using neural network with learning rate improvement. *Computers and Structures* 83(25–26), pp. 2150–2161. doi: 10.1016/j.compstruc.2005.02.029.
- Fazzolari, F.A., Boscolo, M. and Banerjee, J.R. 2013. An exact dynamic stiffness element using a higher order shear deformation theory for free vibration analysis of composite plate assemblies. *Composite Structures* 96, pp. 262–278.
- Fischer, M., Kennedy, D. and Featherston, C.A. 2002. Multilevel optimization of a composite aircraft wing using VICONOPT MLO. *Proceedings of 9th AIAA/ISSMO Symposium on Multidisciplinary Analysis and Optimization*. Reston, Virginia: American Institute of Aeronautics and Astronautics.
- Freund, L.B. and Herrmann, G. 2010. Dynamic fracture of a beam or plate in plane bending. *Journal of Applied Mechanics* 43(1), p. 112. doi: 10.1115/1.3423760.
- Friswell, M.I., Penny, J.E.T. and Garvey, S.D. 1998. A combined genetic and eigensensitivity algorithm for the location of damage in structures. *Computers and Structures* 69(5), pp. 547–556.
- Friswell, M.I. 2007. Damage identification using inverse methods. *Philosophical Transactions of the Royal Society A: Mathematical, Physical and Engineering Sciences* 365(1851), pp. 393–410.
- Fujimoto, T., Wakata, K., Cao, F.Y. and Nisitani, H. 2003. Vibration analysis of a cracked plate subjected to tension using a hybrid method of FEM and BFM. In: *Materials Science Forum*. (ed. M.P.Cartmell) Trans Tech Publications, pp. 407–414.
- Ge, M. and Lui, E.M. 2005. Structural damage identification using system dynamic properties. *Computers and Structures* 83(27), pp. 2185–2196. doi: 10.1016/j.compstruc.2005.05.002.
- Gong, W., Chen, J. and Patterson, E.A. 2016. Buckling and delamination growth behaviour of delaminated composite panels subject to four-point bending. *Composite Structures* 138, pp. 122–133.
- Goodfellow, I., Bengio, Y. and Courville, A. 2016. *Deep Learning*. MIT Press, Cambridge, Massachusetts.
- Gounaris, G. and Dimarogonas, A. 1988. A finite element of a cracked prismatic beam for structural analysis. *Computers and Structures* 28(3), pp. 309–313. doi: 10.1016/0045-7949(88)90070-3.
- Greco, A. and Pau, A. 2012. Damage identification in Euler frames. *Computers and Structures* 92, pp. 328–336.
- Guo, S.J., Keane, A.J. and Moshrefi-Torbati, M. 1997. Vibration analysis of stepped thickness plates. *Journal of Sound and Vibration* 204(4), pp. 645–657.

Gupta, A., Jain, N.K., Salhotra, R. and Joshi, P.V. 2015. Effect of microstructure on vibration characteristics of partially cracked rectangular plates based on a modified couple stress theory. *International Journal of Mechanical Sciences* 100, pp. 269–282.

Gupta, K.K. 1969. Free vibrations of single-branch structural systems. *IMA Journal of Applied Mathematics* 5(3), pp. 351–362.

Gupta, K.K. 1973. Solution of quadratic matrix equations for free vibration analysis of structures. *International Journal for Numerical Methods in Engineering* 6(1), pp. 129–135. doi: 10.1002/nme.1620060113.

Gupta, K.K. 1976. On a finite dynamic element method for free vibration analysis of structures. *Computer Methods in Applied Mechanics and Engineering* 9(1), pp. 105–120.

Hadjileontiadis, L.J. and Douka, E. 2007. Crack detection in plates using fractal dimension. *Engineering Structures* 29(7), pp. 1612–1625. doi: 10.1016/j.engstruct.2006.09.016.

Harris, C.E., Newman, J.C., Piascik, R.S. and Starnes, J.H. 1998. Analytical methodology for predicting widespread fatigue damage onset in fuselage structure. *Journal of Aircraft* 35(2), pp. 307–317.

Harris, J.C. 2001. *Final Report of the Garter Action Group on Structural Optimisation SM(AG13)*. Hampshire. Available at: http://www.garteur.org/Technical%20Reports/SM_AG-13_TP-078.pdf [Accessed at 10 July 2019]

Hassiotis, S. and Jeong, G.D. 1995. Identification of stiffness reductions using natural frequencies. *Journal of Engineering Mechanics* 121(10), pp. 1106–1113.

Hearn, G. and Testa, R.B. 1991. Modal analysis for damage detection in structures. *Journal of Structural Engineering* 117(10), pp. 3042–3063.

Hirano, Y. and Okazaki, K. 1980. Vibration of Cracked Rectangular Plates. *Bulletin of the Japan Society of Mechanical Engineers* 23(179), pp. 732–740.

Hooton, R.D. 2016. *Types of Cracking and Influencing Causes*. Available at: <http://onlinepubs.trb.org/Onlinepubs/webinars/160525.pdf>.

Hopper, C.T. and Williams, F.W. 1977. Mode finding in nonlinear structural eigenvalue calculations. *Journal of Structural Mechanics* 5(3), pp. 255–278. doi: 10.1080/03601217708907314.

Horibe, T. and Watanabe, K. 2011. Crack identification in plates using genetic algorithm. *Transactions of the Japan Society of Mechanical Engineers Series A* 71(710), pp. 1312–1319. doi: 10.1299/kikaia.71.1312.

Hosseini-Hashemi, S., Fadaee, M. and Atashipour, S.R. 2011. A new exact analytical approach for free vibration of Reissner–Mindlin functionally graded rectangular plates. *International Journal of Mechanical Sciences* 53(1), pp. 11–22.

HSL 2001. *Report on the air accident 8 September 1997 in the Norwegian sea approx. 100 NM west north west of Brønnøysund, involving Eurocopter AS 332L1 Super Puma, LN-OPG, operated by Helikopter Service AS*. Available at: <https://www.aibn.no/Aviation/Reports/2001-47-eng> [Accessed: 4 June 2019].

- Hu, H., Wang, B.-T., Lee, C.-H. and Su, J.-S. 2006. Damage detection of surface cracks in composite laminates using modal analysis and strain energy method. *Composite structures* 74(4), pp. 399–405.
- Hu, X.T., Qin, Z.Y. and Chu, F.L. 2011. Damage detection in plate structures based on space-time autoregressive moving average processes. *Journal of Physics: Conference Series* 305(1). doi: 10.1088/1742-6596/305/1/012119.
- Huang, C.S., Leissa, A.W. and Li, R.S. 2011. Accurate vibration analysis of thick, cracked rectangular plates. *Journal of Sound and Vibration* 330(9), pp. 2079–2093. doi: 10.1016/j.jsv.2010.11.007.
- Huang, C.S. and Leissa, A.W. 2009. Vibration analysis of rectangular plates with side cracks via the Ritz method. *Journal of Sound and Vibration* 323(3–5), pp. 974–988. doi: 10.1016/j.jsv.2009.01.018.
- Ip, K.-H. and Tse, P.-C. 2002. Locating damage in circular cylindrical composite shells based on frequency sensitivities and mode shapes. *European Journal of Mechanics-A/Solids* 21(4), pp. 615–628.
- Irwin, G.R. 1962. Crack-extension force for a part-through crack in a plate. *Journal of Applied Mechanics* 29(4), pp. 651–654.
- Ismail, R., 2013. Vibration analysis of a plate with an arbitrarily orientated surface crack. Available at: <http://theses.gla.ac.uk/>.
- Ismail, R. and Cartmell, M.P. 2012. An investigation into the vibration analysis of a plate with a surface crack of variable angular orientation. *Journal of Sound and Vibration* 331(12), pp. 2929–2948. Available at: <http://dx.doi.org/10.1016/j.jsv.2012.02.011>.
- Israr, A. 2008. *Vibration Analysis of Cracked Aluminium Plates*. Available at: <http://theses.gla.ac.uk/261/>.
- Israr, A., Cartmell, M.P., Manoach, E., Trendafilova, I., Ostachowicz, W., Krawczuk, M. and Žak, A. 2009. Analytical modeling and vibration analysis of partially cracked rectangular plates with different boundary conditions and loading. *Journal of Applied Mechanics* 76(1), p. 11005. doi: 10.1115/1.2998755.
- Jiang, Y.Y., Xiang, J.W. and Li, B. 2017. A hybrid multiple damages detection method for plate structures. *Science China Technological Sciences* 60(5), pp. 726–736. doi: 10.1007/s11431-016-9002-0.
- Joseph, P.F. and Erdogan, F. 1991. Surface crack in a plate under antisymmetric loading conditions. *International Journal of Solids and Structures* 27(6), pp. 725–750.
- Joshi, P.V., Jain, N.K. and Ramtekkar, G.D. 2014. Analytical modeling and vibration analysis of internally cracked rectangular plates. *Journal of Sound and Vibration* 333(22), pp. 5851–5864. Available at: <http://dx.doi.org/10.1016/j.jsv.2014.06.028>.
- Kam, T.Y. and Lee, T.Y. 1992. Detection of cracks in structures using modal test data. *Engineering Fracture Mechanics* 42(2), pp. 381–387. doi: 10.1016/0013-7944(92)90227-6.
- Kang, F., Li, J. and Xu, Q. 2009. Structural inverse analysis by hybrid simplex artificial bee colony algorithms. *Computers and Structures* 87(13–14), pp. 861–870. Available at: <http://dx.doi.org/10.1016/j.compstruc.2009.03.001>.

- Karihaloo, B.L. and Stang, H. 2008. Buckling-driven delamination growth in composite laminates: Guidelines for assessing the threat posed by interlaminar matrix delamination. *Composites Part B: Engineering* 39(2), pp. 386–395.
- Kawiecki, G. 2001. Modal damping measurement for damage detection. *Structural Health Monitoring* 10(3), pp. 466–471.
- Keer, L.M. and Sve, C. 1970. On the bending of cracked plates. *International Journal of Solids and Structures* 6(12), pp. 1545–1559.
- Kennedy, D., Ong, T.J., O’Leary, O.J. and Williams, F.W. 1999. Practical optimisation of aerospace panels. *Proceedings of the 1st ASMO UK/ISSMO Conference*, pp. 217–224.
- Kennedy, D., Fischer, M. and Featherston, C.A. 2007. Recent developments in exact strip analysis and optimum design of aerospace structures. *Proceedings of the Institution of Mechanical Engineers, Part C: Journal of Mechanical Engineering Science* 221(4), pp. 399–413. doi: 10.1243/0954406JMES432.
- Kennedy, D. and Featherston, C.A. 2010. Exact strip analysis and optimum design of aerospace structures. *Aeronautical Journal* 114(1158), pp. 505–512. doi: 10.1017/S0001924000003997.
- Khadem, S.E. and Rezaee, M. 2000. Introduction of modified comparison functions for vibration analysis of a rectangular cracked plate. *Journal of Sound and Vibration* 236(2), pp. 245–258. doi: 10.1006/jsvi.2000.2986.
- Khatir, S. and Wahab, M.A. 2019. Fast simulations for solving fracture mechanics inverse problems using POD-RBF XIGA and Jaya algorithm. *Engineering Fracture Mechanics* 205, pp. 285–300.
- Khiem, N.T. and Lien, T. V 2001. A simplified method for natural frequency analysis of a multiple cracked beam. *Journal of Sound and Vibration* 245(4), pp. 737–751.
- Kim, J.-T., Ryu, Y.-S., Cho, H.-M. and Stubbs, N. 2003. Damage identification in beam-type structures: frequency-based method vs mode-shape-based method. *Engineering Structures* 25(1), pp. 57–67. doi: 10.1016/S0141-0296(02)00118-9.
- King, R.B. 1983. Elastic-plastic analysis of surface flaws using a simplified line-spring model. *Engineering Fracture Mechanics* 18(1), pp. 217–231.
- Krawczuk, M. 1993. Natural vibrations of rectangular plates with a through crack. *Archive of Applied Mechanics* 63(7), pp. 491–504.
- Krawczuk, M., Żak, A. and Ostachowicz, W. 2001. Finite element model of plate with elasto-plastic through crack. *Computers and Structures* 79(5), pp. 519–532.
- Krawczuk, M., Palacz, M. and Ostachowicz, W. 2004. Wave propagation in plate structures for crack detection. *Finite Elements in Analysis and Design* 40(9–10), pp. 991–1004. doi: 10.1016/j.
- Krawczuk, M. and Ostachowicz, W.M. 1994. A finite plate element for dynamic analysis of a cracked plate. *Computer Methods in Applied Mechanics and Engineering* 115(1–2), pp. 67–78.

- Labib, A., Kennedy, D. and Featherston, C. 2014. Free vibration analysis of beams and frames with multiple cracks for damage detection. *Journal of Sound and Vibration* 333(20), pp. 4991–5003.
- Labib, A., Kennedy, D. and Featherston, C.A. 2015. Crack localisation in frames using natural frequency degradations. *Computers and Structures* 157, pp. 51–59.
- Lee, H.P. 1992. Fundamental frequencies of annular plates with internal cracks. *Computers and structures* 43(6), pp. 1085–1089.
- Lee, H.P. and Lim, S.P. 1992. Free vibration of isotropic and orthotropic rectangular plates with partially clamped edges. *Applied Acoustics* 35(2), pp. 91–104.
- Lee, J. 2009. Identification of multiple cracks in a beam using natural frequencies. *Journal of Sound and Vibration* 320(3), pp. 482–490.
- Lee, S.Y. and Park, D.Y. 2007. Buckling analysis of laminated composite plates containing delaminations using the enhanced assumed strain solid element. *International Journal of Solids and Structures* 44(24), pp. 8006–8027. doi: 10.1016/j.ijsolstr.2007.05.023.
- Lee, U., Cho, K. and Shin, J. 2003. Identification of orthotropic damages within a thin uniform plate. *International Journal of Solids and Structures* 40(9), pp. 2195–2213.
- Lee, U. and Shin, J. 2002. A structural damage identification method for plate structures. *Engineering Structures* 24(9), pp. 1177–1188.
- Lee, Y.-S. and Chung, M.-J. 2000. A study on crack detection using eigenfrequency test data. *Computers and Structures* 77(3), pp. 327–342.
- Leissa, A.W. 1969. *Vibration of Plates* (Vol. 160). Scientific and Technical Information Division, National Aeronautics and Space Administration: Washington DC.
- Li, L., Jiao, J., Lv, H., He, C. and Wu, B. 2019. Defect characterization in plate structures using Bayesian approach. *AIP Conference Proceedings*. AIP Publishing, p. 90007.
- Li, Y.Y., Cheng, L., Yam, L.H. and Wong, W.O. 2002. Identification of damage locations for plate-like structures using damage sensitive indices: strain modal approach. *Computers and Structures* 80(25), pp. 1881–1894.
- Liang, R.Y., Choy, F.K. and Hu, J. 1991. Detection of cracks in beam structures using measurements of natural frequencies. *Journal of the Franklin Institute* 328(4), pp. 505–518.
- Liang, R.Y., Hu, J. and Choy, F. 1992. Theoretical study of crack-induced eigenfrequency changes on beam structures. *Journal of Engineering Mechanics* 118(2), pp. 384–396.
- Liew, K.M., Hung, K.C. and Lim, M.K. 1994. A solution method for analysis of cracked plates under vibration. *Engineering Fracture Mechanics* 48, pp. 393–404.
- Lin, H.P., Chang, S.C. and Wu, J.D. 2002. Beam vibrations with an arbitrary number of cracks. *Journal of Sound and Vibration* 258(5), pp. 987–999.
- Liu, P.F., Hou, S.J., Chu, J.K., Hu, X.Y., Zhou, C.L. Liu, Y.L., Zheng, J.Y., Zhao, A. and Yan, L. 2011. Finite element analysis of postbuckling and delamination of composite laminates using virtual crack closure technique. *Composite Structures* 93(6), pp. 1549–1560.

Loendersloot, R., Ooijevaar, T.H., Warnet, L., de Boer, A. and Akkerman, R. 2010. Vibration based structural health monitoring of a composite plate with stiffeners. *Proceedings of 24th International Conference on Noise and Vibration Engineering*, pp. 909–924.

Love, A.E.H. 1888. XVI. The small free vibrations and deformation of a thin elastic shell. *Philosophical Transactions of the Royal Society of London (179)*, pp. 491–546.

Lu, Y., Ye, L. Su, Z., Zhou, L. and Cheng, L. 2009. Artificial neural network (ANN)-based crack identification in aluminum plates with Lamb wave signals. *Journal of Intelligent Material Systems and Structures* 20(1), pp. 39–49.

Luo, Y. 2015. *Modelling and Detection of Delamination in Composite Plate Structures*. MSc Dissertation, Cardiff University.

Luo, Y., Kennedy, D. and Featherston, C.A. 2019. Natural frequency degradations in cracked plates. *Proceedings of 12th International Symposium on Vibrations of Continuous Systems*, Corvara in Badia, Italy, pp. 67–69.

Lynn, P.P. and Kumbasar, N. 1967. Free vibration of thin rectangular plates having narrow cracks with simply supported edges. *Development in Mechanics* 4, pp. 911–928.

Maghsoodi, A., Ghadami, A. and Mirdamadi, H.R. 2013. Multiple-crack damage detection in multi-step beams by a novel local flexibility-based damage index. *Journal of Sound and Vibration* 332(2), pp. 294–305.

Maia, N.M.M., Silva, J.M.M., Almas, E.A.M. and Sampaio, R.P.C. 2003. Damage detection in structures: from mode shape to frequency response function methods. *Mechanical Systems and Signal Processing* 17(3), pp. 489–498.

Marcos. 2013. Cutaways. EDForums. Available at: <https://forums.eagle.ru/showthread.php?t=98895> [Accessed: 18 September 2019].

Maruyama, K. and Ichinomiya, O. 1989. Experimental study of free vibration of clamped rectangular plates with straight narrow slits. *JSME International Journal. Series 3, Vibration, Control Engineering, Engineering for Industry* 32(2), pp. 187–193.

MATLAB.1984. Programming Fundamentals, R2019b. Available at: www.mathworks.com [Accessed: 27 September 2019].

McCulloch, W.S. and Pitts, W. 1943. A logical calculus of the ideas immanent in nervous activity. *The Bulletin of Mathematical Biophysics* 5(4), pp. 115–133.

Miyazaki, N. 1989. An application of a line-spring model to a transient analysis of the dynamic stress intensity factor. *International Journal of Fracture* 39(4), pp. R77–R80.

Moazzez, K., Saeidi Googarchin, H. and Sharifi, S.M.H. 2018. Natural frequency analysis of a cylindrical shell containing a variably oriented surface crack utilizing Line-Spring model. *Thin-Walled Structures* 125, pp. 63–75. doi: 10.1016/j.tws.2018.01.009.

Mohan, S.C., Maiti, D.K. and Maity, D. 2013. Structural damage assessment using FRF employing particle swarm optimization. *Applied Mathematics and Computation* 219(20), pp. 10387–10400.

Moore, E.Z., Murphy, K.D. and Nichols, J.M. 2011. Crack identification in a freely vibrating plate using Bayesian parameter estimation. *Mechanical Systems and Signal Processing* 25(6), pp. 2125–2134.

Morassi, A. 1993. Crack-induced changes in eigenparameters of beam structures. *Journal of Engineering Mechanics* 119(9), pp. 1798–1803.

Morassi, A. and Vestroni, F. 2008. *Dynamic Methods for Damage Detection in Structures*. Springer Science and Business Media. doi: 10.1007/978-3-211-78777-9.

Morassi, A. and Rovere, N. 1997. Localizing a notch in a steel frame from frequency measurements. *Journal of Engineering Mechanics* 123(5), pp. 422–432.

Nandwana, B.P. 1997. *On foundation for detection of crack based on measurement of natural frequencies*. PhD Thesis, Indian Institute of Technology, Bombay.

National Transportation Safety Board. 2001. In-Flight Separation of Vertical Stabilizer American Airlines Flight 587. Available at: <https://www.skybrary.aero/bookshelf/books/523.pdf>.

Nikolakopoulos, P.G., Katsareas, D.E. and Papadopoulos, C.A. 1997. Crack identification in frame structures. *Computers and Structures*, 64(1-4), pp.389–406. doi:10.1016/s0045-7949(96)00120-4 64(1–4).

Nikrad, S.F., Keyoursangari, S., Asadi, H., Akbarzadeh, A.H. and Chen, Z.T. 2016. Computational study on compressive instability of composite plates with off-center delaminations. *Computer Methods in Applied Mechanics and Engineering* 310, pp. 429–459.

Noor, A.K., Shuart, M.J., Starnes, J.H. Jr. and Williams, J.G. 1983. *Failure Analysis and Mechanisms of Failure of Fibrous Composite Structures*. United States: NASA.

O'Brien, T.K. 1991. Chapter 5 - Delamination of Composite Materials. *Fatigue of Composite Materials* (ed. K.L. Reifsnider). Elsevier, pp.181–198.

Okamura, H., Liu, H.W., Chu, C.-S. and Liebowitz, H. 1969. A cracked column under compression. *Engineering Fracture Mechanics* 1(3), pp. 547–564.

Ostachowicz, W.M. and Krawczuk, M. 1991. Analysis of the effect of cracks on the natural frequencies of a cantilever beam. *Journal of Sound and Vibration* 150(2), pp. 191–201. doi: 10.1016/0022-460X(91)90615-Q.

Paget, C.A., Grondel, S., Levin, K. and Delebarre, C. 2003. Damage assessment in composites by Lamb waves and wavelet coefficients. *Smart Materials and Structures* 12(3), p. 393.

Pan, J., Zhang, Z., Wu, J., Ramakrishnan, K.R. and Singh, H.K. 2019. A novel method of vibration modes selection for improving accuracy of frequency-based damage detection. *Composites Part B: Engineering* 159, pp. 437–446.

Pandey, A.K., Biswas, M. and Samman, M.M. 1991. Damage detection from mode changes in curvature. *Journal of Sound and Vibration* 145(2), pp. 321–332.

Papadopoulos, C.A. and Dimarogonas, A.D. 1987. Coupling of bending and torsional vibration of a cracked Timoshenko shaft. *Ingenieur-Archiv* 57(4), pp. 257–266.

- Pérez, M.A. and Serra-López, R. 2019. A frequency domain-based correlation approach for structural assessment and damage identification. *Mechanical Systems and Signal Processing* 119, pp. 432–456. doi: 10.1016/j.ymssp.2018.09.042.
- Pipes, R.B. and Pagano, N.J. 1970. Interlaminar stresses in composite laminates under uniform axial extension. *Journal of Composite Materials* 4(4), pp. 538–548.
- Potyondy, D.O., Wawrzynek, P.A. and Ingraffea, A.R. 1995. Discrete crack growth analysis methodology for through cracks in pressurized fuselage structures. *International Journal for Numerical Methods in Engineering* 38(10), pp. 1611–1633.
- Przemieniecki, J.S. 1985. *Theory of Matrix Structural Analysis*. Courier Corporation.
- Qian, G.-L., Gu, S.-N. and Jiang, J.-S. 1991. A finite element model of cracked plates and application to vibration problems. *Computers and Structures* 39(5), pp. 483–487.
- Ratcliffe, C.P. 2000. A frequency and curvature based experimental method for locating damage in structures. *Journal of Vibration and Acoustics* 122(3), pp. 324–329.
- Reddy, J.N. 1999. *Theory and Analysis of Elastic Plates and Shells*. CRC press: Taylor and Francis.
- Reed, R.P. 1983. *The Economic Effects of Fracture in the United States*. US Department of Commerce, U.S: National Bureau of Standards.
- Rice, J.R. and Levy, N. 1972. The part-through surface crack in an elastic plate. *Journal of Applied Mechanics* 39(1), pp. 185–194.
- Rizos, P.F., Aspragathos, N. and Dimarogonas, A.D. 1990. Identification of crack location and magnitude in a cantilever beam from the vibration modes. *Journal of Sound and Vibration* 138(3), pp. 381–388. doi: 10.1016/0022-460X(90)90593-O.
- Rovik, C.L. 1998. *Classification of In-Flight Fatigue Cracks in Aircraft Structures using Acoustic Emission and Neural Networks*. PhD Thesis, Embry Riddle Aeronautical University.
- Roylance, D. 2001. *Introduction to Fracture Mechanics*. Massachusetts Institute of Technology, Cambridge.
- Rucka, M. and Wilde, K. 2006. Application of continuous wavelet transform in vibration based damage detection method for beams and plates. *Journal of Sound and Vibration* 297(3–5), pp. 536–550.
- Rytter, A. 1993. *Vibrational Based Inspection of Civil Engineering Structures*. Dept. of Building Technology and Structural Engineering, Aalborg University.
- Saito, A., Castanier, M.P. and Pierre, C. 2009. Estimation and veering analysis of nonlinear resonant frequencies of cracked plates. *Journal of Sound and Vibration* 326(3–5), pp. 725–739.
- Salawu, O.S. 1997. Detection of structural damage through changes in frequency: a review. *Engineering structures* 19(9), pp. 718–723.
- Sampaio, R.P.C., Maia, N.M.M. and Silva, J.M.M. 1999. Damage detection using the frequency-response-function curvature method. *Journal of Sound and Vibration* 226(5), pp. 1029–1042.

- Shams, S.S. and Elhajjar, R.F. 2013. Repair: Adhesive repair for surface gouges and cracks in continuous carbon fiber/epoxy laminated composites. In: *Joining Composites with Adhesives: Theory and Applications* (ed. M.A. Wahab). DEStech Publications, Inc, pp. 173. doi: 10.13140/RG.2.1.1493.3845.
- Sharma, D.S., Mungla, M.J. and Barad, K.H. 2015. Vibration-based non-destructive technique to detect crack in multi-span beam. *Nondestructive Testing and Evaluation* 30(4), pp. 291–311. doi: 10.1080/10589759.2015.1029475.
- Shen, M.-H. and Pierre, C. 1990. Natural modes of Bernoulli-Euler beams with symmetric cracks. *Journal of Sound and Vibration* 138(1), pp. 115–134.
- Shifrin, E.I. and Ruotolo, R. 1999. Natural frequencies of a beam with an arbitrary number of cracks. *Journal of Sound and Vibration* 222(3), pp. 409–423.
- Singh, D., Castaings, M. and Bacon, C. 2011. Sizing strip-like defects in plates using guided waves. *NDT and E International* 44(5), pp. 394–404.
- Sinha, J.K., Friswell, M.I. and Edwards, S. 2002. Simplified models for the location of cracks in beam structures using measured vibration data. *Journal of Sound and Vibration* 251(1), pp. 13–38.
- Smith, C.S. 1968. Bending, buckling and vibration of orthotropic plate-beam structures. *Journal of Ship Research*, 12(4), pp.249-268.
- Smith, R.A. 2009. Composite defects and their detection. *Materials Science and Engineering* 3, pp. 103–143.
- Solecki, R. 1980. Bending vibration of simply supported rectangular plates with internal rigid support. *International Journal of Engineering Science* 18(11), pp. 1309–1318.
- Solecki, R. 1983. Bending vibration of a simply supported rectangular plate with a crack parallel to one edge. *Engineering Fracture Mechanics* 18(6), pp. 1111–1118. doi: 10.1016/0013-7944(83)90004-8.
- Solecki, R. 1985. Bending vibration of a rectangular plate with arbitrarily located rectilinear crack. *Engineering Fracture Mechanics* 22(4), pp. 687–695. doi: 10.1016/0013-7944(85)90132-8.
- Solís, M., Algaba, M. and Galvín, P. 2013. Continuous wavelet analysis of mode shapes differences for damage detection. *Mechanical Systems and Signal Processing* 40(2), pp. 645–666. Available at: <http://dx.doi.org/10.1016/j.ymsp.2013.06.006>.
- Stahl, B. and Keer, L.M. 1972. Vibration and stability of cracked rectangular plates. *International Journal of Solids and Structures* 8(1), pp. 69–91. doi: 10.1016/0020-7683(72)90052-2.
- Stephens, J.E. and VanLuchene, R.D. 1994. Integrated assessment of seismic damage in structures. *Computer-Aided Civil and Infrastructure Engineering* 9(2), pp. 119–128.
- Stroud, W.J. and Anderson, M.S. 1980. PASCO: structural panel analysis and sizing code, capability and analytical foundations. United States: NASA Langley Research Center.
- Stubbs, N., Kim, J.T. and Topole, K.G. 1992. An efficient and robust algorithm for damage localization in offshore platforms. *Proceedings of the ASCE 10th Structures Congress*, pp. 543–546.

- Suliman, B.S. 2018. A Hybrid Exact Strip and Finite Element Method for Modelling Damage in Composite Plates. PhD thesis, Cardiff University.
- Taghvaei, M., Beck, S.B.M. and Staszewski, W.J. 2006. Leak detection in pipelines using cepstrum analysis. *Measurement Science and Technology* 17(2), pp. 367–372. doi: 10.1088/0957-0233/17/2/018.
- Teughels, A., Maeck, J. and de Roeck, G. 2002. Damage assessment by FE model updating using damage functions. *Computers and Structures* 80(25), pp. 1869–1879.
- Timoshenko, S.P. and Woinowsky-Krieger, S. 1959. *Theory of Plates and Shells*. McGraw-Hill.
- Trendafilova, I. 2006a. A study on vibration-based damage detection and location in an aircraft wing scaled model. *Applied Mechanics and Materials* 3–4, pp. 309–314.
- Trendafilova, I. 2006b. Vibration-based damage detection in structures using time series analysis. *Proceedings of the Institution of Mechanical Engineers, Part C: Journal of Mechanical Engineering Science* 220(3), pp. 261–272. doi: 10.1243/09544062C12904.
- Trendafilova, I. 2009. An investigation on vibration-based damage detection in an aircraft wing scaled model. *Key Engineering Materials* 293–294(4), pp. 321–328.
- Trendafilova, I. and Manoach, E. 2008. Vibration-based damage detection in plates by using time series analysis. *Mechanical Systems and Signal Processing* 22(5), pp. 1092–1106. doi: 10.1016/j.ymssp.2007.11.020.
- Tsou, P. and Shen, M.-H. 1994. Structural damage detection and identification using neural networks. *AIAA journal* 32(1), pp. 176–183.
- TSPNDT 2014. A Brief History of Non-Destructive Testing. Available at: <http://tspndt.com/non-destructive-testing-industrial-supplies-blog/a-brief-history-of-non-destructive-testing> [Accessed: 21 May 2019].
- Vanderplaats, G.N. and Moses, F. 1973. Structural optimization by methods of feasible directions. *Computers and Structures* 3(4), pp. 739–755. doi: 10.1016/0045-7949(73)90055-2.
- Verboven, P., Parloo, E., Guillaume, P. and van Overmeire, M. 2002. Autonomous structural health monitoring—part I: modal parameter estimation and tracking. *Mechanical Systems and Signal Processing* 16(4), pp. 637–657.
- Vestroni, F. and Capecchi, D. 2000. Damage detection in beam structures based on frequency measurements. *Journal of Engineering Mechanics* 126(7), pp. 761–768.
- Vinson, J.R. and Chou, T.-W. 1975. *Composite Materials and their Use in Structures*. United States: Halsted Press.
- Viswanathan, A.V., Tamekuni, M. and Tripp, L.L., 1973. Elastic stability of biaxially loaded longitudinally stiffened composite structures. *AIAA Journal*, 11(11), pp.1553-1559.
- Wang, L. and Chan, T.H.T. 2009. Review of vibration-based damage detection and condition assessment of bridge structures using structural health monitoring. *Proceedings of 2nd Infrastructure Theme Postgraduate Conference: Rethinking Sustainable Development: Planning, Engineering, Design and Managing Urban*

Infrastructure. QUT Conference Proceedings. Available at: <http://eprints.qut.edu.au/26738/>.

Wang, Z. and Ong, K.C.G. 2008. Autoregressive coefficients based Hotelling's T2 control chart for structural health monitoring. *Computers and Structures* 86(19–20), pp. 1918–1935. doi: 10.1016/j.compstruc.2008.02.007.

Werfelman, L. 2011. Crackdown on fatigue. *AeroSafety World* 6, pp. 37–41.

Williams, E.J., Messina, A. and Payne, B.S. 1997. A frequency-change correlation approach to damage detection. *Proceedings of SPIE - the International Society for Optical Engineering* 3089(1), pp. 652–657.

Williams, F.W. 1972. Computation of natural frequencies and initial buckling stresses of prismatic plate assemblies. *Journal of Sound and Vibration* 21(1), pp. 87–106. doi: 10.1016/0022-460X(72)90208-8.

Williams, F.W., Kennedy, D. and Anderson, M.S. 1990. Analysis features of VICONOPT, an exact buckling and vibration program for prismatic assemblies of anisotropic plates. *Proceedings of 31st AIAA/ASME/ASCE/AHS/ASC Structures, Structural Dynamics and Materials Conference*, pp. 970.

Williams, F.W., Kennedy, D., Anderson, M.S. and Butler, R. 1991. VICONOPT-Program for exact vibration and buckling analysis or design of prismatic plate assemblies. *AIAA Journal* 29(11), pp. 1927–1928. doi: 10.2514/3.10820.

Williams, F.W. and Anderson, M.S. 1983. Incorporation of Lagrangian Multipliers into an algorithm for finding exact natural frequencies or critical buckling loads. *International Journal of Mechanical Sciences* 25(8), pp. 579–584. doi: 10.1016/0020-7403(83)90049-8.

Williams, F.W. and Anderson, M.S. 1985. Buckling and ND vibration analysis of shear-loaded prismatic plate assemblies with supporting structures, utilizing symmetric or repetitive cross-sections. In: *Aspects of the Analysis of Plate Structures* (ed. D.J. Dawe, R.W. Horsington, A.G. Kamtekar and G.H. Little). Clarendon, Oxford, pp. 51–71.

Williams, F.W. and Kennedy, D. 1988. Reliable use of determinants to solve non-linear structural eigenvalue problems efficiently. *International Journal for Numerical Methods in Engineering* 26(8), pp. 1825–1841.

Williams, F.W. and Wittrick, W.H. 1969. Computational procedures for a matrix analysis of the stability and vibration of thin flat-walled structures in compression. *International Journal of Mechanical Sciences* 11(12), pp. 979–998.

Williams, F.W. and Wittrick, W.H. 1970. An automatic computational procedure for calculating natural frequencies of skeletal structures. *International Journal of Mechanical Sciences* 12(9), pp. 781–791.

Wittrick, W. and Williams, F.W. 1971. A general algorithm for computing natural frequencies of elastic structures. *The Quarterly Journal of Mechanics and Applied Mathematics* 24(3), pp. 263–284.

Wittrick, W.H. 1968a. A unified approach to the initial buckling of stiffened panels in compression. *The Aeronautical Quarterly* 19(3), pp. 265–283.

Wittrick, W.H. 1968b. General sinusoidal stiffness matrices for buckling and vibration analyses of thin flat-walled structures. *International Journal of Mechanical Sciences* 10(12), pp. 949–966. doi: 10.1016/0020-7403(68)90049-0.

Wittrick, W.H. and Curzon, P.L. V 1968. Stability functions for the local buckling of thin flat-walled structures with the walls in combined shear and compression. *The Aeronautical Quarterly* 19(4), pp. 327–351.

Wittrick, W.H. and Horsington, R.W. 1984. Buckling and vibration of composite folded-plate structures of finite length in combined shear and compression. *Proceedings of the Royal Society of London. A. Mathematical and Physical Sciences* 392(1802), pp. 107–144. doi: 10.1098/rspa.1984.0026.

Wittrick, W.H. and Williams, F.W. 1973. An algorithm for computing critical buckling loads of elastic structures. *Journal of Structural Mechanics* 1(4), pp. 497–518. doi: 10.1080/03601217308905354.

Wittrick, W.H. and Williams, F.W. 1974. Buckling and vibration of anisotropic or isotropic plate assemblies under combined loadings. *International Journal of Mechanical Sciences* 16(4), pp. 209–239. doi: 10.1016/0020-7403(74)90069-1.

Wu, D. and Law, S.S. 2004a. Anisotropic damage model for an inclined crack in thick plate and sensitivity study for its detection. *International journal of solids and structures* 41(16–17), pp. 4321–4336.

Wu, D. and Law, S.S. 2004b. Damage-detection-oriented model for a cracked rectangular plate. *Smart Structures and Materials 2004: Sensors and Smart Structures Technologies for Civil, Mechanical, and Aerospace Systems* 5391, p. 470. doi: 10.1117/12.540902.

Wu, D. and Law, S.S. 2004c. Damage localization in plate structures from uniform load surface curvature. *Journal of Sound and Vibration* 276(1–2), pp. 227–244.

Wu, G.-Y. and Shih, Y.-S. 2005. Dynamic instability of rectangular plate with an edge crack. *Computers and structures* 84(1–2), pp. 1–10.

Xiang, J. and Liang, M. 2012. A two-step approach to multi-damage detection for plate structures. *Engineering Fracture Mechanics* 91, pp. 73–86.

Xiao, Y.-G., Fu, Y.-M. and Zha, X.-D. 2008. Bifurcation and chaos of rectangular moderately thick cracked plates on an elastic foundation subjected to periodic load. *Chaos, Solitons and Fractals* 35(3), pp. 460–465.

Yam, L.H., Li, Y.Y. and Wong, W.O. 2002. Sensitivity studies of parameters for damage detection of plate-like structures using static and dynamic approaches. *Engineering Structures* 24(11), pp. 1465–1475.

Yan, Y.J., Cheng, L., Wu, Z.Y. and Yam, L.H. 2007. Development in vibration-based structural damage detection technique. *Mechanical systems and signal processing* 21(5), pp. 2198–2211.

Yan, Y.J. and Yam, L.H. 2002. Online detection of crack damage in composite plates using embedded piezoelectric actuators/sensors and wavelet analysis. *Composite Structures* 58(1), pp. 29–38. doi: 10.1016/S0263-8223(02)00043-0.

- Yang, C.-Y. 1988. Line spring method of stress-intensity factor determination for surface cracks in plates under arbitrary in-plane stresses. In: *Fracture Mechanics: Nineteenth Symposium* (ed. T. Cruse). ASTM International, pp. 657-668.
- Yang, J.C.S., Tsai, T., Pavlin, V., Chen, J. and Tsai, W.H. 1985. Structural damage detection by the system identification technique. *The Shock and Vibration Bulletin* 55. Shock and Vibration Information Center, pp. 57–65.
- Yang, Z., Chen, X., Yu, J., Liu, R., Liu, Z. and He, Z. 2013. A damage identification approach for plate structures based on frequency measurements. *Nondestructive Testing and Evaluation* 28(4), pp. 321–341. doi: 10.1080/10589759.2013.801472.
- Yavari, A., Sarkani, S. and Moyer, E.T. Jr. 2000. On applications of generalized functions to beam bending problems. *International Journal of Solids and Structures* 37(40), pp. 5675–5705. doi: 10.1016/S0020-7683(99)00271-1.
- Yazdani, S., Rust, W.J.H. and Wriggers, P. 2016. Delamination growth in composite laminates of variable stiffness. *International Journal for Numerical Methods in Engineering* 108(11), pp. 1406–1424.
- Yin, T., Lam, H.-F. and Chow, H.-M. 2010. A Bayesian probabilistic approach for crack characterization in plate structures. *Computer-Aided Civil and Infrastructure Engineering* 25(5), pp. 375–386.
- Zang, C. and Imregun, M. 2001. Structural damage detection using artificial neural networks and measured FRF data reduced via principal component projection. *Journal of Sound and Vibration* 242(5), pp.813–827.
- Zehnder, A.T. and Viz, M.J. 2005. Fracture mechanics of thin plates and shells under combined membrane, bending, and twisting loads. *Applied Mechanics Reviews* 58(1), pp. 37.
- Zhang, C. 2018. Postbuckling Analysis of Isotropic and Anisotropic Plates Assemblies Under Combined Loading. PhD Thesis, Cardiff University.
- Zhang, Y., Wang, L., Lie, S.T. and Xiang, Z. 2013. Damage detection in plates structures based on frequency shift surface curvature. *Journal of Sound and Vibration* 332(25), pp. 6665–6684.
- Zubaydi, A., Haddara, M.R. and Swamidas, A.S.J. 2000. On the use of the autocorrelation function to identify the damage in the side shell of a ship's hull. *Marine Structures* 13(6), pp. 537–551.